Effects of Thickness, Morphology and Molecular Structure of Donor and Acceptor Layers in Thermally Interdiffused Polymer Photovoltaics

Anamika Gopal

Dissertation submitted to the Faculty of the Virginia Polytechnic Institute and State University in partial fulfillment of the requirements for the degree of

Doctor of Philosophy
in
Physics

James R. Heflin
Richey M. Davis
Guy J. Indebetouw
Alfred L. Ritter
Hans Robinson

April 10, 2007
Blacksburg, Virginia

Key words: Organic Photovoltaics, Conjugated Polymers, Concentration Gradient Bulk Heterojunction, Interdiffusion

Effects of Thickness, Morphology and Molecular Structure of Donor and Acceptor Layers in Thermally Interdiffused Polymer Photovoltaics

Anamika Gopal

ABSTRACT

An in-depth study of concentration gradients in thermally-interdiffused polymer – fullerene photovoltaic devices, with a focus on thickness and heat treatments, is presented in this thesis. Device performance is improved from the bilayer by the creation of a concentration gradient of the donor and acceptor materials throughout the active layer of the device. Concentration gradients are expected to improve device performance by optimizing the charge transfer, transport and collection processes. This is achieved through heat-induced interdiffusion of the two materials at temperatures above the glass transition temperature of the polymer. Investigation of the poly(3-octylthiophene) (P3OT) – C_{60} system show a three-fold improvement in the external quantum efficiencies (EQE) as compared with bilayer devices.

Auger spectroscopy, combined with argon-ion beam milling, serves to record the concentration depth profile and identify concentration gradients in the device through detection of the sulfur in the P3OT backbone. Concentration gradients are optimized to yield the best devices through a thickness variation study conducted on the P3OT – C_{60} system for fixed thermal interdiffusion conditions at 118 °C for 5 minutes. An optimum thickness of 40 to 60 nm is obtained for the two materials that yields the ideal morphology of a concentration gradient as recorded by Auger spectroscopy. For such devices, the concentration gradient is seen to extend through the device, ending in a thin layer of pure material at each electrode. A monochromatic power conversion efficiency of 2.05% is obtained for 5.3 mW/cm^2 illumination at 470 nm.

A brief study is also presented to optimize the concentration gradient profile through variations of the thermal parameters. The dependence of the concentration gradient on the interdiffusion time and temperature is investigated. The merits of heat treatment on the crystallinity of P3OT and the overall device performance are also

discussed. It is shown in some case that devices with annealed P3OT layers show almost twice the EQE as non-annealed P3OT layer devices.

Potential alternatives for C_{60} in interdiffused devices with P3OT have been presented. [6,6]-phenyl C_{61}-butyric acid methyl ester (PCBM), a well-investigated acceptor for blend devices, is studied as an acceptor in concentration gradient devices. A method for spin-coating uniform bilayers of P3OT and PCBM, without solution damage to either layer, is presented. A thermal variation study of the interdiffusion conditions on this system indicated higher interdiffusion temperatures and times are preferred for P3OT – PCBM systems. For interdiffusion at 150 °C for ten minutes, EQE values approaching 35 % at 500 nm are obtained. Auger spectroscopy studies on this system yielded the same conclusions about the concentration gradient device morphology that gives optimum device output. 1:1 and 1:2 blends of P3OT – PCBM are also studied. The influence of various thermal treatments on these devices is described.

The endohedral fullerene $Sc_3N@C_{80}$ is introduced as a new acceptor material. The endohedral fullerene consists of Sc_3N cluster enclosed in a C_{80} cage. An order of magnitude increase is seen in device performance upon sublimation of these molecules on a P3OT layer confirming its effectiveness as an acceptor. Preliminary studies done on this system indicated the need for greater thermal treatment to produce optimum concentration gradients. An in depth study for varying temperatures and times is presented. The best device performance was seen for interdiffusion at 160 °C for 25 minutes. The endohedral fullerene devices also show a long-term deterioration and so best result are presented from a set of devices fabricated within the same time period.

The study of these three donor-acceptor systems confirms that the conclusions on the thickness dependence and device performance study conducted for the P3OT – C_{60} system extend to other acceptors.

A model of EQE for varying thicknesses based on absorption in the interdiffused concentration gradient regions is also presented. This model effectively highlights the influence of P3OT layer thickness on the trends observed in the EQE. It did not, however, reproduce the experimental thickness variation results for varying C_{60} thicknesses. Incorporation of the effects of the electric field intensity distribution is expected to correct for this. Suggestions have been given on how this might be achieved.

I would like to dedicate this thesis to the memory of the educators and students who lost their lives at Virginia Tech on the 16th of April, 2007.

Also,

To my family, especially my mom whose arms reached across the world to hold my hand through all my grad-school angst.

Acknowledgements

I would like to thank my advisor, Dr. Randy Heflin, for his unending support both in my academic and personal life. In addition to being an excellent advisor, he has gone beyond the call of duty and has been a true friend through some of the toughest years.

I would also like to thank Dr. Richey Davis for his patient discussions and valuable insight on the thermal aspects of this work. He often provided insight into aspects of my research that would never have occurred to me.

I am very grateful for all the help that was provided to me by every one in the department of physics; the professors and students for their constant encouragement, and the staff; Melvin Shaver, Scott Allen and John Miller from the machine shop, Fred Mahone and Dr. Norman Morgan from the electronics shop and Roger Link and Travis Heath who have all rescued me many times during the course of my research and without whom, I am convinced the sky would fall.

A special thanks goes to Frank Cromer for his tremendous patience, good cheer and encouragement, as well as the many, many, many hours of help with Auger Spectroscopy.

Thanks and a hug to Chris Thomas, all the help she has given me may be summed up in one word...'mommy'. She is a friend and mentor I will cherish for life.

The Snelgroves have been my home away from home, I would like to thank them for all the love, sanity, perspective checks, food and 6 brothers!

I would like to thank Cemil Durak, friend and brother, without whom this thesis would never have been completed.

Sallie, Irene, Josh, Patty, Dean and Brian, a big 'thank-you' to them for all the 5am wake-up calls and hugs!

Thanks to Swapnil Jawkar, Mathew Raum and Jennifer Steding for all the de-stressing, unconditional love and patients...*so* much patients! I am surprised they survived my graduation!

Thanks to Jason Ridley who gave me the love I needed to succeed and the motivation to graduate.

I am grateful for financial support of this work by the National Science Foundation through grant ECS-0524625 and the Air Force Office of Scientific Research*

under contracts FA9550-05-C-0146 and FA9550-06-C-0010, especially Dr. Martin Drees who continued to be my 'senior' and provided me with helpful insights well after his graduation and through out our recent collaborations with Luna nanoWorks.

I would also like to thank Dr. Nibir Dhar, Dr. Gomatam Jagannathan and Dr. Fred Semendy for the many useful discussions and for all their encouragement and support.

A very special 'thank you' to everyone at home; my professors Dr. A. Kumaraswamy and Dr. Harshad Parekh who will always be my role models in physics and in life, my friends, Aditi Kulkarni, Aparajita Sengupta, Deepti Vikram, Subhangi Ghosh, Amit Bothe, Harshad Joshi and Sarita Hardas whose support through the various stages of growing up both personally and in the subject, mean more and more to me with each passing year and my family for always being there for me all my life and making me who I am.

Last, but not least, these years have given me faith that there is a divine presence who helps us make sense of this world. In the light of the recent tragedy, I am grateful for life and for the strength I am being given to live it.

TABLE OF CONTENTS

List of Figures

CHAPTER ONE

CHAPTER TWO

CHAPTER THREE

CHAPTER FOUR

CHAPTER FIVE

CHAPTER SIX

CHAPTER SEVEN

CHAPTER EIGHT

List of Tables

CHAPTER ONE

CHAPTER TWO

CHAPTER THREE

CHAPTER FOUR

CHAPTER FIVE

CHAPTER SIX

CHAPTER SEVEN

CHAPTER EIGHT

CHAPTER ONE

Motivation and Outline

This thesis presents work done to improve the power conversion efficiency of organic photovoltaic devices through the nanoscale control of the morphology of thermally-induced concentration gradients between polymer donor and fullerene acceptor materials. A thickness variation study was conducted to determine the optimum concentration gradient profile to maximize device output. This profile is monitored through Auger spectroscopy. P3OT (poly(3-octylthiophene)) and C_{60} serve as the donor and acceptor, respectively, for the main part of this work. The optimum thicknesses are discussed in terms of the concentration gradient extending throughout the majority of the film and having a center near the position of an antinode in the optical intensity distribution in the film. A brief study on other parameters, besides layer thickness, that could be adjusted to optimize the concentration gradient, is also presented. A fullerene derivative and the endohederal fullerene $Sc_3N@C_{80}$ as alternative acceptor materials that could replace C_{60} are also briefly introduced. Finally, a model is constructed, based on the absorption of light in the device, to theoretically predict the thickness dependence trends observed through experiments.

1.1 Motivation

The last century and a half has seen an exponential growth in technology and consequently, also energy requirements. The current world consumption is around 13 terawatt-years and is expected to reach 30 terawatt-years by the year 2050. The main source of energy today is from fossil fuels which include coal, oil and gas. All of these are limited and fast disappearing. Also, the byproducts of the accelerated consumption of these resources have led to major environmental and climatic deterioration. These issues have recently motivated the search for alternative sources of energy. The most commercially-viable alternative available today is nuclear energy. While this is not based on the consumption of the carbon-based fuels, the disposal of hazardous nuclear waste is

proving to be a major problem. An ideal alternative would be a clean and renewable source of energy. Renewable energy relies on virtually inexhaustible sources. Some of the most popularly investigated renewable sources are biomass, hydropower, geothermal energy, wind energy and solar energy. There is roughly 125,000 terawatts of solar power incident on the earth at any point in time. Efficient harnessing of this energy could potentially satisfy the world's energy requirements. ***Figure 1.1*** shows a breakdown of the electrical energy generation of the U.S. in 2004. Renewable sources accounted for 9% of the energy generation of which 0.2% was solar energy.[1]

One of the ways in which solar energy is harnessed is through photovoltaic (PV) systems that harness solar light energy and convert it to electrical energy. PV systems are generally configured into modules that each generates electric power. These are locked in a grid like system that can collectively harness this power to generate electricity.

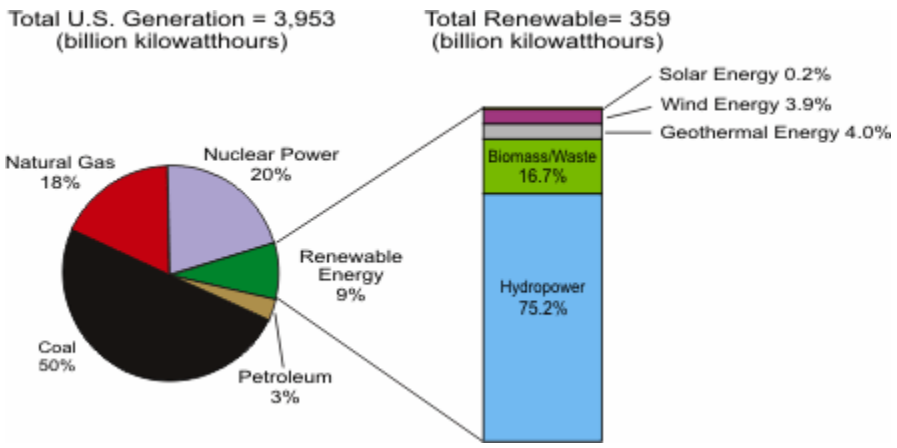

Figure 1.1 Electric power generated in the U.S. in 2004, shown in terms of the energy sources. Renewable energy constitutes 9% of which solar energy is 0.2%. (Source: http://www.eia.doe.gov/neic/brochure/renew05/renewable.html).

Commercially-available PV systems utilize inorganic materials and are predominantly wafer-based crystalline silicon modules, accounting for over 93% of the PV cell distribution in 2006. The most efficient of these are the single crystal silicon (sc-Si) cells. Silicon cells generally have band gaps of the order of visible light. In p-n junction Si cells, n-type doped Si and p-type doped Si are brought in contact to form a junction. The doping in the n-type Si results in an excess of electrons in the crystal lattice while the doping of the p-type yields electron deficient sites (holes). When brought in

contact, the energy difference between these two materials results in band bending that can induce spontaneous flow of excited electrons in the conduction band. When light is absorbed, photoexcitation promotes electrons to the conduction band which then flow along the bent band and are collected as photocurrent. This process will be explained in greater detail in the section 2.1.

One main limiting factor is the theoretical limit for efficiency in a single crystal p-n junction type solar cell, as reported by Shockley and Queisser.[2] The current generated is a function of the number of electrons that can be excited to the conduction band. This will increase as the band gap of the material reduces for a given illumination because a greater fraction of the spectrum is collected. On the other hand, voltages obtained from these devices are directly dependent on the band gap. Hence, decreasing the band gap would result in a decrease in the voltage of the device due to thermalization of carriers to the bottom of the band. The overall efficiency of a device is dependent on the product of the voltage and the current of the device and hence, for a given spectral illumination, there is an optimum band gap that yields a theoretical maximum for the efficiency of a device. This turns out to be only around 31% for 1 sun solar irradiation, AM1.5 (~100 mW/cm^2). AM1.5 or Air Mass 1.5 is the solar spectrum that is measured at sea level.

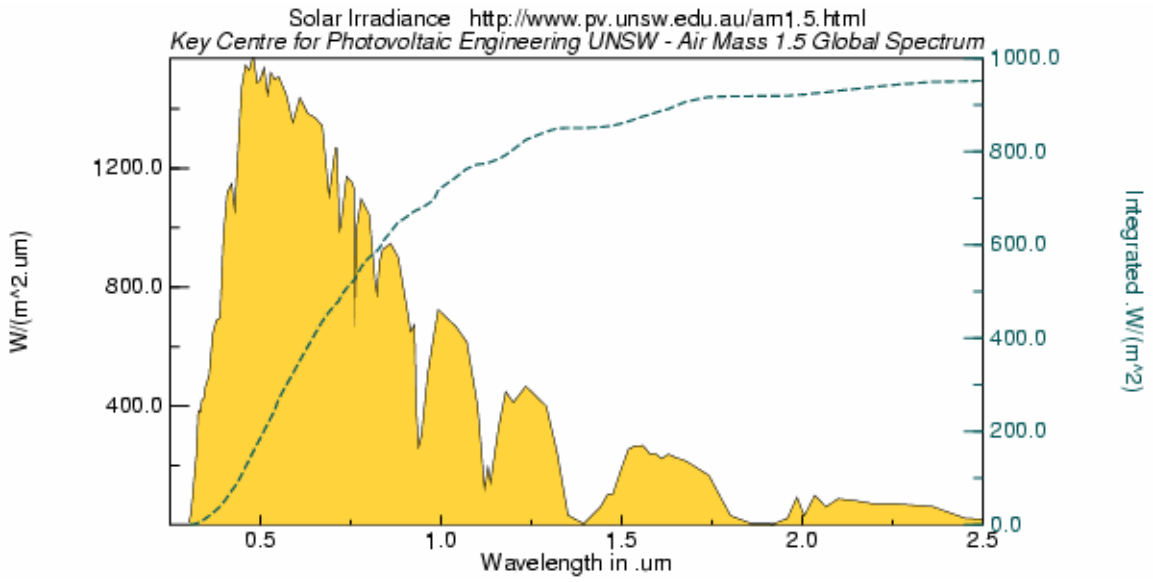

Figure 1.2 The solar spectrum for AM1.5 irradiation. (Source: http://www-swiss.ai.mit.edu/~jaffer/Docupage/grapheps).

Figure 1.2 shows the AM1.5 Global Spectrum, which considers a global clear sky intensity for spectrum generation. Currently, the highest reported sc-Si (1.1eV bandgap) cell efficiency under AM1.5 illumination is 24%.[3] CdTe or GaAs are popular alternatives for sc-Si and constitute a second generation of semicondutors. GaAs shows a higher efficiency, up to about 27.8%, due to a more appropriate band gap of around 1.5eV. These cells are more or less in the lab research phase as compared to sc-Si which still dominates the market. A third generation of inorganic photovoltaics is being investigated that go beyond the single junction morphology, known as tandem cells. These cells can exceed the theoretical efficiency limits imposed on single p-n junction cells.

One of the major issues with inorganic solar technology is the cost of production. If a 20-year life span is assumed for a typical inorganic PV system, based on the power generated over the lifetime of the system and initial cost of fabrication and installation, the average cost of photovoltaic energy works out to between $0.25 to $0.65/kilowatt-hour. This is rather expensive when compared with the current cost of around $0.04/kilowatt-hour for coal-based energy used today.[4] Organic photovoltaic devices are currently being heavily researched because of their potential for far lower costs than silicon solar cells as well as the possibility of lightweight, large area, flexible devices.

Research in organic photovoltaics is part of a growing trend of the study of organic materials in electronics and optoelectronics fields. Potential annual global sales of organic electric and electronic products were predicted to be at $96 billion by the year 2020 of which $15.2 billion is predicted to be in the power sector.[5] These figures were supplied by IDTechEx, which is a knowledge-based consultancy company that provides research and analysis on organic electronics amongst other areas. For photovoltaic applications, organics tend to have high optical absorption coefficients that would allow for efficient light harvesting with thin films of just a few hundred nanometers. Also, since many of the organic materials are soluble in organic solvents, they may be deposited from solution, which would considerably reduce fabrication costs. They are compatible with plastic substrates and can be produced on a large scale by using the roll to roll process.

1.2 Organic Photovoltaics – Polymer Solar Cells

In polymer (or plastic) solar cells, semiconductors like Si and GaAs are replaced by long chain conjugated polymers that demonstrate similar semiconducting properties and can be used for light-induced current generation. In addition to the cost benefits mentioned above for organic materials in general, the band gaps and other optical properties of these materials can be easily tuned through appropriate alterations to the molecular structure of the repeat units. The main challenge with these materials is charge separation of the photo-excited electrons. In one class of polymer photovoltaics, this is achieved through combination of the polymer with high electron affinity fullerenes (C_{60}) and fullerene-based molecules. Ultrafast charge transfer of the photo-excited electrons to a nearby C_{60} molecule in blends of the conducting polymer poly(2-methoxy-5-(2'-ethylhexyloxy)-1,4-phenylenevinylene) or MEH-PPV with the fullerene has motivated a large part of polymer PV research today.[6] A criterion for the charge transfer to occur is the proximity of the fullerene to the site of excitation, which was established to be around 5 to 10 nm.[7,8] (This process, as well as the brief explanation that follows on the development of polymer photovoltaics, will be expanded upon in the next chapter). Photo-excited electrons that do not transfer will recombine with their respective holes to generate photoluminescence. Ultrafast charge transfer is a spontaneous process that occurs within 300 fs,[9] about 10^3 times faster than the photoluminescence lifetime. Hence, if proximity of the two molecules is established, there is almost a 100% probability of charge transfer occurring.

Early devices were bilayers of donor and acceptor molecules which consisted of two layers of the pure materials and a sharp interface between them.[10] These devices displayed low efficiencies since the active region where any charge transfer could occur was restricted to the thin interface, wasting any light absorption that might occur more than 10 nm away from this region. Subsequently, the active charge-separation region was improved by blending the donor and acceptor molecules.[11,12] In this case, the whole film consists of donor – acceptor interfaces and is referred to as a "bulk heterojunction device". For such a device construction, anywhere in the device that light is absorbed,

there will be an acceptor nearby to induce charge transfer. The device efficiencies increased by almost 2 orders of magnitude compared to bilayer devices.

Once this charge separation occurs, the next challenge faced is the transport of the charges to the electrodes on either side of the active layer, where the charges are collected as photocurrents. This process occurs by the hopping of the charges from one molecule to the next till they reached their respective electrode. The acceptor then acts as the electron transporting medium and the polymer transports the hole that is left in its conduction band after electron transfer. This process relies on the existence of a well-connected path of each species from the site of charge transfer to the electrodes. A homogeneous blend can hinder this process by reducing the connectivity between molecules of a species. This issue was recently addressed in blends with the polymer poly(3-hexylthiophene) and soluble C_{60} derivative, (phenyl-[6,6]-C_{61})-butyric acid methyl ester (PCBM). Heat treatment induced phase separated regions with enhanced crystallinity and mobility within the film that greatly enhanced efficiencies of devices (up to almost 5% power conversion efficiency for the P3HT – PCBM system).[13] Such blend systems will be discussed in more detail in section 2.9.1. But there still exists the problem of charge hopping between these regions of high crystallinity. Also, blend devices have a random distribution of the donor and acceptor material. One type of charge is collected at each electrode and hence collection efficiency would be reduced if a random distribution of both materials were found at each electrode instead of just a layer of pure material that carries the charge to be collected.

Device optimization may be achieved by balancing these three processes through a device construction that consists of a bulk heterojunction at the center of the active layer of the device that gets progressively purer as the electrodes are approached, increasing the charge transfer efficiency and finally ending in a pure material at the electrode to facilitate charge collection. This is achieved by creating a concentration gradient of the two materials that consists of a homogeneous mix at the center and a tapering of the concentration of each material as the other material is penetrated, completely disappearing at the electrode.

Creation of concentration gradient devices have been proposed in a number of ways in literature. In one method, the donor and acceptor layers are deposited from

solution on top of each other. The acceptor layer is doctor bladed onto the device from a solution that partially dissolves the donor layer below, hence inducing the solution-motivated diffusion of the acceptor into the donor.[14] In another method, which is especially viable for polymer-donor and polymer-acceptor devices, the polymer films are deposited on separate substrates and are brought in contact and thermally laminated so that they interdiffuse and fuse together while retaining the pure layer at the electrodes.[15] A detailed discussion of these methods can be found in section 2.9.2.

In this thesis, concentration gradient devices are fabricated by thermal interdiffusion of an initial bilayer of the polymer donor and fullerene acceptor layers at temperatures above the glass transition point of the polymer.[16,17] At such temperatures, the polymer is in a soft rubbery phase that will allow the fullerene molecules to diffuse in, creating a concentration gradient. The extent of this diffusion is controlled by monitoring the concentration depth profile and accordingly adjusting the thicknesses of the layers so as to maximize the gradient without compromising on the purity of the materials at the electrodes. An expanded outline of the thesis is given in the next section.

1.2 Outline of Thesis

Chapter Two gives a review of the basic principles of inorganic solar cells as an introduction to the photovoltaic process. The various experimentally measured and calculated parameters such as the photoresponsivity, external quantum efficiency, open circuit voltage, fill factor and overall power conversion efficiency are explained in terms of inorganic photovoltaics but are pertinent to organic photovoltaics, too. Polymer photovoltaics are introduced with a review of the historic evolution of organic materials used for photovoltaics that lead us to the point we are at today in the field. A brief explanation is given on conjugated polymers and what make them conductive. This is followed by an overview of the organic photovoltaic process, involving detailed discussions on the mechanisms of photo-excitation, charge separation and charge transport and the various factors that might hinder these processes. The organic photovoltaic process and the current – voltage characteristic curves are then explained in terms of an analogous equivalent circuit diagram. This is followed by a discussion of the

material dependence and the device fabrication and construction dependence of the PV devices. This leads to a discussion on the various morphologies that are investigated to optimize device performance after which the thermally induced concentration gradient device that is the focus of this work is introduced.

Chapter Three explains the experimental procedures that were followed in our reserach. Detailed descriptions are given of the device construction and experimental set-ups used to both fabricate as well as characterize the photovoltaic devices. Theoretical considerations of the processes of heat and mass transfer that are expected to occur during the thermal interdiffusion are also given. Auger spectroscopy is explained as a method to investigate the concentration depth profile into the film to observe the concentration gradient. Ellipsometry is briefly described as a method to deduce the real and imaginary refractive indices of the principal materials under consideration. Finally, a description of the active layer as well as electrode materials used and their optical properties is given.

The main body of the work done on the primary materials of this thesis is found in Chapter Four. For this part of the work, the donor considered is poly(3-octylthiophene) (P3OT) and the acceptor is the buckminsterfullerene, C_{60}. Single polymer-layer, bilayer and blend morphologies for the P3OT – C_{60} system are briefly discussed before delving into thermally-induced concentration gradient devices, which is the main device construction under consideration. In the work, device quality and possible improvements are discussed through analyses of the features of the measured external quantum efficiency curves and current density – voltage characteristics throughout the rest of the thesis. The investigation into the concentration gradient devices is begun with a study on the thickness dependence of device performance. Interdiffusion conditions are fixed and the P3OT and C_{60} layer thicknesses are varied, each over a range from around 10 nm to 110 nm. This yields starting thickness values for the two layers that show the best device performance. The optimum concentration profile is deduced from the Auger spectroscopy data for the best devices from this study. Brief studies, supported by Auger spectroscopy data, on the effects of varying interdiffusion times and temperatures on the concentration gradient and device performance are also given. These are expected to serve as a starting

point for further investigation into improving concentration gradient devices and thereby concludes our experimental study of the P3OT – C_{60} system.

In Chapters Five and Six, the alternative fullerene-based materials are discussed as possible replacements for C_{60} as acceptor in concentration gradient devices. Chapter Five gives an initial study of the P3OT – PCBM system. Due to the highly soluble nature of PCBM, it is generally used in blend devices. In this study, it has been studied in bilayer and thermally-interdiffused devices, in addition to 1:1 and 1:2, P3OT:PCBM blends. Different thermal treatments have been carried out on these devices to attempt to optimize the interdiffused-devices as well as the blend devices. The effects of crystallinity of the polymer layer on device performance are investigated by comparing devices that were made with annealed and non-annealed P3OT layers, prior to PCBM deposition. The effect of heat treatment post-aluminum deposition is also investigated.

Chapter Six introduces a new potential acceptor material: the endohederal fullerene trimetasphere (TMS), $Sc_3N@C_{80}$. It consists of a Sc_3N cluster enclosed in a C_{80} cage. This material is of interest because its band gap can be easily tuned by changing the metal that is encaged, allowing for tunable acceptor materials. Since this is the first investigation with this acceptor, the main study that was done was to deduce a suitable temperature for interdiffusion of this material into P3OT. This study is also supported by Auger spectroscopy. The optimum concentration gradient profile from Chapter Four is used as the template while examining the concentration gradients obtained for these devices, and from this the optimum interdiffusion conditions are deduced for this system. Data is presented for interdiffusion that occurs above and below this set of optimum conditions.

Chapter Seven presents a simple theoretical study done to model the spectral efficiency of the concentration gradient devices based on Beer's law of absorption in a medium. This model mainly considers absorption of light in the interdiffused, concentration gradient region flanked by pure materials on either side. External quantum efficiency values are calculated under the assumption that these values will be proportional to the energy absorbed in the film during this process. The thicknesses are included as variable parameters and in this way EQE curves are modeled for varying thicknesses and compared with experimental data. Comparison are made with experiment

for the P3OT – C_{60} system. This model has left out the very important consideration of electric field distribution within the device. Suggestions have been made as to how this may be incorporated.

The thesis ends with a chapter on the conclusions reached from the individual studies of the various systems and their concentration gradients. Suggestions are also made for future work that might be done to further improve the quality of thermally-induced concentration gradient devices.

---

[1] http://www.eia.doe.gov/neic/brochure/renew05/renewable.html
[2] W. Shockley, H.J. Queisser, "Detailed Balance Limit of Efficiency of *p-n* Junction Solar Cells," *J. Appl. Phys.* **32**(3), 510-519 (1961).
[3] M.A. Green, *et. al.*, "Solar Cell Efficiency Tables (Version 28)," *Prog. Photovolt: Res. Appl.* **14**, 455-461 (2006).
[4] A. Slaoui, R.T. Collins, "Advanced Inorganic Materials of Photovoltaics," *MRS Bulletin* **32**(3), 211-214 (2007).
[5] http://www.idtechex.com/products/en/view.asp?publicationid=117
[6] N.S. Sariciftci, L. Smilowitz, A.J. Heeger, F. Wudl, "Photoinduced Electron Transfer from a Conducting Polymer to Buckminster Fullerene," *Science* **258**, 1474-1476 (1992).
[7] D. Vacar, E. S. Maniloff, D. W. McBranch, A. J. Heeger, "Charge-Transfer Range for Photoexcitations in Conjugated Polymer/Fullerene Bilayers and Blends," *Phys. Rev. B* **56**(8), 4573-4577 (1997).
[8] J.J.M. Halls *et al.*, "Exciton Diffusion and Dissociation in a Poly(*p*-Phenylenevinylene)/C_{60} Heterojunction Photovoltaic Cell," *Appl. Phys. Lett.* **68**(22), 3120-3122 (1996).
[9] B. Kraabel, *et al.*, "Ultrafast Spectroscopic Studies of Induced Electron Transfer from Semiconducting Polymers to C_{60}," *Phys. Rev. B* **50**(24), 18543-18552 (1994).
[10] N.S. Sariciftci, L. Smilowitz, A.J. Heeger, F. Wudl, "Semiconducting Polymers (As Donors) and Buckminsterfullerene (As Acceptor): Photoinduced Electron Transfer and Heterojunction Devices," *Synth. Met.* **59**, 333-352 (1993).
[11] G. Yu, *et al.*, "Polymer Photovoltaic Cells: Enhanced Efficiencies Via a Network of Internal Donor-Acceptor Heterojunctions," *Science* **270**, 1789-1791 (1995).
[12] G. Yu, A.J. Heeger, "Charge Separation and Photovoltiac Conversion in Polymer Composites with Internal Donor/Acceptor Heterojunctions," *J. Appl. Phys.* **78**(7), 4510-4515 (1995).
[13] W. Ma, *et al.*, "Thermally Stable, Efficient Polymer Solar Cells with Nanoscale Control of the Interpenetrating Network Morphology," *Adv. Funct. Mater.* **15**, 1617-1622 (2005).
[14] C.J. Brabec, *et. al.*, "The Influence of Materials Work Function on the Open Circuit Voltage of Plastic Solar Cells," *Thin Solid Films* **403-404**, 368-372 (2002).
[15] M. Granström, *et al.*, "Laminated Fabrication of Polymeric Photovoltaic Diodes," *Nature* **395**, 257-260 (1998).
[16] M. Drees, *et al.*, "Creation of a Gradient Polymer – Fullerene Interface in Photovoltaic Devices by Thermally Controlled Interdiffusion," *Appl. Phys. Lett.* **81**(24), 4607-4609 (2002).
[17] M. Drees, R.M. Davis, J.R. Heflin, "Improved Morphology of Polymer – Fullerene Photovoltaic Devices With Thermally Induced Concentration Gradients," *J. Appl. Phys.* **97**, 036103 (2005).

CHAPTER TWO

Theoretical and Historical Background to Inorganic and Organic Solar Cells

The basic theoretical aspects of organic photovoltaics are discussed in this chapter. We start with a review of the basic principles of inorganic solar cells in order to define parameters that are common to both the organic and inorganic cases. Organic photovoltaics is introduced with a brief historic back ground that explains the evolution of this field to where it's at today. The theory behind the working of an organic solar cell is given, with detailed descriptions of the charge transfer and transport processes; the factor that influence and hinder them. In order to gain an understanding of measured I-V characteristics, the photovoltaic cell is explained in terms of an equivalent circuit diagram and aspects of the I-V curves are explained using this. A discussion of the experimental parameters such as materials and device morphologies that affect device performance is given. Finally, thermally induced concentration gradient devices are introduced.

2.1 Inorganic Solar Cells

The first solar cells were inorganic. A brief discussion of the physics of inorganic solar cells will provide a good foundation for the understanding of their organic counterparts.

Inorganic solar cells consist of a junction of p-type and n-type semiconductors sandwiched between metal electrodes for charge collection. These semiconductors have band gaps primarily corresponding to near infrared radiation. The most studied semiconductor for photovoltaics is silicon (Si). The crystal has perfect balance with four valence electrons that are covalently bonded symmetrically through the crystal. It is then doped by introducing an impurity which has a similar structure to the host crystal but with either 3 or 5 valence electrons to generate either a p-type or an n-type semiconductor, respectively. When the dopant has 3 valence electrons and these atoms are incorporated into the crystal, there will be a "hole" at the site of the dopant atom

where a bond is missing. Although the p-type material is electrically neutral, taking an excess electron to complete the symmetry of the crystal structure is thermodynamically favorable. Similarly, in n-type semiconductors, the dopant has 5 valence electrons yielding an extra, free electron in the lattice which, does not fit in with the existing crystal structure. When the p-type and the n-type semiconductors are brought in contact, the excess electrons from the n-type semiconductor diffuse to fill the interstitial holes in the p-type semiconductor lattice. As this diffusion occurs at the junction, the p-type material gets progressively more negative and the n-type material more positive, creating a static space charge distribution on either side of the junction. These charges create an electrostatic field that keeps increasing and opposing the diffusion process until, finally, equilibrium is reached, and there is no more net diffusion. The region of the distributed space charges is called the depletion region.

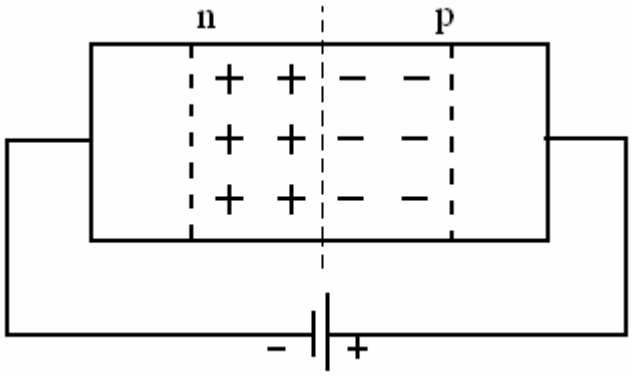

Figure 2.1 Depletion region in an p-n junction under external forward bias.

Figure 2.1 shows the depletion region under an external forward bias; positive terminal connected to the p-type side and negative terminal connected to the n-type side. Under a forward bias voltage, the depletion region reduces, and the forward bias current increases. As this forward bias is increased the depletion region keeps reducing until it disappears and the forward bias current shoots up exponentially. In contrast, fot reverse bias (inverted terminals), as the voltage is increased, the depletion region grows in width. There is only a leakage current that comes from the thermally excited electrons that flow along the biasing. This gives rise to the diode like behavior of the current-voltage characteristics.

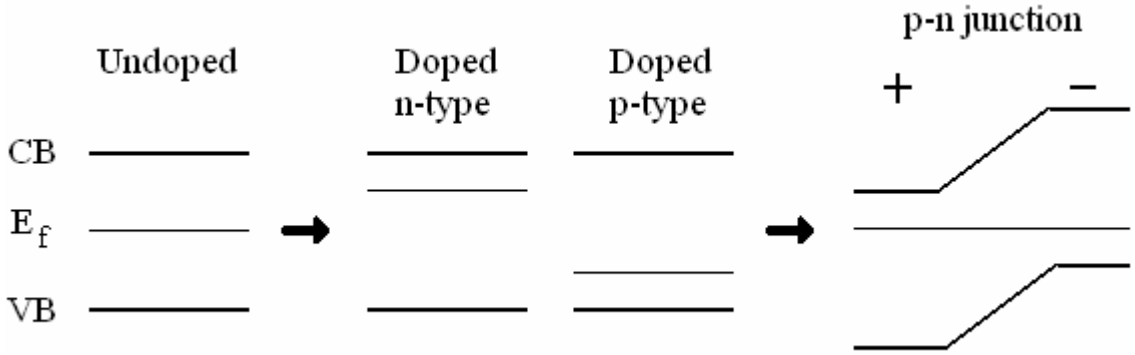

Figure 2.2a Schematic to demonstrate band bending at a p-n junction.

In the band picture, the un-doped state of the crystal has its Fermi level located in the middle of the valence band (VB) and conduction band (CB) edges. Upon doping, the Fermi level moves closer to the conduction band in the n-type semiconductor and closer to the valence band in the p-type semiconductor. When these two materials are brought in contact, to overcome the thermal instability of discontinuous Fermi levels at the junction, band bending occurs at the junction as seen in Figure 2.2a. This region of band bending is the depletion region with the resulting electrostatic field due to build up of space charges mentioned in the previous paragraph[1].

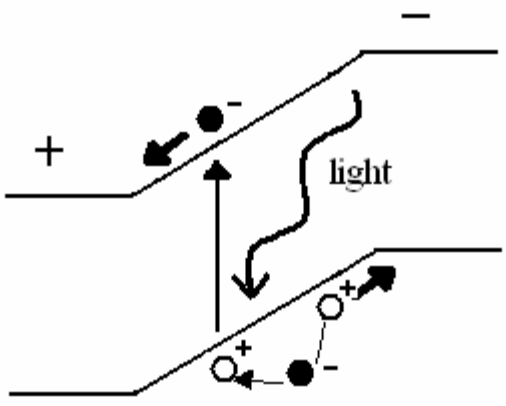

Figure 2.2b Photocurrent generation.

When light shines on this system, photoexcitation occurs and electrons are excited from the valence band to the conduction band. These electrons move spontaneously down

the band to regions of lower energy, leaving holes in the valence band. Electrons, higher in energy and adjacent to these holes will also reduce their energy by hopping down the band to occupy the existing holes, thereby creating holes of slightly higher energy, resulting in a hole current migrating up the valence band. This process is depicted in Figure 2.2b. The electrons and holes migrate till they reach their respective electrodes where they are collected as photocurrents. From the point of view of Figure 2.1 photo-separated electrons and holes are guided by the electrostatic field established by the charge distribution in the depletion region giving rise to photocurrents. Hence the main requirements for a solar cell are materials displaying energy band structures with band gaps of the order of visible light so that photoexcitation can occur and energies that are offset so as to establish a field that will separate these charges and guide them in opposite directions so they can be collected as photocurrents.

2.2 Characterizing Solar Cells

When light shines on a solar cell, the current that is measured is called the photocurrent. The value of the photocurrent is dependent on many factors in addition to just the quality of the device. For example, different photocurrents will be obtained depending on the wavelength or intensity of the incident light or the area of the device that is illuminated. Hence the photovoltaic response should be reported in terms of quantities that are universally comparable.

2.2.1 Photoresponsivity and External Quantum Efficiency

The photoresponsivity (PR) and external quantum efficiencies (EQE) are reported from the current measurements made under illumination, when no external bias is applied. They are wavelength dependent quantities. Photoresponsivity is defined as the conversion efficiency of light to electrical energy and is given by:

$$PR(\lambda) = \frac{I_{SC}(\lambda)}{P_{source}(\lambda)} \tag{1}$$

Here $I_{SC}(\lambda)$ is the short circuit current (the value of the current obtained for a specific illumination wavelength) when no voltage is applied across the device. $P_{source}(\lambda)$ is the power of the illumination for a specific wavelength, at the point of incidence on the device. Photoresponsivity is generally reported in units of mA/Watt.

EQE is defined as the conversion efficiency of incident photons to extracted electrons. As per the definition, it is given by:

$$EQE(\lambda) = {N_e}/{N_{ph}} \tag{2}$$

Here N_e is the number of electrons extracted and N_{ph} is the number of incident photons. The EQE can be determined from the photoresponsivity by:

$$EQE(\lambda) = \left(\frac{hc}{e}\right) \times \left(\frac{PR(\lambda)}{\lambda}\right) \tag{3}$$

Here, h is Plank's constant, c is the speed of light in vacuum, and e is the charge on an electron. EQE has no units and is usually expressed as a percentage.

Although it is not evident in the formulae, these quantities are normalized with respect to the area of illumination on the device; when reporting the power of the lamp source ($P_{source}(\lambda)$), it is the intensity of the lamp source, for a particular wavelength, multiplied by the area of illumination that is reported.

2.2.2 IV Characteristics – Fill Factor and Power Conversion Efficiency

The current-voltage (IV) characteristics are obtained by applying a variable voltage and measuring the current obtained. These characteristics are generally measured in the dark as well as under monochromatic and solar spectrum illuminations. In the dark, the cell displays regular diode-like characteristics with the curve passing through the origin as seen in Figure 2.3a.

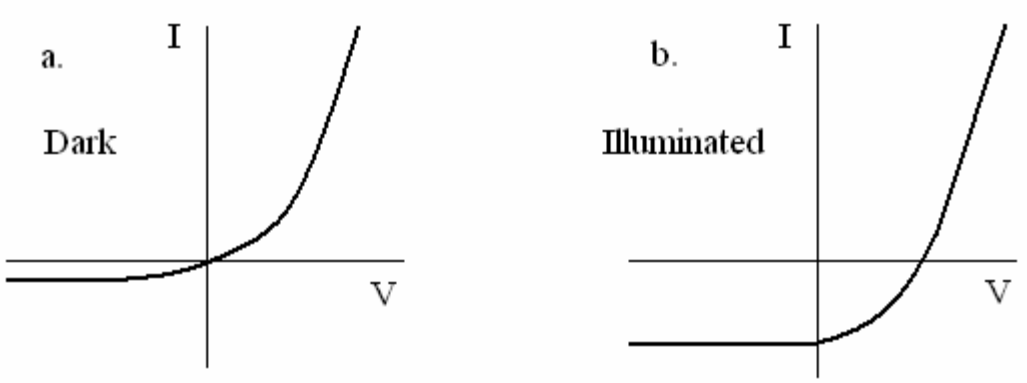

Figure 2.3 Current – Voltage (I-V) characteristics for solar cells (a) in the dark and (b) under illumination.

Under illumination, a non-zero photocurrent, called the short circuit current (I_{SC}), is observed for zero applied voltage. Photo-generated electrons move down the band, from the p-type to the n-type semiconductor side, opposite to the forward bias direction. This negative photocurrent shows up as a curve in the fourth quadrant of the IV characteristics (Figure 2.3b). As the forward bias is increased, this reverse photocurrent reduces. When explained in terms of the band picture, the applied voltage reduces the energy offset, and hence, the extent of band bending. This decreases the driving potential of the photo-generated charges, reducing the photocurrent. The value of the external bias at which the photocurrent is zero is called the open circuit voltage (V_{OC}) and when the biasing crosses this value, majority carriers take over and an exponentially increasing current in the forward bias direction is measured.

IV characteristics are often reported on a semi-log scale. The difference between the asymptotes of the forward bias and reverse bias curves is the rectification of the device which is an indicator of the diode-like quality of the device. Sometimes devices can have a slight ohmic quality due to pin shorts between the electrodes that reduces the rectification. Hence, the greater the rectification, the better the quality of the device.

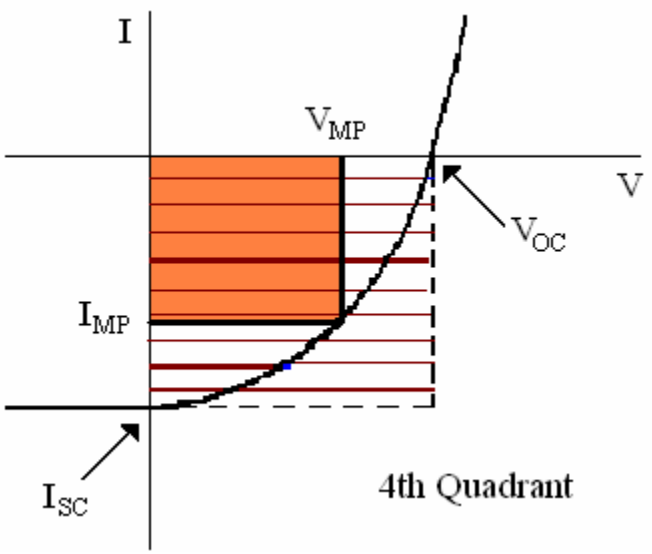

Figure 2.4 4th quadrant of the illuminated I-V characteristics. Solid shaded area is the max power measured and the striped area is the ideal power of the device.

Figure 2.4 shows a close up of the fourth quadrant of the IV characteristics where the main photovoltaic behavior is seen. The y-axis and x-axis intercepts are the short circuit current (I_{SC}) and open circuit voltage (V_{OC}) respectively. At any point, the power output of this device is given by the product of the current and voltage at that point. I_{MP} and V_{MP} are the measured current and voltage values at which the device has the maximum power output (P_{max}). P_{max} is then given by the product of these two values and seen in the diagram as the area of the smaller shaded rectangle. Ideally, when a forward bias is applied, till the voltage crosses the V_{OC} value, there would be no reduction in the photocurrent, and after it is crossed, the forward bias current should immediately become exponentially large. The ideal behavior is given by the dashed curve and the shaded area under this curve (the larger rectangle), which is the product of the V_{OC} and the I_{SC}, is the power (P_{ideal}) of an ideal device. The fill factor (FF), which is the measure of the quality of the IV characteristics of a solar cell, is then given by:

$$FF(\lambda) = \frac{P_{\max}(\lambda)}{P_{ideal}(\lambda)} = \frac{V_{MP} \cdot I_{MP}}{V_{OC} \cdot I_{SC}} \tag{4}$$

This quantity is unitless and works out to be the ratio of the areas of the smaller and larger shaded rectangles from Figure 2.4. It is wavelength dependent since the illuminated IV characteristics are obtained either under monochromatic illumination or under simulated solar light.

The power conversion efficiency (η), which is the overall efficiency of a solar cell under illumination, is given by:

$$\eta(\lambda) = \frac{P_{\max}(\lambda)}{P_{source}(\lambda)} = \frac{V_{MP} \cdot I_{MP}}{P_{source}(\lambda)} = \frac{FF \cdot V_{OC} \cdot I_{SC}}{P_{source}(\lambda)} \quad (5)$$

This is the efficiency of extracted electrical power for inputted optical power. It is unit-less and wavelength dependent and is usually quoted as a percentage. It should be noted that the fill factor is an indicator to the effectiveness of the device fabrication process since it compares the power obtained experimentally to the power that could have been obtained had the same device performed ideally. The power conversion efficiency on the other hand indicates the overall efficiency, which includes not only the quality of device fabrication but also the choice of materials and morphology of the devices.

Presented above in this section were the definitions of the quantities that are reported to characterize a solar cell in general. While these definitions hold true for both organic as well as inorganic devices, the physics behind the origins as well as the limitations of these quantities will be discussed in more detail in the organic photovoltaic section.

2.3 Organic Photovoltaics – An Introduction

Organic solar cells consist of conjugated molecules or semiconducting polymers as donor and acceptor materials sandwiched between electrodes where the donor plays a role similar to the p-type and the acceptor, the n-type material, analogous to an inorganic solar cell. Early work, from more than half a century ago, used different structures , however. The next section gives a brief historic overview of the evolution of organic photovoltaics to its current form. The subsequent sections will discuss the theory behind the functioning of today's organic solar cells.

2.3.1 Historic Evolution of Organic Photovoltaics

One of the early ideas to use organic materials for photovoltaics came from observation of nature where plants convert light to energy using chlorophyll through the

process of photosynthesis. This motivated a study of photon-induced electrical phenomena in biomaterials and organic dyes.[2] Early devices consisted of either a liquid active layer of chlorophyll solutions or microcrystalline films of chlorophyll[3] sandwiched between metal electrodes with offset work functions. Other dyes, that were analogues of chlorophyll, such as phthalocyanines,[4] were also combined with electron acceptor materials to increase charge carrier production and lifetimes. These materials were poor conductors and photovoltaic cells using such materials yielded power conversion efficiencies orders of magnitude below 1%.

The discovery of conducting polymers by doping of conjugated polymers, such as polyacetylene with halogens,[5] sparked the investigation into the electronic properties of these materials[6] with an emphasis on their conductive processes. It was discovered that, in some cases, the electrical conductivity of these polymers could be varied over eleven orders of magnitude by varying dopant concentrations.[7] Over a decade later, when electroluminescence was observed in PPV (poly (*p*-phenylene vinylene)) films,[8] the semiconducting properties of conjugated, conducting polymers and their potential use in flexible large area light emitting displays, were brought into focus. Subsequently, it was shown that these materials could be used as photodetectors by simply inverting the electroluminescent system[9] so that light was incident on the sample and the current and voltage generated were measured. Although these initial devices had a rather low current output, this triggered the interest in conducting polymers for organic photovoltaics. A more detailed explanation of conducting polymers will be given in section 2.3.2 of this chapter.

The conducting polymers in the initial studies were insoluble and to obtain them in film form involved lengthy processing of precursor forms of the polymer. They could also be grown electrochemically on an electrode coated substrate.[10] The development of solution processible conducting polymers[11] by suitable funtionalization rendered applications involving these polymers more commercially viable.

The first conductive polymer photovoltaic devices were mainly single layer devices with a pure polymer layer sandwiched between the electrodes.[10,12] These were basically Schottky diodes, where the nature of the electrodes and the metal-semiconductor junction determined the photovoltaic behavior of the device. Such devices

usually showed a low junction voltage as compared to an inorganic p-n junction. Although the open circuit voltages (V_{OC}) observed were not too much lower than the current organic counterparts, the photocurrent densities and efficiencies had much room for improvement.

The concept of using an electron acceptor with organic materials to improve photovoltaic performance[4] had existed for a while but it was not until 1985 that the first true donor-acceptor bilayer device[13] was built. In this device, two layers of organic dyes, with a sharp interface, served as the donor and acceptor layers. The interface between these two organic layers, more than the dye-metal junction, now determined the photovoltaic properties of the system. The fill factor showed a marked improvement. Also, the interface between these organic layers became the main contributor to the V_{OC}, which opened up the possibility of tuning the V_{OC} by tweaking the material structure. Around the same time the discovery[14] of the buckminsterfullerene, C_{60} was reported. The spherical structural symmetry and highly conjugated nature of all its carbon atoms made it a non-planar semiconducting organic material.[15] It was confirmed as an n-type semiconductor[16] and its high electron affinity[17] and a band gap of around 2.3 ± 0.1eV[18] made it a suitable candidate for use as an acceptor material in organic photovoltaics.

A lot of the work being done today involves the use of a combination of donor and acceptor organic as well as inorganic materials in cells with different morphologies. The cells that use both organic and inorganic materials are called hybrid solar cells. This thesis will be concentrating on purely organic devices.

2.3.2 Conductive Polymers

Conductive polymers consist of long chains of conjugated carbon as well as hydrogen, sulfur, oxygen nitrogen and other such atoms (depending on the polymer), with alternating single and double bonds. The carbon atoms have an sp^2 hybridization where an s and two out of three p orbitals combine to give 3 identical and energetically more favorable hybrid orbitals. In a carbon – carbon double bond, one of the bonds is formed by the overlapping of the sp^2 hybridized orbitals. This is a tight localized covalent bond. The second bond is formed by the overlapping of the remaining more loosely

bound, unhybridized p-orbitals. In a long conjugated polymer chain, a continuous path of overlapping p-orbitals is formed, which results in the delocalization of the π electrons. This is a long range interaction between the π electrons of the carbon atoms, leading to band-like splitting of the energy levels. But unlike the band structure formed due to long range interaction in a crystal, these bands are localized on each, uninterrupted, conjugate polymer chain. The energy level analogous to the valence band edge is called the Highest Occupied Molecular Orbital or HOMO. Similarly, the conduction band edge is called the Lowest Unoccupied Molecular Orbital or LUMO. The difference between the LUMO and the HOMO is the band gap of the polymer. In general, the longer the length of the chain, the lower the HOMO – LUMO gap.

In most conjugated polymers, the extent of conjugation is not always high enough for them to have band gaps in the semiconducting or metallic ranges. So, although the overlapping p-orbitals provide the band structure that would allow for reasonable mobility along the polymer backbone, such conjugated polymers do not have any intrinsic charge carriers.[19] These charge carriers are provided by the process of doping, whereby an electron is either removed from the π-system (p-doping) or added (n-doping). n-doping is relatively rare.

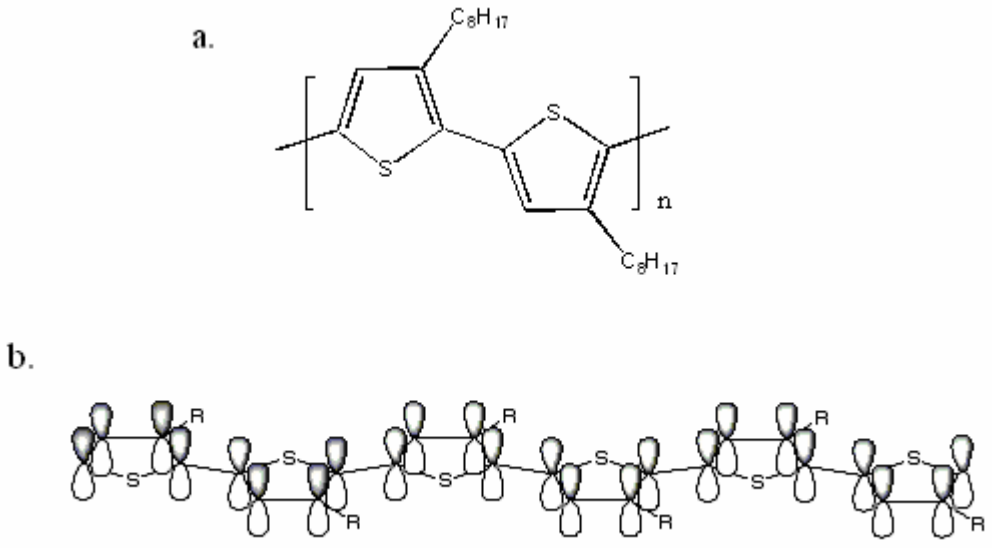

Figure 2.5 (a) Chemical structure of P3OT and (b) a sketch of the general structure for polythiophenes showing un-hybridized p-orbitals.

An example of p-doping is seen in poly(3-octylthiophene-2,5-diyl), more commonly known as P3OT. This is one of the main polymers used in this study. Figure 2.5a shows the chemical structure of P3OT. Figure 2.5b shows the structure of a general poly(3-alkylthiophene) with a sketch of the un-hybridized p-orbitals where S stands for sulfur.[20] When considering P3OT, the R in this Figure is C_8H_{17}, which is a non-conjugated alkyl chain that does not contribute to the conduction process. It mainly affects the solubility of the polymer. The sulfur in the 5 member ring in the polymer acts as the dopant. It has a tendency to get oxidized; it has a loosely held electron that it donates to the conduction band when energy is supplied to the system. This makes P3OT a p-type material which is suitable as a donor in organic photovoltaics.

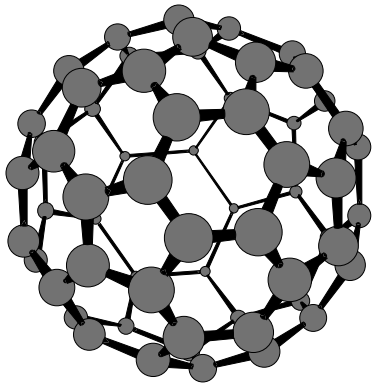

Figure 2.6 Chemical structure of C_{60}.

Another example of a conjugated molecule used extensively in this study is C_{60}, shown in Figure 2.6. In this case there are 60 carbon atoms all contributing π-electrons that participate in conjugation and all constrained to a spherical structure. Thus, there is a high degree of conjugation, resulting in a conjugated molecule with a band gap of 2.3 ± 0.1eV.[18] Also, as mentioned before, this was confirmed to be an n-type material[16] and hence suitable as an acceptor.

2.3.3 Overview of the Organic Photovoltaic Process

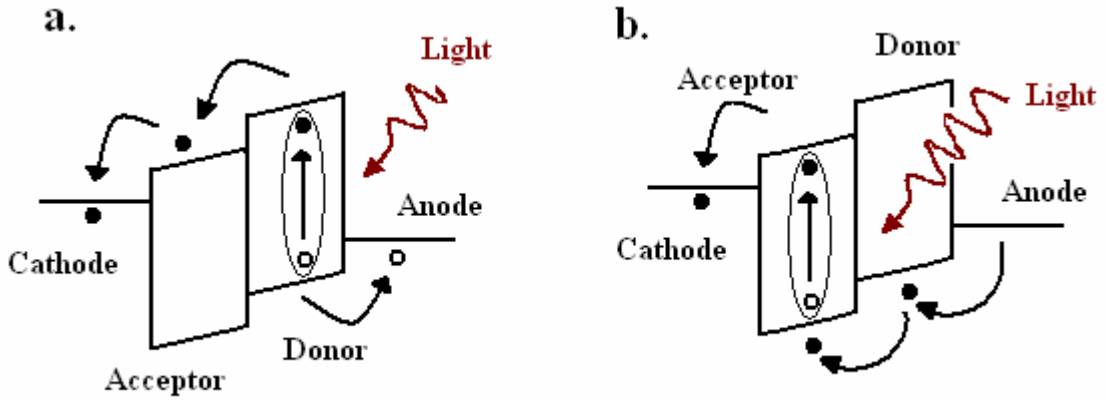

Figure 2.7 Basic operation of an organic solar cell under illumination: Photocurrent generation through exciton formation in (a) the donor and (b) the acceptor.

Figure 2.7a shows the schematic of the operation process of an organic solar cell under illumination. In this thesis, the predominant materials used are P3OT as the donor (D) and C_{60} as the acceptor (A). Indium tin oxide (ITO) with poly(3,4-ethylenedioxythiophene): poly(styrenesulfonate) complex (PEDT:PSS or PDOT) serve as the anode while Aluminum (Al) serves as the cathode. It should be noted that while the ITO-PEDT:PSS layer almost always serves as the hole accepting electrode and the Al layer always is the electron accepting electrode, there is some ambiguity in the definition of these two layers as anode or cathode. If the cathode is defined as the layer that supplies electrons then the cathode would be the ITO-PEDT:PSS layer and the anode the Al layer.[21] But if the cathode and anode were defined as the electrodes at which the negative and positive biases would be applied respectively, for forward biasing the device, then the Al layer is now the cathode and the ITO-PEDT:PSS layer the anode. In this thesis, the latter convention is chosen and is also depicted in Figures 2.7a and 2.7b. The materials, device processing and morphology will be discussed in more detail in later sections of this and the next chapters.

The basic stepwise process for photo-excitation on a donor (D), charge transfer to a nearby acceptor (A) and charge separation[22] is discussed in Table 2.1.

Step Number	The Process
Step 1	$D + A \rightarrow {}^{1,3}D^{*} + A$
Step 2	${}^{1,3}D^{*} + A \rightarrow {}^{1,3}(D - A)^{*}$
Step 3	${}^{1,3}(D - A)^{*} \rightarrow {}^{1,3}(D^{\delta+} - A^{\delta-})^{*}$
Step 4	${}^{1,3}(D^{\delta+} - A^{\delta-})^{*} \rightarrow {}^{1,3}(D^{+\bullet} - A^{-\bullet})^{*}$
Step 5	${}^{1,3}(D^{+\bullet} - A^{-\bullet})^{*} \rightarrow D^{+\bullet} + A^{-\bullet}$

Table 2.1 Step-wise process for photo-excitation and charge separation.

In step 1, when light is incident on the donor polymer (D) photoexcitation occurs to yield the singlet and triplet excited states called excitons (${}^{1,3}D^{*}$). The singlet exciton is the main contributor to the photovoltaic process. In the presence of an acceptor (A), a donor-acceptor complex is formed and there is a delocalization of the excitation over this complex space (step2). Due to the high electron affinity of the acceptor, the negative charge transfer to the acceptor is initiated in step 3 to finally yield an ion radical pair as seen in step 4 (${}^{1,3}(D^{+\bullet} - A^{-\bullet})^{*}$). The donor-acceptor complex finally dissociates to give separated positive and negative charges on the donor and acceptor respectively, thereby completing the charge transfer process in step 5. The separated electron now hops along a well- connected path of C_{60} molecules till it reaches the Al electrode. The holes similarly move towards the ITO. The electrodes have been selected with offset work functions so that a band bending creates an internal field to guide these charges to their respective electrodes as seen in both Figures 2.7a and 2.7b. They are then collected as photocurrents.

Another photon-induced exciton generation process that contributes to the photocurrent, albeit to a lesser extent, is exciton generation through fullerene absorption as seen in Figure 2.7b. Here photo-excitation occurs in the acceptor and there is charg transfer from the HOMO of the donor to that of the acceptor. This results in a hole in the HOMO of the donor and an electron in the LUMO of the acceptor, just as in the case of Figure 2.7a. Here, the hole collection at the anode is depicted as electron injection, but it is basically the same process.

In the following sections, a more detailed description of the photoexcitation, charge transfer and charge transport processes will be given.

2.3.4 Photoexcitation – Polarons and Excitons

It was initially thought that conduction along a polymer chain was only due to separated electron – hole pairs that moved within the conduction and valence bands respectively, as seen in inorganic semiconductors. Subsequent study revealed conduction by a class of electrostatically bound charge carriers. When energy is absorbed and photoexcitation occurs, an electron and hole pair is obtained. These charge carriers are weakly bound to each other and exist in energy levels that are slightly above and below the HOMO and LUMO levels, respectively. Such a bound electron – hole pair is called an exciton.

The nature of the exciton on the polymer is currently under debate. One school of thought believes that the delocalization of the π-electrons, due to closely interacting carbon atoms, would result in a similar delocalized exciton. So, while there does exist a bound electron – hole pair, the wavefunctions of these charge carriers are believed to be spread over the conjugated segment of the polymer.[23] This viewpoint is significant when considering the conduction process along a polymer and will be discussed in greater detail in the next section.

Another theory considers more spatially localized excitons. In organic semiconductor molecules, often the equilibrium geometry is different in the ionized state as compared to the ground state.[24] When energy is absorbed, for transition to occur, the ground state relaxes or distorts to adopt the equilibrium geometry of the ionized state. In an inorganic semiconductor analogy, such distortions are localized lattice polarizations formed around the charge, that weakly trap it in a potential well, creating bound states within the energy gap, near the band edges. Such a charge carrier and its local polarizing field is called a polaron; P^+ when it is a hole and P^- when it is an electron. Excitons are polarons that are weakly bound to each other through coulombic interactions. This theory suggests a similar local distortion in the configuration of the polymer at the site of excitation that results in the bound exciton.

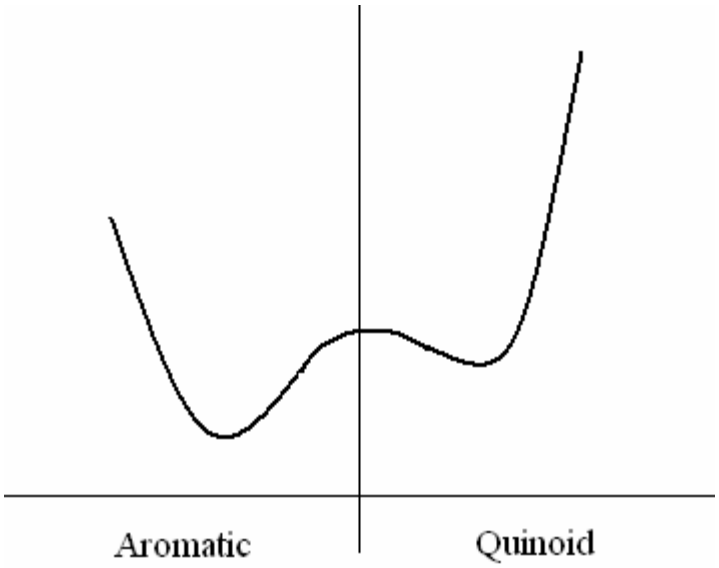

Figure 2.8a Energy states for a non-degenerate ground state conjugated polymer.

Figure 2.8a depicts the ground state and exciton-formed state for a non-degenerate ground state conjugated polymer such as a polythiophene.[25] There are two unequal, local minima or potential wells which correspond to the two configurations possible in a conjugated resonance structure. These are the aromatic and quinoid states of which the aromatic is more stable and represents the non-ionized ground state. Exciton formation transforms the local geometry from the aromatic to the quinoid form where it is weakly bound in a shallow potential well. It can transform back when exciton decay occurs either non-radiatively, by dissipation of energy as phonons, or radiatively, where photoluminescence is observed. Another possibility is that the exciton is split into separated charge carriers, either due to a transfer of an electron from the polymer to an acceptor or due to the trapping of one of the charges at either a defect or oxidation trap site. These processes will be discussed in greater detail in the charge transport and transfer section of this chapter.

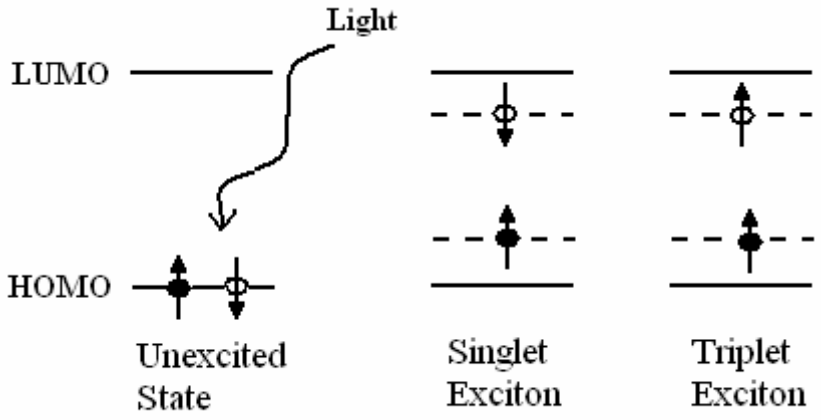

Figure 2.8b Energy band diagram for singlet and triplet excited states.

The bound electron and hole of an exciton have spins, so upon photoexcitation, two types of excitons can be formed; a singlet exciton, where the electron and hole pairs have opposite spins, or a triplet exciton, where they have the same spins. Figure 2.8b shows the energy band diagram of the singlet and triplet exciton states. The triplet exciton is localized on the chain while the singlet exciton was found to be delocalized over a whole conjugated segment of the polymer, the delocalization increasing or decreasing depending on the segment size.[26] It is also the singlet exciton that dissociates by charge transfer to a neighboring conjugated acceptor, yielding separated charge carriers (polarons) and subsequent photocurrent generation.[27]

There continues to be significant debate on the precise mechanism of photoexcitation and the nature of excitons. The primary concern of this thesis is photocurrent generation due to charge transfer from dissociated excitons, hence singlet excitons are considered as the main contributors to this process.

2.4 Charge Transfer and Transport

2.4.1 Charge Carrier Diffusion

In organic semiconductors consisting of donor and acceptor materials, the main process of exciton dissociation that leads to charge transfer is at the donor – acceptor

interface, after which the separated charges need to reach their respective electrodes. This process is based on inter-chain and intra-chain transport of charge carriers.

Much of the work being done today in organic photovoltaics is motivated by the discovery of ultrafast charge transfer from the conducting polymer poly(2-methoxy, 5-(2'-ethylhexyloxy)-1.4-phenylene-vinylene) (MEH-PPV) to the acceptor C_{60}[28]. One of the main material prerequisites for such a charge transfer is that the electron affinity of the acceptor species be greater than the ionization potential of the donor in its excited state and the net Coulombic forces binding the electron to the donor atom. A charge transfer range of electron to acceptor has been experimentally established between 5 to 10 nm.[29,23] This charge transfer was reported to occur within time scales around 300 fs,[29,30] almost 1000 times faster than the electron – hole radiative recombination (photoluminiscence) process. Although most experiments agree with these values, the process of charge transfer and the actual interpretation of the transfer range are still disputed.

There is a consensus that the overlap of the π-states over an uninterrupted conjugated segment of the polymer leads to the delocalization of these electrons but the nature of this delocalization that ties in with charge carrier transport is what is still debated. Halls *et al*. modeled the photocurrent spectra in poly(p-phenylenevinylene) (PPV) – C_{60} bilayer devices assuming that the excitons diffuse from the site of excitation on the polymer to the polymer – acceptor interface.[31] They reported a diffusion range of 6 to 8 nm which yielded the curves that fit best with experimentally obtained data. Vacar *et al.* based their case for the charge transfer mechanism on the femtosecond charge transfer times they experimentally obtained.[23] They argued that, if Einstein's relation for mobility were considered:

$$\mu = \frac{eD}{k_B T} \tag{6}$$

where e is the charge on an electron, D is the diffusion coefficient, k_B is the Boltzman's constant and T is the temperature, the mobility needed for bound charge carriers like polarons or excitons to yield the measured charge transfer times would be unreasonably high, almost two orders of magnitude more than the reported values of mobilities. They

suggested that exciton diffusion is not the dominant mechanism in charge transfer. Instead, the reported approximate 8 nm transfer range is ascribed to the size of the quantum delocalization of the photoexcitation itself.

Despite these different mechanisms that have been suggested for the process of charge transfer, all methods consistently report a charge transfer range of between 5 to 10 nm. Thus, if an excitation occurs on a donor within 5 to 10 nm of an acceptor, considering the reported charge transfer times that are 10^3 times faster than the electron – hole recombination rates, there is almost a 100% probability of charge transfer from donor to acceptor. The charge transfer range is an important parameter for the device morphology study in this thesis and so the accepted range of 5 to 10 nm will be considered without any further discussion on the physical meaning of this quantity.

2.4.2 Interchain Hopping

The exciton diffusion range focuses on the transport of bound electron – hole charge carriers along a conjugated polymer segment. These theories may also be extended to the transport of separated charges through either the donor or acceptor molecules with field-driven mobilities that guide them to their respective electrodes. This field, which is established by the offset in the workfunctions of the electrodes, also directs the hopping of these charge carriers from conjugated segment to conjugated segment, be it donor to donor or acceptor to acceptor. It is believed to be a phonon-assisted tunneling from site to site and so is dependent on intersite spacing and energetic disorders in the path of the charge carriers.

Brédas *et al*. analyzed the charge hopping process between adjacent polymer chains.[32] Quantum-chemical calculations were performed on model systems to study the transfer integrals, which reflect the strength of interaction between the two species between which the charge hopping occurs. The interchain hopping was considered to be thermally activated. They concluded that this process required large transfer integrals which could be achieved structurally or morphologically by adjusting the positioning of the interacting units.

In general, the conclusion that is relevant for our work is that the hopping process requires the proximity of the two conjugated chains between which the hopping occurs. Hence, for effective charge transport, a well-connected path of closely spaced conjugated segments is required from the site of photoexcitation and charge separation to the electrodes.

2.4.3 Role of Electrodes

Electrodes in organic solar cells play the role of guiding the separated photo-generated charges, in the absence of an external bias, so they may be collected as photocurrents. The electrodes are thus chosen to have different workfunctions. When the device is constructed, the Fermi levels of all the layers in contact must match up so that the system is in thermal equilibrium. The matching of the offset workfunctions of the electrodes creates an internal field (band bending). Excited electrons will then flow unidirectionally down the band and the holes, similarly, up the band, giving rise to photocurrents, similar to the inorganic case described in Section 2.1, Figure 2.2b.

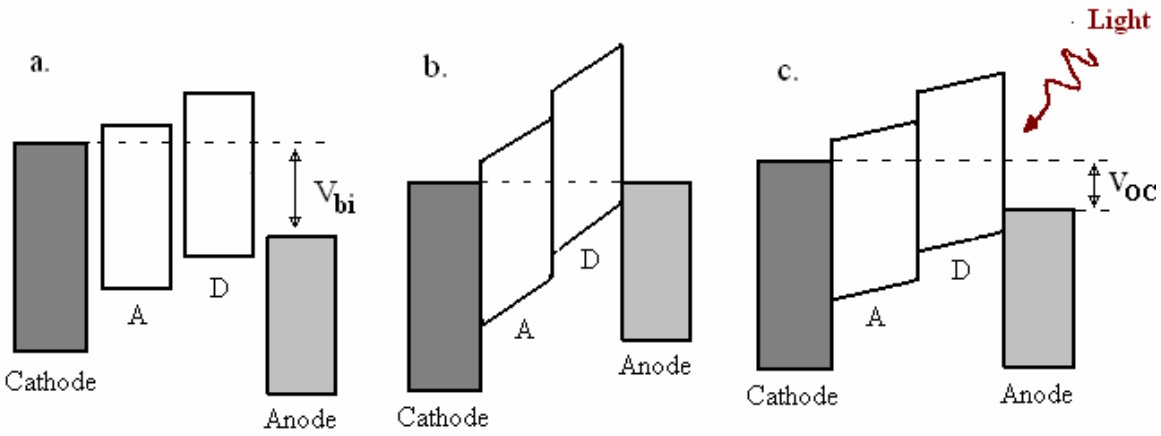

Figure 2.9 Energy levels of a heterojunction solar cell when: (a) levels are not in contact, (b) in contact in the dark and (c) in contact under illumination.

Figure 2.9 gives the schematic of the energy levels in general for a heterojunction solar cell.[21] Figure 2.9a shows the energy band diagram for the layers in a solar cells when they are not in contact with each other. When brought in contact, the Fermi level

matching and the resulting band bending that occurs can be seen in Figure 2.9b. The initial difference in the workfunctions of the electrodes that caused this band bending is called the built in potential (V_{bi}). When light is incident on this system, the photo-generated charges that are transported along the direction of the internal field raise the energy of the cathode and lower that of the anode, thereby creating another offset in the electrode workfunctions as seen in Figure 2.9c. According to some groups, this photo-induced offset is what is measured as the open circuit voltage or V_{OC}. The definition and factors affecting the V_{OC} are still disputed. Some of these theories will be expanded upon in later sections.

2.5 Factors That Hinder the Photovoltaic Process

2.5.1 Photo-oxidation

Exposure of many conjugated polymers to light and oxygen simultaneously results in photo-oxidation. In poly(*p*-phenylene vinylene) (PPV) polymers, oxidation attacks the vinyl double bond resulting in carbonyl formation.[33] These functional groups have a high electron affinity and act as sites for exciton dissociation on the polymer. Such dissociations do not lead to photocurrents since they do not occur at donor-acceptor interfaces. Instead the separated electrons stay trapped on the polymer creating space charges till they recombine with holes on the polymer. Such space charges create local electrostatic fields that hinder charge transport.

A comparative study showed a higher stability of P3OT in oxygen rich environments as compared to a PPV derived polymer[34] due to a difference in the mechanism of oxidation. Long chain polythiophenes do not have a vinyl group like in PPV. They are reported to show carbonyl formation which results in chain scission, instead of carbonyl formation on the polymer. In chain scission, the polymer is broken at the site of oxidation, reducing π-conjugated chain length.[35]

Irrespective of the effect of oxygen on the polymer, photo-oxidation is detrimental to an efficient photovoltaic process. Hence, the devices should be fabricated and handled, as far as possible, in an oxygen-free environment. The devices may also be encapsulated

immediately after fabrication though a suitable encapsulant. Such a material, which can act as a barrier to oxygen and is effective in flexible substrate devices, is still a major area of research.

2.5.2 Traps and Space-Charges

Traps are localized sites in a polymer that may offer alternative sites for exciton dissociation or bind separated charge carriers in a localized potential well, thereby hindering the photovoltaic process. They are commonly a result of structural defects in the chain, oxidation sites or introduction of impurities. They may be found at junctions, interfaces or in the bulk of the device.

Traps can be classified as shallow or deep traps, depending on the strength or lifetime of the charge trapping. In shallow traps, charge carriers are generally trapped for time scales that are less than or comparable to their time of flight in a trap-free scenario. The charges can be thermally released after which they continue the diffusion to the electrode. This introduces a delay in the net time of flight which can be given by:

$$\tau_{eff} = \tau_0 + NL\tau_{trap} \tag{7}$$

where τ_{eff} is the effective time of flight of a charge to the electrode, τ_0 is the time of flight in a trap-free case, τ_{trap} is the average time a charge is trapped, N is the number of traps per unit length and L is the diffusion length for the charge. This increase in the effective time of flight reflects as a proportional reduction in the net mobility of the charges.

Deep traps bind the charge carries for time scales that are considerably greater than the diffusion time. This reduces the number of charge carriers available for diffusion and also affects the mobility of existing charge carriers by building up space charges that affect the net field directing the photocurrent. Such space charges can be randomly found anywhere in the device, depending on the distribution of trap sites, and they hinder the charge carrier transport process.

Space charges may also be formed due to a difference in the charge transport properties of the separated electrons and holes. When the rate of transport of one charge

carrier is greater than the other, an imbalance in the charge collection leads to the accumulation of one charge species. Often hole mobility is smaller than the electron mobility and the build up of positive charges resulting from this will create a field that enhances the extraction of holes at the anode and decreases the extraction of electrons at the cathode. A space charge limited current is postulated for such cases[36] which is the limiting current achieved when a large amount of photo-generated charges with long lifetimes and sufficiently different mobilities are produced. This approach to photocurrents is especially valid for bulk heterojunction devices. Such space charges are not caused by traps though traps might indirectly affect the performance by altering the effective mobilities.

Another group found that the space charges do not really limit the photoresponse.[37] In fact they found around 3 orders of magnitude increase in the hole mobility of a PPV derivative from it's pristine form to when blended with [6,6]-phenyl C_{61}-butyric acid methyl ester (PCBM), a commonly used derivatized fullerene acceptor.

2.5.3 Charge Collection

Electrodes play the important role of providing the internal field to guide separated charges and hence have to have workfunctions offset from each other to generate the required band bending. But such an offset between the metal and the adjacent semiconductor causes a potential barrier due to Fermi level matching, called a Schottky barrier. Charge collection occurs by tunneling through this barrier which acquires a more ohmic character as the barrier grows thinner. Interface defects caused due to oxidation, or reaction of the metal with the semiconductor during deposition, or even diffusion of the metal into the semiconductor would make the charge collection process more complicated and might reduce efficiency. Such efficiency limitations are often grouped with those found in the bulk of devices.

2.5.4 Recombination

Electron – hole recombination reduces the photocurrent and the efficiency by reducing the total number of contributing charge carriers. When the recombination of an electron and hole happens non-radiatively, the electron loses energy to vibrations and returns back to the ground state where it recombines with a hole. In radiative recombination, the electron gives off a photon as photoluminescence as it transitions back to the ground state to recombine with the hole. Recombination may happen after photoexcitation, when there is no donor-acceptor interface nearby and hence no charge transfer within the lifetime of the exciton. It may also happen after charge transfer, if there is no movement of the separated charges, the electron in the LUMO of the acceptor may recombine with a hole in the HOMO of the polymer. A third possibility of recombination is at traps when a trapped electron recombines with a hole that was a part of the conduction current, as discussed in the traps section.

Hence to prevent recombination and generally improve the photovoltaic device performance: 1). Charge transfer should be optimized by increasing the donor – acceptor interface density in the film, 2). Charge transport should be optimized by ensuring there is a transport path for separated charges from the donor – acceptor interface to the electrodes, 3). Devices should be made carefully to avoid oxidation and trap sites, 4). The metal – semiconductor junctions should be clean to facilitate unhindered charge collection. Morphological considerations that would affect this are discussed in the last section of this chapter.

2.6 Characterizing Organic Photovoltaics – Equivalent Circuit Diagrams

The various charge producing and limiting processes of a solar cell can be represented by electrical circuit elements in an equivalent circuit diagram (ECD). The ECD allows us to examine the effect of individual parameters on the system as a whole. Figure 2.10a gives the ECD for an almost ideal solar cell without considering the loss mechanisms found in real organic devices.[38]

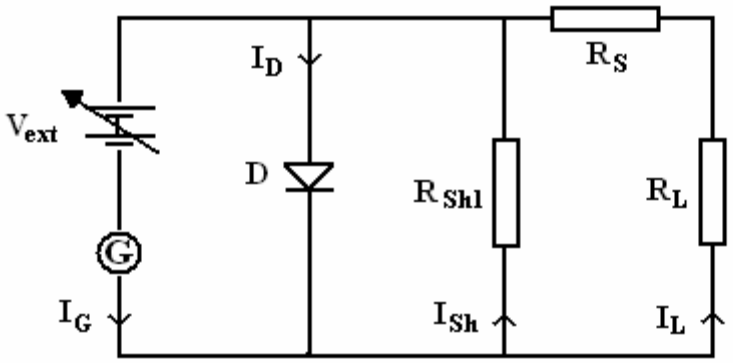

Figure 2.10a Equivalent circuit diagram of a solar cell without considering loss mechanisms.

G is the exciton diffusion current source. I_G, the current from G, is dependent solely on the separated charge carrier creation efficiency. D represents the diode character of the solar cell which is a result of the built in field from the donor – acceptor interface. I_D is the current through the diode. In the dark, I_D is negligible under reverse bias or no bias conditions. When illuminated, under no bias, photocurrent is generated, which is measured as I_L at the load resistor, R_L. The R_L arm of the circuit is a consequence of illumination. V_{ext} is the variable external biasing voltage that is applied to obtain the current – voltage (IV) characteristics. When short circuit current (I_{SC}) measurements are taken V_{ext} is set to zero. The shunt resistor, R_{Sh}, represents the current lost due to recombination of electron – hole pairs at the site of exciton dissociation, before any charge transport can occur. The series resistance R_S represents the different structural parameters that would give rise to the net mobilities in the solar cell.

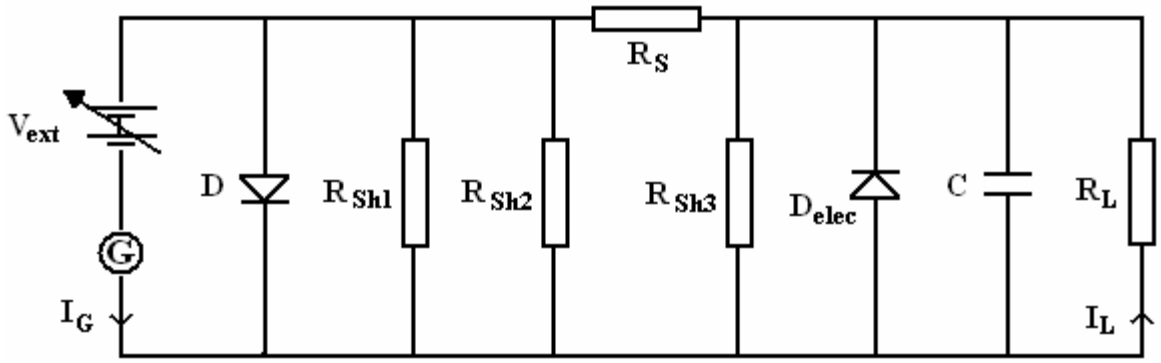

Figure 2.10b Equivalent circuit diagram of a real solar cell.

Figure 2.10b represents an ECD for a real organic solar cell where components are added to account for various loss mechanisms discussed in the previous sections. When device fabrication is not ideal, especially during the deposition of the electrodes on thin organic films, the top electrode might short through to the bottom electrode causing pinhole shorts. These are ohmic contacts that reduce the diode nature of the device and are represented by the shunt resistor R_{Sh2}.

The shunt resistor R_{Sh3} accounts for the separated charge carriers that diffuse and recombine at defect sites at the electrodes before they are collected. It should be noted that the recombinations in the bulk of the film, during the charge transport process, would be incorporated into the net mobility and, hence, be given by a series resistance. These series effects are incorporated into the existing series resistor, R_S.

D_{elec} represents the Schottky barrier or blocking contact that is often formed at the electrode – semiconductor interface and provides an extra rectifying barrier felt mainly during charge collection.

During the entire transport process, charges could get trapped at any point on the film to give rise to space charges. Space charges create a field that opposes the transport of other free charges, acting like a capacitor. This is represented by the capacitor C in the diagram. It should be noted that this phenomenon would affect the net mobility, hence contributing to R_S, the series resistance. The capacitance is a rather important factor because the space charges are distributed over the area of the device that is large compared to the thickness. A similar structure yields very high capacitances in conventional capacitors.

Having accounted for each contributing factor as individual circuit elements, the various parameters that influence the characterization curves of organic photovoltaic devices can now be analyzed by studying these elements. Before delving into this, it should be noted that such a split up of parameters is unnatural to the actual photovoltaic process. These parameters demonstrate a subtle co-dependence that is lost when they are analyzed separately. Nevertheless this study is still a strong starting point to understand the mechanisms of organic photovoltaic devices.

2.7 I-V Characteristics

In this section the current – voltage (I-V) characteristics will be studied with respect to the ECD shown in Figure 2.10b. When a voltage is applied across the device, the current through D and R_L, tempered by R_S in series and all the other loss mechanism shunts, represents the final experimentally measured current. This can be explained as the current left from the total, once the current of the loss mechanisms is shunted away. In the dark, the cell shows diode behavior and hence I_D would be the sole contributor. I_L is an augmentation in the current and is a contribution that is available due to illumination and due to non-ideal reverse-diode behavior. In reality there are no shunt resistor 'currents'. The loss mechanisms correspond to an *absence* of current and hence in a real device, I_D and I_L are the only existing, measurable currents.

2.7.1 Low Shunt Resistance

In the ECD, although the shunt resistances have different origin they will have the same effect on the circuit. As the value of the shunt resistance decreases, they become competitive with the low forward bias impedance of the diode D. Current is shunted away from the diode and the device starts to acquire a more ohmic nature. This can happen, for example, by the existence of pinhole shorts. The I-V curves obtained for such low shunt resistance devices would have a high linear (ohmic) character.

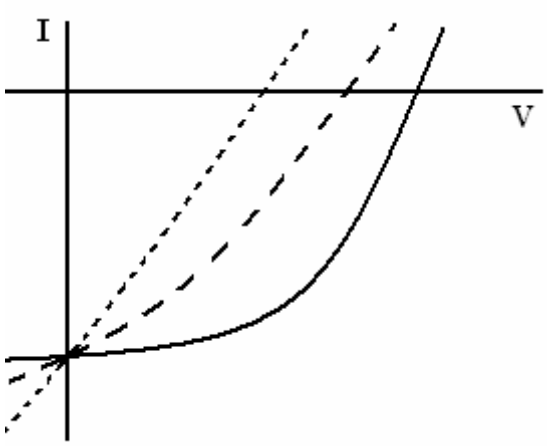

Figure 2.11 4th quadrant I-V characteristics corresponding to decreasing shunt resistances in the ECD; the device with the highest shunt resistance is given by the solid curve and the device with the lowest shunt resistance is the dotted curve.

Figure 2.11 shows a sketch of IV curves; the curves get progressively more linear (solid to dashed to dotted) as the shunt resistances decrease. The open circuit voltage and fill factor (V_{OC} and FF, defined in section 2.2.2) are seen to drop. The short circuit current (I_{SC}) is independent of the diode nature as it is measured under zero biasing. Hence, it stays more or less constant as the diode characteristics change. I_{SC} is mainly dependent on the mobilities and so is affected more by the series resistor, R_S. In the ECD, R_{Sh} is generally a few magnitudes greater than R_S and so the variations in the current through the shunts are negligible compared to the current through the series resistor, keeping I_{SC} more or less constant.

2.7.2 High Series Resistance

In the ECD, as the series resistance, R_S, is increased, less current is drawn in the circuit and hence the net current output is less for the same illumination. This is seen as a drop in the I_{SC} and FF. The V_{OC} is more or less unaffected since it is measured when the current in the circuit is zero. This is illustrated in Figure 2.12.

In terms of the working devices, increased R_S indicates a drop in charge carrier mobilities and hence the photocurrents. V_{OC} is a consequence of the energy levels of the materials used and so is unaffected by the drop in mobilities.

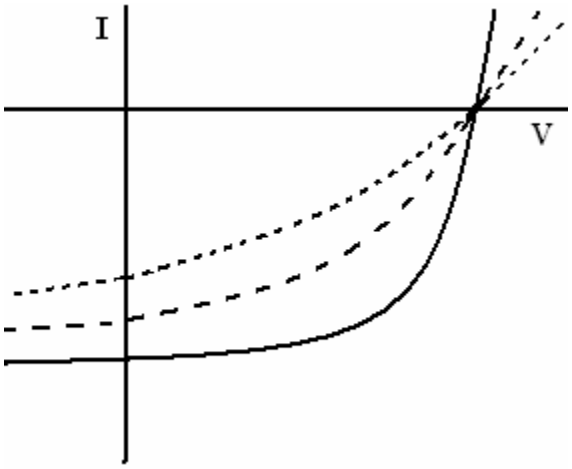

Figure 2.12 4th quadrant I-V characteristics corresponding to increasing series resistances in the ECD; the device with the lowest series resistance is given by the solid curve and the device with the highest series resistance is the dotted curve.

2.7.3 Illumination Intensiy

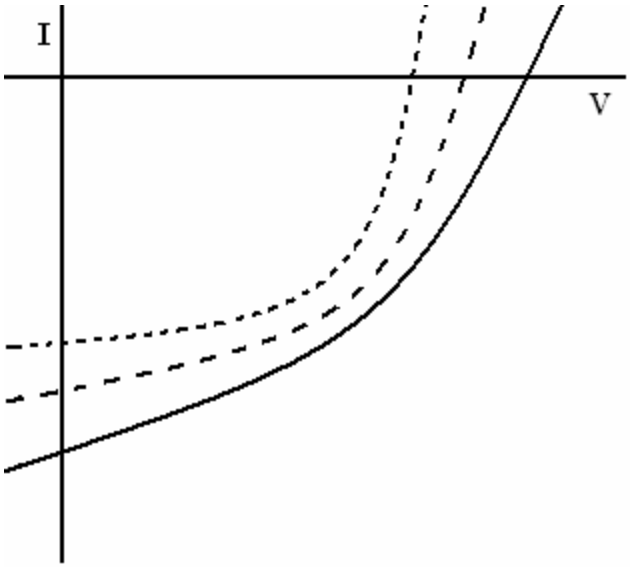

Figure 2.13 4th quadrant I-V characteristics corresponding to decreasing intensity of incident illumination on the device depicted by the ECD; the device with the greatest intensity of illumination is given by the solid curve and the device with the lowest intensity of illumination is the dotted curve.

As the intensity of illumination is decreased, the number of photogenerated charges (I_G) will also decrease and this would directly affect the I_{SC}. One group showed a

linear dependence of I_{SC} on the intensity of incident light.[39] They also predicted a slight decrease in the FF which was attributed to a drop in the shunt resistance values with increasing light intensity. The V_{OC} too was seen to increase with increasing light intensity though there is some discussion on the nature of the dependence.[40] Figure 2.13 gives a sketch of the net effect of varying illumination intensity on the I-V characteristics. It should be noted that similar trends are also seen for devices measured under varying temperature conditions. Since, in this thesis, all devices are measured under room temperature conditions, this study has not been further explored.

2.8 Material Dependence of the Organic Photovoltaic Process

So far in this chapter, mechanisms and limitations of photovoltaic efficiency, mainly from the perspective of photocurrent generation, have been discussed. In this section, the discussion will concentrate on the material dependent properties of organic photovoltaics, with an emphasis on the open circuit voltage and overall cell efficiency.

2.8.1 Origin of Open Circuit Voltage

Open circuit voltage (V_{OC}) is closely connected to the built in potential (V_{bi}) of a device. At room temperature, V_{OC} is generally a little lower than V_{bi} and approaches it as the temperature is lowered. In this limit, V_{OC} is sometimes defined as the offset in the work functions of the electrodes when the device is illuminated as seen in Figure 2.9c.[21] This is just one way of interpreting the V_{OC}, there is actually quite a bit of debate on the exact origin of V_{OC}.

A study conducted on the dependence of the V_{OC} on the donor and acceptor materials and the electrode materials of a device reported that the V_{OC} was insensitive to changes in the cathode work functions and hence independent of the cathode – anode offset.[41] This was explained by Fermi level pinning of the electrode work functions to the Fermi levels of the adjacent semiconductor layers. A strong correlation was instead observed between the V_{OC} and the electron affinity of the acceptor, leading to the conclusion that V_{OC} depends on the offset between the donor HOMO and acceptor

LUMO levels. Acceptor materials with different LUMO levels were studied, and the V_{OC} was seen to scale linearly with increasing LUMO levels.

Another group that used acceptor materials with different LUMO levels reported that either the offset in electrode work functions or the donor HOMO – acceptor LUMO level differences can yield the V_{OC}, depending on the kind of metal – semiconductor contact present.[42] The latter would be the cause of V_{OC} for non-ohmic metal – semiconductor contacts at the electrode (Figure 2.14a). A non-ohmic contact is formed when the work function of the cathode is greater than electron affinity of the acceptor. The electrode work functions offset (V_{OC2}) is less than the donor HOMO – acceptor LUMO offset (V_{OC1}) so the latter will dominate. These contacts are responsible for the Schottky barriers that result in blocking contacts with diode-like rectification at the charge collection interface.

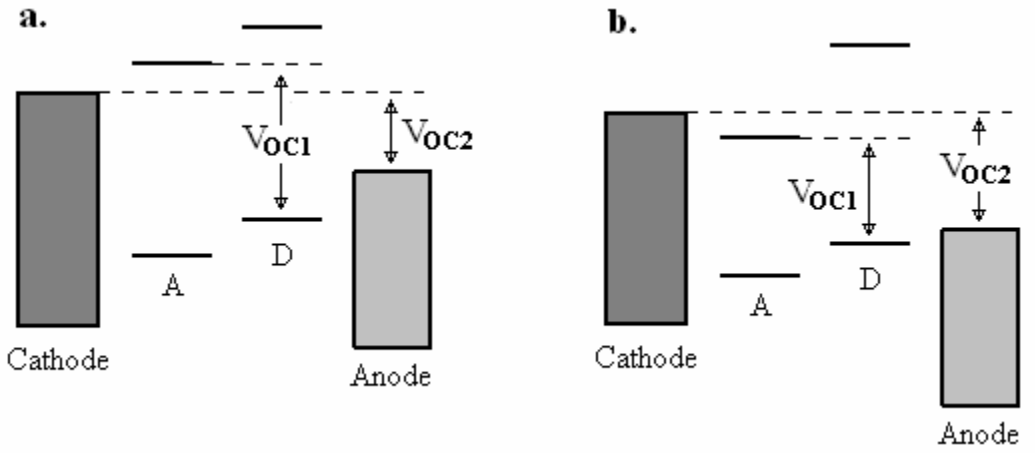

Figure 2.14 Band diagram for the origin of V_{OC} for the case of (a) non-ohmic and (b) ohmic metal – semiconductor contacts.

Figure 2.14b shows the case for an ohmic contact where the work function of the cathode either matches with or is lower than the electron affinity of the acceptor. In this case, the electrode levels offset (V_{OC2}) is greater than the donor – acceptor (V_{OC1}), and so the former is responsible for the V_{OC}. It should be noted that, with the shift in dependence of V_{OC} from the electrodes' to the donor's and acceptor's energy level, the definition of the built in potential will also change accordingly. Depending on the origin of V_{OC}, V_{bi} could either be defined as the difference in the electrode work function offsets as shown

in Figure2.9a, or it could be defined as the difference in the donor HOMO – acceptor LUMO levels. In either case the $V_{OC} \rightarrow V_{bi}$ limit holds. Figures 2.14a and 2.14b are drawn in the $V_{OC} \sim V_{bi}$ limit.

V_{OC} can be controlled by carefully selecting the cathode with appropriate work function or acceptor material with an appropriate LUMO level (electron affinity). Using the same argument for its origin, the V_{OC} might also be controlled by adjusting the HOMO of the donor.[43,44] As the HOMO level is lowered (corresponding to increased oxidation or ionization potential), the V_{OC} is increased.

2.8.2 Dependence of Efficiency on the Donor Energy Levels

Recently, there has been some discussion on the effect of the energy levels of the donor on the power conversion efficiency (Eqn. 5) of the organic solar cell. Scharber *et al.* report a large correlation between the LUMO level of the donor polymer and the power conversion efficiency, as predicted by a model that assumed a 65% EQE and 0.65 FF under AM1.5 illumination (accepted typical values for devices with no recombination losses).[44] They also assumed that an energy-offset of 0.3eV between the LUMOs of the donor and acceptor was sufficient to induce exciton dissociation and charge transfer. Using this model they predicted efficiencies of up to 10% when using PCBM as the acceptor. The dependence of the conversion efficiency on the LUMO level results, in large part, from the lowered band gap and thus increased collection of the solar spectra as the LUMO is lowered.

Koster *et al.* suggest that efficiencies of up to 11% might be obtained by lowering the energy level difference between the LUMOs of the donor and acceptor, to minimize energy lost during exciton dissociation and charge transfer.[45] They began modeling with the energy levels of the known poly(3-hexylthiophene) (P3HT) – PCBM system which they subsequently adjusted to obtain the reported 11%. A popular school of thought suggests that lowering the band gap of the donor polymer (~1.5eV) would enhance the efficiency by increasing the fraction of the solar spectrum collection. They report that such optimization at the charge transfer stage would allow for high efficiencies from devices with moderately high donor band gaps, of the order of 2eV. An efficiency of

8.6% was reached when the donor – acceptor LUMOs' offset was fixed at 0.5eV and the donor band gap then increased to 2.1eV, thereby increasing the donor HOMO – acceptor LUMO offset and consequently the device V_{OC}. This value further increased to 10.8% when the device was optimized for thickness, reflection effects at the electrodes and charge carrier mobilities.

In summary, choosing materials to provide appropriate energy level offsets can improve the V_{OC} and consequently the efficiency of organic solar cells. Care taken during device fabrication can reduce the appearance of limiting factors like oxidation sites, traps, space charges etc., as discussed in previous sections. Assuming optimum materials and fabrication conditions, device performance may be further improved by improving the charge transfer and transport processes. This can be achieved by careful control of morphology and device construction.

2.9 Morphological Dependence of the Organic Photovoltaic Process

In the history of the morphological development of organic photovoltaic devices, the discoveries of C_{60} as an acceptor[16] and ultra-fast charge transfer from poly(2-methoxy-5-(2'-ethylhexyloxy)-1,4-phenylenevinylene) (MEH-PPV) to C_{60}[28] formed the foundation of much of the polymer – fullerene based research today.

Initial devices were bilayer devices consisting of a sharp interface between the donor and acceptor that served as the active layer.[31,46,47] When light was incident on the device, any exciton that was created within around 10 nm of this interface would dissociate, eventually yielding photocurrents.[23] But all excitons that were created anywhere else in the bulk of the polymer, more than 10 nm away from a donor – acceptor interface, would either decay thermally or recombine radiatively to give rise to photoluminescence. This led to low photocurrents and EQEs. Such devices also demonstrated the filter effect.[48] When light is incident on the bilayer device, it must pass through the polymer layer before it reaches the donor – acceptor interface. By then, a large portion of the strongly absorbed wavelengths have already been absorbed without contributing to the photocurrent. This results in a dip in the photoresponsivity (PR) and external quantum efficiency (EQE) spectra in the strongly absorbed wavelength range.

For example, ***Figure 2.15*** shows the PR for a bilayer device superimposed on the optical density spectrum (OD) of P3OT.

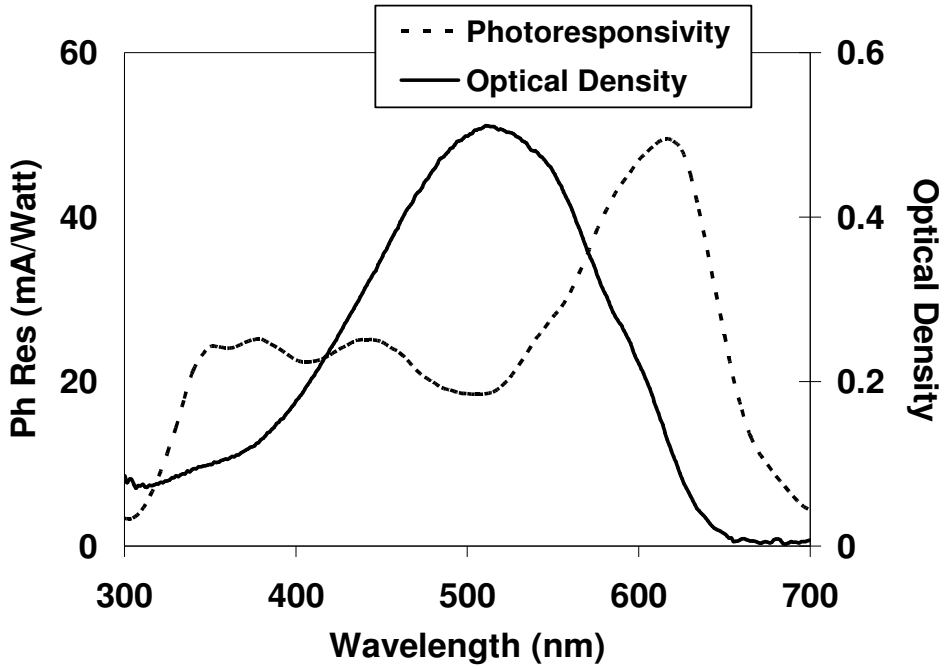

Figure 2.15 Comparison of the optical density (OD) and the photoresponsivity (PR) of a bilayer device. The filter effect is demonstrated in the dip seen in the PR at the same wavelengths that a peak is seen in the OD.

The OD curve shows a peak at 510 nm and absorption edges at 400 nm and 650 nm. A device with P3OT as the donor would be expected to show a similar peak in its PR. Instead, a dip is seen around this wavelength range. The loss of PR due to light being absorbed in the donor layer, far from an exciton – diffusion interface, is called the filter effect.

In order to improve the exciton dissociation efficiency, the donor – acceptor interface density was increased by using the concept of interpenetrating networks of donor and acceptor materials. In such devices, donor – acceptor interfaces are found distributed throughout the bulk of the polymer. Different morphologies and device constructions that depend on the materials used and they are therefore often called "bulk heterojunctions" can yield interpenetrating network devices. Some examples are described in the following sub-sections.

2.9.1 Blend Devices

Following the discovery of solution processible fullerenes, one of the simplest morphologies to form an interpenetrating network was by blending the donor and acceptor materials. Early polymer – fullerene blend devices[49,50] had large phase separated clusters of C_{60} which showed a tendency to aggregate in the polymer matrix. The limiting factor was the low solution processibility of C_{60}. C_{60} was derivatized with a side chain that prevented it from aggregating in solution, thereby rendering it much more soluble than the pure fullerene.[51] The development of the soluble acceptor material, PCBM, opened up the gates for a large portion of the blend devices being studied today.

In an ideal homogeneous blend, every donor molecule would have an acceptor molecule nearby. While this would give a 100% charge transfer efficiency, the lack of crystallinity of each individual species would result in reduced charge transport efficiency. This limitation can be reduced by allowing the layers to crystallize (phase separate) either by annealing the blend or by selecting solvents that would allow for this.

However, study showed that phase separation seemed to be detrimental in devices with PPV and its derivatives as donor and PCBM as acceptor. Shaheen *et al.* reported much higher efficiencies (up to 2.5% versus 0.9%) for (poly)[2-methyl,5-(3,7 dimethyl-octyloxy)]-p-phenylene vinylene (MDMO-PPV) – PCBM blends that were deposited from chlorobenzene as compared to toluene.[52] This was attributed to a more uniform mixing of the polymer and acceptor in chlorobenzene that yielded less phase segregated regions in the film. Hoppe *et al.* studied the effect of annealing on the phase separated morphology and concluded that PCBM formed large phase separated regions and the MDMO-PPV formed nanoclusters.[53] This clustering morphology led to a reduction of donor – acceptor interaction.

In contrast with the PPV – PCBM case, polythiophene (PT) – PCBM systems show more success with thermally-induced phase separation. Post production treatment that involves phase separation after the cathode has been deposited, shows the best results. In 2003, Padinger *et al.* suggested post production annealing while applying an external biasing voltage to poly(3-hexylthiophene) (P3HT) – PCBM devices.[54] This was expected to achieve alignment of the polymer chains along the direction of the field,

thereby increasing the conductivity of charges in the polymer matrix. Although this method gave up to 3.5% efficiency, just annealing after deposition of the cathode and without biasing, also showed a lot of promise.[55,56] In some of the best devices of the P3HT – PCBM system, nearly 5% efficiency was reached, which was attributed to the crystalline phase separated regions formed, and also the improved metal – semiconductor interface.[56] Phase separation may also be achieved through slow film growth in a solvent atmosphere. Yang *et al.* proposed a method by which P3HT – PCBM films were deposited from a common dichlorobenzene solvent.[57] After deposition, the solvent from the film was slowly evaporated, allowing the two components to slowly phase separate. The films were annealed before cathode deposition and showed a maximum power conversion efficiency of 4.4% under AM1.5 illumination.

Although phase separated crystalline regions in PT – PCBM blends yield enhanced conductivity, these regions still need to be well interconnected to achieve overall transport of charge carriers to the electrode. The ratio of the donor and acceptor materials are investigated to optimize the interconnectivity of the phase separated regions. It was found that in PT – PCBM systems, around a 1:1 ratio of the two components yielded the best results.[55,56,58] On the other hand, due to the difference in behavior of the annealed PPV – PCBM systems, a higher concentration of the fullerene was required to achieve optimum charge carrier mobilities in devices made from those two materials.[59]

2.9.2 Other Interpenetrating Networks: Other Materials and Morphologies

In this section, some of the other device structures and fabrication methods that yield interpenetrating networks are briefly discussed. The first interpenetrating network devices were polymer – polymer blend devices, where both donor and acceptor materials were solution processable polymers.[60] Such devices too showed phase separation between the two components but did not demonstrate as high a photovoltaic performance as devices with C_{60}. In addition to long chain polymers, small molecules (dyes like pthalocyanines, pentacenes and perylenes) have also been extensively investigated because their absorption spectra show more of an overlap with the solar spectrum. They

can be used in devices with each other or with fullerene based acceptor materials.[61,62,63,64] Carbon nanotubes that demonstrate semiconducting properties have also been shown to work as an acceptor material.[65] They demonstrate a high open circuit voltage with P3OT and are expected to have large mobilities along the tube, where charge carriers can be transported freely. Carbon nanotubes have also been investigated as an alternate electrode material.[66] A major drawback of this material lies in its difficulty of deposition. They exhibit very low solubilities and need to be oriented for maximum effect, making the production long and tedious. Outside the purely organic domain, hybrid solar cells, which consist of both organic and inorganic semiconductors, are also heavily researched.[67,68,69] One of the most promising approaches here has been the use of inorganic semiconductor nanoparticles and nanorods as acceptor materials in combination with polymer donors.

Different interpenetrating networks may also be created through morphological control. One of the earliest device structures that yielded interpenetrating networks, other than blend devices, were laminated devices.[61,70] In these cases, the donor and acceptor layers were individually deposited onto each electrode that they were in contact with and then sandwiched together and heated under mild pressure to fuse together, a lot like in the process of lamination. This resulted in an interpenetration of the donor and acceptor materials while also ensuring good metal – semiconductor contacts for efficient charge collection.

In other devices, to improve charge transport, the active blend layer was sandwiched between doped charge transport layers, which would increase the net mobility of charge carriers and hence reduce the series resistance of the device.[62]

The open circuit voltage (V_{OC}) output was increased by constructing stacked cells.[63,64] These consists of generally two heterojunction sub-cells that are stacked one on top of the other with a semi-transparent, metallic recombination layer inbetween. They can be considered as cells in series. Hence, ideally, their individual voltages would add up in the circuit but they must have the same current flowing through them. The recombination layer serves as a recombination site for surplus charges that might arise from the imbalance of free charge carrier generation from the different cells, thereby preventing charge build-up at the junctions. When nanoparticle clusters were used instead of a single metallic layer the efficiency was seen to further improve.[63,71] This was

attributed to an enhancement in the incident optical field due to its interaction with the metallic nanoparticles.

One disadvantage of using homogeneous blend active layers is that continuous and separate pathways exist for *both* charge carriers from the cathode to the anode. When, for example, a blend device is constructed, both the donor and the acceptor are in contact with both electrodes. This could result in reduced rectification and, hence, low fill factor values. Thus, ideally, there should be a bulk heterojunction active layer in the device to enhance the charge transfer efficiency, a well connected path with high mobilities that would transport each charge carrier species only to its own respective electrode and a clean semiconductor – metal interface at the electrodes where primarily, only one type of charge carrier is collected. Laminated devices might prevent this since the device fabrication starting point has each type of semiconducting species in contact with just its respective electrode. The success of this procedure would depend on the extent for thermal and pressure treatment giving during lamination. Another way to achieve this was reported by Brabec *et al*., where layers were deposited from solutions chosen such that they swell the layer below without completely dissolving it and removing it.[72] This way, the top layer will diffuse into the swollen bottom layer creating a bulk heterojunction but still preserving the purity of the materials at the electrodes. In such devices, due to the interdiffusion of the donor and acceptor materials, a concentration gradient is created that has a bulk heterojunction at the center of the device which becomes more and more single component as the electrodes are approached, optimizing the charge transfer, transport and collection processes. The disadvantage in creating concentration gradients in this manner is the restriction that is applied on the materials since they need to be selected such that a solvent exists that would dissolve one and only swell the other. In this thesis, a more universal method to create such concentration gradients from the thermal interdiffusion of an initial bilayer is studied.

2.9.3 Concentration Gradient Devices by Thermal Interdiffusion of a Bilayer

Recently, in order to optimize both the processes of charge transfer and transport, interdiffused devices have been investigated.[73,74,75] As mentioned in the previous section,

the ideal interdiffused morphology consists of a thin pure donor layer at the anode, a uniform gradient of increasing acceptor and decreasing donor concentrations into the film away from anode and finally ending with a thin layer of pure acceptor at the cathode. This ensures a bulk heterojunction in the center of the device for improved charge transfer. Yet, in the vicinity of the electrodes, the materials responsible for the charge transport increase in purity and hence provide a well-connected path to the electrode. At the electrodes, the pure material ensures proper band matching for efficient charge collection. Early studies of interdiffused devices were done on the MEH-PPV / C_{60} system.[73] More than an order of magnitude of improvement was seen in the external quantum efficiencies for the interdiffused devices as compared to the similar bilayer devices but TEM studies revealed clustering of the interdiffused C_{60} in the polymer.[74] This was attributed to the low miscibility of C_{60} with MEH-PPV and was expected to lower the photovoltaic efficiency. Subsequently, P3OT / C_{60} devices were studied the results of which will be presented in this thesis. The P3OT – C_{60} combination had been shown to be quite successful for photovoltaic use.[50,76] The increased miscibility of C_{60} in P3OT was expected to reduce the cluster size and allow for better connected paths for charge transport. This system, too, showed an order of magnitude improvement in the EQE for interdiffused devices as compared to bilayer devices.[75] In addition, the sulfur in the P3OT backbone allowed for concentration depth profiling of the devices using Auger spectroscopy combined with Ar ion beam milling. Such a study on the higher efficiency interdiffused devices revealed a concentration gradient, demonstrating that this device morphology is more effective than that of similar bilayer devices.[75] A simple model was generated based on the assumption that the EQE curves depended directly on the thickness of the deposited layers.[77] The curves obtained from this model replicated experimentally obtained results with a scale factor difference indicating the importance of layer thicknesses to obtain efficient interdiffused devices. Subsequently, internal electric field distribution within the device has been incorporated while modeling for the EQE values. In this thesis is presented a detailed study of the effects of varying the donor and acceptor layer thicknesses and interdiffusion conditions on the efficiency of concentration gradient devices. P3OT – C_{60} systems will be mainly investigated along with initial studies of the use of other materials as donor or acceptor.

[1] A. R. Hambley, Electronics (2nd edition), Prentice-Hall Inc., Upper Saddle River, New Jersey – 07458 (2000).
[2] A. Terenin, E. Putzeiko, I. Akimov, "Energy Transfer in Systems of Connected Organic Molecules," *Discuss. Faraday Soc.* **27**, 83 (1959).
[3] C.W. Tang, A.C. Albrecht, "Photovoltaic Effects of Metal-Chlorophyll-a-Metal Sandwich Cells," *J. Chem. Phys.* **62**(6), 2139-2149 (1975).
[4] D.R. Kearns, G. Tollin, M. Calvin, "Electrical Properties of Organic Solids. II. Effects of Added Electron Acceptor on Metal-free Phthalocyanine," *J. Chem. Phys.* **32**(4), 1020-1025 (1960).
[5] H. Shirakawa, *et al.*, "Synthesis of Electrically Conducting Organic Polymers: Halogen Derivatives of Polyacetylene," *J. Chem. Soc., Chem. Commun.*, 578-580 (1977).
[6] W.P. Su, J.R. Schrieffer, A.J. Heeger, "Solitons in Polyacetylene," *Phys. Rev. Lett.* **42**(25), 1698-1701 (1979).
[7] C.K. Chiang, *et al.*, "Electrical Conductivity in Doped Polyacetylene," *Phys. Rev. Lett.* **39**(17), 1098-1101 (1977).
[8] J.H. Burroughes, *et al.*, "Light-Emitting Diodes Based on Conjugated Polymers," *Nature* **347**, 539-541 (1990).
[9] G.Yu, C. Zhang, A.J. Heeger, "Dual-Function Semiconducting Polymer Devices: Light-Emitting and Photodetecting Diodes," *Appl. Phys. Lett.* **64**(12), 1540-1542 (1994).
[10] S. Glenis, G. Horowitz, G. Tourillon, F. Garner, "Electrochemically Grown Polythiophene and Poly(3-methylthiophene) Organic Photovoltaic Cells," *Thin Solid Films* **111**, 93-103 (1984).
[11] Y. Cao, P. Smith, A.J. Heeger, "Counter-Ion Induced Processibility of Conducting Polyaniline and of Conducting Polyblends of Polyaniline in Bulk Polymers," *Synth. Met.* **48**, 91-97 (1992).
[12] B.R. Weinberger, S.C. Gau, Z. Kiss, "A Polyacetylene:Aluminum Photodiode," *Appl. Phys. Lett.* **38** (7), 555-557 (1980).
[13] C.W. Tang, "Two-Layer Organic Photovoltaic Cell," *Appl. Phys. Lett.* **48**(2), 183-185 (1986).
[14] H.W. Kroto, *et al.*, "C_{60}: Buckminsterfullerene," *Nature* **318**, 162-163 (1985).
[15] R.C. Haddon, "π-Electrons in Three Dimensions," *Acc. Chem. Res.* **21**, 243-249 (1988).
[16] B. Miller, *et al.*, "Photoelectrochemical Behavior of C_{60} Films," *J. Sm. Chem. Soc.* **113**, 6291-6293 (1991).
[17] P.M. Allemand, A. Koch, F. Wudl, "Two Different Fullerenes Have the Same Cyclic Voltammetry," *J. Am. Chem. Soc.* **113**, 1050-1051 (1991).
[18] R.W. Lof, *et al.*, "Band Gap, Excitons, and Coulomb Interaction in Solid C_{60}," *Phys. Rev. Lett.* **68**(26), 3924-3927 (1992).
[19] L. Dai, "Advanced Syntheses and Microfabrications of Conjugated Polymers, C_{60}-containing Polymers and Carbon Nanotunes for Optoelectronic Applications," *Polym. Adv. Technol.* **10**, 357-420 (1999).
[20] a. http://en.wikipedia.org/wiki/Poly%283-hexylthiophene%29
b. http://en.wikipedia.org/wiki/Image:Polythiophenes_Conjugation.png
c. Copy Rights: http://en.wikipedia.org/wiki/Image:CC_some_rights_reserved.svg
[21] Sam-Shajing Sun, Niyazi Serdar Sariciftci, "Organic Photovoltaics, Mechanisms, Materials and Devices", (CRC print, Taylor & Francis Group, Boca Raton, 2005) pp 56.
[22] C.J. Brabec, D. Lomoretto, I. Moggio, G. Dellepiane, "Plastic Solar Cells: from Basic Research to Devices," RICHMAC Magazine, *La Chimica e lÌndustria* **80**, 1301-1307 (1998).
[23] D. Vacar, E. S. Maniloff, D. W. McBranch, A. J. Heeger, "Charge-Transfer Range for Photoexcitations in Conjugated Polymer/Fullerene Bilayers and Blends," *Phys. Rev. B* **56**(8), 4573-4577 (1997).
[24] J.L. Brédas, G. B. Street, "Polarons, Bipolarons and Solitons in Conducting Polymers," *Acc. Chem. Res.* **18**, 309-315 (1985).
[25] C. Brabec, V. Dyakonov, J. Parisi, N. S. Sariciftci (Eds.), "Organic Photovoltiacs, Concepts and Realization", Springer Series in Material Science, Vol 60, Springer-Berlin, Heidelberg (2003).
[26] S.C. Graham, D.D.C. Bradley, R.H. Friend, C. Spangler, "Raman and Photoluminescence Spectra of PPV Oligomers," *Synth. Met.* **41-43**, 1277-1280 (1991).
[27] E.L. Frankevich, *et al.*, "Polaron-Pair Generation in Poly(Phenylene Vinylenes)," *Phys. Rev. B* **46**(15), 9320-9324 (1992).

[28] N.S. Sariciftci, L. Smilowitz, A.J. Heeger, F. Wudl, "Photoinduced Electron Transfer from a Conducting Polymer to Buckminster Fullerene," *Science* **258**, 1474-1476 (1992).
[29] B. Kraabel, *et al.*, "Ultrafast Spectroscopic Studies of Induced Electron Transfer from Semiconducting Polymers to C_{60}," *Phys. Rev. B* **50**(24), 18543-18552 (1994).
[30] B. Kraabel, *et al.*, "Subpicosecond Photoinduced Electron Transfer form Conjugated Polymers to Functionalized Fullerenes," *J. Chem. Phys.* **104**(11), 4267-4273 (1996).
[31] J.J.M. Halls *et al.*, "Exciton Diffusion and Dissociation in a Poly(*p*-Phenylenevinylene)/C_{60} Heterojunction Photovoltaic Cell," *Appl. Phys. Lett.* **68**(22), 3120-3122 (1996).
[32] J.L. Brédas, J.P. Calbert, D.A. da Silva Filho, J. Cornil, "Organic Semiconductors: A Theoretical Charecterization of the Basic Parameters Governing Charge Transport," *PNAS* **99**(9), 5804-5809 (2002).
[33] M. Yan, *et al.*, "Defect Quenching of Conjugated Polymer Luminescence," *Phys. Rev. Lett.* **73**(5), 744-747 (1994).
[34] B.H. Cumpton, K.F. Jensen, "Photo-oxidation of Polymers Used in Electroluminescent Devices," *Synth. Met.* **73**, 195-199 (1995).
[35] S. Holdcroft, "A Photochemical Study of Poly(3-hexylthiophene)," *Macromolecules* **24**, 4834-4838 (1991).
[36] V.D. Mihailetchi, J. Wildeman, P.W.M. Blom, "Space-Charge Limited Photocurrent," *Phys. Rev. Lett.* **94**, 126602 (2005).
[37] C. Melzer, E.J. Koop, V.D. Mihailetchi, P.W.M. Blom, "Hole Transport in Poly(phenylene vinylene)/Methanofullerene Bulk-Heterojunction Solar Cells," *Adv. Funct. Mater.* **14**(9), 865-870 (2004).
[38] K. Petritsch, "Organic Solar Cell Architectures," *Ph.D. Thesis*, Technical University Graz (2000), (available at http://www.solarpassion.com/solar_thesis/thesis.zip).
[39] I. Riedel, *et al.*, "Effect of Temperature and Illumination on the Electrical Characteristics of Polymer – Fullerene Bulk – Heterojunction Solar Cells," *Adv. Funct. Mater.* **14**(1), 38-44 (2004).
[40] L.J.A. Koster, V.D. Mihailetchi, R. Ramaker, P.W.M. Blom, "Light Intensity Dependence of Open – Circuit Voltage of Polymer:Fullerene Solar Cells," *Appl. Phys. Lett.* **86**, 123509 (2005).
[41] C.J. Brabec, *et al.*, "Origin of Open Circuit Voltage of Plastic Solar Cells," *Adv. Funct. Mater.* **11**(5), 374-380 (2001).
[42] V.D. Mihailetchi, P.W.M. Blom, J.C. Hummelen, M.T. Rispens, "Cathode Dependence of the Open-Circuit Voltage of Polymer-Fullerene Bulk Heterojunction Solar Cells," *J. Appl. Phys.* **94**(10), 6849-6854 (2003).
[43] A. Gadisa, M. Svensson, M.R. Andersson, O. Inganäs, "Correlation Between Oxidation Potential and Open-Circuit Voltage of Composite Solar Cells Based on Blends of Polythiophenes/ Fullerene Derivative," *Appl. Phys. Lett.* **84**(9), 1609-1611 (2004).
[44] M.C. Scharber, *et al.*, "Design Rules for Donors in Bulk-Heterojunction Solar Cells – Towards 10% Energy-Conversion Efficiency," *Adv. Mater.* **18**, 789-794 (2006).
[45] L.J.A. Koster, V.D. Mihailetchi, P.W.M. Blom, "Ultimate Efficiency of Polymer/Fullerene Bulk Heterojunction Solar Cells," *Appl. Phys. Lett.* **88**, 093511 (2006).
[46] N.S. Sariciftci, *et al.*, "Semiconducting Polymer-Buckminsterfullerene Heterojunctions: Diodes, Photodiodes and Photovoltaic Cells," *Appl. Phys. Lett.* **62**(6), 585-587 (1993).
[47] N.S. Sariciftci, L. Smilowitz, A.J. Heeger, F. Wudl, "Semiconducting Polymers (As Donors) and Buckminsterfullerene (As Acceptor): Photoinduced Electron Transfer and Heterojunction Devices," *Synth. Met.* **59**, 333-352 (1993).
[48] A.C. Arias, *et al.*, "Doped Conducting-Polymer – Semiconducting-Polymer Interfaces: Their Use in Organic Photovoltaic Devices," *Phys. Rev. B* **60**(3), 1854-1860 (1999).
[49] G. Yu, *et al.*, "Polymer Photovoltaic Cells: Enhanced Efficiencies Via a Network of Internal Donor-Acceptor Heterojunctions," *Science* **270**, 1789-1791 (1995).
[50] G. Yu, K. Pakbaz, A.J. Heeger, "Semiconducting Polymer Diodes: Large Size, Low Cost Photodetectors With Excellent Visible-Ultraviolet Sensitivity ," *Appl. Phys. Lett.* **64**(25), 3422-3424 (1994).
[51] J.C. Hummelen, *et al.*, "Preparation and Characterization of Fulleroid and Methanofullerene Derivatives," *J. Org Chem* **60**, 532-538 (1995).
[52] S.E. Shaheen, *et al.*, "2.5% Efficient Organic Plastic Solar Cells," *Appl. Phys. Lett.* **78**(6), 841-843 (2001).
[53] H. Hoppe, *et al.*, "Nanoscale Morphology of Conjugated Polymer/Fullerene – Based Bulk-Heterojunction Solar Cells," *Adv. Funct. Mater.* **14**(10), 1005-1011 (2004).

[54] F. Padinger, R. S. Rittberger, N. S. Sariciftci, "Effects of Postproduction Treatment on Plastic Solar Cells," *Adv. Funct. Mater.* **13**(2), 1-4 (2003).
[55] D. Chirvase, J. Parisi, J.C. Hummelen, V. Dyakonov, "Influence of Nanomorphology on the Photovoltaic Action of Polymer – Fullerene Composites," *Nanotechnology* **15**, 1317-1323 (2004).
[56] W. Ma, *et al.*, "Thermally Stable, Efficient Polymer Solar Cells with Nanoscale Control of the Interpenetrating Network Morphology," *Adv. Funct. Mater.* **15**, 1617-1622 (2005).
[57] G. Li, *et al.*, "High – Efficiency Solution Processable Polymer Photovoltaic Cells by Self – Organization of Polymer Blends," *Nature Materials* **4**, 864-868 (2005).
[58] J. Huang, G. Li, Y. Yang, "Influence of Composition and Heat – Treatment on the Charge Transport Properties of Poly(3-hexylthiophene) and [6,6]-phenyl C_{61}-butyric acid methyl ester Blends," *Appl. Phys. Lett.* **87**, 112105 (2005).
[59] G. Dennler, *et al.*, "Charge Carrier Mobility and Lifetime Versus Composition of Conjugated Polymer/Fullerene Bulk – Heterojunction Solar Cells," *Organic Electronics* **7**, 229-234 (2006).
[60] J.J.M. Halls, *et al.*, "Efficient Photodiodes from Interpenetrating Polymer Networks," *Nature* **376**, 498-500 (1995).
[61] K. Petritsch, *et al.*, "Dye – Based Donor/Acceptor Solar Cells," *Sol. Energy Mater. Sol. Cells* **61**, 63-72 (2000).
[62] D. Gebeyehu, *et al.*, "Bulk – Heterojunction Photovoltaic Devices Based on Donor – Acceptor Organic Small Molecule Blends," *Sol. Energy Mater. Sol. Cells* **79**, 81-92 (2003).
[63] A. Yakimov, S.R. Forrest, "High Photovoltage Multiple – Heterojunction Organic Solar Cells Incorporating Interfacial Metallic Nanoclusters," *Appl. Phys. Lett.* **80**(9), 1667-1669 (2002).
[64] D. Cheyns, *et al.*, "Stacked Organic Solar Cells Based on Pentacene and C_{60}," *Sol. Energy Mater. Sol. Cells* **91**, 399-404 (2007).
[65] E. Kymakis, I. Alexandrou, G.A.J. Amaratunga, "High Open – Circuit Voltage Photovoltaic Devices from Carbon-Nanotube – Polymer Composites," *J. Appl. Phys.* **93**(3), 1764-1768 (2003).
[66] R. Ulbricht, *et al.*, "Transparent Carbon Nanotube Sheets as 3-D Charge Collectors in Organic Solar Cells," *Sol. Energy Mater. Sol. Cells* **91**, 416-419 (2007)
[67] D. Gebeyehu, *et al.*, "Hybrid Solar Cells Based on Dye – Sensitized Nanoporous TiO_2 Electrodes and Conjugated Polymers as Hole Transport Materials," *Synth. Met.* **125**, 279-287 (2002).
[68] S. Günes, *et al.*, "Hybrid Solar Cells using PbS Nanoparticles," *Sol. Energy Mater. Sol. Cells* **91**, 420-423 (2007).
[69] S. Bereznev, *et al.*, "Hybrid Solar Cells Based on $CuInS_2$ and Organic Buffer – Sensitizer Layers," *Thin Solid Films – **in press*** (2007).
[70] M. Granström, *et al.*, "Laminated Fabrication of Polymeric Photovoltaic Diodes," *Nature* **395**, 257-260 (1998).
[71] B.P. Rand, P. Peumans, S.R. Forrest, "Long – Range Absorption Enhancement in Organic Tandem Thin – Film Solar Cells Containing Silver Nanoclusters," *J. Appl. Phys.* **96**(12), 7519-7526 (2004).
[72] C.J. Brabec, *et al.*, "The Influence of Materials Work Function on the Open Circuit Voltage of Plastic Solar Cells," *Thin Solid Films* **403-404**, 368-372 (2002).
[73] M. Drees, *et al.*, "Creation of a Gradient Polymer – Fullerene Interface in Photovoltaic Devices by Thermally Controlled Interdiffusion," *Appl. Phys. Lett.* **81**(24), 4607-4609 (2002).
[74] M. Drees, R.M. Davis, J.R. Heflin, "Thickness Dependence, *In Situ* Measurements, and Morphology of thermally Controlled Interdiffusion in Polymer – C_{60} Photovoltaic Devices," *Phys. Rev. B* **69**, 165320 (2004).
[75] M. Drees, R.M. Davis, J.R. Heflin, "Improved Morphology of Polymer – Fullerene Photovoltaic Devices With Thermally Induced Concentration Gradients," *J. Appl. Phys.* **97**, 036103 (2005).
[76] D. Gebeyehu, *et al.*, "The Interplay of Efficiency and Morphology in Photovoltaic Devices Based on Interpenetrating Networks of Conjugated Polymers with Fullerenes," *Synth. Met.* **118**, 1-9 (2001).
[77] A. Gopal, M. Drees, R.M. Davis, J.R. Heflin, "Modelling of External Quantum Efficiency Spectra as a Function of Varying P3OT Thickness in P3OT – C_{60} Polymer Photovoltaic Devices," *SPIE Proc.* **5938, 593813:1-10** (2005).

CHAPTER THREE

Experimental Details –Methods and Materials

In this chapter is presented an introduction to the experimental procedures utilized and materials employed in this study. The work in this thesis is based on thermally interdiffused (ID) concentration gradient devices. Our aim was to understand the dependence of device performance on the extent of concentration gradient formation. Thus, for a controlled study, an initial bilayer of the donor and acceptor material is required, which can then be heated to produce interdiffusion. In the following sections, device fabrication and characterization methods will be explained. A brief theoretical background on the heat and mass transfer processes occurring during interdiffusion will also be given. The principles of Auger spectroscopy, used to obtain the concentration gradient profile, as well as the principles of ellipsometry, used to obtain the real and imaginary refractive indices of P3OT and C_{60} will be outlined. Finally, the details of the donor (P3OT), acceptor (C_{60}, PCBM and the endohederal fullerene $Sc_3N@C_{80}$) and electrode (ITO, PEDT:PSS and aluminum) materials used in this work, will be discussed.

3.1 Device Construction – Bilayer and Interdiffused Devices

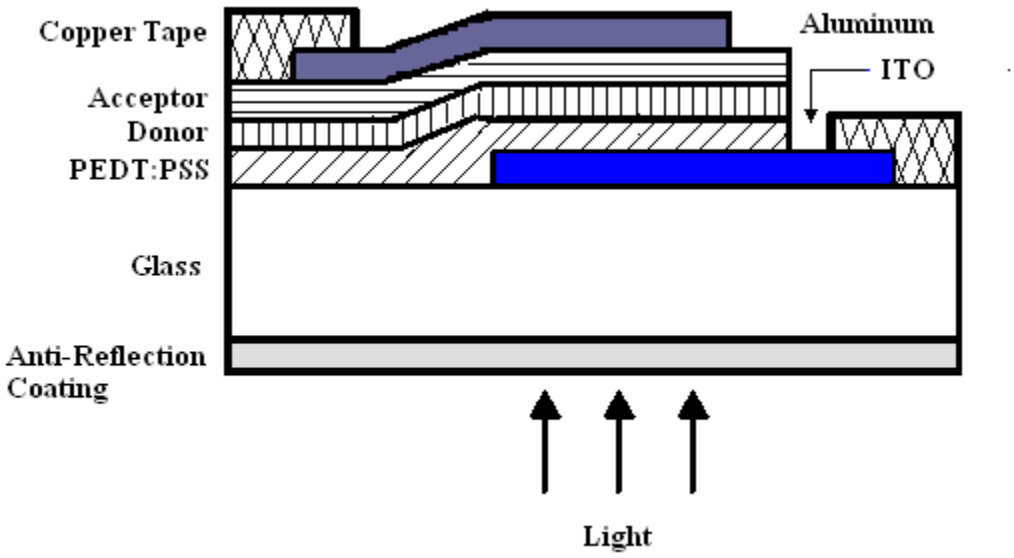

Figure 3.1 Construction of a typical bilayer device.

Figure 3.1 gives the schematic for a typical bilayer device. ITO-coated glass with a layer of poly(3,4-ethylenedioxythiophene): poly(styrenesulfonate) complex (PEDT:PSS or PDOT) serves as the transparent anode through which light is incident on the device. An anti-reflection coating minimizes reflection losses. The PEDT:PSS is followed by a layer of donor and then acceptor material, on top of which aluminum is evaporated to form the cathode. The layers deposited on the ITO have thicknesses in the nanometer range and hence can easily be scratched. To prevent damage to the devices while making contacts to the electrodes, conductive adhesive copper contacts are used that allow wires to be clipped onto the device without damaging the films. Also, to prevent the electrodes from shorting through the film, the copper contact is placed on the Al in a region where the ITO layer has been removed. To do so, prior to film depositions, the substrate was subjected to an acid etching process followed by a base cleaning step. The anti-reflection coating and the un-etched ITO regions are masked using electric insulation tape. The slide was then immersed in a 50% 12.1 M HCl and de-ionized water solution for half an hour, to dissolve the exposed ITO. After this, the tape was removed and the slide rinsed and cleaned with acetone to remove any adhesive from the masking tape. It was then sonicated in a diluted 30% NH_4OH – H_2O_2 base cleaning solution. The slide was finally rinsed and wiped again with acetone before film deposition. The electrical contact to the ITO layer is made by removing the organic film by rubbing with an organic solvent and placing the copper tape on the exposed ITO region. The effective area of the device is then the region in the middle that is sandwiched by both the ITO and Al electrodes.

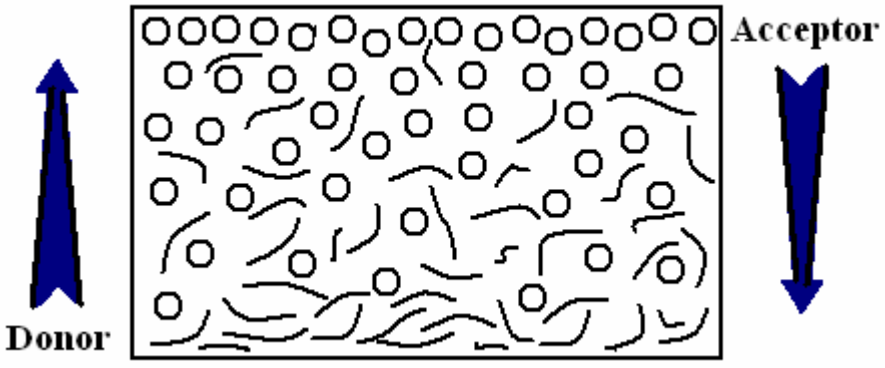

Figure 3.2 Interdiffused donor (curved lines) – acceptor (circles) layers. The arrows indicate the direction of reducing concentration for each species.

Concentration gradient devices are constructed similarly the bilayer devices with an extra heat treatment step to produce the donor – acceptor interdiffusion (ID) layer. The interdiffusion is normally done immediately after the acceptor deposition, though the effect of interdiffusion after Al deposition has also been investigated. Figure 3.2 is a cartoon of a heated bilayer. We have with pure material on either end that reduces in concentration as we proceed deeper into the layer.

Bilayer and ID devices are deposited on 1" by 1" glass substrates. Up to 8 devices can be made on one slide, each with an approximate 5mm by 3mm active region. This is achieved by using a mask during Al deposition that separates the slide into 8 parts. Figure 3.3 shows a cartoon for a completed slide with 8 devices. The devices are labeled A to H. ITO is etched such that a 0.5" by 1" strip down the center of the slide would remain to serve as a common cathode for all the devices. The organic film is wiped off at one end of the slide to make contact with the ITO.

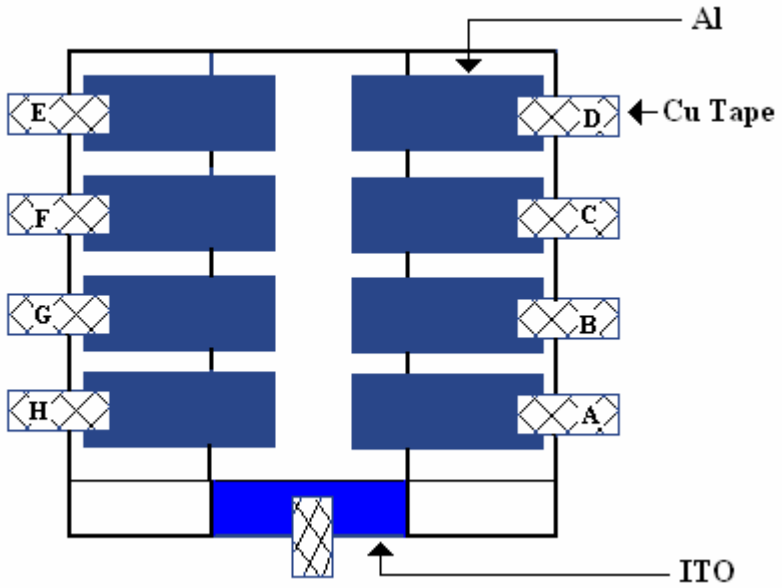

Figure 3.3 Completed slide with 8 devices.

3.2 Experimental Set-ups for Device Construction

3.2.1 Spin-Coater

A Spin-Coater from Chemat Technologies (KW-4A) was used to spin-cast the PEDT:PSS and the donor layers onto the ITO-coated glass substrate. The solution is dropped and smeared onto the substrate which is then spun at speeds ranging from 1000 to 3000 rpm. As the solution is spun off the slide, the solvent evaporates, producing a uniform film. The PEDT:PSS layer was spun-cast from an aqueous solution at 1500 rpm while the donor polymers were cast from solutions in volatile organic solvents such as chloroform. In the case of chloroform, the solvent evaporation and film formation is almost instantaneous which allows for a reasonably sensitive control of layer thickness.

Thickness of spin-coated films may be varied in two ways. Different solution concentrations will produce films with different thicknesses; the greater the concentration, the thicker the film. Also, varying the spin speed will change the film thickness; the lower the spin speed, the thicker the film. This was studied in detail for P3OT dissolved in chloroform. Changing spin speeds does not seem to produce as much of a thickness variation as does using solutions with different concentrations.

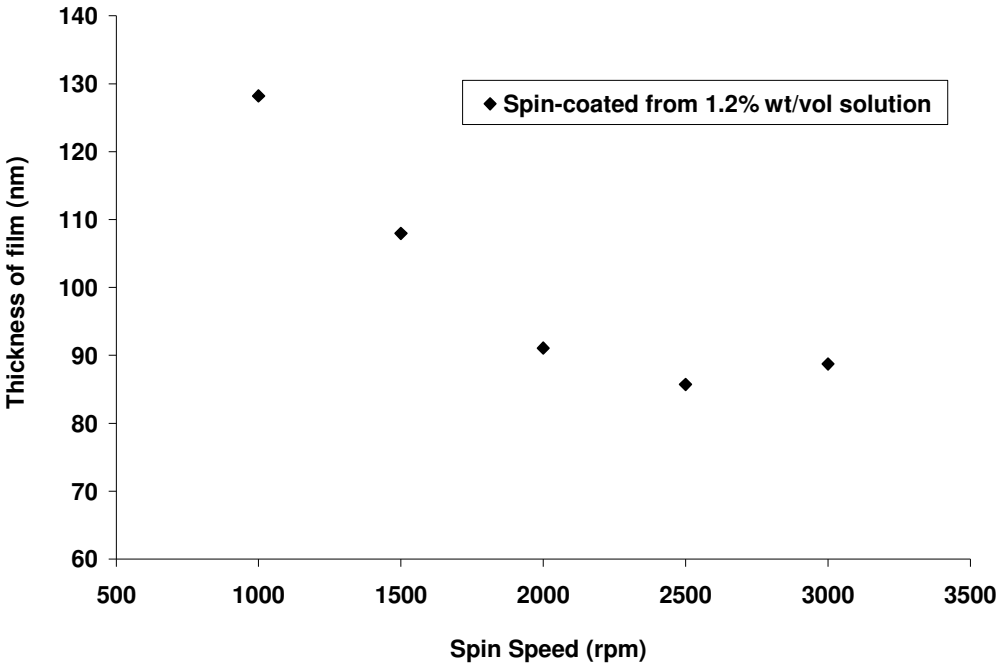

Figure 3.4 Plot of thickness versus spin speeds for films cast from 1.2% weight/volume solutions of P3OT in chloroform. The solution was spread on the slide and then spun, in order to obtain uniform films.

Figure 3.4 shows the variation in thickness versus spin speeds for a 1.2% weight/volume solution of P3OT in chloroform deposited on plain glass slides. For low spin speeds, as the speed changes the thickness changes. This sensitivity to speed change decreases as the speed is increased, due to a combination of the moment of inertia of the system that spins the slide and the highly volatile nature of chloroform. In an ideal case, the spin coater system would reach the set speed as soon as it was set to spin, but practically, it would take some time as the speed ramps up from zero. As the set point is increased, it would take longer to reach the set speed, especially if the ramp rate hits a saturation maximum. In the meantime, before the final speed is reached, the majority of the solvent evaporates, thereby establishing a film thickness greater than what would be obtained had it reached final speed instantaneously.

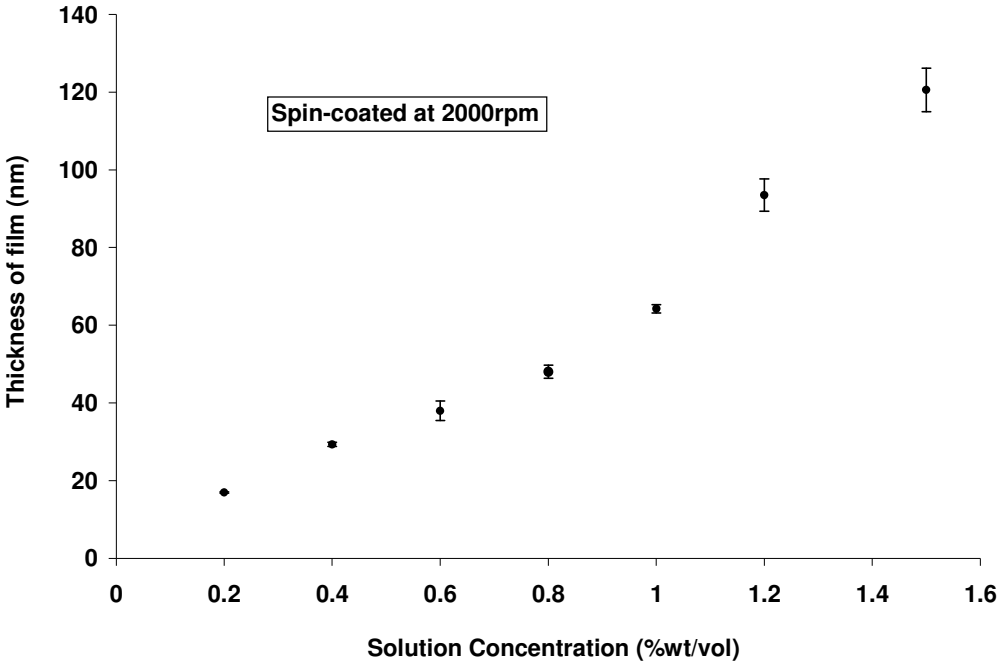

Figure 3.5 Plot of thickness versus solution concentrations of P3OT in chloroform, for films spread on the slide and spin-coated at 2000rpm. Error represented is the standard deviation of the set of values of thickness for each concentration that was averaged to yield a data point.

Figure 3.5 shows the variation in P3OT film thicknesses, spin – coated at 2000 rpm, versus the concentrations of the original solutions in chloroform. The thickness of the film increases as the concentration of the solution increases. These data points were

obtained by averaging over a set of 3 or more thickness values for each solution concentration and the error shown is the standard deviation of the averaged values. This method was used to vary the thickness of the spin – coated layers since it allowed for a larger range of thicknesses as compared to the previous method where spin speeds were varied.

3.2.2 Vacuum Evaporator

For devices containing C_{60} or $Sc_3N@C_{80}$ endohedral fullerene (also known as Trimetasphere, TMS), the acceptor layers were evaporated in a vacuum evaporator from Ladd Inc. (#30000), under typical pressures of 4 to 7 μTorr. Figure 3.6 shows the set-up for acceptor sublimation along with a schematic for the evaporator. The acceptor material is placed in a quartz cuvette that sits in a brass container with a 2 mm diameter hole in the cap to achieve good directionality of the sublimed material. This reduces waste of the sublimed material, making the deposition process more efficient. A drawback of this was that the films are often not completely uniform; the thickest portion is at the center of the deposition and the tapers to lower values at the edges of the slide. To account for this, thickness measurements were taken at 3 points on the slide to quantity, non-uniformity in film thickness. The brass holder is placed in an electrically insulating and thermally conducting ceramic holder. A tungsten resistive-heating coil is wrapped around the ceramic holder that is connected to electrodes in the vacuum deposition unit. This is held on an insulating stand that isolates it from the rest of the evaporator system. A thermocouple and heater interfaced with an Omega CN9000A temperature controller are connected to the stage holding the substrate to allow for controlled heating of the substrate under vacuum. This heating step was performed to anneal the donor layer prior to acceptor deposition as well as, in some cases, to produce interdiffusion under vacuum.

The aluminum layers were also deposited under vacuum by evaporating Al granules (purchased from R.D. Mathis Co. part #: ME17-3X.025W) from tungsten wire boats.

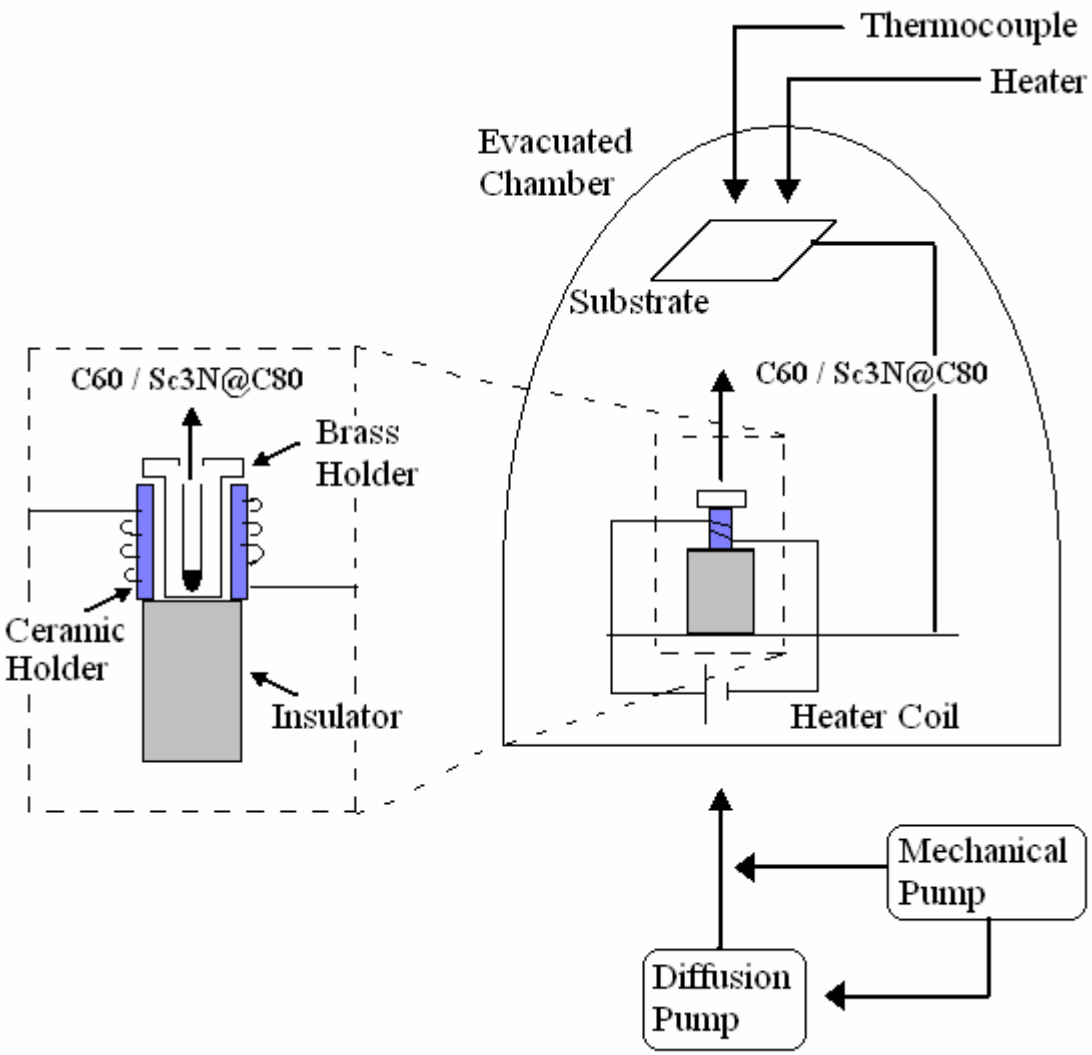

Figure 3.6 Schematic of the vacuum deposition unit and the C_{60} and $Sc_3N@C_{80}$ sublimation set-up.

3.2.3 Heat Transfer

Thermal interdiffusion is achieved by placing the ITO-coated glass slide, with a bilayer on it, on a hotplate and subjecting it to controlled heating conditions. Three different set-up conditions were followed for the intediffusion process:

1. The sample was placed on a hotplate in a dark plexiglass box that had flowing Argon, creating a mild over-pressure that prevented oxygen from entering the system. The sample was cooled in a similar atmosphere.

2. The sample was heated on a hotplate, under vacuum on the order of a few μTorr and was cooled similarly.
3. The sample was heated on a hotplate, under vacuum on the order of a few μTorr. For the cooling step, argon was let into the chamber till atmospheric pressure was reached.

Ideally, when steady state equilibrium is reached, the interdiffusing films would be at the same temperature as the hotplate. But various losses, dependent on the material or environment, occur in the heat transfer process and would result in a lower temperature at the film as compared to the hotplate. Since these experimental set-ups mainly state the hotplate temperature, it is important to study the heat transfer processes so as to get an idea of the error margin between the measured, hotplate temperature and the actual film temperature during interdiffusion. In addition to this, the dynamics of the cooling process can also determine some properties of the interdiffused region such as the extent of interdiffusion and the degree of aggregation of the materials. In this section, a brief theoretical background on the heat transfer process will be given before a more detailed description of the interdiffusion processes are given in subsequent sections.

Heat transfer is the transfer of energy motivated by a difference in temperature. The three main processes of heat transfer are conduction, convection and radiation.

1. Conduction: This is the process of heat transfer through a medium induced by a thermal gradient. It occurs due to the diffusion of energy through random molecular motion but it does not result in any net displacement of the medium. In fluids, this can occur through transfer of energy during collisions. In solids, this transfer occurs through phonons generated by lattice vibrations. One-dimensional heat conduction, which is energy transfer perpendicular to a wall, is most valid for our case. The heat conduction equation is given by Fourier's law that states that the rate of flow of heat (dQ/dt) through a unit area (A), from one point to another, is directly proportional to the difference in temperatures (ΔT) and inversely proportional to the distance between these two points (L). It is given by:

$$\frac{1}{A}\frac{dQ}{dt} = k\frac{\Delta T}{L} \tag{3.1}$$

The proportionality constant k (W/(K·m)) is a material dependent property known as the thermal conductivity. In this study conduction contributes to both the heating process as well as the cooling processes by the transfer of energy to and away from the slide when the slide is in contact with a solid surface.

2. Convection: This is the heat transfer that is achieved by motion of energetic particles, guided by a thermal gradient. This phenomenon is found mainly in fluids (liquids and gasses). It may occur in two ways: random molecular motion which results in the net diffusion of the energetic particles or a net flow of matter that occurs in the presence of a thermal gradient and hence leads to energy transfer. Convection may be classified depending on the nature of the flow of the fluid. Free convection (or natural convection) occurs when motion is motivated by buoyancy forces, due to differences in density within the fluid, caused by a thermal gradient. Forced convection occurs when heat is transferred by matter that flows due to an external force, for example, when air is blown on a hot surface by a fan. Both processes can be expressed by the convection heat transfer rate equation:

$$\frac{d^2Q}{dx^2} = h(T_S - T_\infty) \tag{3.2}$$

This states that the convective heat flux, d^2Q/dx^2 (W/m^2), is proportional to the difference between the temperatures of the hot surface, T_S (K), and the ambient fluid at infinity, T_∞ (K), as measured along the direction of the considered component of convection (x-direction in this case). The proportionality constant, h (K.W/m^2), is the convection heat transfer coefficient, which is dependent on the hot surface-fluid interface geometry, nature of fluid motion and the thermodynamic and transport properties of the fluid.

In this thesis, convective heat transfer mainly appears in relation to cooling of the sample. This can also be expressed by Newton's Law of cooling, which states that the rate of change of the temperature (dT/dt) is proportional to the difference between the temperature of the hot surface (T_S) and the ambient temperature (T_∞):

$$\frac{dT_S}{dt} = -k_N(T_S - T_\infty) \tag{3.3}$$

This is another form of equation 3.2, expressed in terms of temperature instead of heat flux. The displacement dependent thermal gradient properties of the ambient fluid would

be one of the factors that determine the proportionality constant k_N. The negative sign indicates temperature drop of the surface due to heat that is transferred out. This equation yields an exponential decay of surface temperature with time. The curve would be steeper for forced convection of the fluid as compared to free convection, indicating a faster cooling rate.

3. Radiation: This is the energy emitted by matter at a finite temperature. This is independent of the surroundings or material properties and is purely a function of the temperature of the hot surface. For the case of a plane surface of uniform temperature, the heat transfer through radiation may be expressed as:

$$Q_{rad} = h_{rad} A(T_S - T_{amb}) \tag{3.4}$$

The surface area is given by A, the surface temperature is T_S and the ambient temperature is T_{amb}. The proportionality constant, h_{rad}, is given by:

$$h_{rad} = \varepsilon\sigma(T_S + T_{amb})(T_S^{\,2} + T_{amb}^{\,2}) \tag{3.5}$$

where, ε is the emissivity, which is a radiative property of the surface relative to that of a perfect blackbody ($0 \leq \varepsilon \leq 1$) and σ is the Stefan-Boltzmann constant (5.67×10^{-8} K^4W/m^2). Equations 3.4 and 3.5 give a net radiation heat transfer of:

$$Q_{rad} = \varepsilon\sigma(T_S^{\,4} - T_{amb}^{\,4}) \tag{3.6}$$

Normally, for the scale of temperatures of the order of a 100^0C to 200^0C, radiation is negligible as compared to conduction and convection. In this thesis, interdiffusion was sometimes done in an enclosed vacuum chamber. In this special case, where the lack of ambient gas molecules makes convection contributions negligible, the process of radiation becomes more prominent.

3.2.4 Temperature of the Film Surface

The temperature of the film undergoing interdiffusion may be modeled in terms of the heat transfer through a single wall. For this modeling, the case of heat treatment on a hotplate under atmospheric pressure is considered. Conduction is responsible for heat transfer to the film through the glass slide and convection and radiation are responsible for heat transfer away from the film and into the ambient. In steady-state, energy

conservation dictates that the rate of heat supplied equals the rate of heat lost at the film. The total thickness of the film is of the order of only a few hundred nanometers and, hence, any temperature gradient within the film is considered negligible. The conduction process that transfers heat in (Q_{in}) is given by:

$$Q_{in} = k_{glass} A \frac{T_{hp} - T_{film}}{L_{glass}} \tag{3.7}$$

Here, k_{glass} is the thermal conductivity of glass (1W/(K.m)), A is the surface area of the slide (6.25×10^{-4} m^2), T_{hp} is the hot plate temperature, T_{film} is the temperature of the film and also the temperature at the surface of the glass slide and L_{glass} is the thickness of the glass slide (9×10^{-4}m). The convection process that transfers heat out (Q_{out}) is given by:

$$Q_{out} = hA(T_{film} - T_{amb}) \tag{3.8}$$

where, h is the convection heat transfer coefficient (upper limit of 25K.W/m^2 for free convection) and T_{amb} is the ambient temperature (293K). A schematic for the geometry of the process is shown in Figure 3.7.

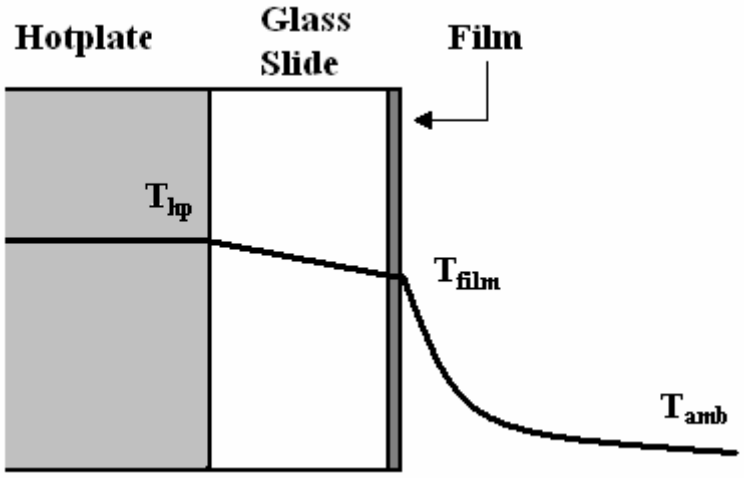

Figure 3.7 Temperature profile during heat treatment in the presence of convective losses.

In steady-state, $Q_{in} = Q_{out}$. Equating 3.7 and 3.8, we can solve for the temperature of the film as:

$$T_{film} = \frac{k_{glass} T_{hp} + hL_{glass} T_{amb}}{k_{glass} + hL_{glass}} \tag{3.9}$$

$$T_{film} = (\frac{k_{glass}}{k_{glass} + hL_{glass}})T_{hp} + (\frac{hL_{glass}T_{amb}}{k_{glass} + hL_{glass}}) \quad (3.10)$$

This shows a linear dependence of T_{film} on T_{hp} which is shown in Figure 3.8 as a plot of ($\Delta T = T_{hp} - T_{film}$) versus T_{hp}.

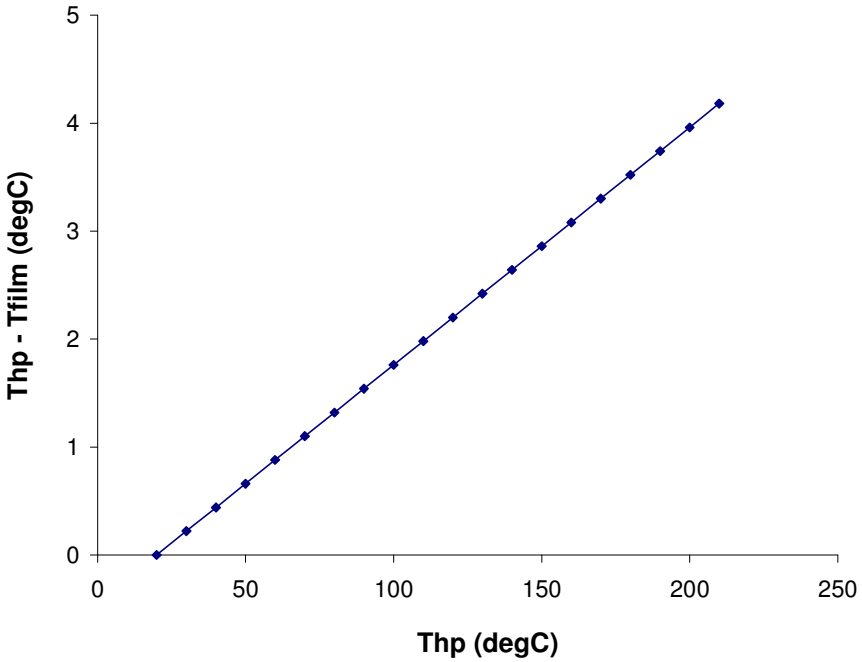

Figure 3.8 Modeled data for ΔT versus T_{hp}, where $\Delta T = T_{hp} - T_{film}$.

A maximum of 4.2 °C of difference is calculated between the temperature of the hotplate and that of the film for a hotplate temperature of 210 °C. Prior work showed good agreement between the modeled data and experimental data for the correlation between ΔT and T_{film}.[3] This is low enough for the effect of the temperature difference to be insignificant and so, henceforth, the hotplate temperature will be quoted.

For the case of heat treatment under vacuum, the main mechanism of heat transfer out of the film (Q_{out}) is by radiation. The vacuum chamber was sealed and insulating, thus any heat supplied to the ambient could not be dissipated easily and would increase the ambient temperature. This would reduce the temperature difference between the hot surface and the ambient, reducing the radiative loss. This is considerably more difficult to model and the set-up in the vacuum chamber does not provide for temperature measurements to be taken at the surface of the glass as well as at the hot plate.

Nevertheless, it would be safe to assume that the heat lost in this case is less than that for the case with convective heat loss, implying a smaller ΔT than before.

3.2.5 Thermal Interdiffusion

Thermal interdiffusion was generally done at temperatures above the glass transition temperature of the polymer so that the polymer is soft and allows the C_{60} to more easily diffuse into it. This was done in three different ways as mentioned in section 3.2.3; in a dark box with an over-pressure of Argon and under vacuum, where the sample was either also cooled under vacuum or under atmospheric pressure of argon gas. For majority of the work done with the P3OT – C_{60} system, the first interdiffusion process was followed. Bilayer samples were heated on a hotplate controlled by a CNi1622-C24 temperature controller from Omega Engineering Inc. that was computer controlled to ramp the temperature at a specified rate to a specified value where it would stay steady for a specified time and finally air cooled in the Argon atmosphere. The ramp rate was generally fixed at 20 °C/min. For set temperatures above 100 °C, the controller would over-swing by about 15 °C to 16 °C. Hence, to achieve heating at 130 °C, for 5 minutes, the controller was set for 118 °C, so it would over-swing to around 134 °C and cool back down to about 125 °C in 5 minutes, giving an average of ~130 °C in those 5 minutes. The sample was then allowed to cool under the same atmosphere, which can be understood by Newton's law for cooling (Convection). The measured interdiffusion temperature profile for this heating and cooling process is plotted in Figure 3.9.

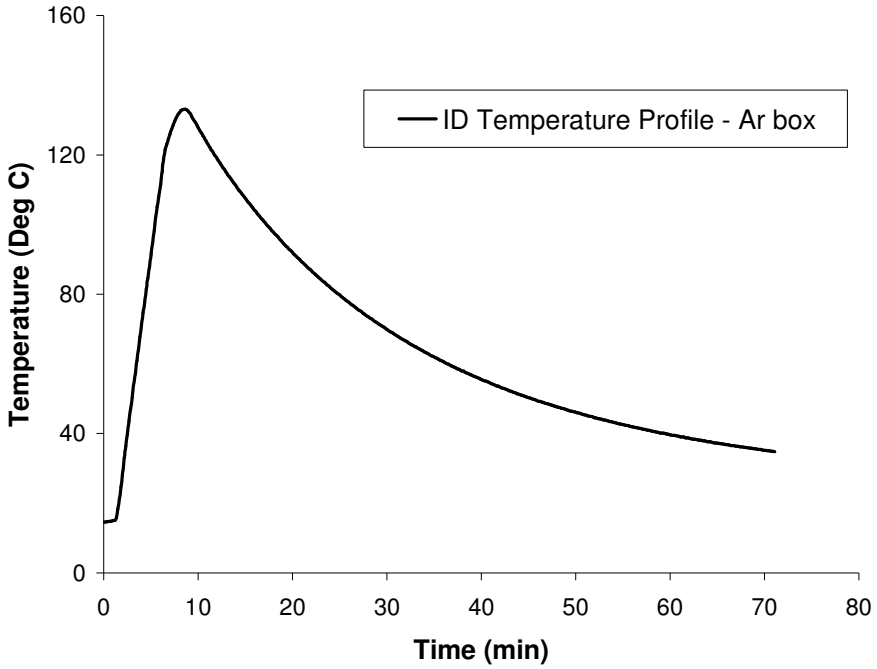

Figure 3.9 Plot of the heating and cooling temperature profile for devices interdiffused in the argon-filled box. Temperature was ramped at 20 °C /min, to a set-point of 118 °C, where it was held steady for 5 minutes after which it was allowed to cool under mildly flowing argon. An over-swing of the temperature was observed up to 134 °C.

In order to examine the kind of concentration gradient that would be obtained when an acceptor material was deposited on a heated donor layer, interdiffusion was also attempted during the deposition of the acceptor material, under vacuum. Vacuum interdiffusion was also done after acceptor deposition to minimize the exposure of the slide to oxygen, by not breaking the vacuum and exposing the set-up to air.

The heat transfer to the film during interdiffusion has been discussed in the previous section. One of the main differences between the procedure in the argon box and in the vacuum chamber is the rate of cooling of the slide after the heat treatment. In each case, the heat supply is turned off and the slide is allowed to cool in the same set-up. The temperature reduction is not instantaneous and so there may be morphological changes in the film during the cooling process, making it an important consideration. It was initially expected that the cooling under vacuum would be the slowest due to the lack of convective heat transfer in the absence of air. It was instead observed that this cooling process was much faster than that in the argon box. This is because the slide cools while still on the hotplate. In the argon box, the hotplate is isolated on an insulating stand

whereas in the vacuum chamber it is in contact with a metal holder that is in contact with the rest of the metallic systems of the deposition unit. Thus the cooling rate for the slide in the argon box is limited by the rate of convective air-cooling of the hotplate, whereas in the vacuum chamber, the hotplate and the slide are in contact with a large metallic reservoir that quickly conducts heat away from the sample, cooling it faster.

The cooling process in the vacuum chamber was slightly modified by allowing argon into the chamber, up to atmospheric pressure, during the cooling step. We believed that filling the chamber with argon would increase the cooling rate by adding free air-convection to the heat transfer processes. Each time this was done an initial sudden increase was observed in the temperature of the slide. The extent of the spike depended on the temperature and time of the previous heating step. This could be explained as the conduction of heat *to* the slide from the ambient, due to the energy given to it through radiation earlier, during the heating step. The slide very rapidly cools back down to its original temperature (within a minute) after which it cools at a rate that was just marginally faster than when the slide was cooled under vacuum. The extent of this temperature spike was moderated by waiting for a few minutes to allow the system to cool under vacuum and then allowing argon in slowly. Figure 3.10 shows the plot for cooling under argon after heat treatment at 140 °C for 20 minutes, under vacuum. Argon was allowed in immediately after the heat supply was turned off and so a spike in the temperature to 147 °C was seen. Allowing argon into the chamber served the purpose of matching the energy of the sample with the rest of the ambient, but it only marginally increased the cooling rate. This indicated that the main heat transfer process of cooling in the vacuum chamber is conduction which overshadows any convective cooling processes that may occur. This explanation has not yet been investigated. The rapid temperature increase and drop every time argon was allowed into the chamber requires more study before it can be fully understood.

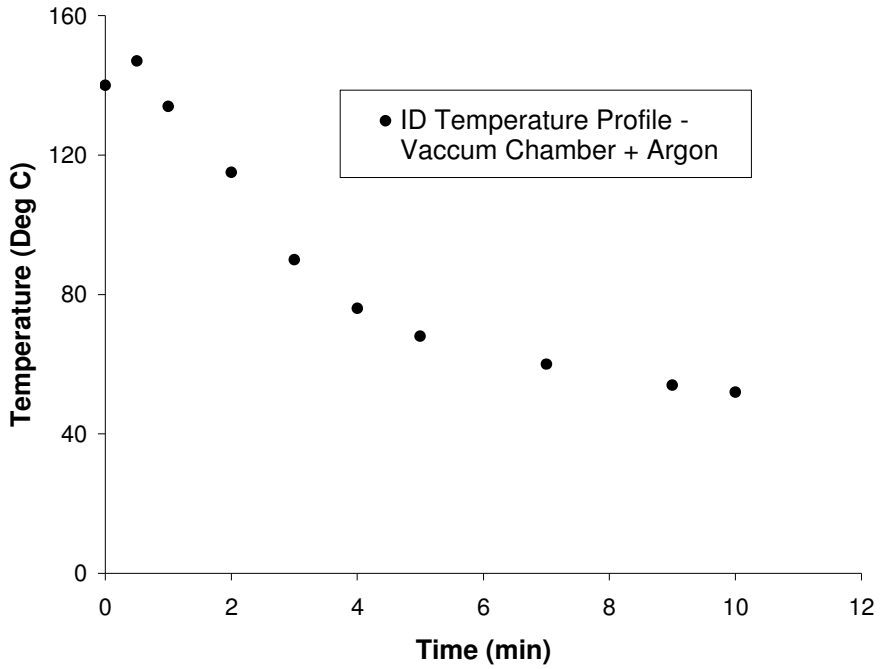

Figure 3.10 Cooling curve for a device interdiffused at 140 °C for 20 minutes in the vacuum chamber and cooled under an atmosphere of argon.

3.2.6 Mass Transfer

The temperature-driven interdiffusion process between polymer – fullerene films may be explained as mass transfer by diffusion. In this process, the diffusion of one mass species into another is driven by the concentration gradient of the diffusing mass within the other mass species. In our case, the two species are the polymer donor (B) and fullerene acceptor (A). The symbol D is not used for the donor since D is also the diffusion coefficient in these equations. When polymer and fullerene layers are brought in contact and heated, the thermal energy induces mixing of the materials, creating a concentration gradient which can be simply explained by Fick's laws of diffusion.[1] This explanation makes the following assumptions:

1. When the bilayer is heated, the layers are thin enough that the temperature is uniform throughout the layers so that no temperature gradient induced diffusion occurs.
2. Concentration gradient is the sole cause of diffusion.
3. Diffusion occurs at a steady temperature which makes the diffusion coefficient constant.

4. A is completely miscible in B.
5. The average polymer chain length (of B) is less than the critical entanglement molecular weight, hence in still in an un-entangled state.[2]
6. Flow rates are measured relative to one species (B in our case), so only A is considered to diffuse into B along the z-direction. B is considered stationary and the A – B interface (z = 0) does not move. This is based on the assumption that z = 0 is at the boundary between two semi-infinite media. Experimentally, B has a finite thickness which would result in the interface moving as fullerene molecules diffuse into and swell the polymer.
7. Mass diffusion flow is unidirectional, perpendicular to the A – B interface, along the z-direction.
8. There is an infinite reservoir of A which maximizes the concentration of A at the interface, $C_{A,z=0} = C_{max.}$ Thus, this model of diffusion is valid as long as there is still some pure material of species A on one side of the interface.
9. There is no chemical generation, hence, there is conservation of species.

Fick's law for the molar flow rate of A in B (J_A, in units of kmols/m^2s) can then be expressed as:

$$J_A = -C \cdot D_{AB} \cdot \nabla X_A \tag{3.11}$$

Where C is the total molar concentration (total # moles/unit volume), given by the sum of molar concentrations of each species in the region of mixing, C_A+C_B (kmol/m^3). D_{AB} is the binary diffusion coefficient, which is the diffusion coefficient of A in B and X_A is the mole fraction, given by C_A/C. Since this is concentration gradient driven, the molar flow rate of A at any depth in B will a function of the flow rate at a certain distance behind it and the gradient between these 2 regions. This is expressed by the equation for molar flow:

$$J_{A,\,z\,+\,dz} = -J_{A,\,z} + \frac{\partial J_{A,z}}{\partial z} dz \tag{3.12}$$

where, $J_{A,z}$ is the molar flow rate of A at depth z in B.

Conservation of species dictates that the amount flowing into a region should equal the amount flowing out and the amount stored in the region. This can be expressed in terms of the molar rates of flow and storage for A:

$$\dot{M}_{A,in} - \dot{M}_{A,out} = \dot{M}_{A,stored} \tag{3.13}$$

Hence, storage occurs if the rate of material going in is greater than the rate coming out. The rate of mass storage then can be expressed as:

$$\dot{M}_{A,stored} = \frac{\partial C_A}{\partial t} dz \tag{3.14}$$

Equation 3.13 is analogous to equation 3.12 and yields the relation:

$$\dot{M}_{A,stored} = -\frac{\partial J_{A,z}}{\partial z} dz \tag{3.15}$$

Combining these equations we get:

$$-\frac{\partial J_{A,z}}{\partial z} = \frac{\partial C_A}{\partial t} \tag{3.16}$$

Solving this we get the concentration of A in B as a function of depth in B (z) and the time (t):

$$C_A(z,t) = G + g(0)\int_0^{a'} da \exp(-a^2/4D_{AB}) \tag{3.17}$$

Where a is a function of z and t, as shown below, and C_A can be expressed as function of just a:

$$a = z/\sqrt{t} \Rightarrow C_A(z,t) = C_A(a) \tag{3.18}$$

The constants G and $g(0)$ are solved using the boundary conditions that:

1. The initial molar concentration (at $t = 0$) of species A at the interface, in B, is zero. At $t = 0$, no diffusion has occurred yet:

$$C_A(z, t=0) = C_A(a=\infty) = 0 \tag{3.19}$$

2. As specified in the assumptions, pure A can be found at the interface, $z = 0$, at any time t. At $z = 0$, C_A is maximum.

$$C_A(z=0, t) = C_A(a=0) = C_{A,\max} \tag{3.20}$$

It should be noted that the interface, z = 0, has no thickness in the z-direction. The term z = 0 could be viewed from the side of layer B, like in the first boundary condition, or from layer A, like in the second boundary condition. Both cases would be located at z = 0. This gives a final expression for the molar concentration of species A at a distance z into B, from the interface, after time t:

$$C_A(z,t) = C_{\max}[1 - erf(z / \sqrt{4 \times D_{AB} \times t})] \quad (3.21)$$

This model is useful for getting a feel of the interdiffusion process. But this theory, as is, is an over simplification that cannot be used directly to model the interdiffusion process of our system. A brief explanation of some of the parameters and assumptions that could be modified to make this model more suitable for our system, are as follows:

1. Control of the Temperature Profile During Heat Treatment: For the given experimental set-up, the heating profile, that induced the interdiffusion, was not constant. This can be clearly seen in Figure 3.9 in the Thermal Interdiffusion section. In order to prevent accelerated oxidation of the polymer at elevated temperatures, the heating chamber was first rendered oxygen free before the samples were heated. A finite time was required before the heater reached the set temperature, exposing the sample to a temperature gradient. The feedback control of the temperature controller was such that the temperature would over-swing before reaching the set value. Also, the sample was argon-cooled and so showed a typical exponential cooling profile. In the future, this may be rectified by creating an inert chamber that allows for the slide to be placed on the heater after it has reached the set temperature so it does not see a varying temperature ramp. Prior work done on the MEH-PPV system showed cracking of the polymer of thickness greater than 110nm, when the temperature was ramped at a rate greater than 30 °C/min. Hence the heating step would involve a careful choice of a ramp rate based on the thickness of the polymer under consideration. Also, the slow cooling curve may be minimized by an active cooling approach with a well defined cut off for the heating cycle. This may be achieved by rapidly quenching the device immediately after the heating step.
2. Study of the Polymer Diffusion Dynamics: In order to make the simplification that just A diffuses into B, the diffusion dynamics of both species A and B need to be similar. In this case, the dynamics of polymer diffusion can be very complicated and so must be studied in detail before incorporation into the model.
3. Study of the Fullerene Diffusion Dynamics: It is assumed that the fullerene diffusion is molecular. Prior work for the MEH-PPV – C_{60} system has shown aggregated clusters of fullerenes in the polymer matrix after interdiffusion. It is unclear if this

aggregation occurred during the cooling step or if the fullerene diffused into the polymer in clusters. If the latter were the case, that would greatly affect the diffusion dynamics and hence the choice of diffusion coefficient. Quenching the devices after heat treatment, as suggested in the first point, might freeze the mixed morphology, allowing for a better understanding of the origins of these clusters.

4. Evaluation of the Diffusion Coefficient (D_{AB}): In this explanation for the diffusion process, it was assumed that the diffusion coefficient was constant. If all the points mentioned above were considered, the final diffusion coefficient would be temperature and depth dependent. For example, during the temperature ramp, the polymer undergoes phase transitions. The rate of diffusion may vary by a few orders of magnitude, especially around the glass transition temperature, due to the phase transitions[3]. The method explained above, whereby the sample does not see a heating ramp, would allow for the use of a constant temperature diffusion coefficient.
5. Boundary Conditions: The boundary condition, that requires that pure A be found at the interface, $z = 0$, at any time t, is only valid as long as the limited fullerene layer does not all diffuse into the polymer. Also, this model does not account for the fullerenes diffusing all the way through the polymer till they encounter the polymer – ITO interface. Hence the boundary conditions used to evaluate the final integral would need to be modified.

3.3 Characterizing the Devices – Instrumentation and Theory

Characterization of the devices during and after fabrication was carried out under controlled lighting conditions. During device fabrication, reflectance and transmittance measurements were performed at each stage of film deposition to obtain the optical density curves and thickness values of the materials deposited. After fabrication, the photovoltaic properties such as the photoresponsivity and IV characteristics of the devices were measured under an inert argon atmosphere. The following sections detail the procedures followed to obtain these measurements.

3.3.1 Optical Density and Thickness

Optical density (OD) represents the amount of light that is absorbed (i.e., not transmitted) with respect to the light that *enters* the film and is related to the transmittance (T) of the film by:

$$T_{\text{int}} = 10^{-OD} \tag{3.22}$$

Transmittance is defined as the ratio of the transmitted light intensity to the initial intensity. The transmittance in this formula (T_{int}) is with respect to the internal intensity (I_{int}) or the intensity in the film just after the light has entered it. Experimentally, the initial incident intensity is measured for the light prior to entering the film and prior to reflection (I_0). Hence, T that is experimentally obtained is actually T_{ext}, the transmittance with respect to the initial intensity of light in air (I_0), which will henceforth be referred to as T. We now have:

$$T = \frac{I_T}{I_0} \tag{3.23}$$

$$T_{\text{int}} = \frac{I_T}{I_{\text{int}}} = \frac{I_T / I_0}{I_{\text{int}} / I_0} = \frac{T}{I_{\text{int}} / I_0} \tag{3.24}$$

where I_T is the intensity of the transmitted light. If I_A and I_R are the intensities of the absorbed and reflected light and R and A are the reflectance and absorption with respect to I_0, we can write:

$$I_0 = I_T + I_A + I_R = I_{\text{int}} + I_R \tag{3.25}$$

since I_{int} comprises the absorbed and transmitted components. Dividing through by I_0 to get the coefficients:

$$1 = T + A + R = \frac{I_{\text{int}}}{I_0} + R \tag{3.26}$$

Using equations 3.24, 3.25 and 3.26 in 3.22 we get an expression for OD in terms of the measured quantities, R and T, where the formula has been corrected for the reflectance.

$$OD = -\log \frac{T}{1-R} \tag{3.27}$$

A Filmetrics F20-UV thin-film spectrometer system with a deuterium-halogen (DH2000) light source from Ocean Optics was used to collect transmittance (T) and reflectance (R)

data after each layer was deposited. It should be noted that in equation 3.27, the contribution due to scattering is considered to be negligible.

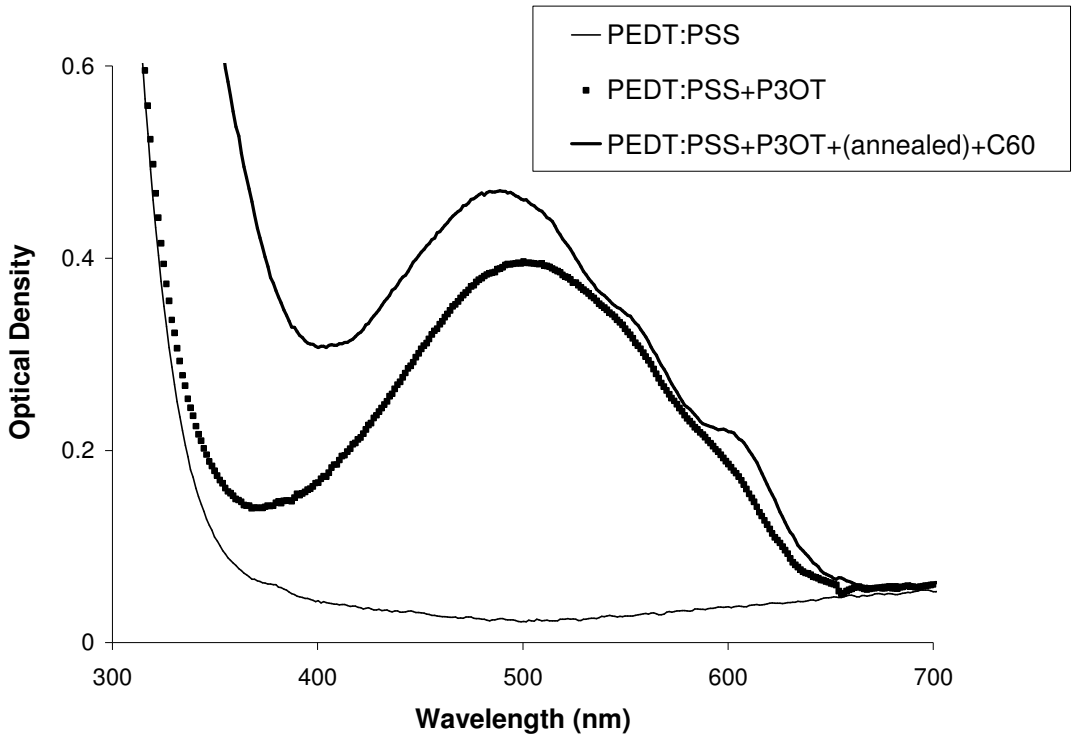

Figure 3.11 Plot of the optical densities of PEDT:PSS, P3OT and C_{60} as each layer was added to an ITO-coated substrate. The P3OT was annealed prior to C_{60} deposition.

The OD curves thus obtained were additive with each deposited layer, indicating no ground state interaction between the layers. This can be seen in Figure 3.11 which shows the optical density curves for a P3OT – C_{60} bilayer film, as each layer was deposited. This enabled us to find individual layer thickness in a multilayer structure by isolating the OD of the layer in consideration by simple subtraction. Hence OD of the n^{th} layer would be the OD calculated after the $(n-1)^{th}$ layer was deposited subtracted from the OD calculated after the n^{th} layer was deposited.

In addition to equation 3.22, T_{int} may also be expressed in terms of the absorption coefficient (α – defined as the absorption per unit length in the film) and the film thickness (d).

$$T_{\text{int}} = e^{-\alpha d} \tag{3.28}$$

Using equations 3.22 and 3.28, an expression for the thickness of the film in terms of the OD and α can be derived as:

$$d = \frac{OD}{\alpha \cdot \log(e)} \tag{3.29}$$

It should be noted that OD and α are wavelength dependent quantities, and hence, while performing this calculation, the values selected must all correspond to the same wavelength.

3.3.2 Photocurrent and I-V Characteristic Measurements

Unbiased photocurrents (I_{SC}) were measured using a Keithley 485 picoammeter. A 300 W Xe lamp, combined with a CVI CM 110 monochromator, served as the optical source. A Si diode of calibrated photoresponsivity was used to measure photocurrents, which was then used in equation 2.1 to obtain the power spectrum of the source ($P_{source}(\lambda)$). The average intensity of the source at the sample was around 4.2 mW/cm^2, at 470 nm illumination. The monochromator was computer-controlled to sweep the range of wavelengths from 300 nm to 700 nm, in steps of 5 nm, yielding photocurrent versus wavelength data. The unbiased photocurrent is also known as the short-circuit current (I_{SC}), since it is measured with no external bias being applied nor resistive load. This data was corrected for baseline (non-zero base currents measured when the devices is not illuminated) and then used to determine the photoresponsivity (PR) and external quantum efficiencies (EQE) as specified by equations 2.1 and 2.3.

The current – voltage (I-V) characteristic curves were measured in the dark and under monochromatic illumination, using a Keithley 236 Source Measurement Unit combined with the lamp and monochromator set-up to obtain photocurrents. The source measurement unit supplied a varying external bias and measured the resulting current through the device to yield the I-V characteristics. This instrument was also computer-controlled to sweep through a range of voltages in steps that could be externally specified. From this data, the fill factor values (FF) and the power conversion efficiency (η) were computed using equations 2.4 and 2.5 respectively.

Figure 3.12 shows the schematic of the set-up that was used to obtain the photocurrents and I-V characteristics. All data was collected with the devices placed in a box that was filled with argon gas to minimize photo-oxidation. It was also shielded from any other light except that from the source thereby minimizing errors due to photocurrents that might be generated by light sources that were not accounted for.

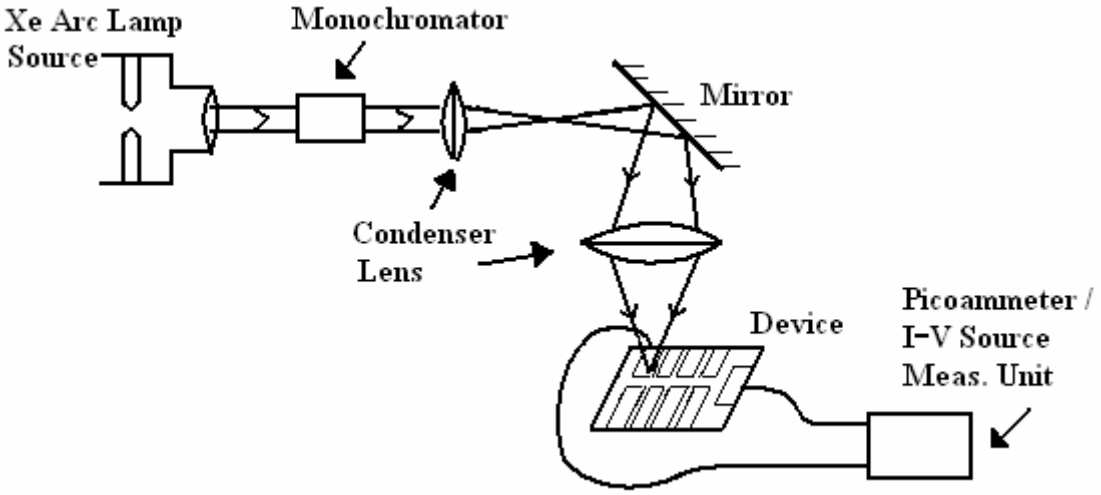

Figure 3.12 Experimental set-up to obtain I-V characteristics and photocurrent measurements.

In addition to measurements under monochromatic illumination, measurements were also taken under simulated AM1.5 solar spectrum. AM0 and AM1.5 filters, calibrated for the 300 W Xenon arc lamp, were purchased from Oriel instruments to produce the simulated solar spectrum. Another set-up was constructed to take photocurrent and I-V measurements, which was identical to the previous set-up (except for the monochromator) and these filters were placed in front of the lamp. The AM1.5 solar spectrum has an intensity of 100 mW/cm^2, which is the intensity of one sun (solar intensity at the Earth's surface) and corresponded to a current of 0.104 mA in our calibration diode. Using this information, the source of the second set-up was adjusted to emit the correct intensity of AM1.5 illumination. This second set-up was constructed during the course of this thesis work, hence the first set of measurements do not have measurements for AM1.5 illumination. In such cases, just monochromatic illumination results will be reported.

3.3.3 Auger Spectroscopy

Auger spectroscopy is an elemental analysis technique used to determine the composition of surface layers of a sample. In this process high energy electrons are incident on a sample and knock out a core orbital electron, for example, from the 1s orbital. A higher energy electron, such as the 2s orbital, then transitions to the core orbital, releasing energy equal to the difference between these orbitals ($E_{1s} - E_{2s}$). This energy may then be absorbed by another outer orbital electron, such as the 2p orbital. If the energy absorbed exceeds the energy of the 2p electron (E_{2p}), it will escape the atom. The kinetic energy of this escaped electron is then equal to the difference between the original binding energy and energy absorbed by it. These are called Auger electrons and their energies are given by:

$$K.E._{Auger} = (E_{1s} - E_{2s}) - E_{2p} = E_1 - 2E_2 \tag{3.31}$$

where E_{2s} is approximately equal to E_{2p} under the degeneracy approximation. When measured, this will appear as a peak in the energy spectrum of the emitted electrons. These kinetic energy peaks are characteristic of each element and can be used to identify the composition of the sample being tested. The Auger process is illustrated in Figure 3.13.

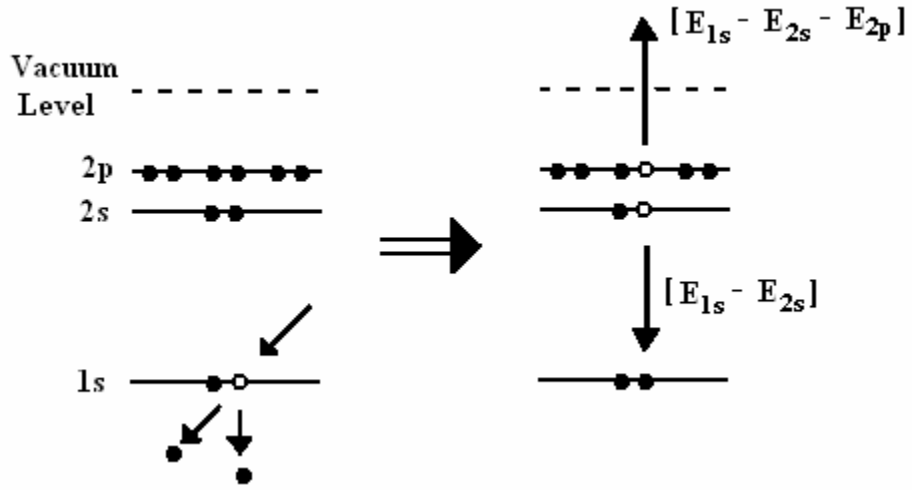

Figure 3.13 Schematic showing the Auger process; A core electron is knocked out, a higher electron transitions to the lower hole and the energy given out during this transition is absorbed by another high energy electron which escapes.

There are a few points to be noted:

- This process is similar to the production of X-rays. If the 2p electron does not absorb the energy of the transition, it is released as X-rays.[4]
- Only one type of transition, absorption and emission process is illustrated here, while, in fact, there may be many. For example: When a 2s electron transitions, another 2s electron may escape, or a 2p electron may also transition instead of a 2s electron. All these possible transitions have different energies and different probabilities. They will be seen as different peaks, with varying heights, that appear over a range of energies. All these peaks may be used to identify the material.[5]
- The emitted Auger electrons have typically low energies that lie between 50 eV and 3 keV. Hence, to prevent loss through collisions and scattering, the measurements need to be performed under ultra-high vacuum.[6]
- Another consequence of the low Auger kinetic energies is that only electrons from the top few nanometers of the sample are energetic enough to escape. This makes Auger spectroscopy predominantly a surface analysis technique.
- Not all materials lend themselves to analysis by Auger spectroscopy. Lighter elements, whose 2p orbital electrons are not as tightly bound, show a larger sensitivity to this process.

A 610 Perkin-Elmer Scanning Auger Spectroscopy system was used to study the surface of our samples. This system analyzed up to a depth of 5 nm into the film. It was combined with argon ion beam milling that removed the analyzed surface layer, by bombarding it with high energy argon ions and exposing a new layer for Auger analysis. The cycle was repeated and a layer by layer depth composition profile of the film was obtained. The amount of film removed at the end of each analysis cycle was controlled by varying the intensity of the argon milling beam. The films in this thesis are comparatively soft materials and hence the Ar ion beam milling process tended to create rough surfaces that gave rise to noisy depth profiles. To see the compositional trends better, these curves have been smoothened before they were presented in this thesis. Another consequence of the violent milling process was that the depth of milling could not be calibrated exactly. Therefore, any depth values reported for Auger spectroscopy results in this thesis are only

approximate values. All the same, in most cases, they tally quite well with thickness values calculated for the layers through OD measurements.

Our samples were analyzed starting from the top layer (generally the acceptor layer) and proceeding down into the film till the ITO layer was reached. The sulfur in the P3OT backbone was tagged by Auger spectroscopy as an indicator of donor material in the film. The presence of a concentration gradient between the donor and acceptor layers would then be seen as a gradual increase in the sulfur content as the analysis proceeded deeper into the film. The PEDT:PSS layer was removed prior to P3OT deposition in regions of the devices used for Auger measurements since PEDT:PSS also contains sulfur and is strongly detected by Auger spectroscopy. Carbon too gave a strong Auger signal, but since it was present in all the materials used, analyzing it would not yield any information on the composition of the films. Indium and oxygen were monitored to indicate the end of the active layer of the films.

3.3.4 Ellipsometry

Ellipsometry is a versatile optical technique used to investigate properties such as dielectric constants, real (n) and imaginary (k) refractive indices and thicknesses of thin films on a substrate by measuring the polarization dependence of reflected intensity as a function of incident polarization.

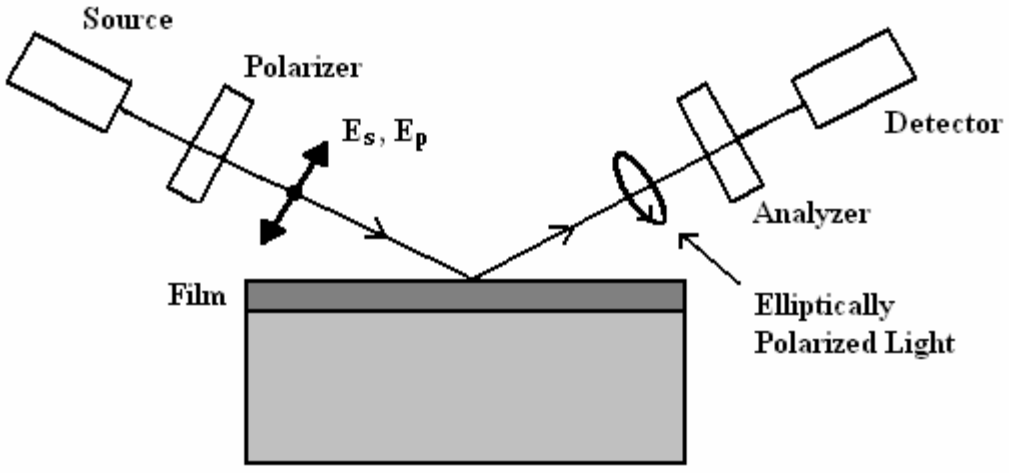

Figure 3.14 Schematic for the basic operation of the ellipsometer.

The incident polarized light has electric field components E_P and E_S in the directions parallel and perpendicular to the plane of incidence. It is reflected off a thin film of the material to be studied and the reflected light is examined by an analyzer and detector, as seen in Figure 3.14. When reflection occurs, the incident electric field components interact differently with the reflecting material. This is dependent on the properties of the material and is represented by the Fresnel equations. The reflected light has s-polarized and p-polarized components that have different relative attenuations and phase shifts, giving rise to elliptical polarization. The ratio of the electric field amplitude after reflection to that before reflection, for each component, gives the Fresnel reflection coefficients (R_S and R_P). The ratio of R_S and R_P represents the basic ellipsometry equation and is given as:

$$\frac{R_P}{R_S} = \tan\Psi \cdot e^{i\Delta} \tag{3.32}$$

Ψ represents the tilt of the reflected ellipse and Δ, its ellipticity. These ellipsometry parameters are then used to generate a theoretical model for the optical constants of the material. Generally, experimental data is obtained for one of these optical constants, which is then used as a reference to which the theoretical model is fit. When a good fit is achieved the other optical parameters that the model generates can be considered trustworthy.

In this thesis, this technique was used to determine the n and k values of P3OT and C_{60} by analyzing the experimentally obtained optical density curves from films of each of these materials. The results of this analysis will be given later in the chapter when these materials are discussed in greater detail.

3.4 Materials Used – Active Layer

Materials selection involved finding donor and acceptor materials that demonstrated good photovoltaic behavior and that could be deposited as a bilayer prior to the heating step. The main system studied is the P3OT – C_{60} system which showed a lot of promise in interdiffused devices.[7] Although C_{60} does not readily dissolve in any

solvents, a bilayer can be easily formed by evaporating the fullerene. This system has been used to optimize the interdiffused device fabrication by studying the different parameters that affect the concentration gradient and device performance. When ease of fabrication is considered, an acceptor material that can be cast from solution would be ideal. But solvent-processable acceptors greatly restrict the morphological study of organic photovoltaics to blend devices. To make a bilayer, when an acceptor like PCBM is deposited from most solvents, there is the danger that it would damage or remove the thin donor layer below it. Bilayers and interdiffused devices have been made with PCBM as acceptor using pyridine, which dissolves PCBM but barely dissolves P3OT. The endohedral fullerene $Sc_3N@C_{80}$ has also been studied as a new acceptor. The materials mentioned will be discussed in greater detail in the following sections.

3.4.1 Donor – P3OT

P3OT (poly(3-octylthiophene-2,5-diyl)) is used as the donor material in the work presented in this thesis. Its chemical structure is given in Figure 2.5a. P3OT was purchased from Sigma – Aldrich Co. in its regioregular form (rr-P3OT), which has a microcrystalline nature as compared to the regiorandom form, which is more amorphous. The regioregular structure displays crystallinity that grows upon heat treatment where as the regiorandom form stays amorphous.[8] The crystallinity leads to higher conductivities in the regioregular form and hence is preferred to the regiorandom P3OT. Figure 3.15 shows the optical density (OD) spectra of rr-P3OT films, as cast and after heat treatment at 120 °C for 40 mins and cooled under vacuum from 120 °C to 40 °C in about 50 minutes. The increased crystalline nature of the annealed film is seen as a slight increase in the peak at 510 nm and shoulders at around 550 nm and 600 nm.

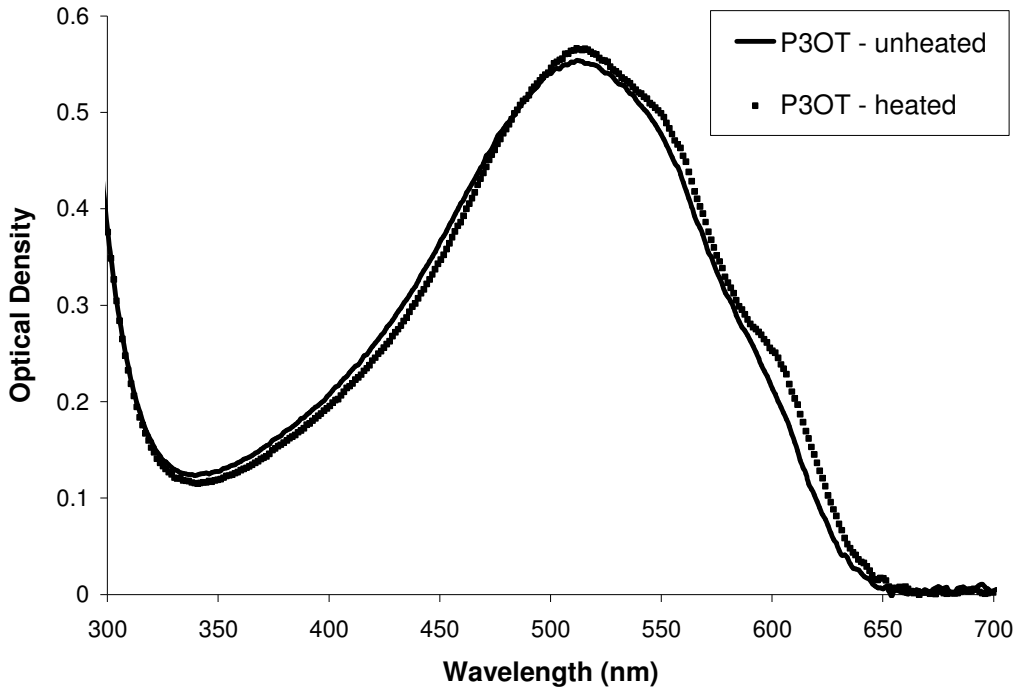

Figure 3.15 Optical density (OD) curves for P3OT film on glass, before and after annealing at 120 °C for 40 minutes.

The microcrystalline P3OT exhibits a glass transition and a melting transition. The glass transition can not be easily observed by differential scanning calorimetry (DSC) but is believed to occur at around 100 °C. The glass transition is of importance since, above this temperature, in the rubbery state, the polymer becomes soft which makes it easier for the acceptor to diffuse into it to produce the concentration gradient. The melting point (T_m) of rr-P3OT can be determined by DSC, but it changes depending on the degree of crystallinity, number of repeat units (chain length) and other such parameters. A range of values have been reported for the T_m of 187 °C[9] to 200 °C – 205 °C[8] and 230 °C[10]. Based on observations from heating studies on P3OT, 187 °C seems the most likely value for the melting point in our case. This will be more evident after the P3OT – $Sc_3N@C_{80}$ system and Auger spectroscopic study results are discussed in the following chapters.

HOMO and LUMO values can be determined using oxidation and reduction potential values from cyclic voltammetry measurements and absorption edges of the UV-vis spectra. Due to the various experimental parameters that these measurements rely on, in addition to the variation in the exact structure of the polymer film (degree of

crystallinity, average conjugation length etc.), the reported HOMO and LUMO values also fall in a range, as in the case of T_m. In 2003, Sensfuss *et al*. reported a HOMO value of -5.25eV and LUMO of -3.55eV for P3OT.[11] In 2004, the same group also reported -5.20eV and -3.61eV for the same.[12] Gebeyehu *et al.* (2002) had reported a P3OT HOMO of -4.9eV and LUMO of -2.8eV.[13] The important point to note is that, although the HOMO – LUMO gap seems to range from about 1.6eV to 2.1eV, the corresponding absorption spectrum is still within the range of visible wavelengths and, hence, is viable for organic photovoltaic use.

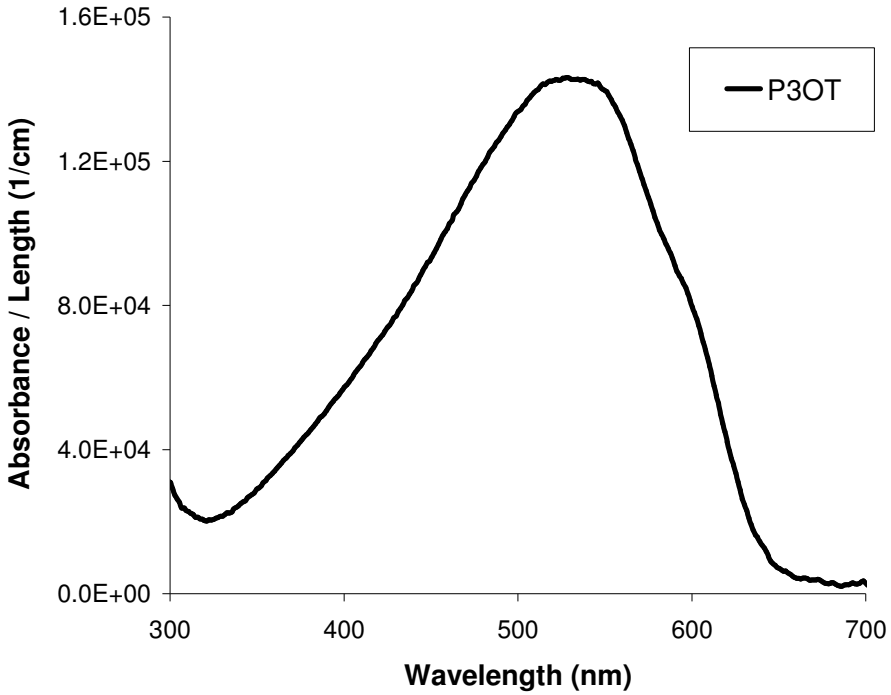

Figure 3.16 Plot of the absorbance per unit length (α cm^{-1}) of P3OT, for wavelengths ranging from 300 nm to 700 nm, obtained as an average over 18 data points from 8 slides and computed using an α of 14×10^4 cm^{-1} at 512nm as reference. This data set showed as standard deviation of around 1×10^4 cm^{-1}.

The α (absorbance per unit length) values for P3OT, as reported from previous work is 14×10^4 cm^{-1}, measured at 512 nm [7]. Optical density (OD) measurements were performed on a P3OT film and this value of α was used in equation 3.29 to find thickness of the film. The value of the thickness was then re-substituted in the same equation, along with ODs for other wavelengths, to obtain α values for all wavelengths. While calculating

α for P3OT, 18 data points from 8 slides, with varying thicknesses, were measured. The OD was measured at different positions on the slide. The α values were calculated for each and then averaged to give the final set of experimental α values as shown in Figure 3.16. This data set had a more or less constant standard deviation of around 1×10^4 cm^{-1}.

Real and imaginary refractive indices (n and k) were obtained from ellipsometric calculations performed on a P3OT film deposited on glass. OD curves for P3OT show a single predominant peak around 510 nm to 520 nm. Based on this, the 1-oscillator Lorentz model, with known parameter of peak wavelength of 518 nm was used to model for the refractive indices. This process was iterative and wavelengths ranging from 510 nm to 530 nm were tried as the peak wavelengths, due to the peak being broad. Although there was not much variation in the values for the different wavelengths, the curves corresponding to 518 nm were found to be most appropriate, since they were most centrally situated and hence the closest to an average. Figures 3.17a and 3.17b show the plots of the n and k values measured, respectively.

a.

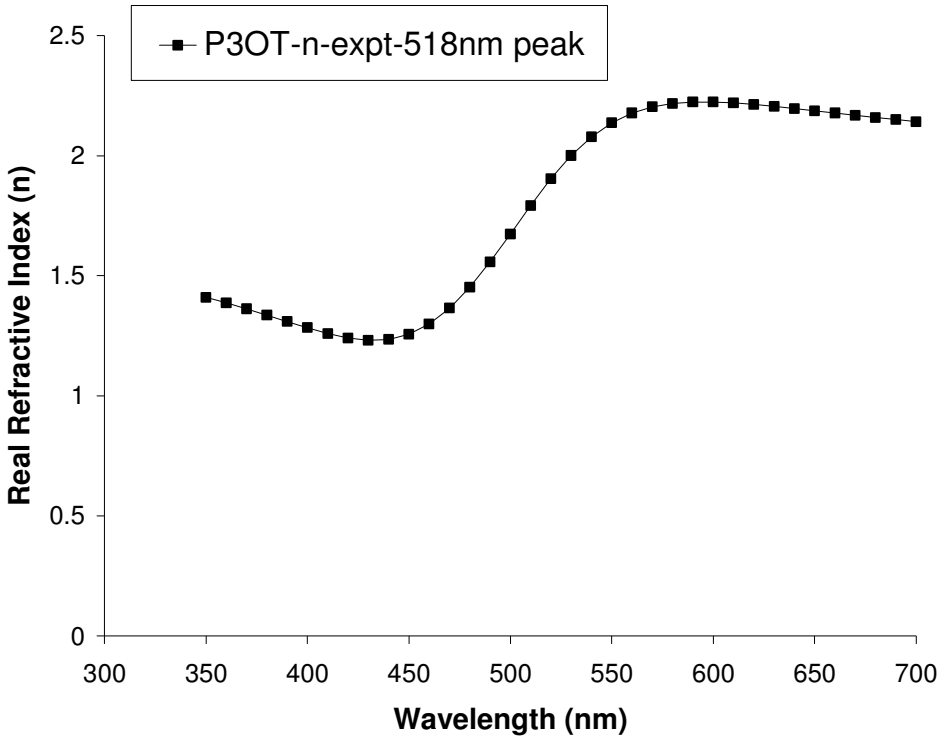

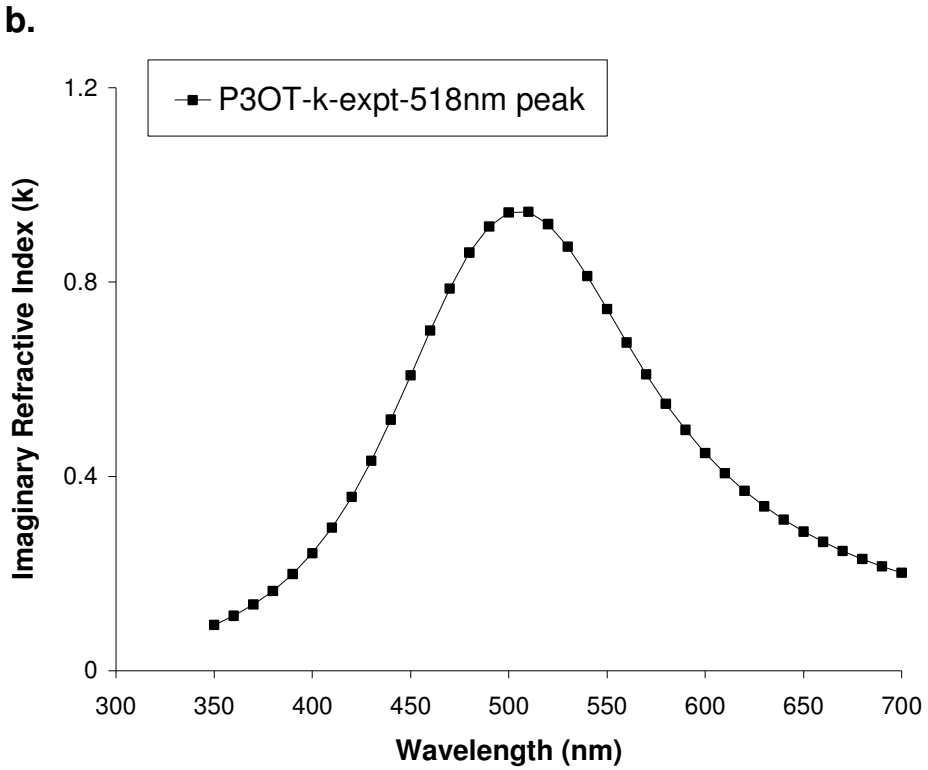

Figure 3.17 Plots of the (a) real and (b) imaginary refractive indices of P3OT, from ellipsometry, using the 1-oscillator Lorentz model for peak absorption considered at 518 nm.

3.4.2 Acceptor – C_{60}

A majority of the work in this thesis has been carried out using C_{60} as the acceptor. A brief history of the discovery of C_{60}, its chemical structure and effectiveness as an acceptor material for use in organic photovoltaics, can be found in sections 2.3.1 and 2.3.2. C_{60} was selected as an acceptor material for this work due to prior success with the P3OT – C_{60} system.[7,14] Reported room temperature diffusion of C_{60} into P3OT from a bilayer indicated that this system would be highly suitable for interdiffusion study.[15]

HOMO – LUMO values for C_{60} have been determined by various groups, mainly using the technique of cyclic voltammetry. The results reported show minor variation with respect to each other. Sensfuss *et al.* reported HOMO – LUMO values of 6.1 eV and 3.83 eV respectively, giving rise to a HOMO-LUMO gap of 2.27 eV.[11] Brabec *et al.* reported HOMO – LUMO values of 6.1 eV and 3.7 eV respectively that gave rise to a 2.4

eV gap.[16] The important point to note is that, while these values seem slightly different they still fall within the 2.3±0.1 eV band gap, reported for solid C_{60}.[17]

C_{60} was purchased from MER Corporation (Tucson, Arizona). It demonstrates poor solubility in most organic solvents. One of the better solvent choices for C_{60} is carbon disulfide (CS_2). C_{60} has been reported to show up to 7.9 mg/ml room temperature solubility in this solvent, which would yield a 0.8% wt/volume solution, at best.[18,19] Hence C_{60} in this study was thermally evaporated, under a vacuum of around 4 to 5 μTorr. A description of the C_{60} sublimation system has been explained in detail in section 3.2.2. For the sake of comparison, a few blend devices of P3OT and C_{60} have been studied, cast from a solution in CS_2. These were not as successful as the thermally interdiffused devices, since, to maintain the P3OT – C_{60} ratio in the blend, very small amounts of P3OT were used, resulting in very thin films with low optical densities and efficiency of light absorption.

The absorbance per unit length (α) of C_{60} used in this study, as obtained from previously reported work is 6×10^4 cm^{-1} at 435nm.[7] Using this value in equation 3.29, α values were calculated for a range of wavelengths from 300 nm to 700 nm, using a similar method as explained in the previous section for P3OT. Figure 3.18 a shows the experimentally obtained α values, averaged over 17 data points from 6 slides (measurements were taken on different parts of the slide). Figure 3.18b shows the OD spectrum for a 95 nm thick C_{60} film. The similarities between the two curves are because OD and α are proportional.

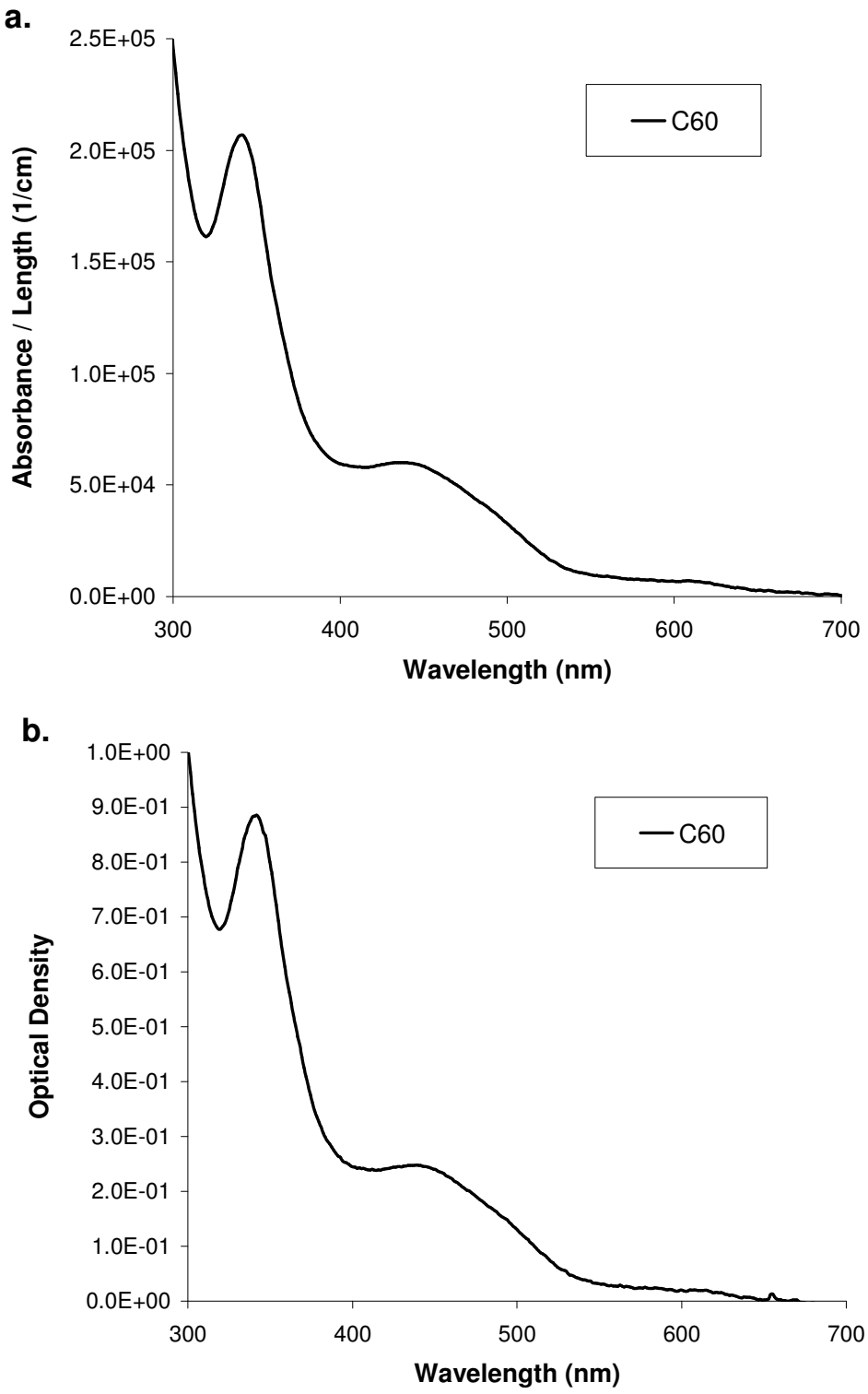

Figure 3.18 (a) Plot of the absorbance per unit length (α cm^{-1}) for C_{60}, wavelengths ranging from 300 nm to 700 nm, obtained as an average over 17 data points from 6 slides and computed using an α of 6×10^4 cm^{-1} at 435 nm as reference. This data set showed as standard deviation of approximately 0.3×10^4 cm^{-1}. (b) Plot of the OD of a 95 nm thick C_{60} film, thickness was computed using the above quoted α value at 435 nm.

Real and imaginary refractive indices (n and k) were obtained from ellipsometric calculations performed on a C_{60} film deposited on glass. OD curves for C_{60} show two predominant peaks around 340 nm and 435 nm. Based on this, the 2-oscillator Lorentz model was used to model the refractive indices, with the two peak wavelengths considered as the known parameters. The refractive index values were compared with those reported by Pettersson *et al.*[20], who used 3 absorption peaks to model their curves. The two most prominent absorption peak values that they reported (354 nm and 447 nm) were used in our model to generate n and k values, thereby offering a comparison of just the modeling. A direct comparison has also been made by reading off their values from the published curves and matching them up with our data. Figures 3.19a and 3.19b show the plots of these three methods, for the n and k values respectively. Except for a slight shift in the peak at around 450 nm, the 3 data sets are in quite good agreement; within an error of a few percent over most of the wavelength range. This indicated that the modeling done using our parameters reproduced standard results within a reasonable error margin.

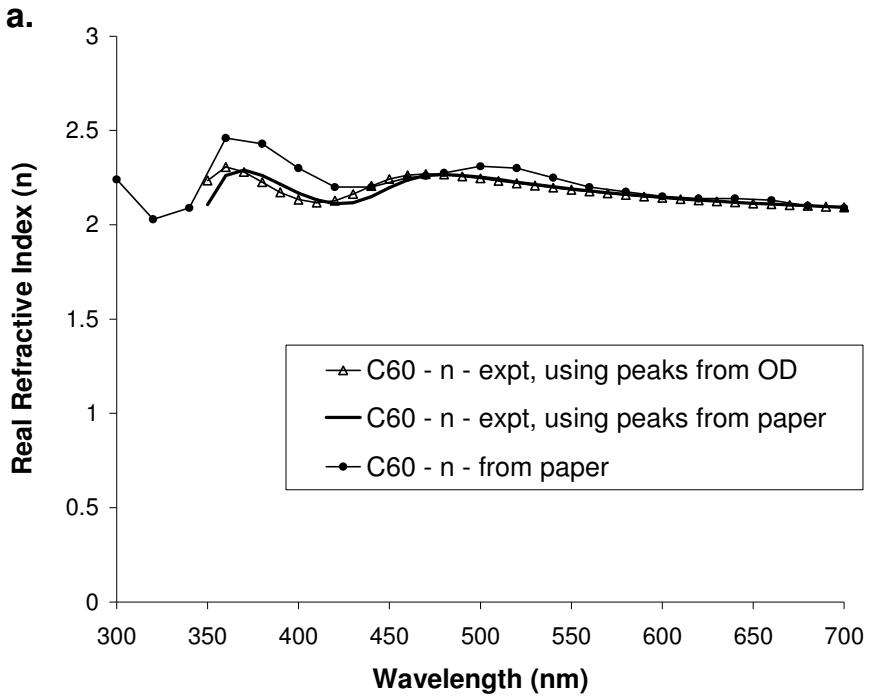

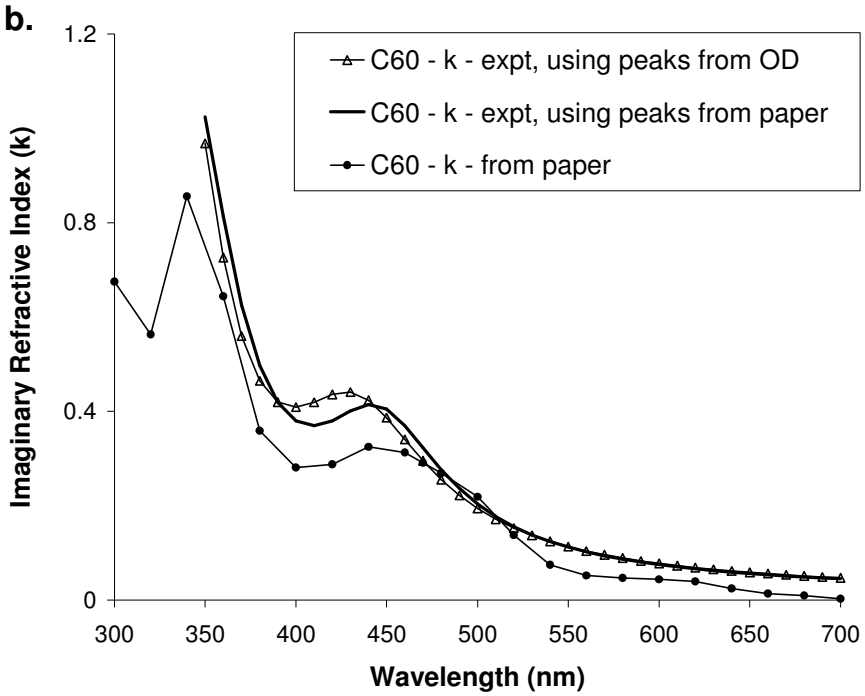

Figure 3.19 Plots of the (a) real and (b) imaginary refractive indices of C_{60}, from ellipsometry, using the 2-oscillator Lorentz model. Absorption peaks for modeling, were considered from OD data: 340 nm and 435 nm (Δ) and from peaks reported in reference[20]: 354 nm and 447 nm (—). Curves from the reference[20] are reproduced here for comparision with our data (●).

3.4.3 Acceptor – PCBM

1-(3-methoxycarbonyl)-propyl-1-1-phenyl-(6,6)C_{61} (PCBM), the derivatized, solution processable form of C_{60}, is a highly investigated acceptor material in much of the polymer – fullerene bulk heterojunction device work currently being conducted today. A brief overview of blend devices using PCBM has been given in section 2.9.1 of the previous chapter. In this work, following the success of C_{60}, PCBM has been investigated as an acceptor in thermally interdiffused concentration gradient devices. Figure 3.20 shows the structure of a PCBM molecule.

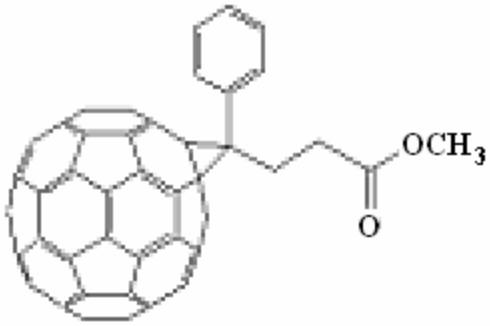

Figure 3.20 Chemical structure of PCBM.

The most commonly accepted values for the HOMO – LUMO levels of PCBM are 6.1 eV and 3.7 eV respectively.[21,22] These values are very close to those of C_{60} due to the similarity in the conjugated structures of the 2 molecules but the LUMO of PCBM is a little higher than that of C_{60}, thereby resulting in higher V_{OC} devices when PCBM is used as an acceptor.

The PCBM used in this work was provided by Luna Innovations Incorporated.

To find the absorbance versus wavelength dependence of PCBM, thickness values for a reference film needed to be obtained. A thick film of PCBM was spin-cast on a glass slide, from a 2% solution in chloroform, which would be used to compute α and whose thickness was to be deduced. This thick film yielded fringes in the reflectance spectrum as per the interference effects of light. An example of such fringes is shown in Figure 3.21. In such a case, light reflecting off the top surface of the film, at the air – film interface (hard reflection) and the light reflecting off the bottom surface of the film, at the film – glass interface (soft reflection) interferes to give rise to these fringes. The hard reflection adds a π phase to the reflected light. λ_1 and λ_2 are wavelengths that correspond to an adjacent pair of maxima and minima in the reflection spectrum. The conditions for constructive and destructive interference are given by:

$$2nt = (m + \frac{1}{2})\lambda_1 \tag{3.33}$$

$$2nt = m\lambda_2 \tag{3.34}$$

respectively. Here, n is the real refractive index at wavelengths λ_1 and λ_2, m is the order of the fringes and t is the thickness of the film. If an adjacent maximum and minimum are

considered, *m* stays constant. Substituting equation 3.34 in 3.34 an expression for the thickness of the film is obtained as:

$$t = \frac{1}{4n} \cdot \frac{\lambda_2 \lambda_1}{\lambda_2 - \lambda_1} \tag{3.35}$$

The values of λ_1 (450.51nm) and λ_2 (611.5nm) were taken from the graph and the refractive index values were found from literature.[23] Although n shows a dependence on wavelength, in the higher wavelength limit (were absorption is minimal), n is more or less constant. A refractive index value of n = 2, along with the λ_1 and λ_2 values were substituted in equation 3.35 and solved for the thickness *t*, of the film. The OD data was obtained for the same film (Figure 3.22b) and substituted along with the deduced t, in equation 3.29 to generate α values (Figure 3.22a). In this thesis, α value of 3.07×10^4 cm^{-1} at 450 nm is used to calculate thicknesses of PCBM films. It should be noted that this α value has not been cross-checked by any other method, but it is believed that it will yield thickness values that are within a reasonable error margin of the correct value.

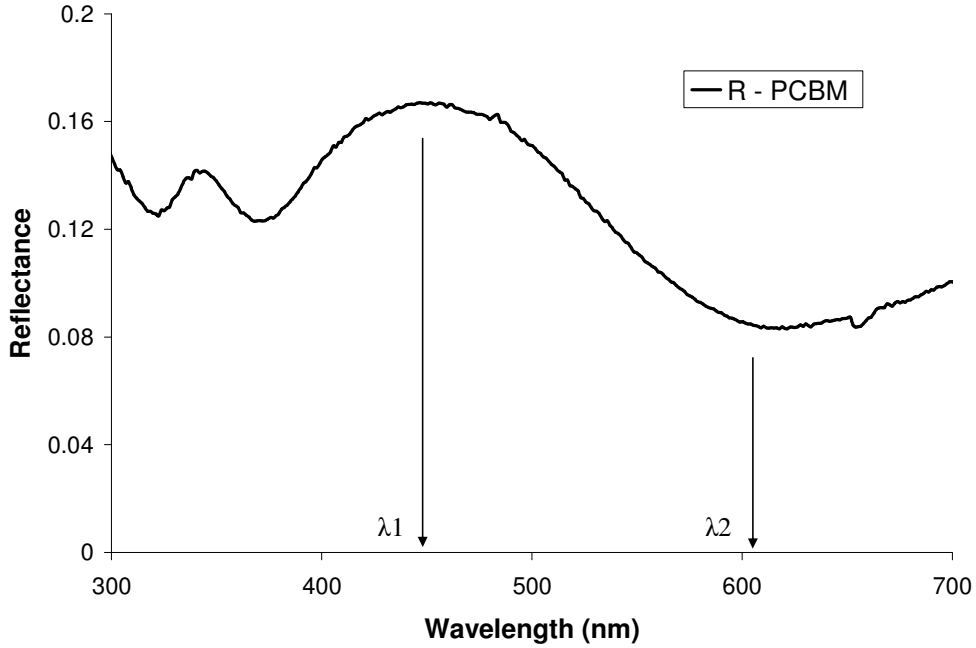

Figure 3.21 Reflectance vs. wavelength for thick PCBM film that shows interference fringes. λ_1 (450.51 nm) and λ_2 (611.5 nm) were the maxima and minima selected to deduce thickness of the film.

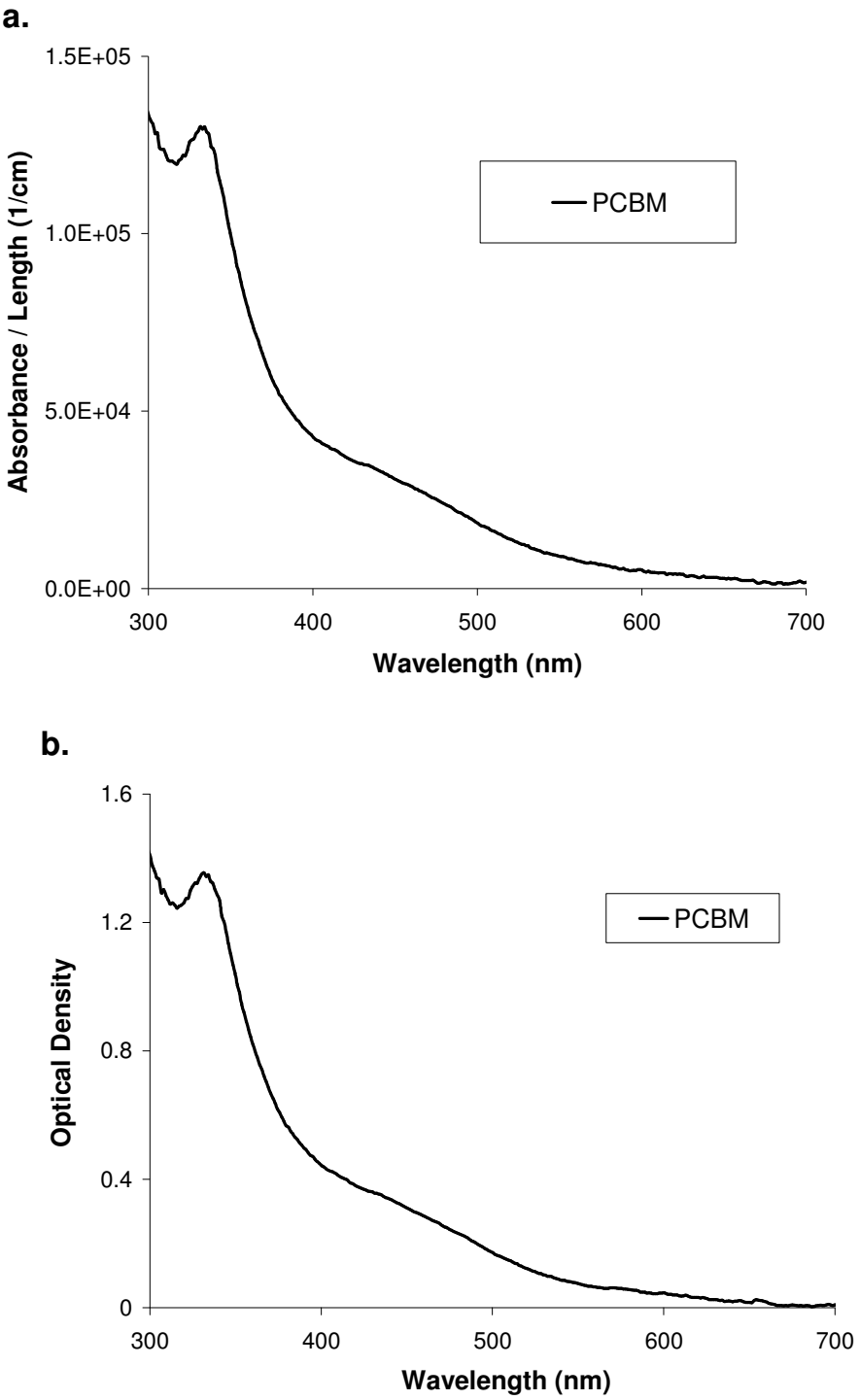

Figure 3.22 Plots of (a) absorbance vs. wavelength and (b) optical density vs. wavelength for a PCBM film.

3.4.4 Acceptor – $Sc_3N@C_{80}$

The endohederal fullerene (or trimetasphere) $Sc_3N@C_{80}$, is investigated here for the first time as a potential acceptor material. Figure 3.23 shows the chemical structure of the trimetasphere. The C_{80} fullerene cage encapsulates one nitrogen and three scandium atoms.

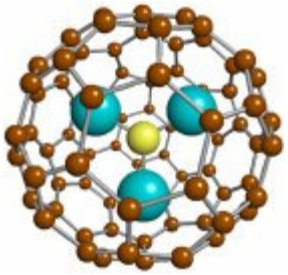

Figure 3.23 Chemical structure of $Sc_3N@C_{80}$ Trimetasphere, image taken from webpage: http://www.lunainnovations.com/products/products.htm

Absorbance per unit length values for the endohederal fullerene were supplied to us by Luna nanoWorks, Danville, Virginia. They measured the thickness of a $Sc_3N@C_{80}$ film by scratching it to obtain a sharp edge. The height of this edge, which corresponded to the thickness, was measured using an Atomic Force Microscope (AFM). The α value for $Sc_3N@C_{80}$ thus obtained and used in this thesis is 21.49×10^4 cm^{-1} at 471 nm.

α values reported in the α vs. wavelength plot shown in Figure 3.24a were calculated using equation 3.29 with OD and thickness data measured in our lab. An example of the OD curves obtained for $Sc_3@C_{80}$ is shown in Figure 3.24b. The thickness used in this calculation, were obtained using the initial α supplied by Luna nanoWorks as mentioned above. The α curve shown was obtained as an average of 13 data points from 2 slides, where each measurement was taken on different parts of the slide. These data points showed a higher standard deviation than for C_{60} or P3OT, approximately 3.1×10^4 cm^{-1} for wavelengths above 400 nm and reaching a maximum of 33.4×10^4 cm^{-1} below 400 nm.

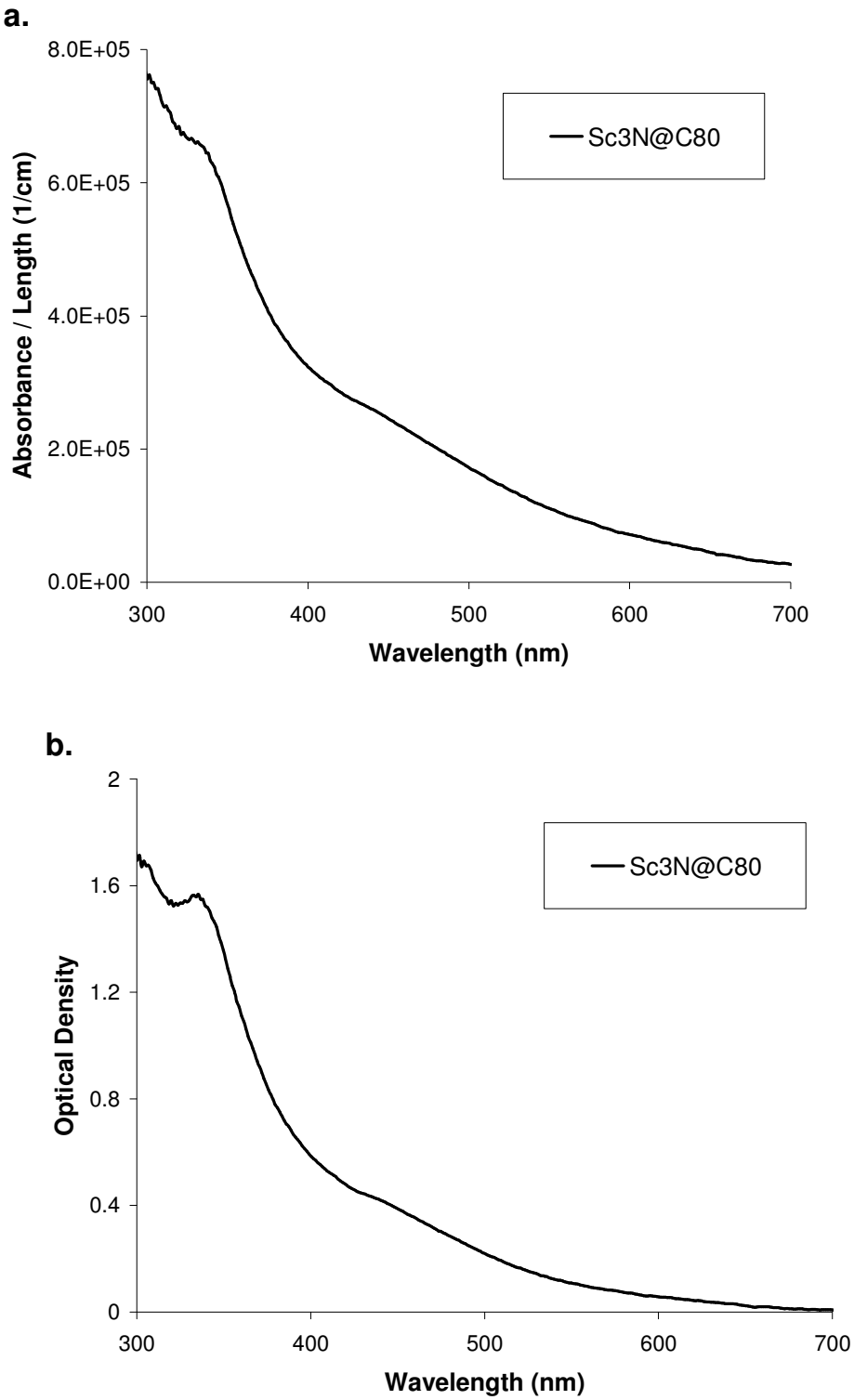

Figure 3.24 (a) Plot of the absorbance per unit length (α cm^{-1}) for $Sc_3N@C_{80}$, for wavelengths ranging from 300 nm to 700 nm, obtained as an average over 13 data points from 2 slides and computed using an α of 21.49×10^4 cm^{-1} at 471 nm as reference. The reference α value was supplied to us courtesy of Luna nanoWorks, a division of Luna

Innovations Incorporated. The data showed a standard deviation of approximately 3.1×10^4 cm^{-1} for wavelengths above 400 nm. Below 400 nm, the standard deviation was considerably higher, reaching a maximum of 33.4×10^4 cm^{-1} (b) Plot of the OD of a 34 nm thick $Sc_3N@C_{80}$ film, thickness was computed using the above quoted α value at 471 nm.

3.5 Materials Used – Electrodes

Electrodes were chosen with work functions offset such that an internal field is created to guide the photo-generated charges to their respective electrodes. When a higher work function cathode and a lower work function anode are selected, Fermi level matching results in a bending of the bands enclosed between the two electrodes. Electrons spontaneously move down the bands to the cathode and holes up the bands to the anode, giving rise to currents in the 4th quadrant of the IV characteristics as explained in sections 2.1 and 2.4.3.

3.5.1 Anode

Indium tin oxide (ITO)-coated glass slides that serve as the transparent anode were ordered from Delta Technologies, part #: CH-50IN-S109. These were 1 x 3 x 0.036 inch unpolished float glass slides, SiO_2 passivated with ITO coated on one surface with a sheet resistance of 8 to 12Ω and an anti-reflection coating on the other side. These slides had minimal absorption in the visible region of the spectrum and allowed light to penetrate to the working layers of the device.

Poly(3,4-ethylenedioxythiophene): poly(styrenesulfonate) complex (PEDT:PSS or PEDOT) was obtained as an aqueous dispersion purchased from Bayer Corp. Initial devices were made using the product Baytron-P which was filtered through a 0.45 micron nylon syringe from Pall Life Sciences (AP-4438T) before it was deposited. Subsequently Baytron-PH was used which is compositionally the same as Baytron-P but has smaller particle size and higher conductivity. This, too, was similarly filtered before deposition.

ITO, with a work function of 4.7 eV[24,25] and PEDT:PSS, with a HOMO level of 5.2 eV[26] together constitute the hole discharging layer or anode. The PEDT:PSS layer helps achieve a better alignment between the workfunction of the ITO and the HOMO

level of the acceptor polymer layer. The PDOT layer also smoothens the roughness of the ITO surface thereby reducing the risk of pinhole shorts.

Flexible ITO-coated polyethylene films from CPFilms (OC50/ST504/500 GA) were also briefly studied as possible substrates. The ITO coating was not robust enough to withstand the cleaning and processing done to the substrates before device fabrication and they often were scratched and had large variation in resistance.

3.5.2 Cathode

Aluminum (Al), with a work function of 4.3 eV[16] was chosen as the negative electrode. In addition to having a suitable work function to produce bend bending when coupled with the ITO/PEDOT anode, the Al layer was opaque and highly reflective. Hence, any light that entered the device and was not absorbed would be reflected by the Al layer back into the film, doubling the effective absorptivity of the active layers of the device. The Al electrodes were evaporated from 99.9% pure Al granules purchased from Alfa-Aesar.

---

[1] F.P. Incropera, D.P. De Witt, "Fundamentals of Heat Transfer," John Wiley& Sons, New York (1981).
[2] W.R. Veith, "Diffusion In and Through Polymers – Principles and Applications," Oxford Univeristy Press (1991).
[3] R.P. Wool, "Polymer Interfaces Structure and Strength", Hanser Publishers, p. 11; see also p.148 (1995).
[4] http://www.matter.org.uk/tem/electron_atom_interaction/x-ray_and_auger.htm
[5] http://www.chem.qmul.ac.uk/surfaces/scc/scat5_2.htm
[6] http://en.wikipedia.org/wiki/Auger_electron_spectroscopy
[7] M. Drees, R.M. Davis, J.R. Heflin, "Improved Morphology of Polymer – Fullerene Photovoltaic Devices With Thermally Induced Concentration Gradients," *J. Appl. Phys.* **97**, 036103 (2005).
[8] T.A. Chen, X. Wu, R.D. Rieke, "Regiocontrolled Synthesis of Poly(3-alkulthiophenes) Mediated by Rieke Zinc: Their Characterization and Solid – State Properties," *J. Am. Chem. Soc.* **117**, 233-244 (1995).
[9] R.J. Young, P.A. Lovell, "Introduction to polymers," Chapman & Hall, New York (1991) p.297.
[10] S. Malik, A.K. Nandi, "Crystallization Mechanism of Regioregular Poly(3-alkylthiophene)s," *J. Polym. Phys.* **40**, 2073-2085 (2002).
[11] Sam-Shajing Sun, Niyazi Serdar Sariciftci, "Organic Photovoltaics, Mechanisms, Materials and Devices," CRC print, Taylor & Francis Group, Boca Raton (2005). Chapter 23.
[12] S. Sensfuss, *et al.*, "Characterisation of Potential Donor Acceptor Pairs for Polymer Solar Cells by ESR, Optical and Electrochemical Investigations," *Proc. of SPIE* **5215**, 129-140 (2004).
[13] D. Gebeyehu, *et al.*, "Hybrid Solar Cells Based on Dye – Sensitized Nanoporous TiO_2 Electrodes and Conjugated Polymers as Hole Transport Materials," *Synth. Met.* **125**, 279-287 (2002).
[14] D. Gebeyehu, *et al.*, "Interplay of Efficiency and Morphology in Photovoltaic Devices Based on Interpenetrating Networks of Conjugated Polymers with Fullerenes," *Synth. Met.* **118**, 1-9 (2001).
[15] C. Schlebusch, B. Kessler, S. Cramm, W. Eberhardt, "Organic Photoconductors and C_{60}," *Synth. Met.* **77**, 151-154 (1996).

[16] C.J. Brabec, N.S. Sariciftci, J.C. Hummelen, "Plastic Solar Cells," *Adv. Funct. Mater.* **11**(1), 15-26 (2001).
[17] R.W. Lof, *et al.*, "Band Gap, Excitons, and Coulomb Interaction in Solid C_{60}," *Phys. Rev. Lett.* **68**(26), 3924-3927 (1992).
[18] R.S. Ruoff, D.S. Tse, R. Malhotra, D.C. Lorents, "Solubility of C_{60} in a Variety of Solvents," *J. Chem. Phys.* **97**, 3379-3383 (1993).
[19] N. Sivaraman, *et al.*, "Solubility of C_{60} in Organic Solvents," *J. Org. Chem* **57**, 6077-6079 (1992).
[20] L.A.A. Pettersson, L.S. Roman, O. Inganäs, "Modeling Photocurrent Action Spectra of Photovoltaic Devices Based on Organic Thin Films," *J. Appl. Phys.* **86**(1), 487-496 (1999).
[21] E.J. Meijer, *et al.*, "Solution-Processed Ambipolar Organic Field-Effect Transistors and Inverters," *Nature Materials* **2**, 678-682 (2003).
[22] V.D. Mihailetchi, P.W.M. Blom, J.C. Hummelen, M.T. Rispens, "Cathode Dependence of the Open-Circuit Voltage of Polymer-Fullerene Bulk Heterojunction Solar Cells," *J. Appl. Phys.* **94**(10), 6849-6854 (2003).
[23] H. Hoppe, N.S. Sariciftci, D. Meissner, "Optical Constants of Conjugated Polymer/Fullerene Based Bulk – Heterojunction Organic Solar Cells," *Mol. Cryst. Liq. Cryst.* **385**, 233[113]-239[119] (2002).
[24] Y. Park, *et al.*, "Work Function of Indium Tin Oxide Transparent Conductor Measured by Photoelectron Spectroscopy," *Appl. Phys. Lett.* **68**(19), 2699-2701 (1996).
[25] J.S. Kim, *et al.*, "Indium-Tin Oxide Treatments for Single- and Double – Layer Polymeric Light – Emitting Diodes: The Relation Between the Anode Physical, Chemical, and Morphological Properties and the Device Performance," *J. Appl. Phys.* **84**(12), 6859-6870 (1998).
[26] T.M. Brown, *et al.*, "Built-in Field Electroabsorption Spectroscopy of Polymer Light-Emitting Diodes Incorporating a Doped Poly(3,4-ethylene dioxythiophene) Hole Injection Layer," *Appl. Phys. Lett.* **75**(12), 1679-1681 (1999).

CHAPTER FOUR

P3OT Donor and C_{60} Acceptor: Dependence of Concentration Gradient on Layer Thickness and Time – Temperature Parameters

In this chapter is presented the main work of this thesis that was done on the P3OT – C_{60} system. This system will be introduced with a brief study that compares the different morphologies of film fabrication: single layer devices, bilayer devices, blend devices and thermally interdiffused devices, with P3OT as the donor and C_{60} as acceptor. This will be followed by an in-depth experimental study of the thickness dependence of concentration gradient devices for a specific set of thermal interdiffusion conditions. Following the investigation on thickness dependence, a brief study that was done on varying other parameters like the thermal conditions for interdiffusion will also be presented.

4.1.1 Comparing Different Morphologies of Device Fabrication

Concentration gradient devices achieved by thermal interdiffusion (ID) have been extensively studied in our lab over the last six years. Other commonly investigated device morphologies were attempted with P3OT and C_{60} as donor and acceptor to get an idea of the effectiveness of the ID process. A comparison was made between single layer, bilayer, blend and ID devices, all with comparable active layer thicknesses. P3OT single layer devices were spin-coated and annealed under vacuum at 120 °C for over 30 minutes, prior to Al electrode deposition. C_{60} was thermally evaporated onto an annealed layer of P3OT in the vacuum chamber to produce bilayer devices. In this comparison, blend devices were fabricated following the method of post-production treatment that demonstrated up to 5% efficiency for the P3HT – PCBM blend systems.[1] P3OT – C_{60} in a 1:1 ratio blend was spin-coated from a solution in CS_2. CS_2 was chosen since C_{60} demonstrated the highest solubility in it as compared to most other commonly available organic solvents.[2] Al was deposited on this film after which it was annealed at 130 °C in an inert atmosphere for 35 minutes. The annealing was done in the vacuum chamber

without breaking vacuum and exposing the slide to air after Al deposition. Most of the ID studies were done at similar average temperatures and hence it was chosen to anneal the blend, in order to generate a closer comparison of the two types of devices. The ID device in this first study was fabricated by thermally evaporating a layer of C_{60} onto a layer of P3OT that had been annealed at 120 °C for 30 minutes as described above. This yielded a bilayer that was then heated in the argon box and was kept steady for five minutes at a set point of 118 °C, which showed an over-swing to 134 °C to give an average temperature of ~ 130 °C. This was then cooled under mildly circulating Argon. The temperature profile for the ID step is shown in Figure3.9. To calculate thickness of the blend it was assumed that at any point, P3OT contributes to half of the absorbance and C_{60}, the other half. α values at 470 nm for P3OT and C_{60} ($11.01\times10^{4}cm^{-1}$ and $5.13\times10^{4}cm^{-1}$ respectively) are averaged to give α_b, which is substituted in equation 3.29.

Figure 4.1 shows the comparison of the performance of the various types of devices mentioned. Figure 4.1a gives the EQE versus wavelength, Figure4.1b, the current density (J) – Voltage (V) characteristics for a device under 470 nm illumination and Figure 4.1c, the fourth quadrant J-V characteristics under 470 nm illumination. The V_{OC} (open circuit voltage) and J_{SC} (short circuit current density) can be read from the x and y axis intercepts, respectively, of Figure 4.1c. The bilayer devices seem to show a greater performance than expected which could be because of a slight interdiffusion of C_{60} into P3OT during the C_{60} deposition. C_{60} has been shown to spontaneously diffuse into P3OT even at room temperatures.[3] Hence it is very likely that some interdiffusion occurs during C_{60} deposition, especially since the substrate gets warm (sometimes up to 60 °C) as the C_{60} is sublimed. While this does not yield a perfect bilayer, the interdiffusion is not deep enough for it to be classified as concentration gradient device.

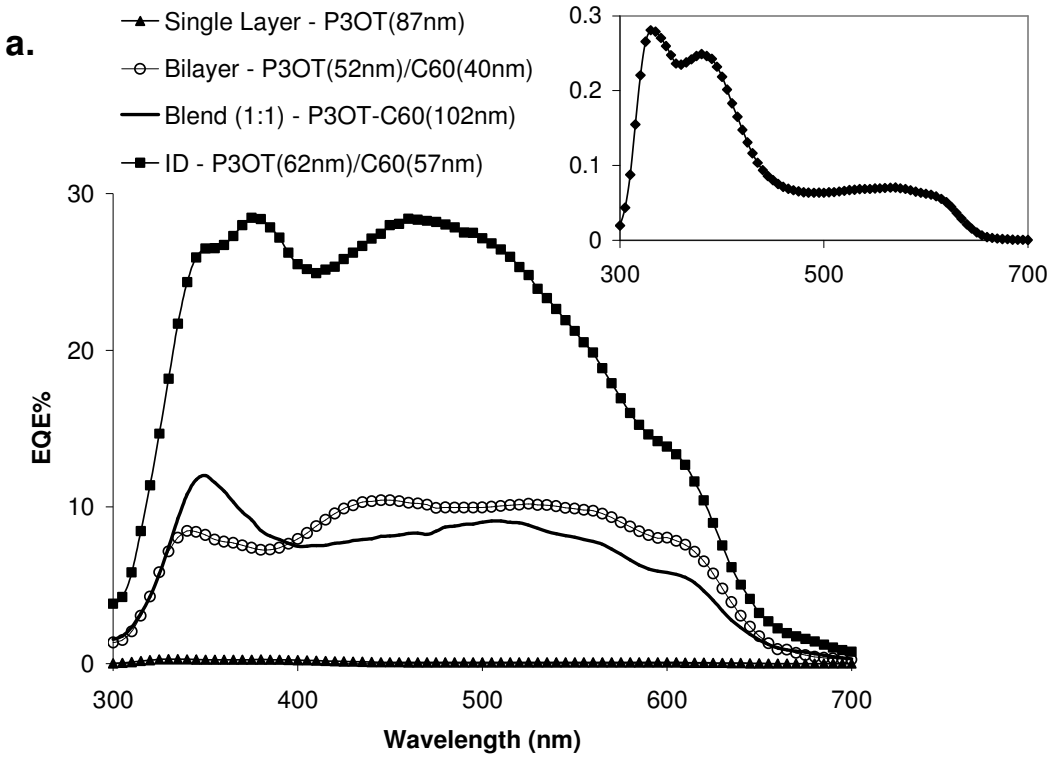
a.
Single Layer - P3OT(87nm)
Bilayer - P3OT(52nm)/C60(40nm)
Blend (1:1) - P3OT-C60(102nm)
ID - P3OT(62nm)/C60(57nm)
EQE%
Wavelength (nm)
0
10
20
30
300
400
500
600
700
0
0.1
0.2
0.3
300
500
700

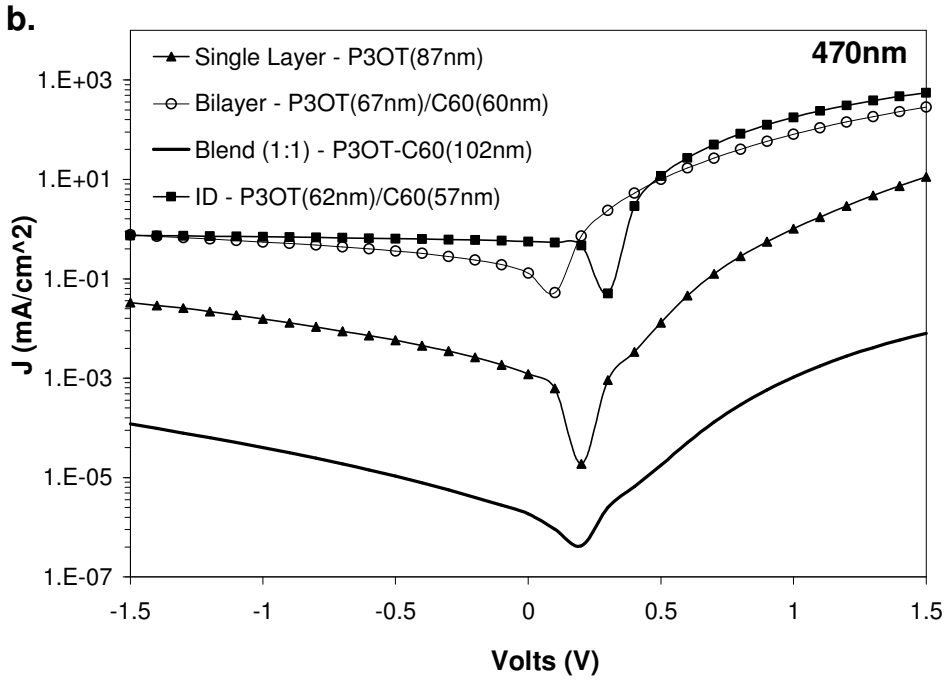
b.
470nm
Single Layer - P3OT(87nm)
Bilayer - P3OT(67nm)/C60(60nm)
Blend (1:1) - P3OT-C60(102nm)
ID - P3OT(62nm)/C60(57nm)
J (mA/cm^2)
Volts (V)
1.E+03
1.E+01
1.E-01
1.E-03
1.E-05
1.E-07
-1.5
-1
-0.5
0
0.5
1
1.5

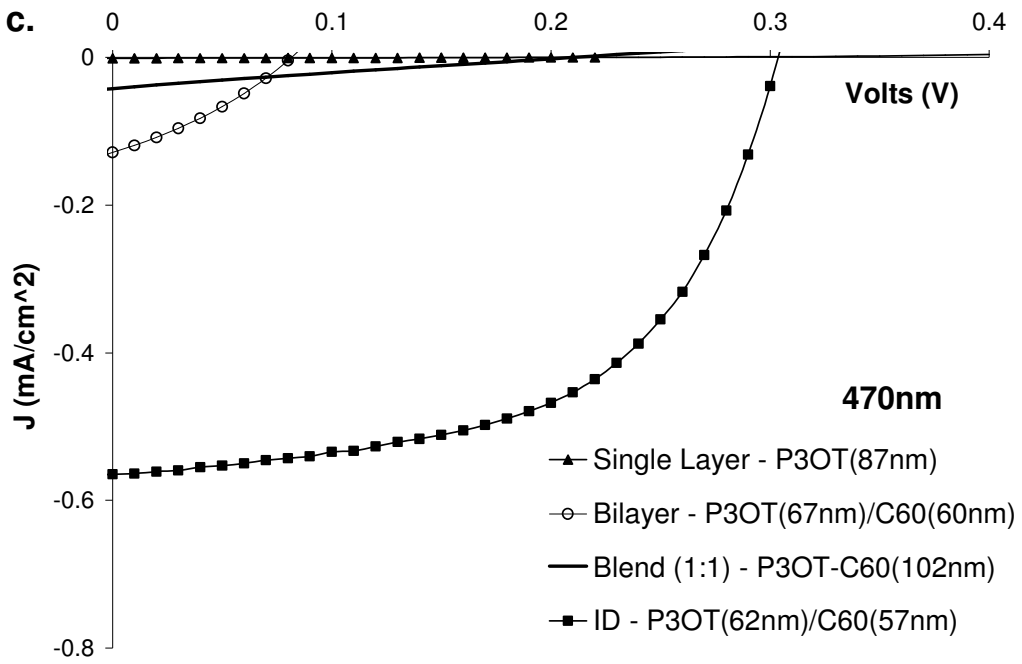

Figure 4.1 Plots comparing the performance of P3OT – C_{60} devices constructed with different morphologies. The P3OT single layer device has a thickness of 87 nm and is represented by the solid triangles (▲). The bilayer device, with 52 nm thick P3OT and ~40 nm thick C_{60} layer, is represented by the open circles (○). The 1:1 blend device with an overall thickness of 108 nm, is given by the solid line (**—**). The ID device had a starting bilayer P3OT thickness of 62 nm and C_{60} thickness of 57 nm, prior to interdiffusion, and is given by the solid squares (■). (a) gives the EQEs, the inset shows the single layer device EQE (b) gives the J-V characteristics under 470 nm illumination, with the current normalized for device area to yield current densities (J) and plotted on a semi-log plot, (c) gives the 4th quadrant J-V curves for devices under 470 nm monochromatic illumination.

Device	**Thickness(nm)**		**Voc**	**Jsc**	**FF**	**Eff**
	P3OT	**C_{60}**	**(V)**	**(mA/cm^2)**		**%**
Single Layer	87	-	0.205	-0.00115	0.256	0.0013
Bilayer	52	~ 40	0.085	-0.129	0.306	0.098
Blend (1:1)	102		0.205	-0.042	0.239	0.062
ID	62	57	0.305	-0.565	0.543	1.811

Table 4.1 Overview of the I-V measurement results under 470 nm illumination for the single layer, bilayer, blend and interdiffused devices. Eff is the power conversion efficiency.

An overview of the I-V measurement under 470 nm illumination, for these devices is shown in Table 4.1. A general improvement in the photovoltaic parameters is seen from the single layer to the bilayer to the ID devices. The blend devices seem to show some unexpected trends, the V_{OC} of the blends is higher than that of the bilayer and lower than that of the ID devices, as is the case for the overall power conversion efficiency (η) for 470 nm illumination. But the J_{SC} seems to be lower than that of the bilayer which was probably indicative of a low quality device. It should be noted that the blend device presented is not necessarily representative data for the P3OT – C_{60} system.[4] A brief study was done to try to optimize blend devices for the P3OT – C_{60} system, the results of which are presented in the next section. The device shown here was chosen because it had similar thickness to the others shown. We found higher efficiencies for blend devices of 40-50 nm thickness.

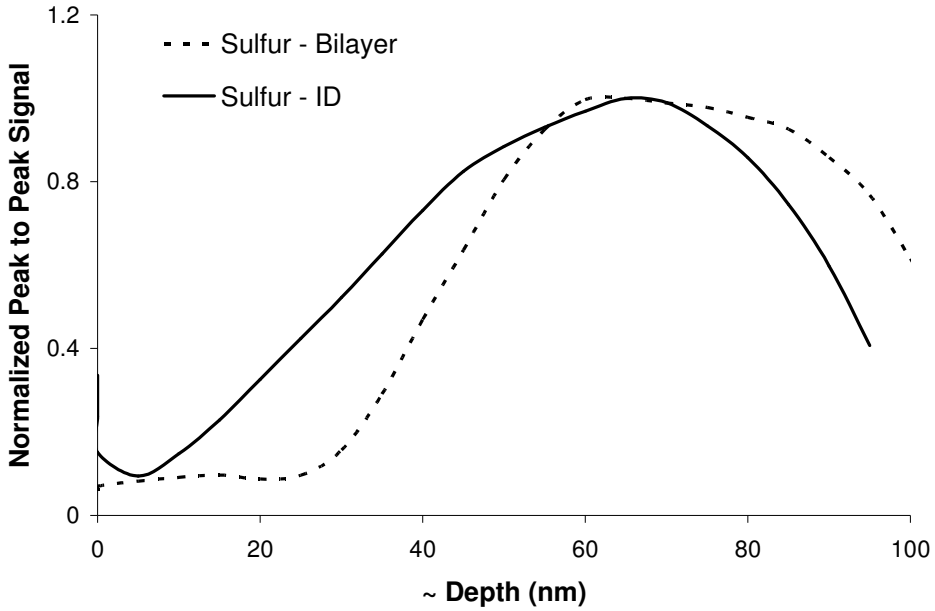

Figure 4.2 Plot of the depth profiles by Auger spectroscopy for the bilayer device and a thermally interdiffused (ID) device of similar layer thicknesses and ID conditions as the one presented in Figure 4.1. The approximate depth into the film is given on the x-axis while the y-axis is the peak to peak signal intensity whose absolute values have no physical significance and hence were normalized to 1.0. Sulfur indicates presence of P3OT. The ID device shows a gradual increase in sulfur, indicating a concentration gradient of P3OT and C_{60}. The bilayer device shows a much sharper rise in sulfur, sandwiched between significant low and high flat regions, indicative of pure C_{60} and P3OT layers, respectively, with a thin interface between them.

The difference in concentration gradients between a bilayer and thermally interdiffused device can be examined using Auger spectroscopy. Figure 4.2 shows the sulfur content for a typical bilayer and ID device. The sulfur indicates the presence of P3OT in the film. Measurements were done in the film starting from the top of the C_{60} layer and hence no sulfur is seen in the beginning, especially for the bilayer. As measurements are taken deeper into the film, P3OT is encountered and the sulfur signal rises. In the case of the ID device, this rise appears early and shows a gradual slope that indicates a concentration gradient between the two materials through most of the active layer. On the other hand, P3OT is observed a lot later in the bilayer, after almost 30 nm of pure C_{60}, seen as a low flat region in the curve. The rise in the sulfur content is much steeper than in the case of the ID device indicating a sharp increase in the polymer content of the film. After the thin interface there is a high flat region in the curve due to a pure polymer region. Ideally, the sulfur signal rise in this interface should be almost vertical, to represent the sharp polymer-fullerene layer interface of a bilayer. In this case, we do see some degree of gradient. This could be due to a small degree of interdiffusion occurring during the C_{60} deposition as explained above, or this could be an error originating from the violent ion-beam milling process that is used to mill the surface that might blur the resolution of the interface. The surface is blasted with argon ions to remove the top 5 nm. Due to the soft nature of the materials being blasted, larger chunks of the film may come off thereby yielding a deeper local measurement as compared to other regions on the film. More explanations on this process are given in section 3.3.3. We believe this gradient is most likely due to the first reason with a little contribution from the second.

To summarize, a substantial improvement is seen for thermally interdiffused devices for the P3OT – C_{60} system. These interdiffused devices demonstrate a concentration gradient of the polymer in the C_{60} layer (and hence of the C_{60} in the polymer) which can be observed using Auger spectroscopy to tag the sulfur in the P3OT back bone.

4.1.2 Brief Study of Blend Devices

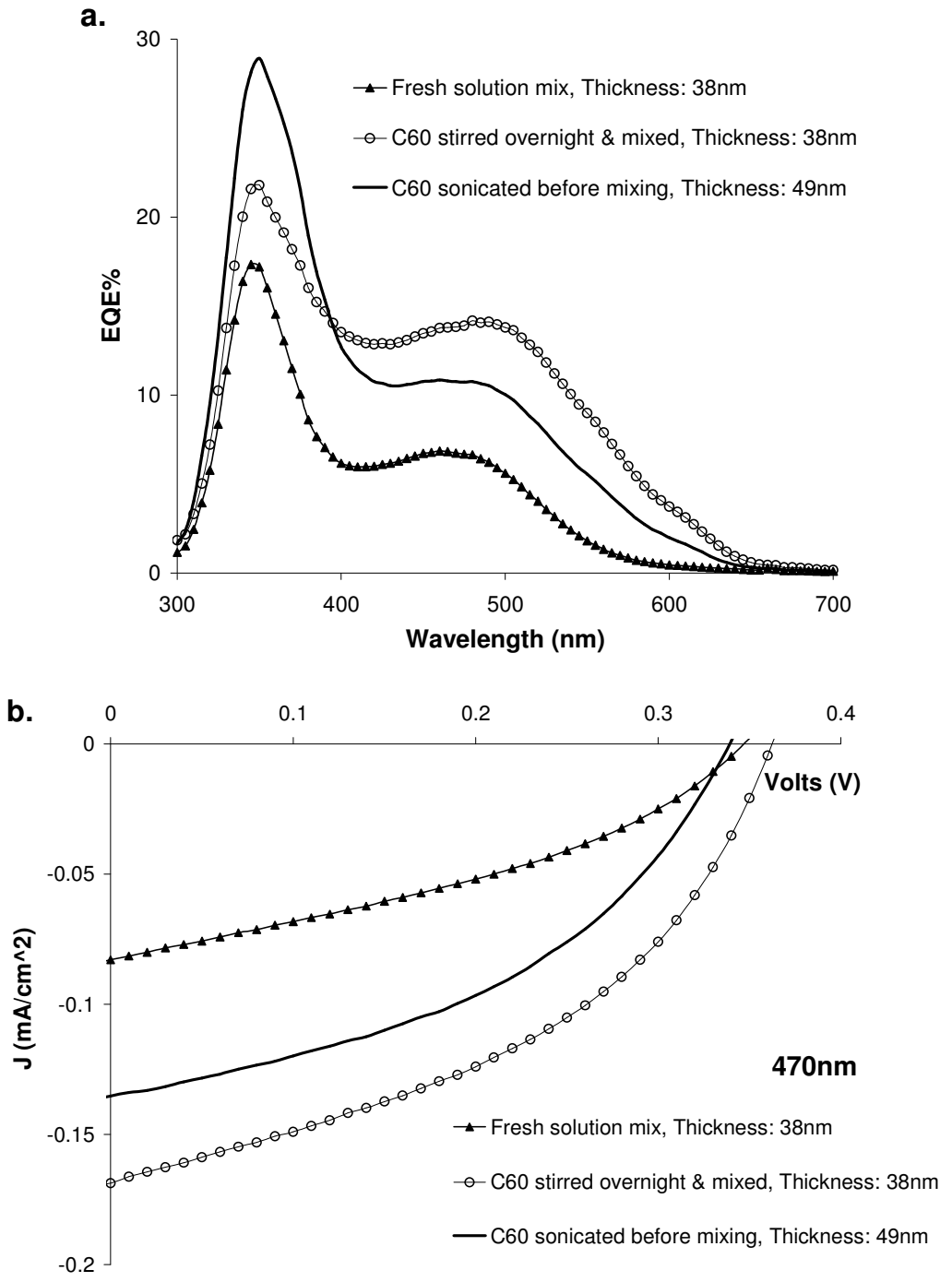

Figure 4.3 (a) EQE curves and (b) 4th quadrant J-V curves under 470 nm illumination for 1:1 P3OT – C_{60} blend devices made from differently processed solutions in CS_2: mixed and spin-coated (▲), C_{60} stirred overnight and mixed before spin-coating (○) and C_{60} sonicated for a few minutes then mixed with P3OT (—).

In this section, a brief study made to get an idea of P3OT – C_{60} blend device performance is described. It should be mentioned that just one or two devices were fabricated for each case in order to see a trend. Since our main focus for this study was ID devices, more work than this was not done to optimize the blends. While making blend devices, the biggest obstacle was low solubility of C_{60}. One of the more popular solvents for C_{60} is carbon disulfide (CS_2) which has also been used for this study. Maximum solubilities of between 5 mg to 8 mg per ml of CS_2 have been reported in literature.[2, 3] 0.5% solutions of P3OT and C_{60} (0.01 g of P3OT in 2 ml of CS_2 + 0.01 g of C_{60} in 2 ml of CS_2) were mixed to give a 1:1 solution. This yielded a solution with 0.5% wt/vol net concentration but the concentration of each individual component was just 0.25% wt/vol (0.1 g of P3OT or C_{60} each in a total of 4 ml of CS_2). A device was made from this solution after stirring for about 10 minutes. The slide was not uniform and showed marbled pattern of yellowish and purplish regions where the P3OT and C_{60} seemed to have separated. For the next device, the C_{60} solution was stirred overnight and then mixed with a P3OT solution before spin-casting in order to allow C_{60} more time to dissolve. The slide still showed similar separated regions. For the third device, the C_{60} was sonicated for 3 to 4 minutes and mixed with the P3OT solution and immediately spin-coated. Sonicating the C_{60} was expected to break any large insoluble clusters and the device was made as soon after that as possible, to minimize re-aggregation. This film was still not completely uniform, showing the same yellow and purple regions but they were much smaller than for the other two cases. None of these devices were annealed prior to measurement. The P3OT – C_{60} mixture was not sonicated since we were unsure of the effects of sonication on the polymer chains. Figure 4.3 gives the EQE curves and 4th quadrant current density – voltage (J-V) characteristics for these devices. Mixing the two components well seemed important, showing a marked improvement for the device made from the solution stirred overnight as compared to the one stirred for a few minutes. But the device made with the sonicated C_{60} solution was comparable to the second one. For the sonicated C_{60} solution, the C_{60} peak in the EQE at ~370 nm is larger than the P3OT peak at ~490 nm while the trend is reversed for the device made from a C_{60} solution stirred overnight.

Next, the effect of annealing blends to produce microcrystalline phase separated regions of enhanced charge carrier conductivity was attempted. Also, to improve absorption efficiencies, thicker blend films were made. 0.017 g of C_{60} was sonicated in 2.8 ml carbon disulfide (CS_2) to which 0.017 g of P3OT was added, to give a 1:1 blend solution of 1.2% wt/vol concentration. This mix was then kept stirring to try to incorporate both the initial de-aggregation of C_{60} through sonication and the improved performance of well-mixed solutions from before. The first device was a control device that was prepared and measured without annealing. The next device was subjected to annealing treatments that were comparable with the thermal interdiffusion step for concentration gradient devices. This annealing was done under vacuum at 130 °C for 10 minutes prior to Al deposition. A temperature of 130 °C was chosen so a comparison could be made with similarly interdiffused films. The last device was annealed at 130 °C for 35 minutes after Al deposition following the success of post production treatment in P3HT – PCBM blends,[1] as explained in the beginning of section 4.1.1. That work quotes a temp of 150 °C for P3HT. We chose 130 °C for P3OT to stay consistent with the temperatures used in the majority of our other P3OT - C_{60} device fabrications.

Figure 4.4 gives the EQE curves and 4th quadrant current density – voltage (J-V) characteristics for these devices. Annealing the device dramatically improved photovoltaic performance whereas there is only a marginal difference between the devices with the two different annealing conditions. In this case, annealing before Al deposition seems to be better, but more tests at other carefully chosen temperatures should be conducted. When these devices are compared to those in Figure 4.3, a change in the shape of the curve is observed corresponding to increased contribution from the wavelengths in the 400 nm to 600 nm range. At the same time the net EQE has gone down. This could be due to a number of reasons including the time lapse between sonication of the C_{60} solution and device fabrication and the increased thickness.

It has been recently suggested that the increase of thickness in blends increases the short circuit current but this is countered by a decrease in the fill factor and overall efficiency.[5] The thicker the blend layer, the longer the path length for separated charge carrier transport. This would increase the risk of traps and space charges. This was said to affect photocurrents differently for different applied bias voltages, affecting the transport

less for voltages closer to zero or to the V_{OC}. This would lead to the curve straightening out in the 4th quadrant of J-V characteristics, seen as the decrease in fill factor in Figure 4.4b.

The point to note that is most pertinent to this thesis is that these different methods of blend device fabrication did not yield devices that exceeded the performance of similar thermally interdiffused, concentration gradient devices, demonstrating the effectiveness of interdiffusion for the P3OT – C_{60} donor – acceptor system.

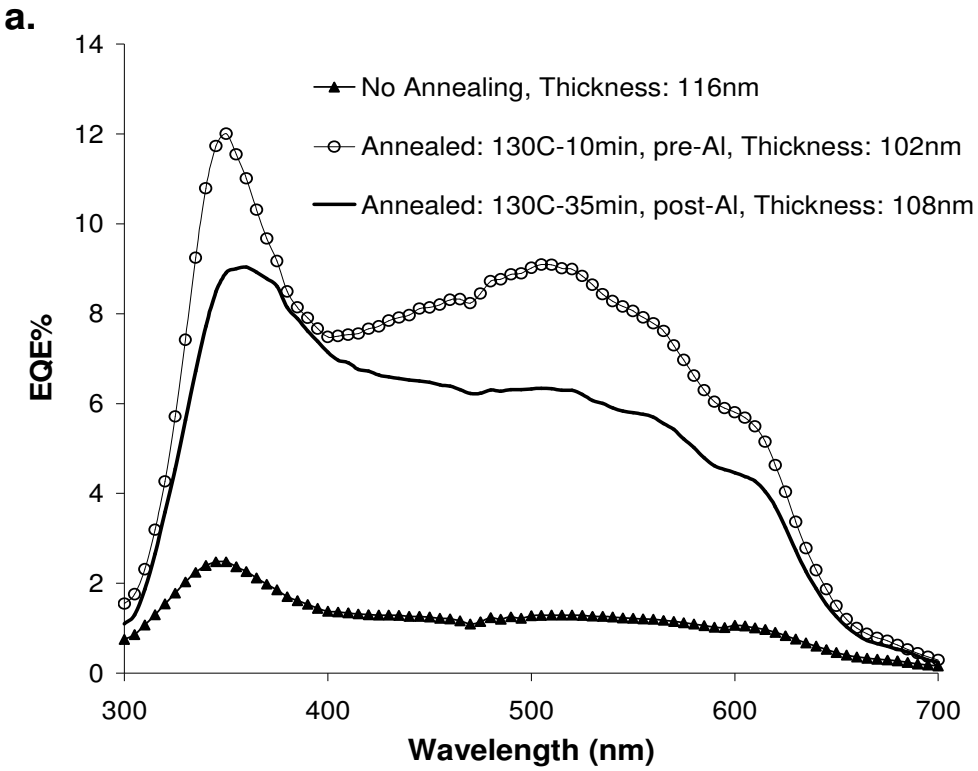

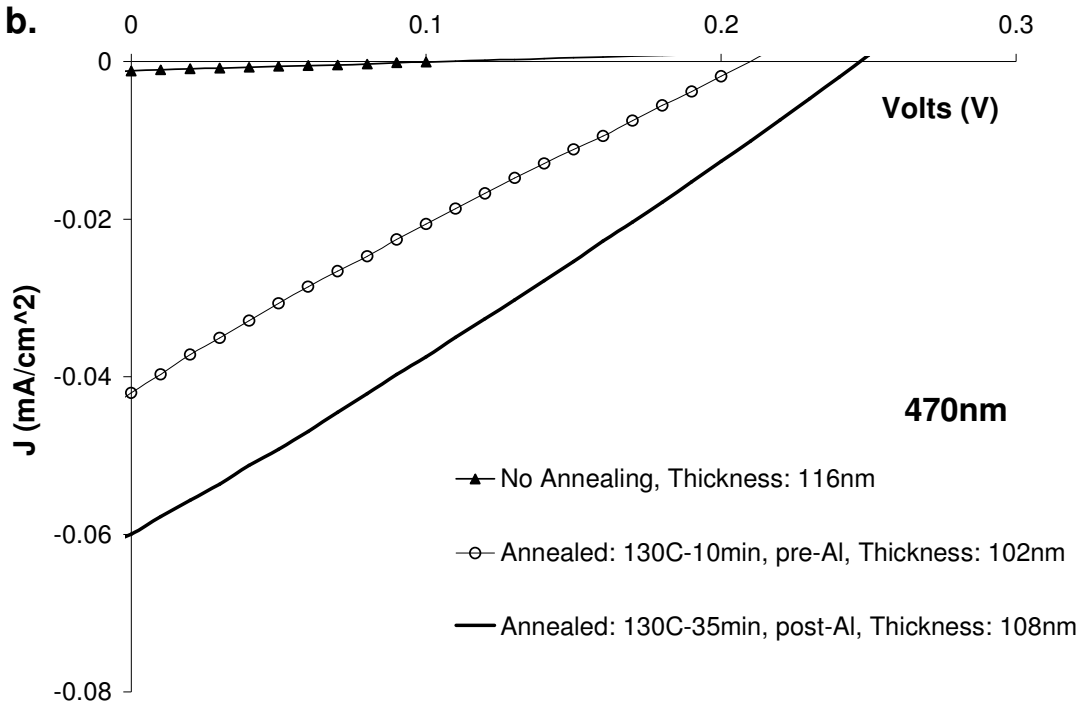

Figure 4.4 (a) EQE curves and (b) 4th quadrant J-V curves under 470 nm illumination for 1:1 P3OT – C_{60} blend devices that underwent different thermal processing: blend not annealed (▲), annealed at 130 °C for 10 mins prior to Al deposition (○) and annealed at 130 °C for 35 mins after Al deposition (—).

4.2 Thickness Dependence Study of P3OT – C_{60} Concentration Gradient Devices

In the previous section, thermally interdiffused concentration gradient devices were shown to be a suitable morphology for the P3OT – C_{60} system. An efficient photovoltaic process relies on the maximum absorption of incident light to create excitons, efficient exciton dissociation and charge separation, uninterrupted transport of the separated free charges and unhindered charge collection at the electrodes. The morphology of a concentration gradient device is such that the bulk heterojunction in the middle provides the donor – acceptor interfaces for exciton dissociation, charge transport is optimized by the increasingly purer material as the electrodes are approached, and the layer of pure material at the electrode ensures clean band matching to allow for efficient charge collection. We hypothesized that a device that has a concentration gradient that stretches through the entire film, ending in a thin layer of pure material at the electrode, will have the highest efficiency. Such a morphology could be achieved either by thermally

controlling the extent of interdiffusion or by optimizing the thickness of the starting layers with respect to the applied thermal conditions. In this section is presented a study to optimize such devices thorough thickness control. An Auger spectroscopy study of the devices is also presented to experimentally verify the expected morphology of the most efficient devices.

Thickness is an important parameter in any type of photovoltaic device. In addition to determining the absorption efficiency, the thickness has subtle influences on device performance, depending on the morphology of the device. Pettersson *et al*. modeled the device performance dependence on the thickness of individual layers of a bilayer device by calculating the electric field distribution inside the film.[6] They assumed a multilayer structure where exciton dissociation occurs at the interfaces of the active layers. Unabsorbed light that passes though the film reflects off the Al electrode and interferes with the incoming light. This produces an electric field distribution of varying intensities within in the film. For efficient device performance, the high intensity portion of the field (antinode in an interference pattern) should coincide with the active layer interface so that the maximum number of excitons are generated within the diffusion distance of a dissociating interface. This was achieved by controlling the thickness of the acceptor layer just below the reflecting surface (the C_{60} layer), so that the antinode fell at the donor – acceptor interface. They proposed an optimum C_{60} layer thickness of around 40 nm.

In the case of bulk heterojunction blend devices, since the whole device consists of donor-acceptor interfaces, the position of the antinode is not so important vis-à-vis exciton dissociation. The concern instead in such devices is to optimize the thickness, in order to balance the efficient absorption of light and the transport of the charges.[5] This has been explained in a little more detail in the previous section on blends.

Concentration gradient devices that have a bulk heterojunction created from an initial sharp bilayer interface should show a thickness dependence is a combination of both the cases mentioned above. The maximum number of donor-acceptor interfaces would be located at the region of the initial bilayer, where there is a 1:1 ratio of the donor and acceptor. The antinode from light interference should fall in this region in order to optimize the separated charge carrier production.

For a given set of interdiffusion conditions, one can maximize the extent of the gradient by reducing the thickness of the layers to ensure that a larger percentage of the film behaves as a bulk heterojunction. At the same time, if the thicknesses are reduced too much for the same set of interdiffusion conditions, the materials will go right through to the electrodes and still continue to diffuse, resulting in too much mixing. This would take the film beyond a concentration gradient such that a more blend-like morphology would be obtained, increasing the risk of low space charge limited currents. Increasing the layer thicknesses would prevent formation of blend morphology. But increasing the layer thicknesses may also result in the interdiffusion only going part of the way through the film, leading to an interdiffused region flanked by a layer of pure material on either side. This would lead to absorbed light that does not generate separated charges and the appearance of the filter effect, as seen for bilayer devices[7] (explained in detail in section 2.9). Hence, for a given set of thermal interdiffusion conditions, the thickness should be adjusted such that an optimum concentration gradient is obtained that balances all three of these concerns to yield the most efficient interdiffused devices. This is depicted in Figure 4.5 which shows the antinode as an intensity maxima at a certain distance from the Al-acceptor interface, for various thicknesses of the donor and acceptor layers.

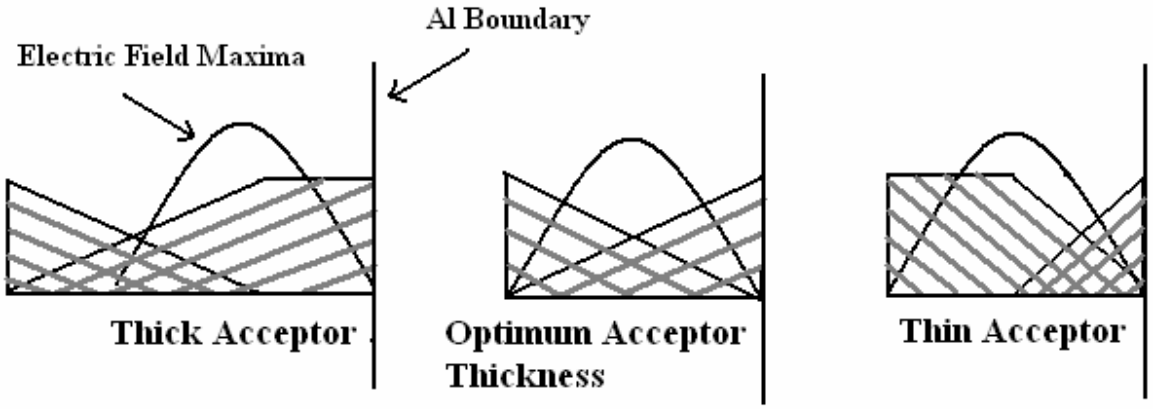

Figure 4.5 Schematic of electric field distribution in interdiffused devices of varying thickness of the acceptor layer. Cross-hatching represents the region of interdiffusion.

The shaded layer next to the Al boundary is C_{60} and the other shaded layer is P3OT. The concentration of each is represented by the height of the shaded region. The region of interdiffusion is cross-hatched. The optimum performance will be obtained for the

electric field distribution maxima coinciding with the location of the maximum cross-hatched area.

To experimentally determine these optimum values, devices of varying layer thicknesses, from 10 nm to 120 nm for each material, were fabricated and measured. In the following results, the devices were all made similarly. C_{60} was deposited on a layer of P3OT that had been annealed at 120 °C for over 40 minutes, under vacuum. This bilayer was then interdiffused in the argon box, ramped up by 20 °C/min to a set point of 118 °C for 5 minutes. The temperature over-shot the set point and went up to 134 °C, giving an average of ~ 130 °C in those 5 minutes. (Heating and cooling profile given in Figure 3.9).

4.2.1 Device Layers with Extreme Thicknesses

Devices with layer thicknesses from the extremes of the thickness range being studied are presented. This study gives us an idea of the contribution of each layer to the device performance. The best devices showed moderate thickness values, in the range 40 nm to 60 nm each for the P3OT and C_{60} layers. An example of such a device (ID54G) is also presented for the sake of comparison. The analysis is done in terms of the EQE curves and the 4^{th} quadrant current density vs. voltage (J-V) characteristic curves, measured under 470 nm illumination. When analyzing EQE curves, the two main aspects to consider are the shape of the curve and the overall numerical values (height) of the curve. In an ideal device, where every photon absorbed would contribute to a charge collected at the electrode, the EQE would mirror the absorption curve (given by the optical density (OD) spectrum) of the device. Hence, the closer the EQE curves reproduce the key features of the OD, the better the device from the point of view of charge separation. The height of the EQE curve, of course, also indicates the quality of the device, in addition to which it would also indicate the absorption efficiency of the devices. (Some groups report the IQE, internal quantum efficiency, which is the number of electrons collected for number of photons *absorbed*. The IQE would not reflect absorption efficiencies).

Figure 4.6a shows the EQE curves for devices with various combinations of very thin and very thick layers. Device ID54G is one of the best devices measured and has

intermediate layer thicknesses. It shows a peak at around 450 nm, similar to the OD peak for P3OT (Figure 3.15). This device also shows approximately an overall factor of 2 improvement with respect to the extreme layer thickness devices. ID16E has very thin P3OT and C_{60} layers (26 nm and 22 nm respectively). This curve has a shape that is almost like that of ID54G indicating the same amount of relative contributions from the P3OT and C_{60} layers and their region of interdiffusion, but the overall efficiency is low. This could be due to a number of reasons, the most obvious of which is that the layers are thin and so therefore results in reduced absorption efficiency.

For thick P3OT layer films (ID48G ad ID21C), the peak around 450-500 nm disappears. This is due to the filter effect where a majority of the photons absorbed in P3OT do not contribute to the photocurrent. A similar filter effect can be seen for thick C_{60} devices (ID13 and ID21), where a reduction in the curve is seen at around 350 nm to 380 nm. The C_{60} filter effect is on a smaller scale as compared to that of P3OT since P3OT is the main absorption layer pertinent to photocurrent generation. Also, any loss of light in a pure C_{60} layer would occur after the initial incidence through the P3OT layer and the interdiffusion interface. Hence, the C_{60} filter effect will only affect the EQE contribution from the reflected light.

The P3OT absorption peak is prominent for ID13D, which has a thin polymer and thick C_{60} layers; there is enough C_{60} present in the body of the polymer, providing the required donor – acceptor interfaces, so that almost all the photons absorbed by P3OT contribute to the photocurrent. Hence, the P3OT absorption peak is reproduced, but the overall EQE level is low, most likely again due to the low thickness of P3OT and hence low absorption efficiency. For an optimum device is considered, the concentration gradient extends throughout most of the film, which is seen as combination of reduced filter effects for both the P3OT and C_{60} layers and an overall improvement in the EQE.

Figure 4.6b shows the 4^{th} quadrant J-V curves for 470 nm illumination. The short circuit current density is proportional to the EQE at 470 nm and hence displays a similar trend. The V_{OC}, which is mainly material and incident intensity dependent, does not show as much variation. All the curves have a similar shape indicating similar quality of fabrication and diode behavior for these devices. Hence, the trends observed are not affected by fabrication differences and mainly reflect differences in the morphology.

Table 4.2 gives an overview of the performance of these devices under 470 nm illumination.

To summarize, extreme thicknesses do not yield optimum device performance. The best device had P3OT and C_{60} thicknesses that were similar and in the 40 – 60 nm thicknesses range. By comparing the devices with extreme thicknesses we can deduce the contribution of individual layers, especially in terms of the absorption efficiency, to the device performance.

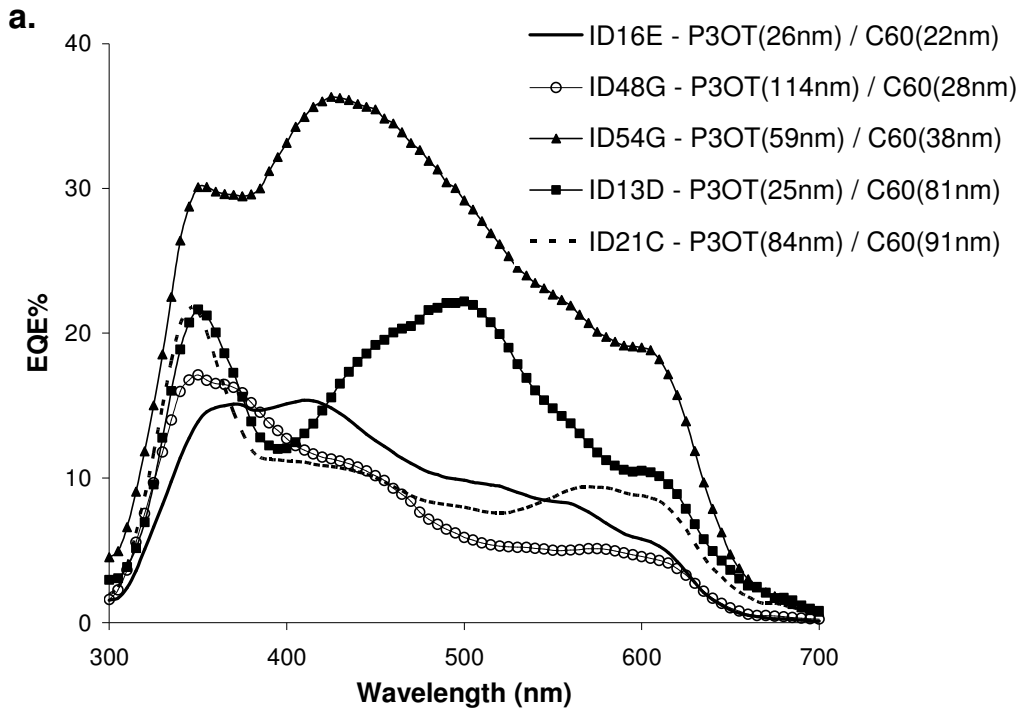

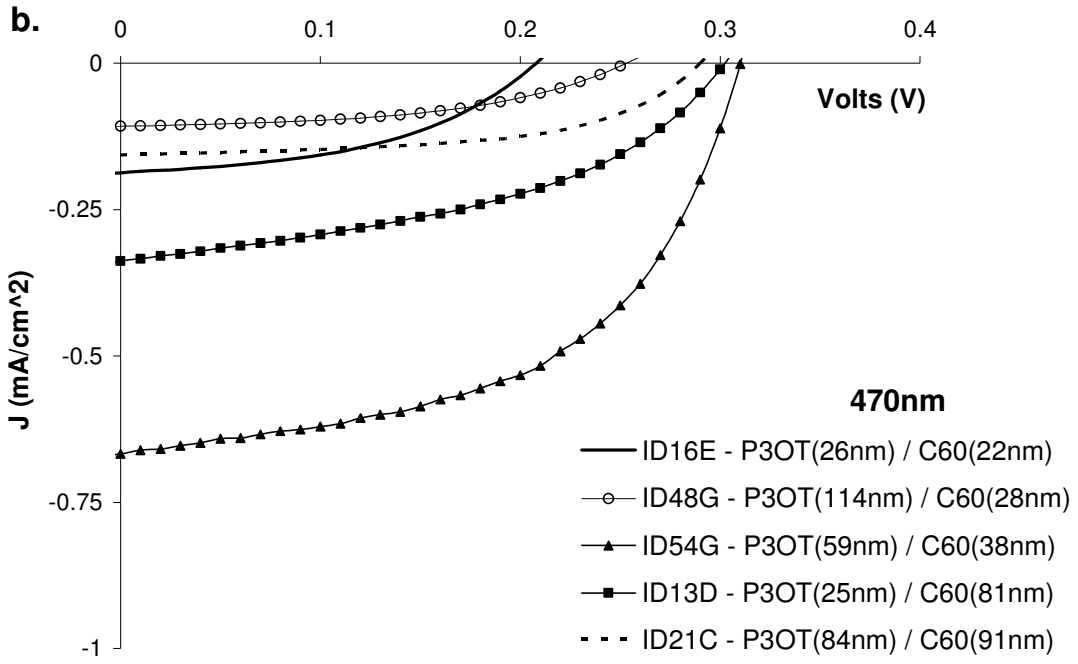

Figure 4.6 (a) EQE and (b) 470 nm illumination, 4th quadrant J-V characteristics for devices with varying layer thicknesses and interdiffused under similar conditions. The thicknesses of the layers are given in the legend along with the device name.

Device	Thickness(nm)		Voc	Jsc	FF	Eff
	P3OT	C_{60}	(V)	(mA/cm^2)		(%)
ID16 E	26	22	0.205	-0.19	0.46	0.35
ID48 G	114	28	0.255	-0.11	0.48	0.38
ID54 G	59	38	0.315	-0.67	0.52	2.05
ID13 D	25	81	0.265	-0.34	0.43	0.72
ID21 C	84	91	0.295	-0.16	0.55	0.54

Table 4.2 Overview of the photovoltaic performance under 470 nm illumination, of the devices under study in Figure 4.6.

4.2.2 Dependence of Device Performance on the Variation of Individual Layer Thickness

Comparison of extreme thickness devices demonstrated the general absorption effects, but a gradual thickness variation would demonstrate variational trends better. In this section, such an in-depth study of the effects of varying individual layer thicknesses is given.

Figure 4.7 a and b show the EQE and the 470 nm illumination 4th quadrant J-V curves for a set of devices with C_{60} thickness varying from 25 nm to 90 nm and P3OT thickness contained within 50 nm to 60 nm. Table 4.3 gives an overview of the photovoltaic performance of these devices for 470 nm illumination.

In Figure 4.7a, an overall increase is seen in the EQE curves magnitude. In this figure, the P3OT thickness is kept constant. Hence for a given set of interdiffusion conditions, there should be no variation in the interdiffusion profile in this layer and hence absorption efficiency considerations for this layer should be constant. Yet an initial increase and subsequent decrease is seen in the peak at around 450 to 500 nm as the C_{60} thickness is increased. The largest EQE is obtained for a C_{60} thickness of 38 nm. This is due to the interference effects of incident and reflected light as proposed by Pettersson *et al.*[6] and explained in Figure 4.5 in the introduction to this section. For maximum intensity of light at the active region, the antinode of the light interference distribution should fall in the center of the interdiffusion region. This is determined roughly by the position of the pre-interdiffusion bilayer interface, relative to the Al reflection boundary. Thus, it is determined by the thickness of the C_{60} film. As the C_{60} thickness increases, this antinode will move from a predominantly P3OT-rich region (ID47A) to the center of the interdiffused region (~ ID54G) to deeper into the purer C_{60} region (ID59C to ID6A to ID6E). We note that the optimum C_{60} thickness we observe is in excellent agreement with the 40 nm value predicted by Petterson *et al*. for bilayer devices.

Another trend that is observed in Figure 4.7a is the variations in the peak heights at around 350 nm and around 450 nm to 500 nm. This is mainly due to the overall increase in the EQE but there could also be the contribution of photocurrents from light absorbed by the C_{60} layer which would vary as the thickness of C_{60} varied. The 350 nm peak corresponds to the secondary contributions to the EQE process whereby

photocurrents are generated due to photoexcitation in the C_{60} and subsequent transfer of electrons from the HOMO of the polymer to the HOMO of C_{60} (explained in section 2.3.3). It should be noted that for a given set of interdiffusion conditions, the extent of interdiffusion will be constant. For thin C_{60}, starting at 25 nm for device ID47A, there is enough interdiffusion and presence of P3OT in the C_{60} to induce the charge separation of these C_{60} excitons, but the absorption efficiency is low since the C_{60} layer is thin. Then, as the C_{60} layer gets gradually thicker, the absorption improves, increasing the peak height (device ID54G). With further increase in the thickness, the pure C_{60} layer starts to increase relative to the interdiffusion region. This would lead to a mild filter effect at 350 nm as explained in the previous section. This is seen as the continued reduction in the peak value with increasing thickness (Devices ID59C to ID6A to ID6E).

Figure 4.7b, once again serves as an indicator of the quality of diode device fabrication as seen in the shape of the curves. The variation in the short circuit current density (J_{SC}) mirrors the EQE variation trends for 470 nm illumination.

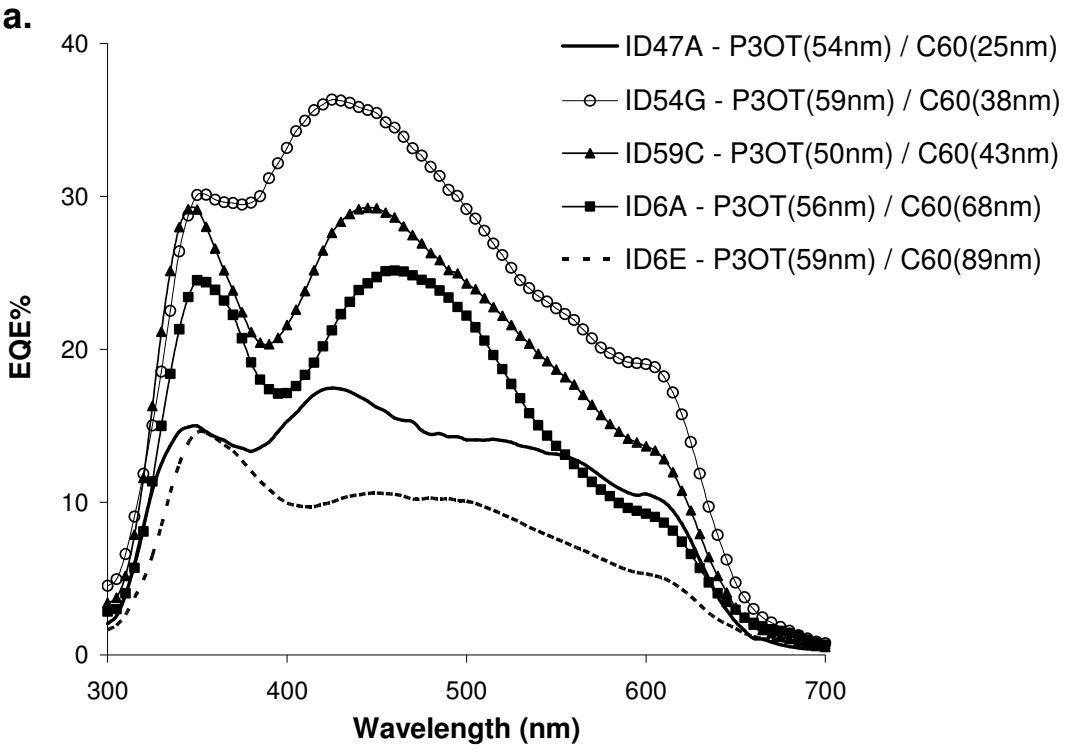

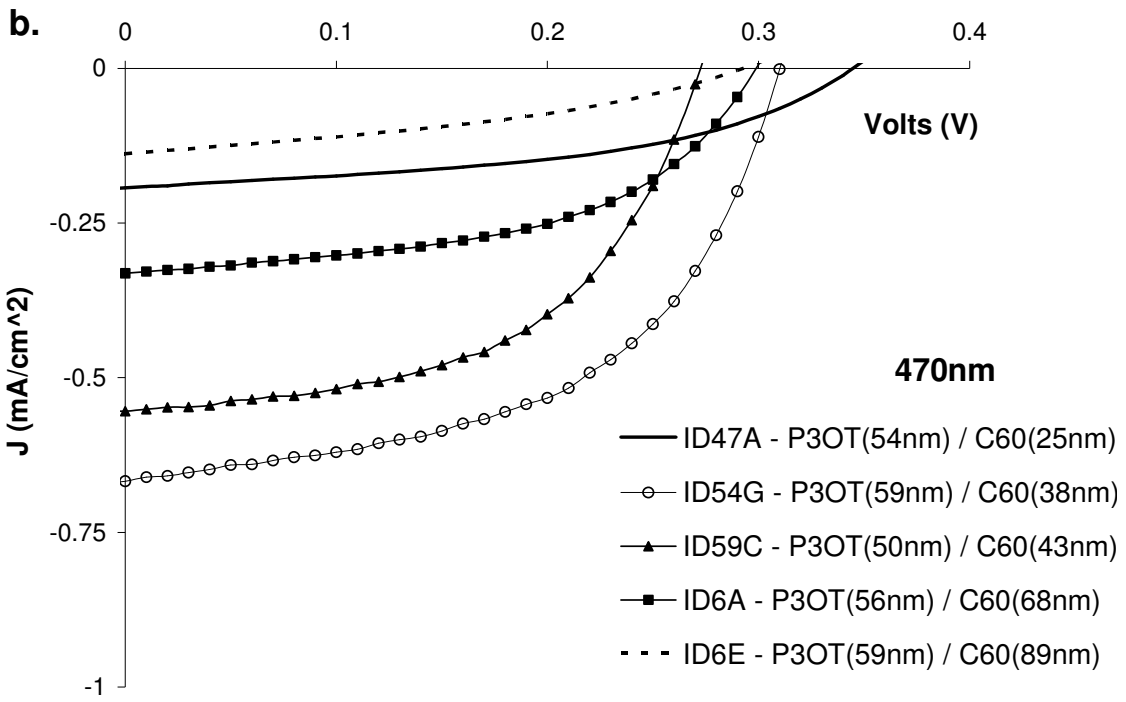

Figure 4.7 (a) EQE and (b) 470 nm illumination, 4th quadrant J-V characteristics for selected devices with C_{60} thicknesses varying within the range of 10 nm to 110 nm and P3OT thicknesses more or less constant within 50 nm to 60 nm. All devices were interdiffused under similar conditions and the thicknesses of the layers are given in the legend along with the device name.

Device	Thickness(nm)		Voc	Jsc	FF	Eff
	P3OT	C_{60}	(V)	(mA/cm^2)		(%)
ID47A	54	25	0.345	-0.19	0.46	0.9
ID54G	59	38	0.315	-0.67	0.52	2.05
ID59C	50	43	0.275	-0.55	0.53	1.52
ID6A	56	68	0.295	-0.33	0.52	1.36
ID6E	59	89	0.295	-0.14	0.36	0.40

Table 4.3 Overview of the photovoltaic performance at 470 nm of the devices presented in Figure 4.7.

Figure 4.8 a and b show the EQE and the 470 nm illumination 4th quadrant J-V curves for a set of devices with P3OT thickness varying from 15 nm to ~ 110 nm and C_{60} thickness contained within 40nm to 50nm. Table 4.4 gives an overview of the photovoltaic performance at 470 nm of these devices. Since the C_{60} thickness is kept constant in these

devices, the interference effect, due to light reflection off the C_{60} – Al boundary, is not a contributing factor to the trends observed here. The position of the intensity maximum is now fixed with respect to the center of the interdiffused region of the film. Instead, an important consideration in this case is the extent of interdiffusion of C_{60} in the polymer layer. This is because the incident light first encounters the P3OT layer and the interdiffused region before it reaches the Al boundary. For a thin P3OT layer, the C_{60} can diffuse all the way through to yield exciton dissociation sites throughout the polymer. But this is countered by the absorption efficiency, which is small for thin films, giving an overall low device performance (device ID14E). Then, as the P3OT layer thickness increases, it is still thin enough to have a concentration gradient throughout the P3OT but the absorption efficiency goes up. This is seen as an increase in the overall EQE as well as an increase in the 450-500 nm peak.

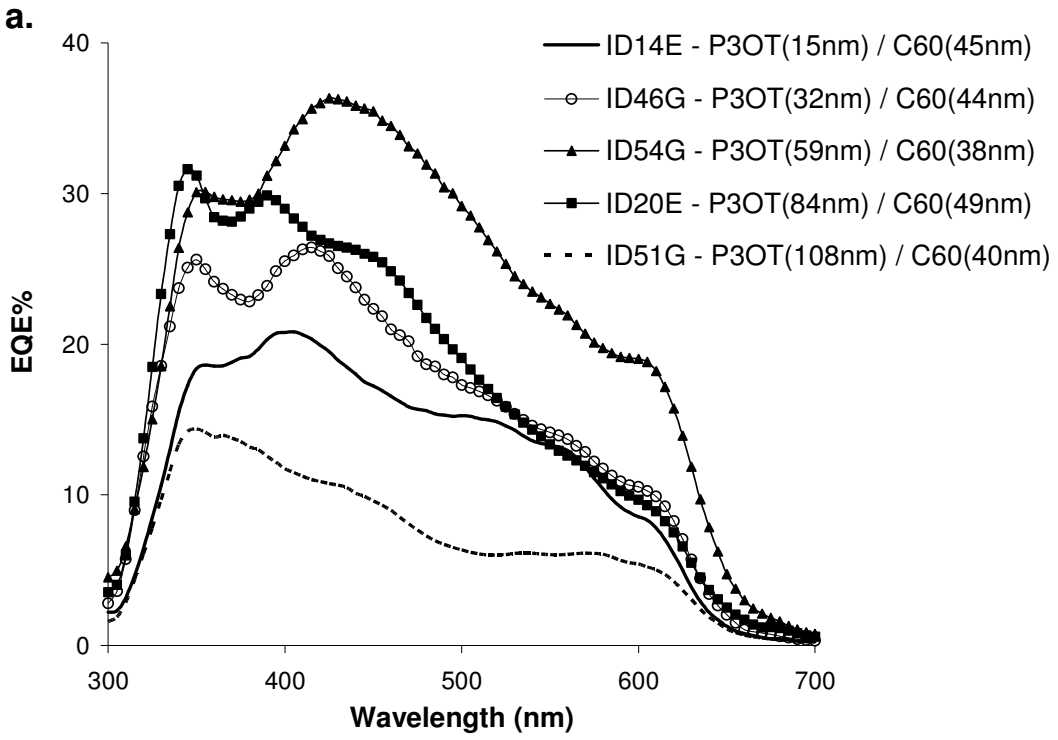

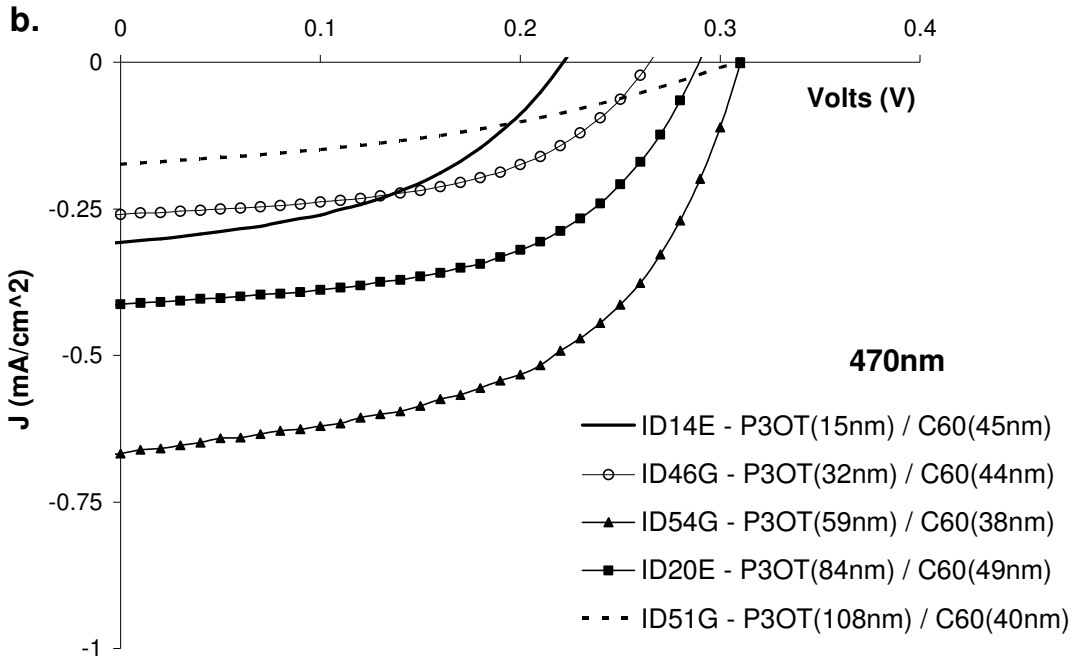

Figure 4.8 (a) EQE and (b) 470 nm illumination, 4th quadrant J-V characteristics for selected devices with P3OT thicknesses varying within the range of 10 nm to 110 nm and C_{60} thicknesses in the vicinity of 40 nm to 50 nm. All devices were interdiffused under similar conditions and the thicknesses of the layers are given in the legend along with the device name.

Device	Thickness(nm)		Voc	Jsc	FF	Eff
	P3OT	C_{60}	(V)	(mA/cm^2)		(%)
ID14E	15	45	0.225	-0.31	0.45	0.61
ID46G	32	44	0.265	-0.26	0.52	1.04
ID54G	59	38	0.315	-0.67	0.52	2.05
ID20E	84	49	0.285	-0.41	0.54	1.38
ID51G	108	40	0.305	-0.17	0.39	0.37

Table 4.4 Overview of the photovoltaic performance at 470 nm of the devices presented in Figure 4.8.

Once again, the point should be stressed that the extent of interdiffusion will be constant for the same interdiffusion conditions. As the thickness increases, it will eventually exceed the thickness value through which complete interdiffusion occurs, and a layer of pure P3OT will appear. This leads to the filter effect seen as the reduction of this peak. For this data set, the optimum P3OT thickness is ~ 60 nm.

4.2.3 Overview of Dependence of Device Performance on Thickness

So far, in the previous two sections, ~60 nm of P3OT and ~40 nm of C_{60} were arrived at as optimum layer thicknesses for interdiffusion of bilayers at 118 °C for 5 minutes in the Argon box. This study consisted of comparing EQE and J-V curves of representative devices of different layer thicknesses. The values quoted were specific to the best device in each thickness range. These devices were selected from a larger experimental set that has been consolidated and presented in this section and hence yields a more general range of optimum thicknesses for the P3OT and C_{60} layers. The following figures show more general trends for the monochromatic photovoltaic parameters as a function of P3OT and C_{60} thicknesses variation.

Figures 4.9 through 4.12 show the trends for the EQE, V_{OC}, fill factor (FF) and overall power conversion efficiency (η) values respectively, which were all measured at 470 nm. Around 50 to 60 devices were fabricated for this study and grouped into 20 nm P3OT and C_{60} thickness bins. The values for each of these measurements were averaged over the devices in each bin and plotted in the figures. Each data point is plotted at the central thickness of its respective bin. Part (a) of each figure shows the variation of the measured parameter with respect to varying P3OT thickness, plotted for each C_{60} thickness bin. Similarly, part (b) of these figures shows the measured parameter with respect to varying C_{60} thickness, plotted for each P3OT thickness bin. Tables 4.5 through 4.8 show the data plotted in these figures in a matrix form, along with the standard deviation over the points averaged and the number of points averaged, to give an idea of experimental variance in the reported values. The standard deviation is a result of random experimental error and hence does not show any trend.

The EQE measured at 470 nm, shows a similar trend as was seen in the curves presented in the previous sections (Figure 4.9). A maximum EQE is obtained for devices in the 40 nm to 60 nm bin for both P3OT and C_{60}. This same trend would be observed for the short circuit photocurrent density (J_{SC}), which is proportional to the EQE.

From Figures 4.10a and 4109b, we see that the V_{OC} curves (470 nm illumination) do not exhibit consistent features. The curves corresponding to C_{60} thickness between 20

to 40 nm and between 40 to 60 nm show a slight peak for the 40 to 60 nm thick P3OT devices. The other curves are featureless with a slight monotonic increase with increasing P3OT thickness. These features are not strong enough to conclude any dependence of V_{OC} on the P3OT layer thickness. Moreover, the curves indicate a lack of dependence of V_{OC} on C_{60} layer thickness too. V_{OC} is a material property and is reported to be predominantly dependent on the HOMO and LUMO levels of the materials used as well as the work function of the electrodes. Our conclusion that the V_{OC} is not dependent on layer thicknesses is consistent with this theory (explored in some detail in section 2.8.1)**.**

Figure 4.11 shows a plot of the average fill factor values for varying polymer and C_{60} thickness. It is represented in the shape of the illuminated current-voltage characteristics in the 4th quadrant and is mainly a function of the diode quality of each individual device. There is no clear dependence of the fill factor on the layer thicknesses, seen as more or less flat curves for both P3OT and C_{60} thickness variations.

Figures 4.12a and 4.12b show plots of the average power conversion efficiencies (η), determined under 470 nm illumination, as a function of varying C_{60} and P3OT thicknesses, respectively. From these plots, we can see that devices whose P3OT layer thickness and C_{60} layer thickness both fall within 40 nm to 50 nm had the highest power conversion efficiencies. This follows the trend of the EQE data since the other two factors that determine the efficiency (fill factor and V_{OC}) are independent of thickness essentially.

The analysis of the last three sections demonstrate that for the given interdiffusion conditions (heating at an average temperature of 130 °C, ramped up at a rate of 20 °C/min, kept steady for 5 minutes and cooled in an atmosphere of circulating argon) the optimum P3OT layer thickness lies between 40 nm and 60 nm, closer to 60 nm, and the optimum C_{60} layer thickness lies between 40 nm and 60 nm, closer to 40 nm.

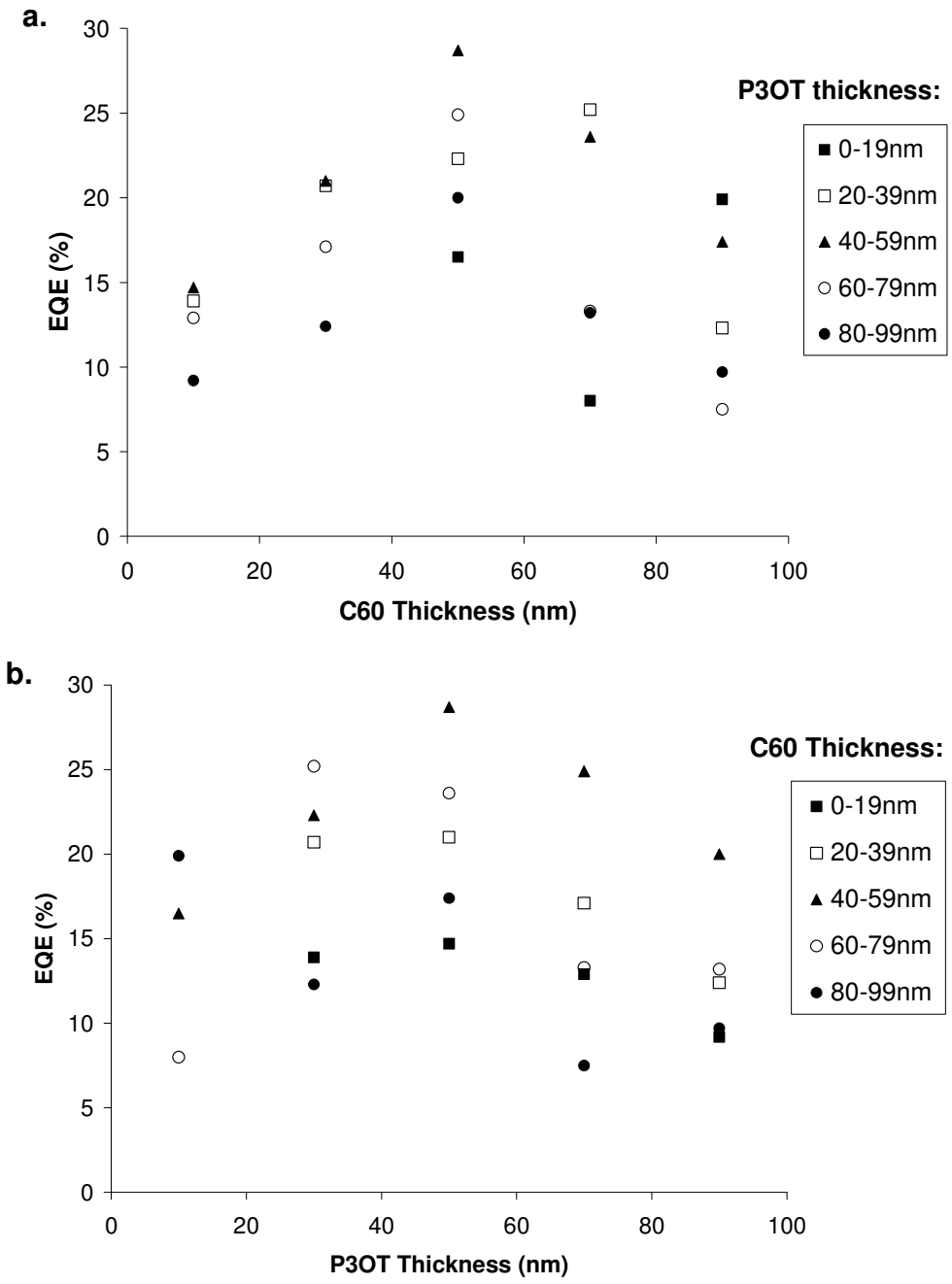

Figure 4.9 Monochromatic external quantum efficiencies (EQE), measured under 470 nm illumination, for devices of (a) varying C_{60} thicknesses, at each value of P3OT thickness and (b) varying P3OT thicknesses, at each value of C_{60} thickness.

		P3OT THICKNESS					
C_{60} THICKNESS		0-19	20-39	40-59	60-79	80-99	100-119
	10-19		**13.9**, 2.6, 6			**9.2**, 0.4, 2	
	20-39		**20.2**, 7.6, 11	**16.8**, 2.8, 5	**17.1**, 1.4, 6	**12.4**, 2.5, 8	**8.4**, 1, 3
	40-59	**16.5**, 0.8, 4	**22.3**, 4.1, 5	**29.9**, 1.7, 7	**22.6**, 17.1, 10	**18.6**, 3.5, 4	**17.9**, 0.5, 3
	60-79	**8.0**, 2.1, 2	**25.2**, 7.7, 4* **	**23.6**, 2.1, 4	**13.3**, 0.07, 2	**13.2**, 1.5, 2 **22.5**, 1.5, 2***	
	80-99	**19.9**, 8.0, 2*	**19.6**, 3.8, 10	**17.4**, 7.5, 3***	**7.6**, 2.8, 2	**12.4**, 5.9, 9	
	100-119						**6.9**, 2.0, 4
	120-139						**4.5**, 0.9, 5

***not used, ** think there is time decay here, *not averaged over whole set of data.

Table 4.5 EQE (470 nm): Overview of all the devices considered in this study.
Data represented should be interpreted as so: **Average Values EQE%s**, Standard Deviation, # of data considered

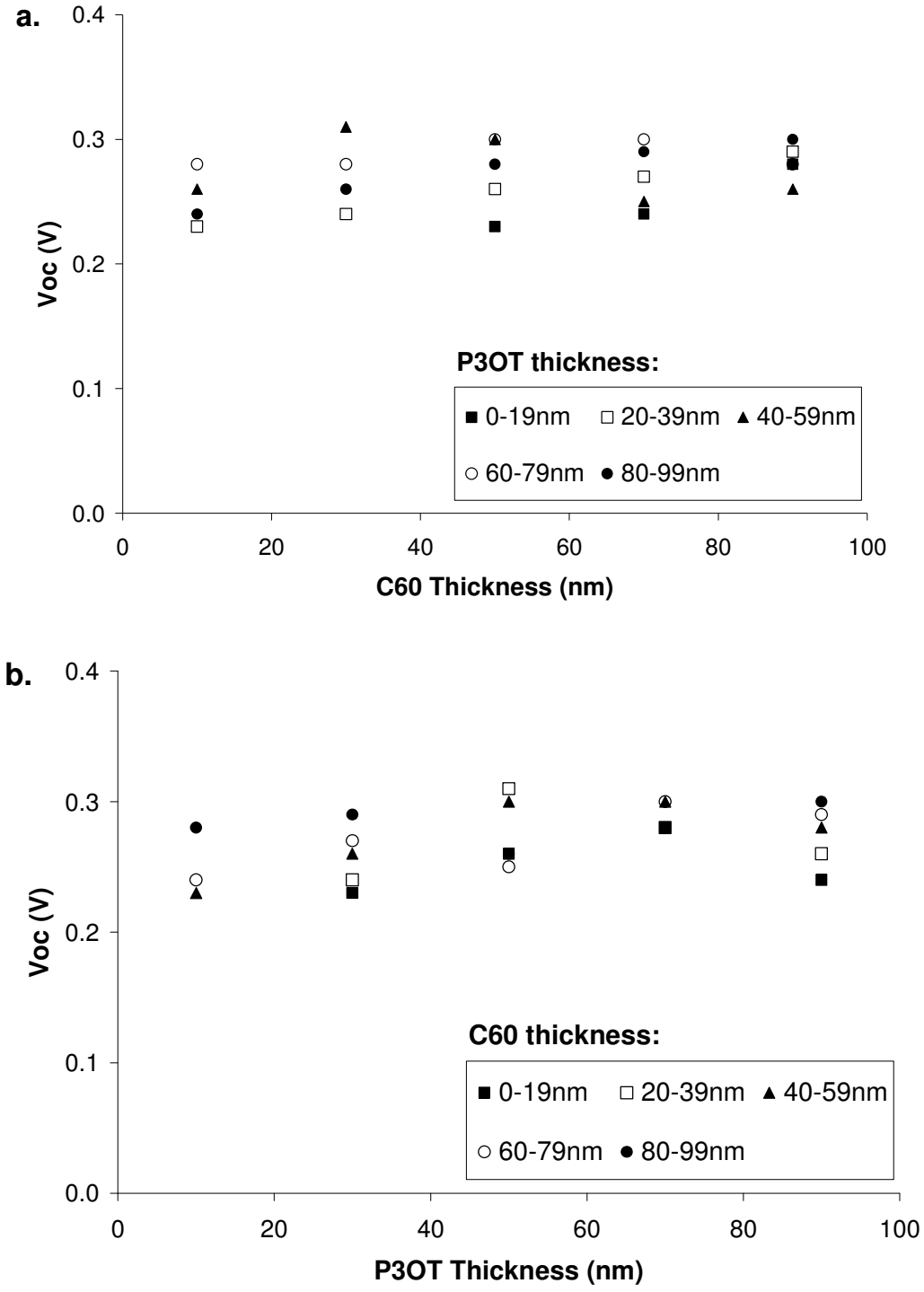

Figure 4.10 Open circuit voltages (V_{OC}), determined under monochromatic 470 nm illumination, for devices of (a) varying C_{60} thicknesses, at each value of P3OT thickness and (b) varying P3OT thicknesses, at each value of C_{60} thickness.

P3OT THICKNESS

C_{60} THICKNESS		0-19	20-39	40-59	60-69	80-99	100-119
	0-19		**0.23**, 0.02, 6	**0.26**, 0.01, 2	**0.28**, 0.03, 3	**0.24**, 0.01, 2	
	20-39		**0.24**, 0.02, 11	**0.31**, 0.04, 7	**0.28**, 0.04, 5	**0.26**, 0.02, 8	**0.28**, 0.03, 6
	40-59	**0.23**, 0.01, 5	**0.26**, 0.02, 6	**0.30**, 0.02, 5	**0.30**, 0.01, 9	**0.28**, 0.01, 5	**0.35**, 0.01, 3
	60-79	**0.24**, 0, 1	**0.27**, 0.02, 6	**0.25**, 0.07, 4	**0.30**, 0.01, 2	**0.29**, 0.01, 4	
	80-99	**0.28**, 0.01, 2	**0.29**, 0.02, 11	**0.26**, 0.06, 3	**0.28**, 0.01, 2	**0.30**, 0.01, 9	
	100-119						**0.25**, 0.01, 4
	120-139						**0.25**, 0.01, 5

Table 4.6 V_{OC} (470 nm): Overview of all the devices considered in this study.
Data represented should be interpreted as so: **Average Values V_{OC}s**, Standard Deviation, # of data considered

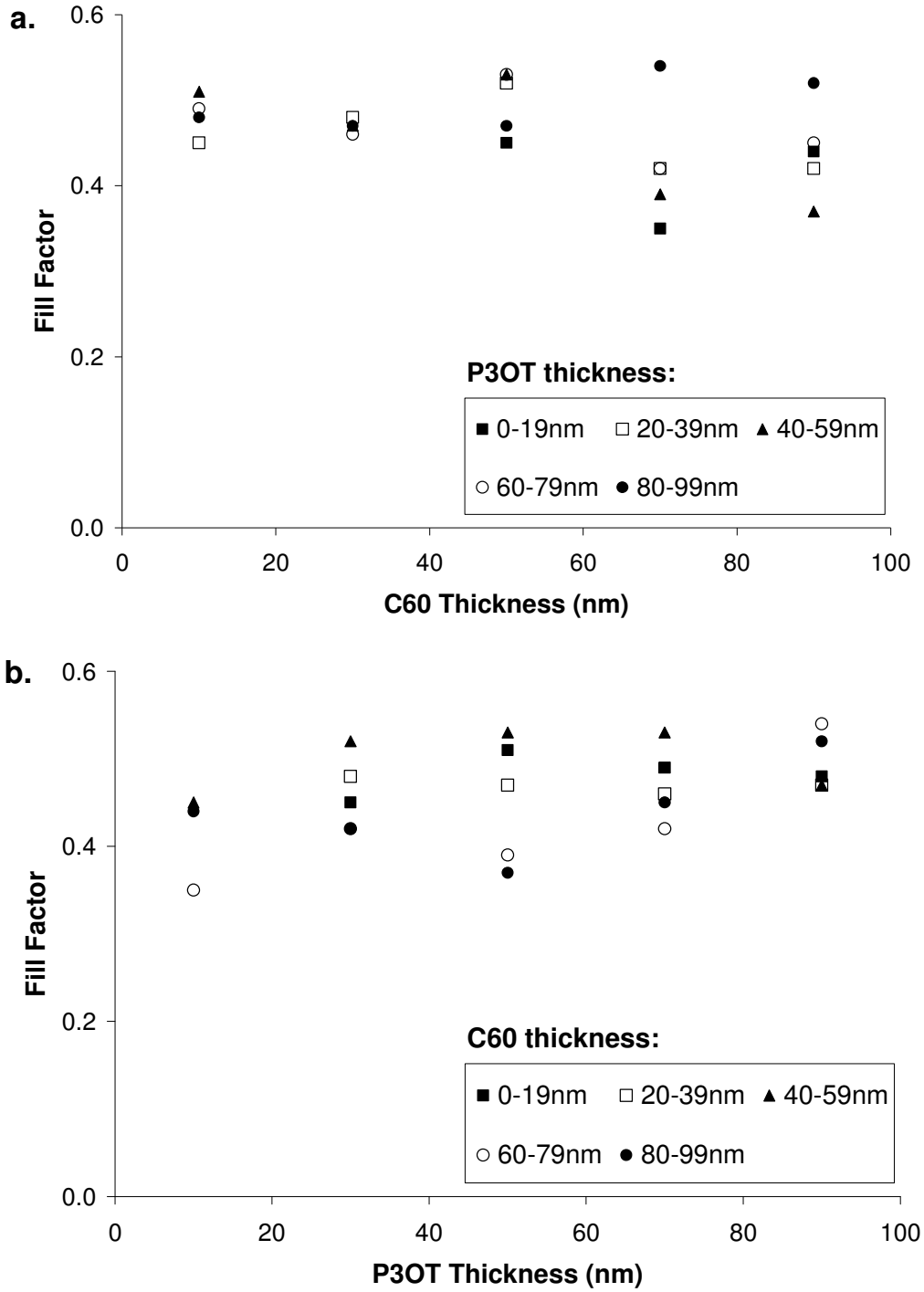

Figure 4.11 Fill factor values (FF), determined under monochromatic 470 nm illumination, for devices of (a) varying C_{60} thicknesses, at each value of P3OT thickness and (b) varying P3OT thicknesses, at each value of C_{60} thickness.

P3OT THICKNESS

C_{60} THICKNESS		0-19	20-39	40-59	60-79	80-99	100-119
	0-19		**0.45**, 0.07, 6	**0.51**, 0.01, 2	**0.49**, 0.05, 3	**0.48**, 0,	
	20-39		**0.48**, 0.05, 11	**0.47**, 0.04, 7	**0.46**, 0.07, 5	**0.47**, 0.03, 8	**0.41**, 0.08, 6
	40-59	**0.45**, 0.02, 5	**0.52**, 0.02, 5	**0.53**, 0.01, 5*	**0.53**, 0.04, 9* Dev5	**0.47**, 0.04, 5	**0.51**, 0.02, 3
	60-79	**0.35**, 0, 1	**0.42**, 0.09, 6	**0.39**, 0.11, 4	**0.42**, 0.04, 2	**0.54**, 0.02, 4	
	80-99	**0.44**, 0.07, 2*	**0.42**, 0.07, 10* **	**0.37**, 0.07, 3	**0.45**, 0.04, 2*	**0.52**, 0.04, 9	
	100-109						**0.43**, 0.02, 4
	120-129						. **0.51**, 0.03, 5

***not used, ** think there is time decay here, *not averaged over whole set of data.

Table 4.7 Fill Factor (470 nm): Overview of all the devices considered in this study.
Data represented should be interpreted as so: **Average Values FFs**, Standard Deviation, # of data considered

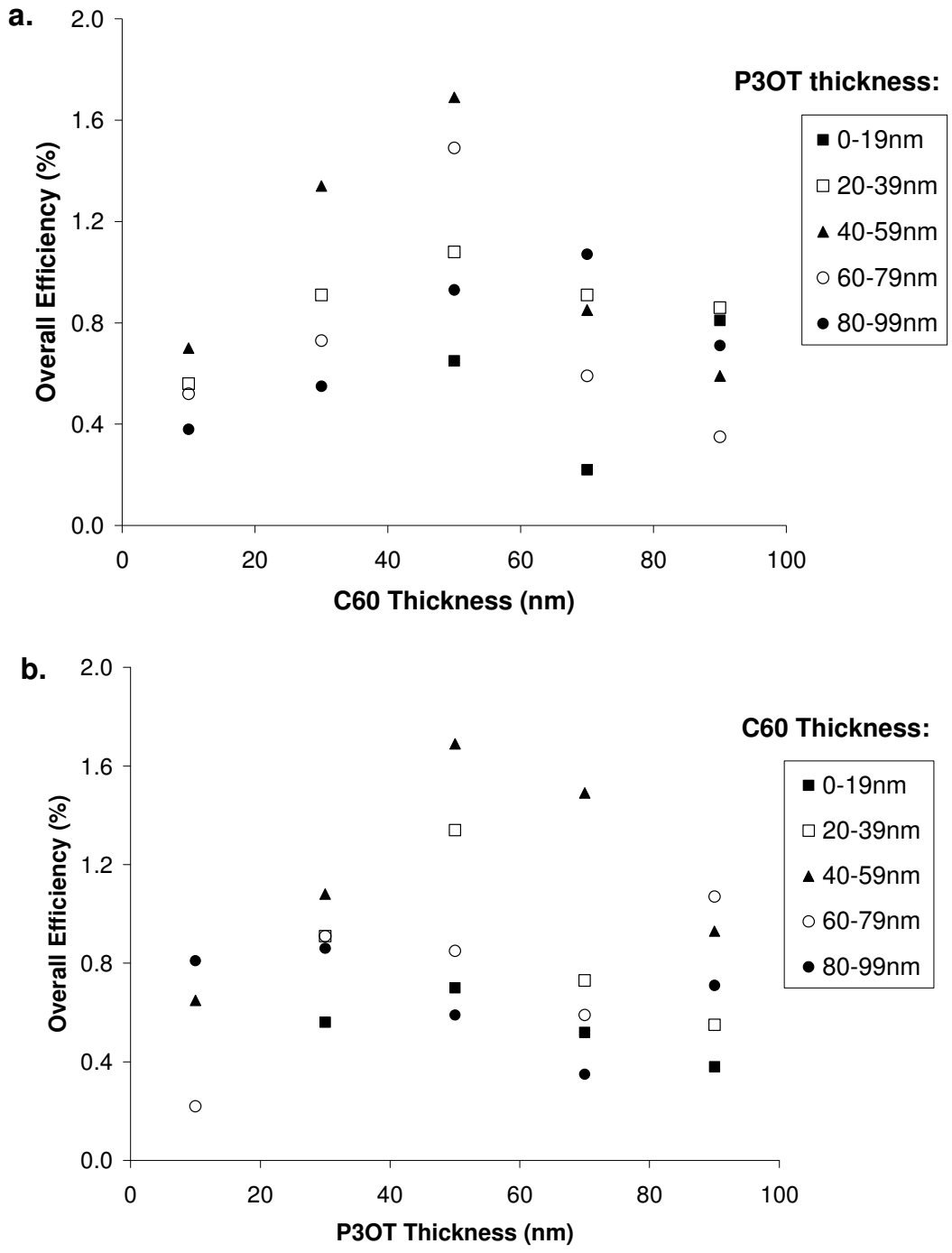

Figure 4.12 Monochromatic power conversion efficiencies (η),determined under 470 nm illumination, for devices of (a) varying C_{60} thicknesses, at each value of P3OT thickness and (b) varying P3OT thicknesses, at each value of C_{60} thickness.

P3OT THICKNESS

C_{60} THICKNESS		0-19	20-39	40-59	60-79	80-99	100-119
	10-19		**0.56**, 0.19, 6	**0.70**, 0.05, 2	**0.52**, 0.20, 3	**0.38**, 0, 2	
	20-39		**0.91**, 0.46, 11	**1.34**, 0.54, 7	**0.73**, 0.19, 5	**0.55**, 0.12, 8	**0.35**, 0.06, 6
	40-59	**0.65**, 0.10, 5	**1.08**, 0.14, 5	**1.69**, 0.19, 5*	**1.49**, 0.42, 9*	**0.93**, 0.27, 5	**1.17**, 0.06, 3
	60-79	**0.22**, 0, 1	**0.91**, 0.67, 6	**0.85**, 0.44, 4	**0.59**, 0.11, 2	**1.07**, 0.26, 4	
	80-99	**0.81**, 0.42, 2*	**0.86**, 0.34, 10	**0.59**, 0.17, 3	**0.35**, 0.15, 2*	**0.71**, 0.36, 9	
	100-119						**0.26**, 0.10, 4
	120-139						**0.21**, 0.06, 5

***not used, ** think there is time decay here, *not averaged over whole set of data.

Table 4.8 Power conversion efficiency, η(470 nm): Overview of all the devices considered in this study.
Data represented should be interpreted as so: **Average Values η%s**, Standard Deviation, # of data considered

4.2.4 Auger Spectroscopy Study of Devices with Varying Layer Thicknesses

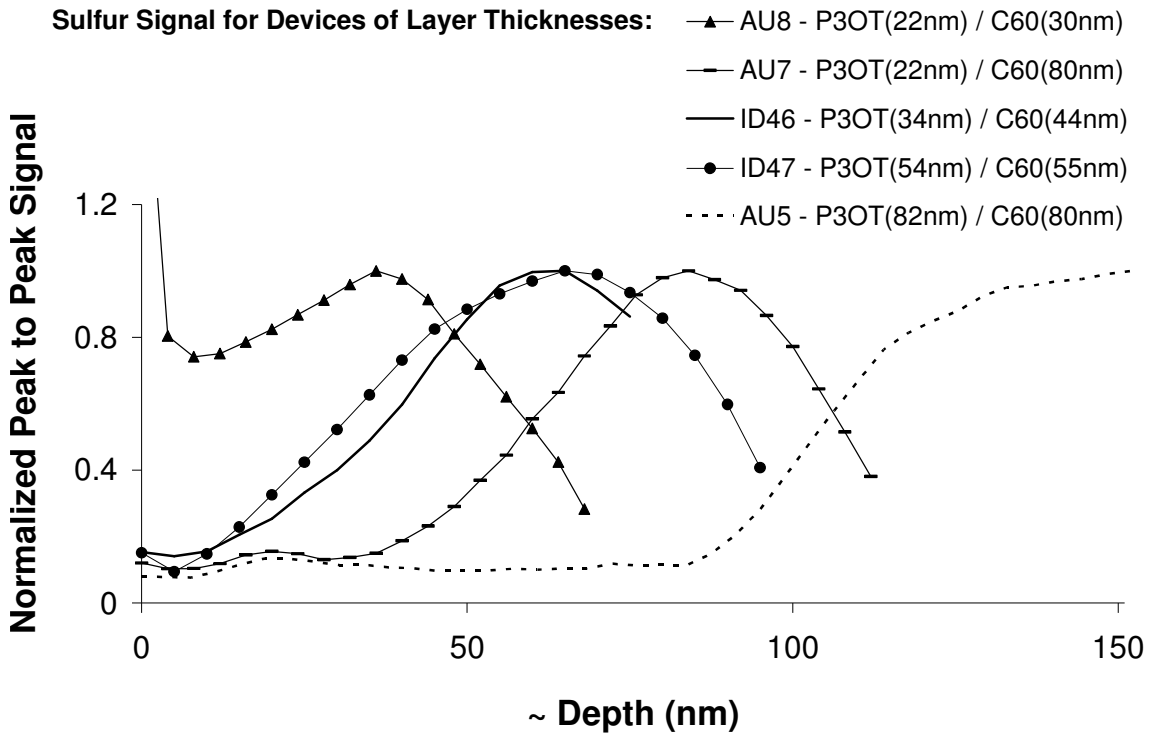

Figure 4.13 Plot of the depth profiles by Auger spectroscopy for devices of varying P3OT and C_{60} thicknesses interdiffused under similar conditions. The approximate depth into the film is given on the x-axis while the y-axis is the peak to peak signal intensity normalized to one. Sulfur indicates presence of P3OT. The gradual increase in sulfur signal indicates a concentration gradient between the P3OT and C_{60}.

Auger spectroscopy combined with argon-ion beam milling was used to monitor the sulfur content (which corresponds to the amount of P3OT) into the depth of the film. The analysis starts at the top of the C_{60} layer and, after milling through the film, it ends at the ITO layer. It should be noted that the Auger measurement is done starting at the C_{60} edge of the device while incident light enters the P3OT edge of the device. Indium and oxygen are also monitored (not shown), the rise of which indicates entry into the ITO layer and the end of the film under consideration. Except in the case of AU5, the end of the active layers and the start of the ITO edge is characterized by the drop-off in sulfur content at the extreme right of the curves. It is not a sharp step as would be expected, probably due to the detection of polymer debris when measuring in the top few nanometers of the ITO layer. It might be argued that the slope seen in the concentration gradient region is also an

effect of debris from previous layers being erroneously detected but the clear difference between bilayer and interdiffused films indicates that this is a true measure of a concentration gradient.

The Auger curve for a typical bilayer as compared to a typical ID device is given in section 4.1.1. Figure 4.13 shows Auger curves for ID devices of varying polymer and fullerene layer thicknesses which will be compared to their corresponding device EQEs from previous sections (especially Figure 4.6 of section 4.2.1). In the case of the thick P3OT, thick C_{60} device (AU5), we see an initial region of no sulfur followed by a gentle rise that ends in a high plateau. This indicates an initial region of no P3OT (pure C_{60}) followed by slowly increasing P3OT content in the film (concentration gradient) and finally a constant high concentration of P3OT (pure P3OT). The corresponding device (Device ID21C from Figure 4.6) showed a strong filter effect due to loss of light through absorption in the pure polymer and fullerene layers that is clearly indicated in this Auger curve.

As the P3OT layer thickness decreases, the plateau region decreases and the edge approaches the concentration gradient region. Now there is no pure polymer layer, and the filter effect due to that should reduce. There is still a layer of pure C_{60} which will continue to result in loss of light through absorption that does not yield separated charges. An example of a thick fullerene and thin P3OT is device ID13D from Figure 4.6 that shows a reduction of the filter effect for the polymer while retaining that for the fullerene layer.

As the C_{60} layer is reduced in thickness, the fullerene edge is seen to come closer to the concentration gradient region, reducing the filter effect of C_{60} in addition to that of P3OT. With the exception of AU8, as the thicknesses of the layers are reduced, the concentration gradient stays the same, seen as a line with the same slope that has the same x-axis width. This indicates that for a given set of interdiffusion conditions, the extent of interdiffusion is constant. In this manner, a direct correspondence is seen between the interpretation of the depth profile of the active layers from EQE curves and the concentration depth profile obtained using Auger.

The anomaly of AU8 requires further investigation. The given ID conditions produce a concentration gradient of fixed slope and x-axis length. But a requirement to

obtain this would be that the combined thickness of the polymer and fullerene layers should exceed the extent of the interdiffusion so that there is enough material to produce the full gradient. In the case of AU8, the layers are too thin and so, before the ID process is complete, the materials diffuse all the way through and start to "pile up" at the opposite edge. This is clearly seen as a high rise in sulfur (P3OT) at the C_{60} edge. The recognition of the fullerene pile up at the P3OT edge is a little more subtle. As the C_{60} piles up between the ITO and the polymer, the sulfur signal will start to reduce before the ITO is reached. Hence the sulfur "peak" from the Auger curve will taper off more gradually on the ITO side and also the peak gets a little sharper. This sharpening of the peak may also be seen to a lesser extent for the thin P3OT devices, ID46 and AU7 where the peaks are sharper than for ID47, whose P3OT layer is not very thin. A possible explanation for this pile up of materials at the surface is blooming, which is defined as the process in which one component of a polymer mixture phase separates and migrates to an external surface of the mixture.[8] AU8 is an extreme case where the pile up has gone so far as to create a concentration inversion and back diffusion of the materials. This would reduce the original concentration gradient, seen as a reduction in the slope and x-axis extent in the new gradient. A blend-like morphology is approached. ID16E from Figure 4.6 comes closest to AU8 in thicknesses. Although no filter effect was observed (no dips in the EQE curve at 450 nm and 350 nm), the overall level had reduced. This had been interpreted as mainly due ot the reduction in absorption by thin layers but the Auger curve has revealed prominent morphological issues that would also reduce the efficiency. A main concern for such thin layers is the pile-up that occurs at the electrodes. The appearance of the donor at the cathode (Al) and acceptor at the anode (ITO) would affect the clean Fermi level pinning and band matching and hence undermine the charge collection efficiency. Hence, in all the cases of thin layers (just one or both), this is an extra contributing factor to the reduction in the net performance of the device.

ID47 from the Auger curves has thicknesses closest to the optimum thicknesses that were determined from the previous sections (for example, ID54G from Figure 4.6), This device shows a concentration gradient that extends all the way through the film. At the ITO boundary, the sulfur peak is blunted, with a hint of a plateau. At the fullerene edge, there is a very small, single data point rise seen in the sulfur. Thus, there is minimal

filter effect and minimal pile-up and also a full concentration gradient which corresponds to the best device. Hence, we can confirm that the ideal morphology we expect to give us the best concentration gradient devices is one where the concentration gradient extends all the way through the active layer, stopping just short of the electrode, which sees a thin layer of pure material for efficient charge collection. We see these depth-profiling plots that the concentration gradient has a total extent of 60-70 nm for this set of interdiffusion conditions, in good agreement with the optimal device performance for thicknesses of ~50 nm each for the P3OT and C_{60} layers.

4.2.5 Summary: Thickness Dependence Study for P3OT – C_{60} Photovoltiac Devices

This study was conducted for P3OT – C_{60} devices interdiffused from a bilayer, at 118 °C (over swing to 134 °C) under an atmosphere of argon. The temperature was kept high for 5 minutes after which the sample was allowed to air cool. The P3OT layer was annealed at 120 °C for over 35 minutes under vacuum prior to C_{60} deposition and interdiffusion. For this set of thermal treatment and interdiffusion conditions the thicknesses for the starting P3OT and C_{60} layers that gave the best device performance were within the 40 nm to 60 nm range, closer to 60 nm for P3OT and closer to 40 nm for C_{60}. This corresponded to a depth profile that showed a concentration gradient that spanned the entire active layer of the device till the electrodes are reached, where it ends in a thin layer of pure material.

4.3 Thermal Interdiffusion Conditions Variation Study

In previous sections it has been shown that the most efficient concentration gradient devices were those that had the gradient extend all the way through the active layer. These devices were obtained by optimizing the thicknesses for a fixed set of ID parameters. Concentration gradient device performance may also be improved by varying these interdiffusion conditions. A brief overview of such a study done on this system is given in this section. ID conditions can be varied in two ways, either by varying the time of interdiffusion for a given temperature or by varying the temperature of interdiffusion.

Prior work had shown that devices heated above the melting point (T_m) of the donor resulted in a drop in the device quality.[9] Hence, all temperature variation studies were carried out below the T_m of the polymer. It is hoped that the results presented in this section help to establish a direction in which further investigation into improving concentration gradient devices could proceed.

4.3.1 Effects of Varying Interdiffusion Time

In this section, a study on the effects of varying the interdiffusion times on the concentration gradient in P3OT – C_{60} systems is presented. In addition to this, the effects of annealing the P3OT film, prior to C_{60} deposition, have also been investigated. An ID temp of 135 °C was chosen. Samples were interdiffused for either 5 minutes or 20 minutes. A few of these samples were annealed at 120 °C for 35 minutes prior to C_{60} deposition. EQE curves for the various devices are compared and explanations for the trends seen are supported by Auger spectroscopy studies.

In P3OT – C_{60} devices, the main purpose that annealing serves is to improve the crystallinity and hence hole mobilities in the polymer. Blom *et al*. report an increase in the hole mobility of P3HT – PCBM blends from 3×10^{-12} m^2/Vs to around 2×10^{-8} m^2/Vs for films annealed at 150 °C.[10] The regions of enhanced crystallinity thus formed would have a different thermodynamic response to heating. It was expected that C_{60} would find it harder to diffuse into crystallized P3OT as compared to more amorphous P3OT. On the other hand, since it is most likely that the C_{60} diffuses only into the amorphous regions of the semi-crystalline polymer, and the crystalline fraction is less than 50%, it is also understandable that the diffusion of C_{60} would still occur into the remaining amorphous regions of the polymer. This comparative study was done to see if device performance improved for device with non-annealed P3OT layers.

Heat treatments in this study were done in vacuum, under a constant ID temperature of 135 °C. There was an over-swing up to 4 °C on this set temperature, which would cool back down to 135 °C within a few minutes. Since it was important to keep temperature constant for this study, performing interdiffusion in the vacuum chamber with its low over-swings and fast cooling rates, helped us obtain a more

trustworthy constant-temperature reading. While these heating parameters are similar to the ones used in the thickness variation study, a direct comparison cannot be made between these two sets of data, due to the varied heating and cooling temperature profiles of these two experimental systems. (An explanation of this can be found in section 3.2.5) Thus, while general trends observed are expected to be universal, detailed comparisons of individual device performance should be restricted to the devices presented in this section.

The variation of interdiffusion times was expected to show different extents of interdiffusion and accordingly better or worse device performance. Figure 4.14a shows the EQE curves for devices that were interdiffused at 135 °C for 5 minutes and cooled under vacuum. Figure 4.14b shows similar EQE curves for devices also interdiffused at 135 °C, but for 20 minutes and cooled under an atmosphere of trapped Argon gas. Initially, drastically different cooling rates were expected of the two cases, due to added presence of convective air-cooling in the second case. But these rates were found to not be very different since the main cooling process in both cases was by conduction through the metal stand. Both figures show data for annealed and non-annealed devices. Thicknesses of the layers prior to interdiffusion have been quoted in the legend of the EQE curves. They are also found in Table 9, which gives an overview of the photovoltaic performance of the devices under 470 nm illumination.

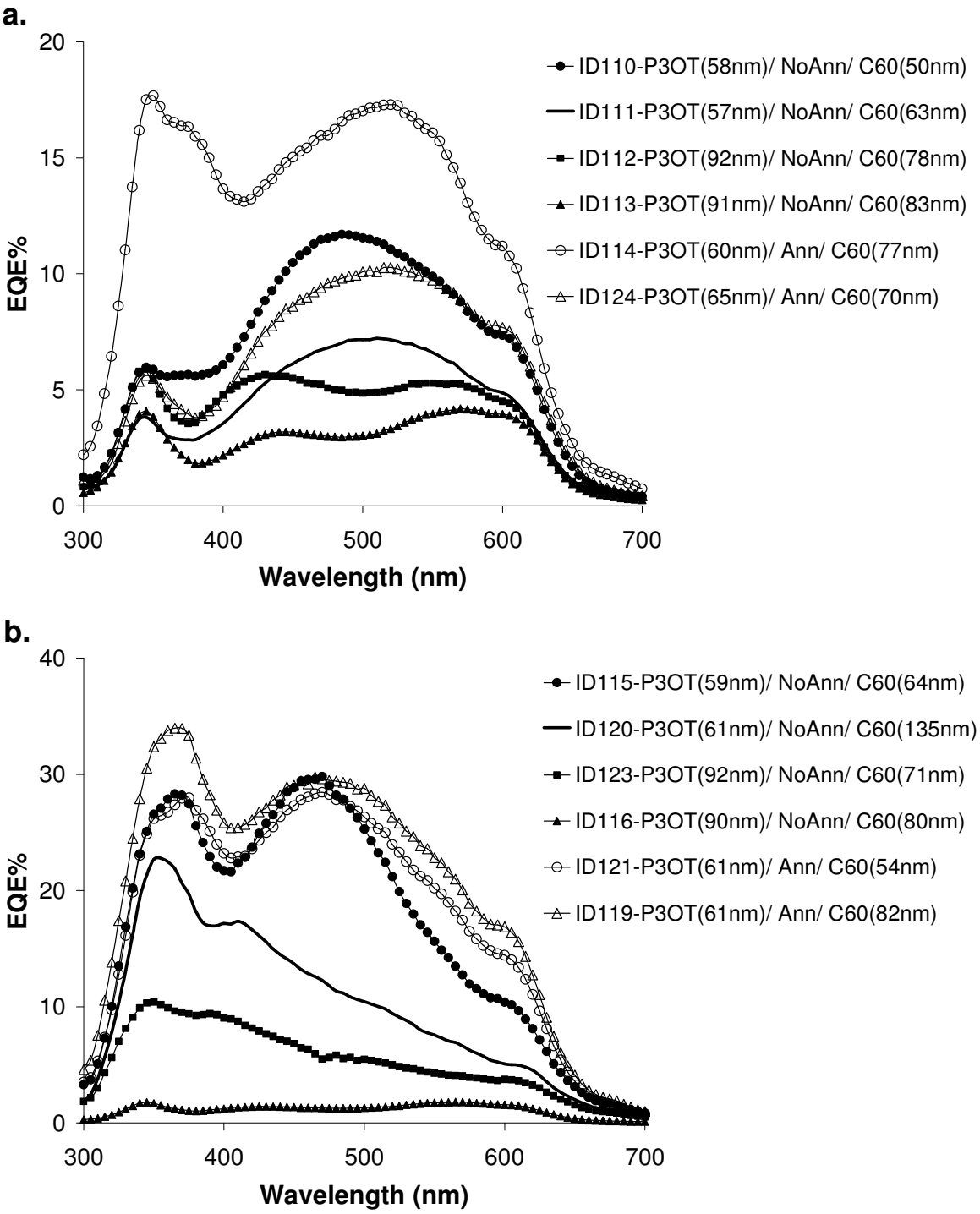

Figure 4.14 EQE curves for devices interdiffused at 135 °C for (a) 5 minutes and (b) 20 minutes, under vacuum. Device layer thicknesses and device names are given in the legend. Both plots contain devices that were either annealed or not annealed, represented by 'Ann' and 'NoAnn' in the legend. Annealed devices have P3OT layers that were heated to 120 °C for 35 minutes, under vacuum, prior to C_{60} deposition and ID step. Non-annealed devices did not undergo any heat treatment prior to the ID step.

Device	Thickness(nm)		ID time	Anneal	Voc	Jsc	FF	Eff
	P3OT	C_{60}	(min)	`120°C, 35min	(V)	(mA/cm^2)		
ID110	58	50	5	N	0.315	-0.18	0.43	0.59
ID111	57	63	5	N	0.275	-0.11	0.41	0.28
ID112	92	78	5	N	0.415	-0.08	0.49	0.39
ID113	91	83	5	N	0.305	-0.05	0.41	0.15
ID114	60	77	5	Y	0.325	-0.25	0.47	0.92
ID124	65	70	5	Y	0.195	-0.15	0.38	0.27
ID115	59	64	20	N	0.335	-0.46	0.49	1.82
ID120	61	135	20	N	0.315	-0.19	0.50	0.71
ID123	92	71	20	N	0.235	-0.10	0.20	0.11
ID116	90	80	20	N	0.255	-0.02	0.28	0.03
ID121	61	54	20	Y	0.305	-0.45	0.54	1.78
ID119	61	82	20	Y	0.235	-0.47	0.40	1.06

Table 4.9 Overview of the photovoltaic performance at 470 nm of the devices presented in Figure 4.14.

In both figures, similar thickness trends are seen, as were concluded from the previous sections:

1. The best devices have P3OT and C_{60} layer thickness in the range of around 60 nm each. This is especially evident in the case of devices ID119 and ID115 in Figure 4.14b. This is not so obvious in Figure 4.14a, which will be discussed shortly.
2. As the layers get thicker, the EQE values fall. This is seen when comparing ID 110 with ID113 and to some extent ID112 with ID113 in Figure 4.14a. It should be noted that both of these are non-annealed devices. This is also seen when comparing ID123 with ID115.
3. Filter effect is observed for thick P3OT layers, seen as the disappearance of the 450 nm to 500 nm peak. This is especially evident for devices ID112 and ID113 in Figure 4.14a, where a dip is seen at around 490 nm.

When comparing data from the two figures, interdiffusion for 20 minutes seems to produce better devices than interdiffusion for 5 minutes. The best device of Figure 4.14a (ID114) has a similar shape of the curve, but only half of the EQE as the best device of Figure 4.14b (ID119 or ID121). Also, in general, annealing the P3OT layer prior to C_{60} deposition seems to yield better results. This is seen as an enhanced wavelength range response, probably due to the increased crystallinity of P3OT. Shoulders at around 550 nm and 600 nm become more prominent, which correspond to similar shoulders that appear in the optical density spectrum in annealed P3OT films (Figure 3.15 of chapter 3). The improvements due to annealing are more evident for the case of interdiffusion for 5 minutes than for 20 minutes. This is because, during interdiffusion, the exposure to elevated temperatures would also lead to annealing and, hence, when interdiffused for a longer time, the non-annealed P3OT device has a chance to "catch up" with the annealed P3OT device, in terms of P3OT crystallinity. On the other hand, when interdiffused for just 5 minutes, there is insufficient time for the non-annealed films to crystallize, and so the resulting differences in device performance between the annealed and non-annealed devices are more evident. This competes with the effects of varying layer thicknesses, making that trend less evident as was mentioned earlier in point 1.

Figure 4.15 shows the Auger spectroscopy measurements done on selected devices from this data set. During fabrication, the substrates were partitioned and one half was reserved for Auger spectroscopy measurements. The PEDT:PSS layer was removed from this half and it was completely masked off to protect it from Al deposition. Devices were made as usual on the other half of the slide. This way, a direct measurement of the morphology of the devices is obtained, which proved useful in drawing conclusions from a study that was not as extensive as the one on the thickness variation dependence.

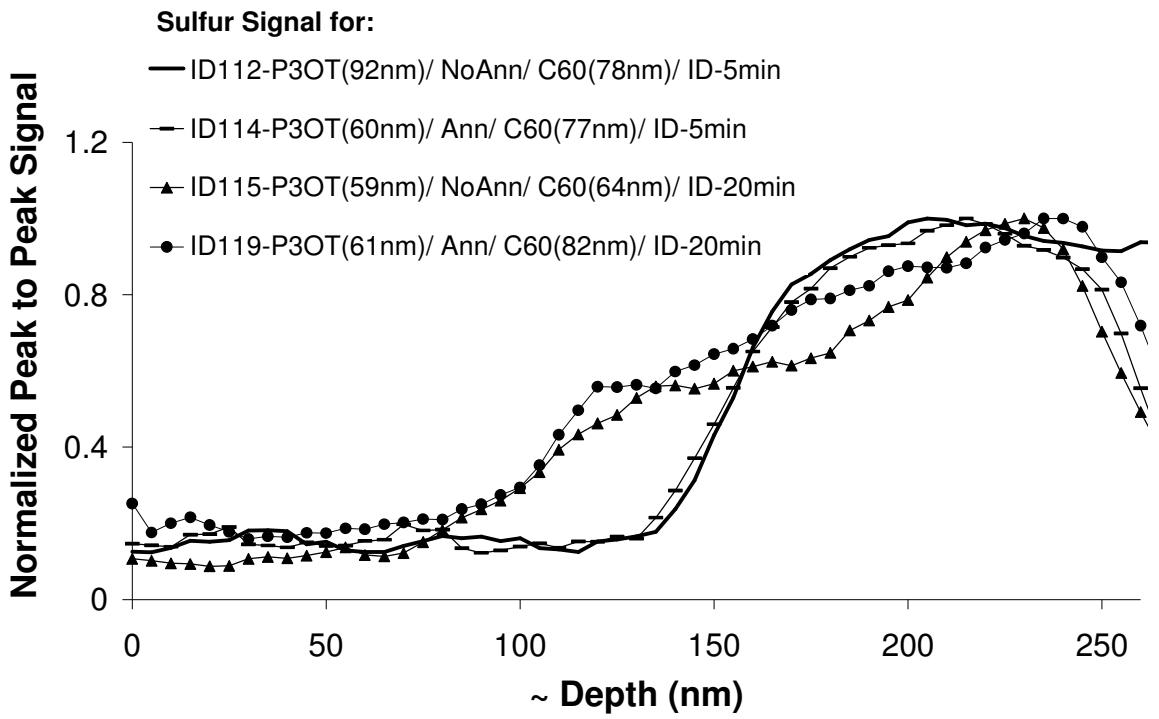

Figure 4.15 Plot of the depth profiles by Auger spectroscopy for devices of varying P3OT and C_{60} thicknesses, interdiffused under vacuum, at 135 °C, for different time spans. Device names, layer thicknesses and annealing status are given in the legend.

ID119 and ID115 were the most efficient devices and were interdiffused for 20 minutes. These demonstrated the highest EQEs and also show a concentration gradient all the way through the active layer, confirming the conclusion from the thickness dependence study on the connection between morphology and device performance. ID119 was annealed and ID115 was not. This seems to make no difference to the interdiffusion process, which looks almost identical in the Auger plots.

ID114 and ID112 were interdiffused for 5 minutes. They show a much smaller and steeper concentration gradient compared to ID119 and ID115, which explains their lower EQEs. ID112 has a thicker P3OT layer and shows a plateau of sulfur in its Auger curve, indicating a region of pure P3OT. This would explain the strong filter effect seen in the EQE curve of this device. Also, as in the previous case, the interdiffusion process is independent of the annealed status of the P3OT films; both ID114 and ID112 show similar slopes of concentration gradients and hence had similar extents of interdiffusion.

In conclusion, a concentration gradient that stretches through the entire active layer still yields the best devices. Longer interdiffusion times give rise to a larger region

of concentration gradient. Hence the ideal morphology can be achieved for thicker layer devices by interdiffusing for longer times. The effect of varying annealing conditions on the device performance is more prominent in devices interdiffused for short time scales. P3OT layer crystallinity does not appear to affect the diffusion of C_{60} into the polymer layer, but annealing the P3OT layer, prior to C_{60} deposition, improves the EQE results.

4.3.2 Effects of Varying Interdiffusion Temperature

In this section, the effects of varying interdiffusion temperature on the concentration gradient have been touched upon. These results are preliminary and are presented only as a starting point of what could be a very useful study for concentration gradient devices in the future.

Devices compared here were heated at 80 °C and 125 °C for 10 minutes in the Argon box. These devices had P3OT layers that were annealed in vacuum, prior to C_{60} deposition. During interdiffusion, the temperature was ramped up at the rate of 20 °C/min and kept steady at the final temperature for 10 minutes before being allowed to air-cool in an atmosphere of mildly flowing argon. The devices that were set to 80 °C showed an over-swing to about 92 °C and the ones heated to 125 °C over shot to 138 °C, from which the system cooled in a few minutes and stabilized at the set point for the rest of the set time. Figures 4.16a and 4.16b show the temperature versus time profile for heating at 80 °C and 125 °C respectively.

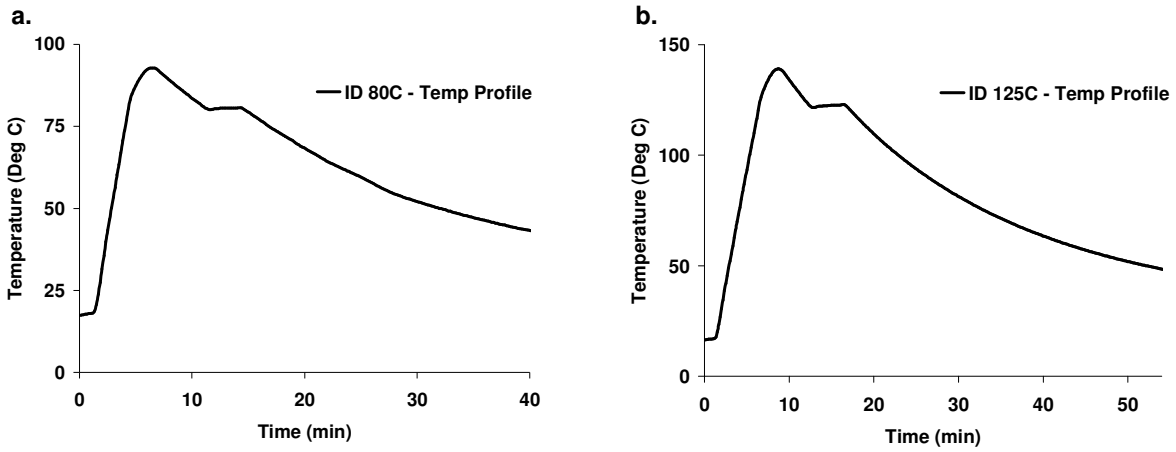

Figure 4.16 Plot of the heating and cooling temperature profile for devices interdiffused in the argon filled box for 10 minutes, at a set point of (a) 80 °C and (b) 125 °C, after which it was allowed to cool under 20 psi of flowing argon.

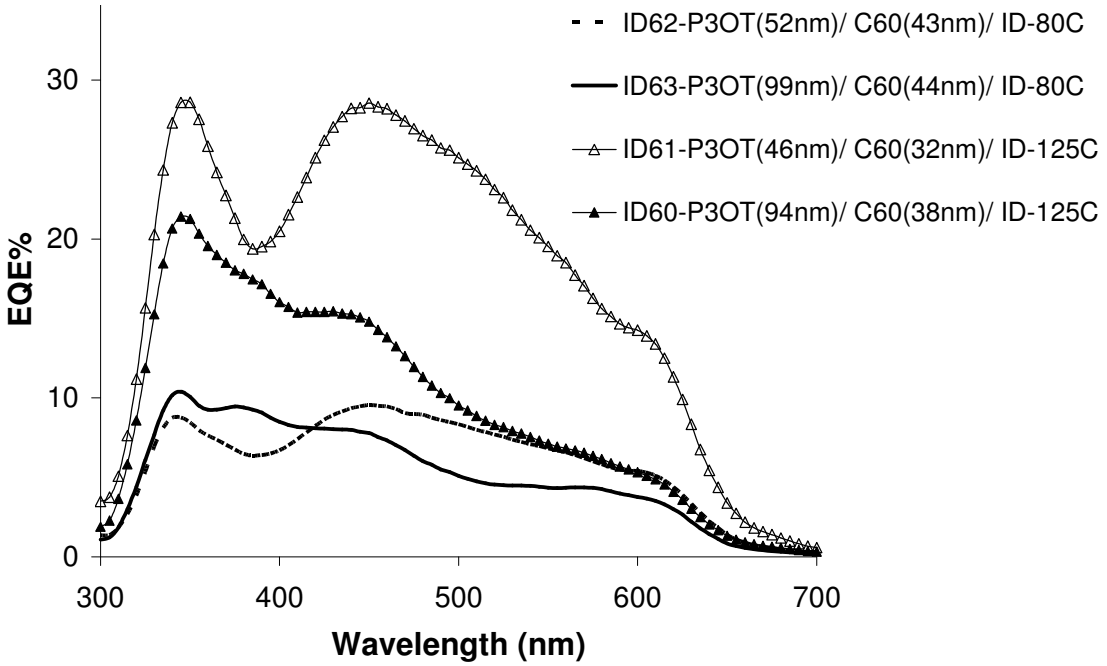

Figure 4.17 EQE curves for devices with varying P3OT layer thickness, interdiffused in the argon box for 10 minutes at 80 °C and 125 °C.

This short study was mainly done in order to see the variation in concentration gradients as the interdiffusion temperature was changed by using Auger spectroscopy. The C_{60} thickness was kept more or less constant and a thin and thick P3OT layer device was compared for each temperature. When the interdiffusion temperature was varied, we

expected to see different extents of interdiffusion, seen as different slopes for the concentration gradient in the Auger curves. We also expected the higher temperature to show more interdiffusion and hence better device performance.

Figure 4.17 shows the EQE curves for these four devices. The thickness and interdiffusion condition for each of these devices can be found in the legend of the plot. These details are also presented in Table 4.10, which also gives the summary of the photovoltaic performance for these devices. It is seen that the devices heated at 125 °C show an overall better performance as compared to the ones heated at 80 °C. Devices ID61 and ID62 both have similar layer thicknesses and hence show similar shapes of the EQE curves. But ID62, which was interdiffused at 80 °C, shows lower general performance values as compared to ID61 (interdiffused at 125 °C). Similar trends are seen for the EQE curves of devices ID63 (80 °C) and ID60 (125 °C), which also have comparable layer thicknesses. This reduction in device performance for lower interdiffusion temperatures, ties in well with the Auger concentration profiles of these devices, seen in Figure 4.18. The lower temperature, corresponding to the worse devices, also shows lesser extent of interdiffusion, confirming the requirement of a large concentration gradient for optimum device performance.

Device	**Thickness(nm)**		**ID Temp**	**Voc**	**Jsc**	**FF**	**Eff**
	P3OT	**C_{60}**	**(°C)**	**(V)**	**(mA/cm^2)**		**%**
ID62	52	43	80	0.255	-0.20	0.35	0.34
ID63	99	44	80	0.135	-0.14	0.39	0.14
ID61	46	32	125	0.235	-0.55	0.50	1.20
ID60	94	38	125	0.295	-0.25	0.51	0.71

Table 4.10 Overview of the photovoltaic performance at 470 nm of the devices under study in Figure 4.17.

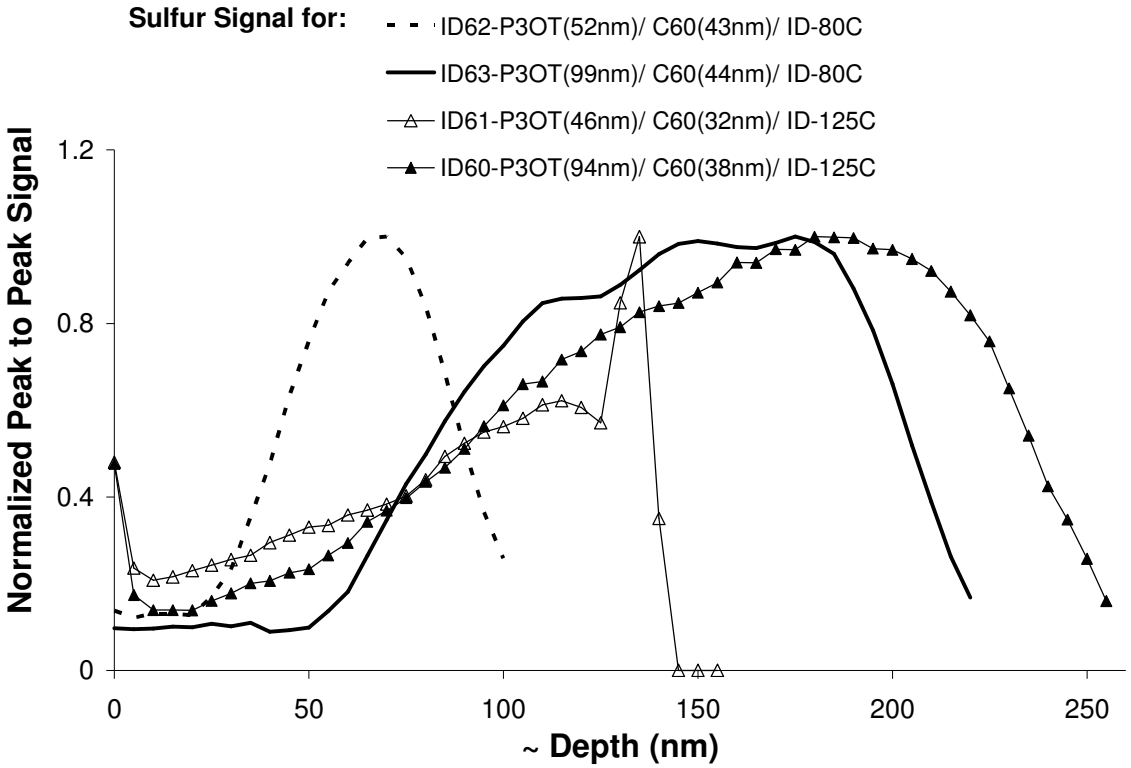

Figure 4.18 Auger spectroscopy depth profiles for devices with varying P3OT layer thickness, interdiffused for 10 minutes each, at different temperatures in the argon box. Sulfur signal indicates the presence of P3OT.

Hence, the conclusion about the most effective concentration gradient morphology still holds. Also, this concentration gradient is sensitive to interdiffusion temperature, and so the interdiffusion temperature may be varied to produce the required gradient morphology to optimize device performance.

4.4 Summary of P3OT – C_{60} Concentration Gradient Devices

Concentration gradient devices have shown considerable success for the P3OT – C_{60} system. Such devices optimize both charge transfer and transport by having a bulk heterojunction in the middle for exciton dissociation and increased paths to the electrodes for the transport of separated charges, achieved by increasing material purity as the electrodes are approached. If the gradient ends with a thin layer of pure material at each electrode, this also facilitates more efficient charge collection. Thus an ideal morphology

that would yield the best devices is one where the concentration gradient streaches through the entire active layer of the device, ending in a thin pure layer at each electrode.

These gradients can be achieved by thermal interdiffusion of an initial bilayer. For a given set of interdiffusion conditions, the starting layer thicknesses can be optimized to obtain the ideal morphology. The ideal morphology may also be achieved by controlling the interdiffusion temperatures or the interdiffusion times. Irrespective of which parameter is modified, the best devices still show the same ideal morphology, the depth profile of which was recorded using Auger spectroscopy combined with Argon-ion beam milling.

---

[1] W. Ma, *et al.*, "Thermally Stable, Efficient Polymer Solar Cells with Nanoscale Control of the Interpenetrating Network Morphology," *Adv. Funct. Mater.* **15**, 1617-1622 (2005).
[2] R.S. Ruoff, D.S. Tse, R. Malhotra, D.C. Lorents, "Solubility of C_{60} in a Variety of Solvents," *J. Chem. Phys.* **97**, 3379-3383 (1993).
[3] C. Schlebusch, B. Kessler, S. Cramm, W. Eberhardt, "Organic Photoconductors and C_{60}," *Synth. Met.* **77**, 151-154 (1996),
[4] D. Gebeyehu, *et al.*, "The Interplay of Efficiency and Morphology in Photovoltaic Devices Based on Interpenetrating Networks of Conjugated Polymers with Fullerenes," *Synth. Met.* **118**, 1-9 (2001).
[5] M. Lenes, L.J.A. Koster, V.D. Mihailetchi, P.W.M. Blom, "Thickness Dependence of the Efficiency of Polymer:Fullerene Bulk Heterojunction Solar Cells," *Appl. Phys. Lett.* **88**, 243502 (2006).
[6] L.A.A. Pettersson, L.S. Roman, O. Inganäs, "Modeling Photocurrent Action Spectra of Photovoltaic Devices Based on Organic Thin Films," *J. Appl. Phys.* **86**(1), 487-496 (1999).
[7] A.C. Arias, *et al.*, "Doped Conducting-Polymer – Semiconducting-Polymer Interfaces: Their Use in Organic Photovoltaic Devices," *Phys. Rev. B* **60**(3), 1854-1860 (1999).
[8] W.J. Work, K. Horie, M. Hess, R.F.T. Stepto, "Definitions of Terms Related to Polymer Blends, Composites, and Multiphase Polymeric Materials," *Pure Appl. Chem.* **76**(11), 1985-2007 (2004).
[9] M. Drees, R.M. Davis, J.R. Heflin, "Improved Morphology of Polymer – Fullerene Photovoltaic Devices With Thermally Induced Concentration Gradients," *J. Appl. Phys.* **97**, 036103 (2005).
[10] V.D. Mihailetchi *et al.*, "Charge Transport and Photocurrent Generation in Poly(3-hexylthiophene):Methanofullerene Bulk – Heterojunction Solar Cells," *Adv. Funct. Mater.* **16**, 699-708 (2006).

CHAPTER FIVE

P3OT Donor – PCBM Acceptor: Dual Spin-Casting of the Initial Bilayer

[6,6]-phenyl C_{61}-butyric acid methyl ester (PCBM) is a derivatized form of C_{60} whose side chain prevents close-packed aggregation, hence rendering it more soluble. A range of values have been quoted for the LUMO level PCBM going from 3.7eV[1] to 4.3eV.[2] One study from cyclic voltammetry study showed a diminished electron affinity of 0.09eV[3] and hence higher LUMO for PCBM as compared to C_{60} indicating that PCBM devices would have a higher V_{OC} as compared to C_{60} devices. PCBM is usually studied in blends, most often with poly(3-hexylthiophene), P3HT. In this thesis, it is studied as an acceptor material substitute for C_{60} in thermally interdiffused concentration gradient devices with P3OT.

In order to prepare concentration gradient devices, an initial bilayer of P3OT – PCBM was required. In early experiments, evaporation of PCBM under vacuum, like in the case of C_{60}, was attempted. This resulted in very little deposition and the remaining PCBM seemed to fuse to the quartz cuvette that was holding it. A study of this fused sample was attempted but it could not be removed or dissolved in order for it to be analyzed. It was suggested that there may be some sort of polymerization occurring with the side chains of PCBM, and it was not certain if the film obtained was still PCBM (results of this analysis, courtesy Luna nanoWorks). Hence, PCBM had to be cast from solution. A solvent had to be selected such that it would dissolve PCBM and not P3OT so it could be used to cast the PCBM layer with out dissolving off the P3OT layer below it. The organic solvent pyridine was used to make solutions of PCBM for this study.

In this chapter is presented the work done on P3OT – PCBM systems. A preliminary study was conducted to test the suitability of pyridine as a solvent for PCBM. Bilayer devices, thermally interdiffused devices and blend devices have been studied. Different thermal treatments for the interdiffused and blend devices have also been investigated, and this study has been supported by Auger spectroscopy measurements.

5.1 Preliminary Studies: Suitability of Pyridine as Solvent

While choosing a solvent for PCBM, most common solvents were found to be unsuitable since they dissolved both PCBM as well as P3OT. Such a solvent would immediately remove a thin layer of P3OT if a PCBM solution in this solvent was cast on the polymer layer. Solubility tests were conducted using various solvents, and pyridine was reported to be a good solvent for PCBM (more than 25 mg/ml) while it barely dissolved P3OT.[4] Often, materials that demonstrate low solubilities in a particular solvent may have trouble going into solution from a solid dense form. On the other hand, these same materials may dissolve much more easily if they were originally in thin film form before exposure to the solvent. This was tested for the P3OT – pyridine system prior to device fabrication. Pyridine was spin-cast at 3000 rpm on a ~60 nm P3OT film to see if this resulted in any loss of polymer.

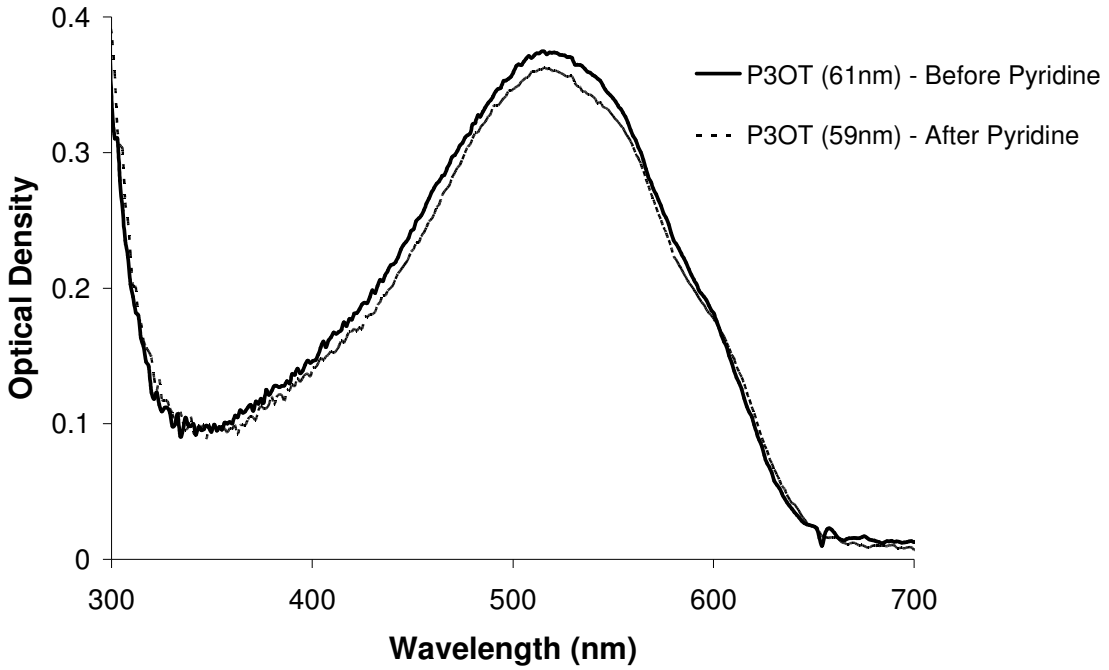

Figure 5.1 Optical densities for a P3OT film before and after pyridine was spin-coated on it, at 3000rpm. The thickness of the layer obtained for the two cases is given in the legend.

Figure 5.1 shows the optical density (OD) curves for a P3OT film measured before and after the pyridine treatment. The two curves obtained were almost identical with the

differences being within an expected error margin of the system. The calculated thickness prior to the pyridine treatment was 61 nm and after the treatment was 59 nm, which reflects a negligible loss of P3OT. While a single coating of pyridine did not affect the P3OT layer, repeated spin coating of pyridine in quick succession resulted in the polymer layer lifting off the glass substrate, after more than 3 to 4 coats. Hence, even if there is no dissolution, prolonged exposure to pyridine might swell the polymer. For temporary exposure, this solvent would allow for the fabrication of P3OT – PCBM bilayers without damaging the P3OT layer.

5.2 Bilayers and Heated Devices

Bilayers were fabricated by spin coating P3OT, dissolved in chloroform, onto ITO-coated glass that had an initial layer of PEDT:PSS. This layer was annealed at 120 °C for over 35 minutes under vacuum after which PCBM dissolved in pyridine was cast on top of this layer. Although PCBM was fairly soluble in pyridine, it should be noted that the solutions prepared were slightly murky, indicating that complete dissolution was not obtained. All the same they were stable and when left standing for a few days there was no precipitation observed. This solution did not seem to wet the surface well, resulting in blotchy films with macroscopic regions that appeared to have no PCBM. To improve the film quality, the P3OT film was first washed with pyridine by dropping a few drops on the film spun at 3000 to 3500 rpm. The PCBM was then spin cast from a 1% wt/vol solution in pyridine on the P3OT while spinning at 3000 rpm. A thin layer of pyridine helps the PCBM solution wet the P3OT surface better to give a uniform PCBM film. To fabricate the heated devices, these bilayers were then heated for 5 minutes at 118 °C (over-swing to 134 °C) in the argon box and allowed to ambient-cool. Since this is the first time thermal interdiffusion is being studied for P3OT – PCBM, this study was conducted in order to test for the presence of thermally induced concentration gradients. The PCBM layer thickness was varied in the range 33 to 64 nm and the effect of varying the P3OT layer thickness was studied.

Figure 5.2a shows the EQE curves and Figure 5.2b shows the 4^{th} quadrant J-V curves measured under 470 nm illumination obtained for bilayer devices with P3OT

thicknesses varying within a 50 nm to 100 nm range. Table 5.1 gives an overview of the performance of these devices, also under 470 nm illumination.

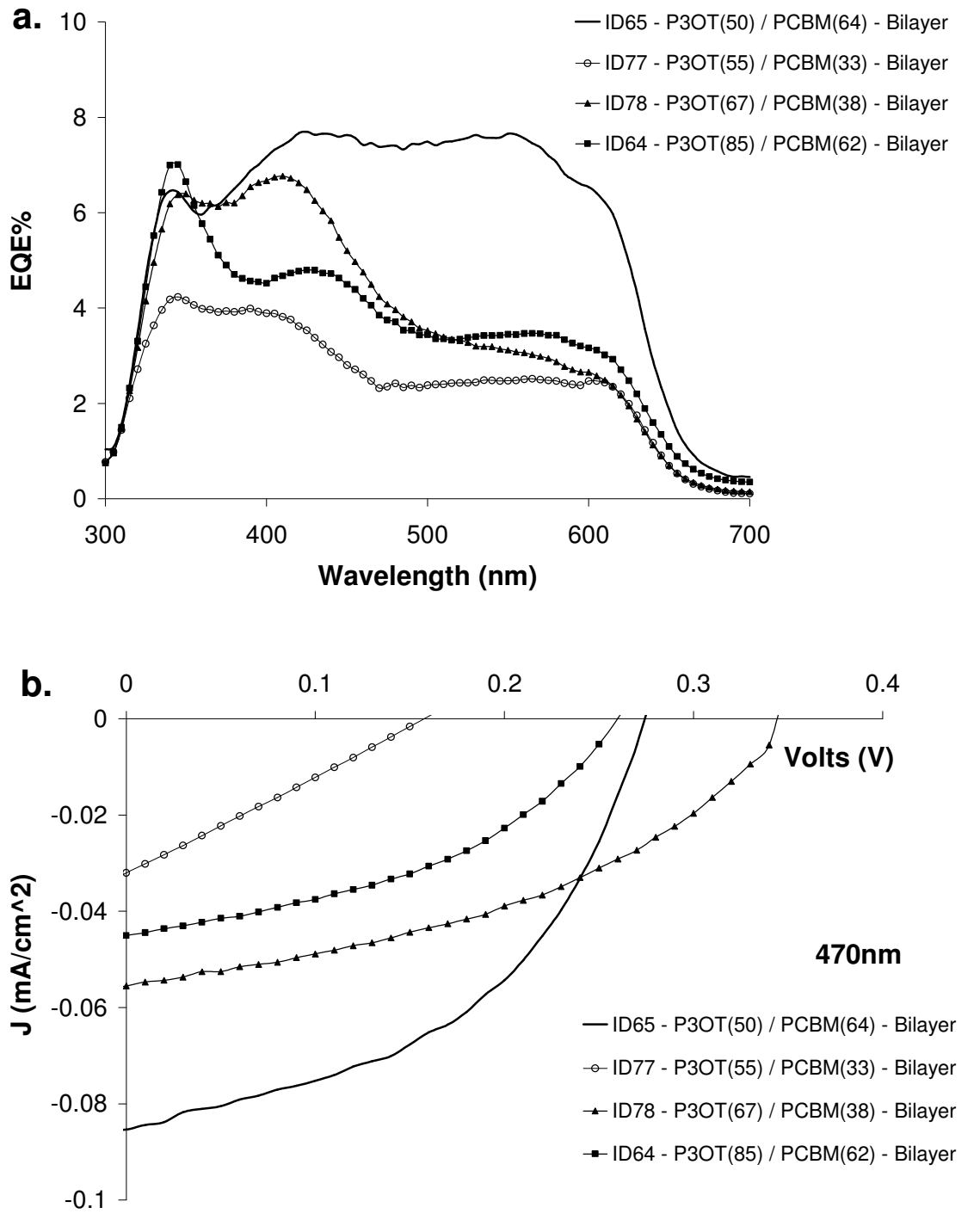

Figure 5.2 (a) EQE and (b) 470 nm illumination, 4th quadrant J-V characteristics for P3OT – PCBM bilayer devices with varying layer thicknesses.

Device	Thickness(nm)		Voc	Jsc	FF	Eff
	P3OT	PCBM	(V)	(mA/cm^2)		(%)
ID65	50	64	0.275	-0.09	0.47	0.35
ID77	55	33	0.155	-0.03	0.24	0.04
ID78	67	38	0.345	-0.06	0.42	0.23
ID64	85	62	0.255	-0.05	0.43	0.16

Table 5.1 Overview of the photovoltaic performance at 470 nm of the devices presented in Figure 5.2.

The peak at 350 nm, which corresponds to an absorption peak in the OD spectrum of PCBM (Figure 3.22b), is fairly constant for all the devices except in ID77. This indicates a relatively constant value for the density of the P3OT – PCBM interfaces that would act as dissociation sites for excitons formed by light absorption in PCBM. The thick P3OT device (ID64) shows the filter effect, seen as a dip in the EQE spectrum near 500 nm, consistent with the presence of a thick pure P3OT layer in the film. As the P3OT layer gets thinner, the filter effect is reduced considerably for ID65, which has a 50 nm thick P3OT layer. The short-circuit current densities (J_{SC}) show a similar trend in Figure 5.2b whereas the V_{OC} values do not follow a pattern and are all located within a 0.1 eV range around 0.3 eV.

Figures 5.3a and 5.3b shows the EQE curves and the 470 nm illumination - 4^{th} quadrant J-V curves obtained for heated devices with constant PCBM thicknesses and varying P3OT thicknesses. Table 5.2 gives an overview of the performance of these devices, also under 470 nm illumination. In these devices, the P3OT thickness was varied from 35 nm to 62 nm. The thicker P3OT device (ID76) shows the lowest EQE and also demonstrates the filter effect. It also has the thinnest PCBM layer. These two factors result in that device having the lowest efficiency. As the P3OT layer gets thinner, the EQEs go up and the filter effect is reduced. As in the bilayer case from the previous figure, the J_{SC} values show a similar trend as the EQEs while the V_{OC} values do not show any clear trend.

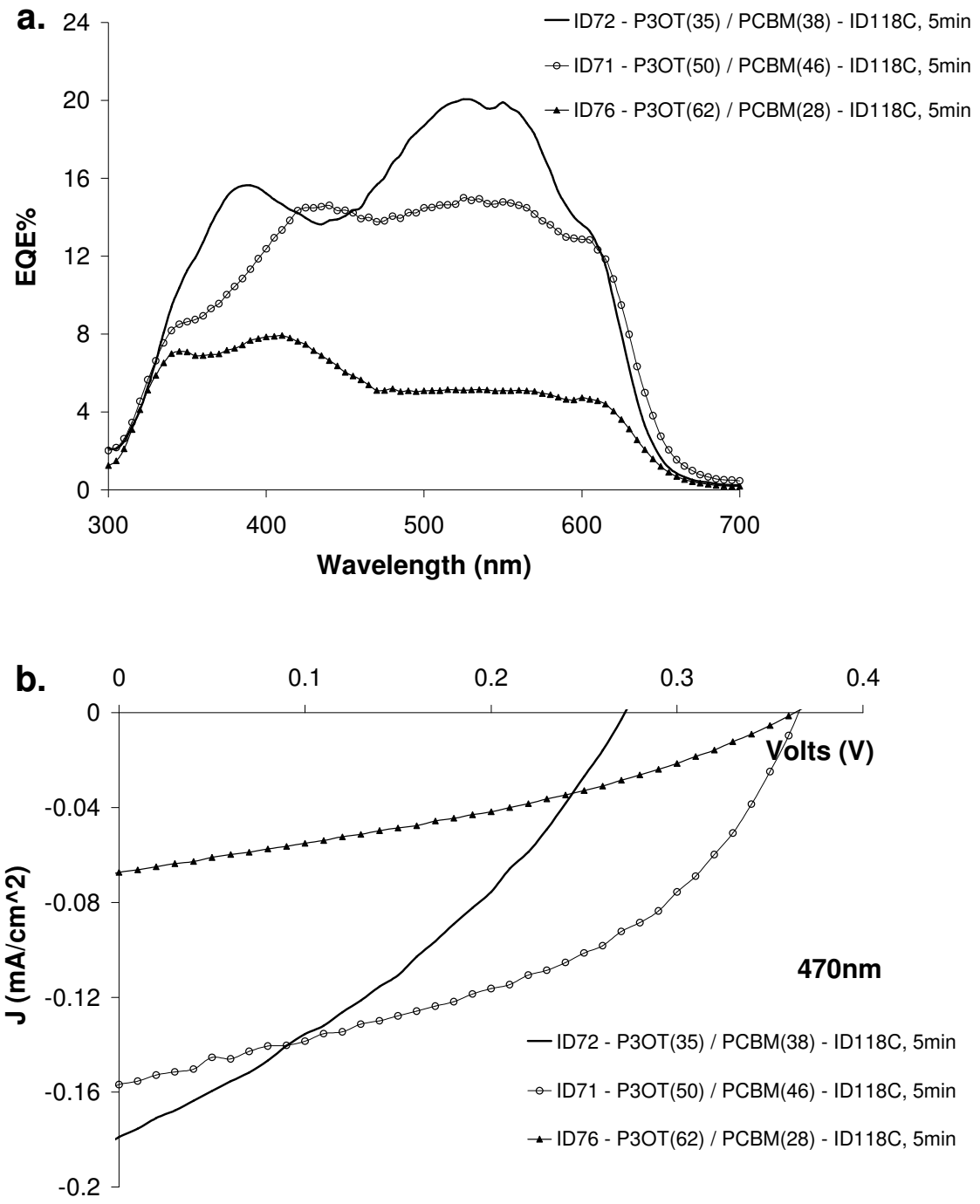

Figure 5.3 (a) EQE and (b) 470 nm illumination, 4th quadrant J-V characteristics for P3OT – PCBM devices heated at 118 °C for 5 minutes in the argon box.

Device	Thickness(nm)		Voc	Jsc	FF	Eff
	P3OT	PCBM	(V)	(mA/cm^2)		(%)
ID72G	35	38	0.275	-0.18	0.34	0.54
ID71G	50	46	0.365	-0.16	0.45	0.83
ID76G	62	28	0.365	-0.67	0.34	0.24

Table 5.2 Overview of the photovoltaic performance at 470 nm of the devices presented in Figure 5.3.

When the bilayer and interdiffused devices are compared, a varied trend is seen for the given heating conditions. When comparing the bilayer device ID65 (P3OT: 49 nm) with the heated device ID71 (P3OT: 48 nm), over a factor of 2 improvement is seen in the EQE values and the V_{OC} goes up by 0.1 eV for the heated device. This was expected since ID71 had been heated and had probably undergone thermal interdiffusion. When comparing the heated device ID76 (P3OT: 62 nm) and the bilayer device ID78 (P3OT: 63 nm), the curves seem almost identical, inspite of the heating step for ID76. However, ID76 has a thinner PCBM layer and this may counter the effect of improved interdiffusion. The J-V curves too are almost identical, except for a marginally higher V_{OC} for ID76. Auger spectroscopy measurements were taken for these two devices in order to compare their morphologies. (When these devices were fabricated, each slide had a portion that was reserved for Auger spectroscopy measurements where the PEDT:PSS layer was removed and no Al electrodes were deposited). The Auger curves obtained are shown in Figure 5.4.

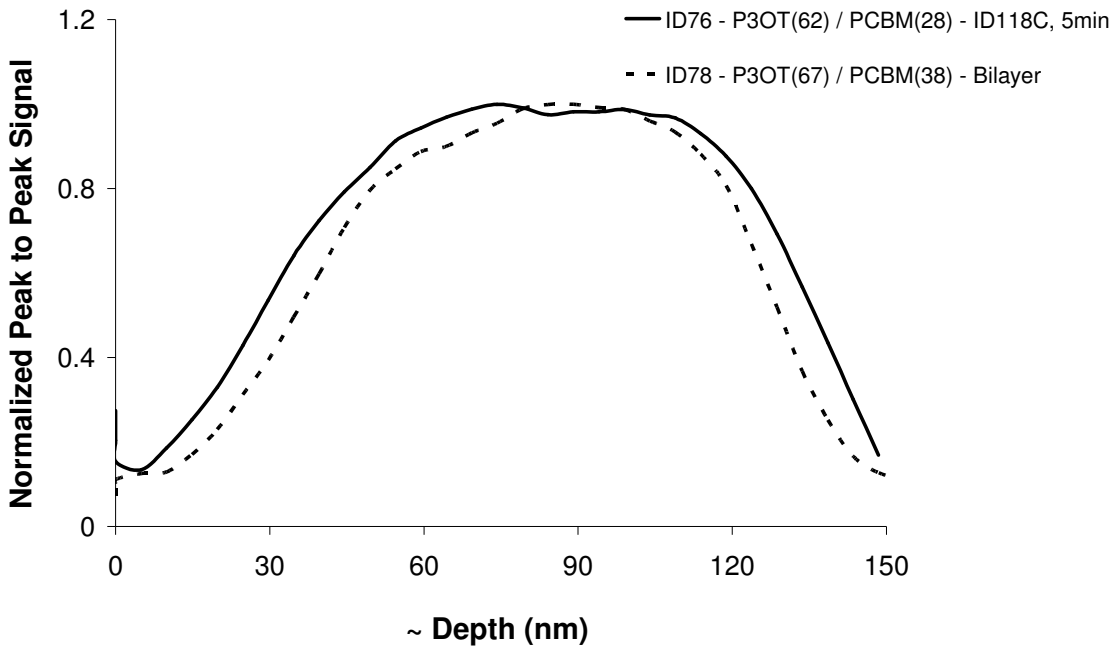

Figure 5.4 Plot of the depth profiles by Auger spectroscopy for the bilayer device and a heated device. The approximate depth into the film is given on the x-axis while the y-axis is the peak to peak signal intensity normalized to one.

The depth profiles for the bilayer and heated devices look quite similar which would explain why their photovoltaic measurements were so similar. This seems to indicate that the heating step at 118 °C for 5 minutes was not sufficient to really change the bilayer morphology for these two devices. Both the devices seem to show concentration gradients which seems to have been formed during the bilayer fabrication step, which is independent of the heating step. However, ID76 does show the effect of the thinner PCBM layer, which results in a pile-up of P3OT at the edge of the PCBM layer. One possible explanation for the similar concentration profiles is that the pyridine wetting step that was done in order to obtain uniform films of PCBM, swells the polymer and induces interdiffusion. Such concentration gradients have been reported to occur in the presence of a solvent.[5] The heat supplied was probably high enough to ensure that the solvent evaporated but still too low to induce interdiffusion for this system of materials. Overall, the studies in this section support the conclusion that thermally-induced interdiffusion can improve the photovoltaic efficiency of P3OT – PCBM bilayers formed by sequential spin-casting steps.

5.3 Varying Interdiffusion Conditions

In order to observe a better concentration gradient, the interdiffusion temperature was increased to 150 °C for 10 minutes. The P3OT was not initially annealed under the assumption that annealed P3OT would have more crystalline regions that would hinder the PCBM diffusion into the polymer, though we later determine that this is not the case. Similar work, done on the P3OT – C_{60} system at around the same time (presented in section 4.3) has shown that annealing the polymer is advantageous to the device performance. It was also shown that the difference between annealed and non-annealed devices reduces as the interdiffusion temperature increases. Hence more work needs to be done along these lines in order to see which fabrication procedure would yield better devices.

The heating step was done under vacuum in order to minimize the exposure of the sample to air. Two variations were studied in this fabrication procedure. In one case, the bilayer was heated prior to Al electrode deposition as had been done so far. In the other case, the heat treatment was done after Al deposition following the post production treatment procedure suggested for P3HT – PCBM blends, in order to improve the charge collection interface at the aluminum electrode.[6]

In this study, both the P3OT and C_{60} layer thicknesses were intended to be kept constant in order to better judge the difference in device output for the pre and post Al deposition heat treatments. Due to the increased heating step temperature, we believed that interdiffusion would occur to a greater extent as compared to the 118 °C heating step devices. The thickness of the PCBM layer was increased to about 55 nm (cast from a 2% wt/vol solution in pyridine) and the P3OT thickness was maintained between 60 nm to 70 nm.

Figures 5.5a and 5.5b shows the EQE curves and the 470 nm illumination - 4th quadrant J-V curves obtained for heated devices with constant PCBM thicknesses and varying P3OT thicknesses. Devices ID 135 and ID152 were heated after Al deposition while the rest were heated before. At this point of time, a solar simulator, calibrated to AM1.5 illumination intensity, was set up. Figure 5.5c gives the 4th quadrant J-V curves

measured under AM1.5 illumination. Tables 5.3a and 5.3b give an overview of the performance of these devices under 470nm and AM1.5 illumination respectively.

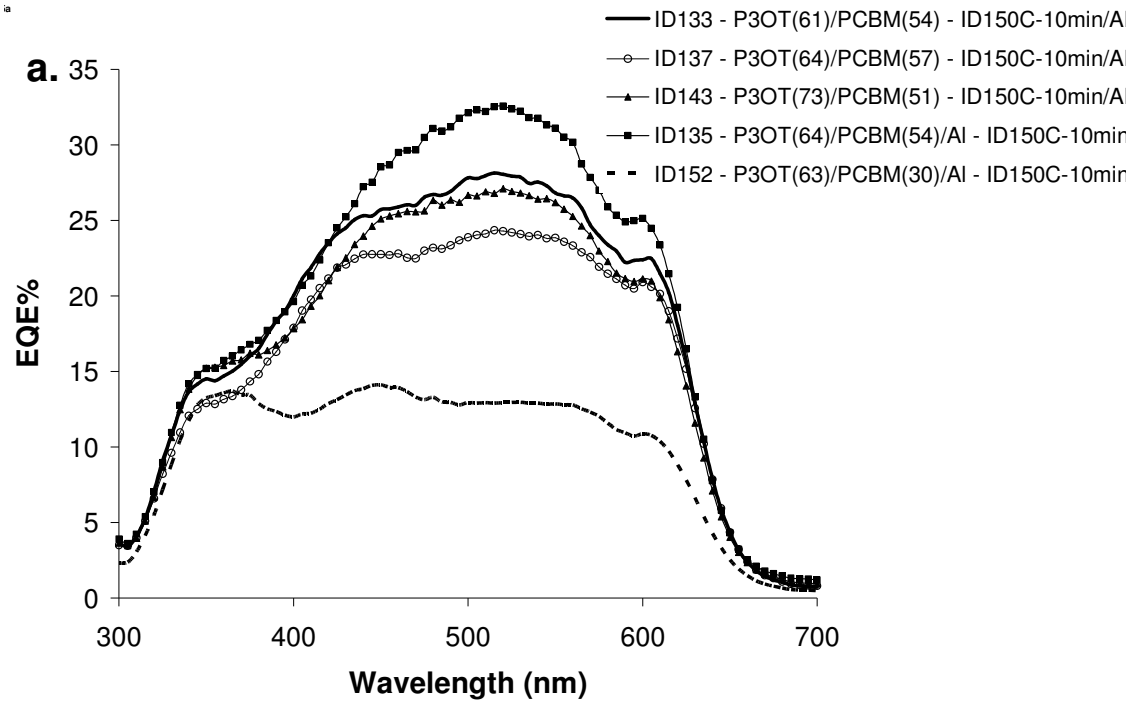

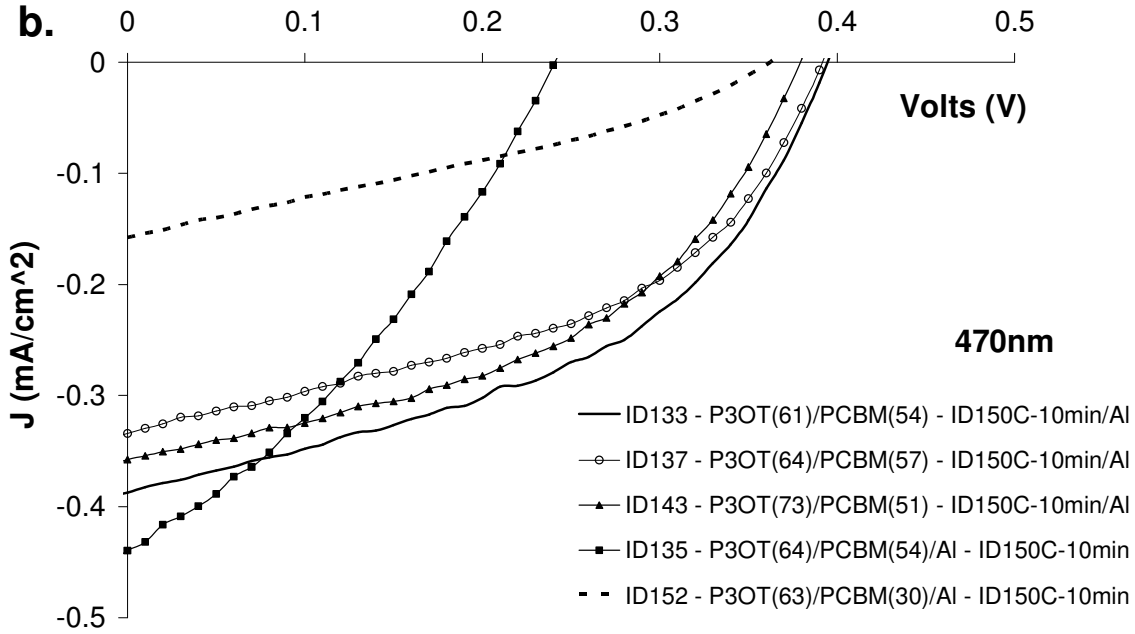

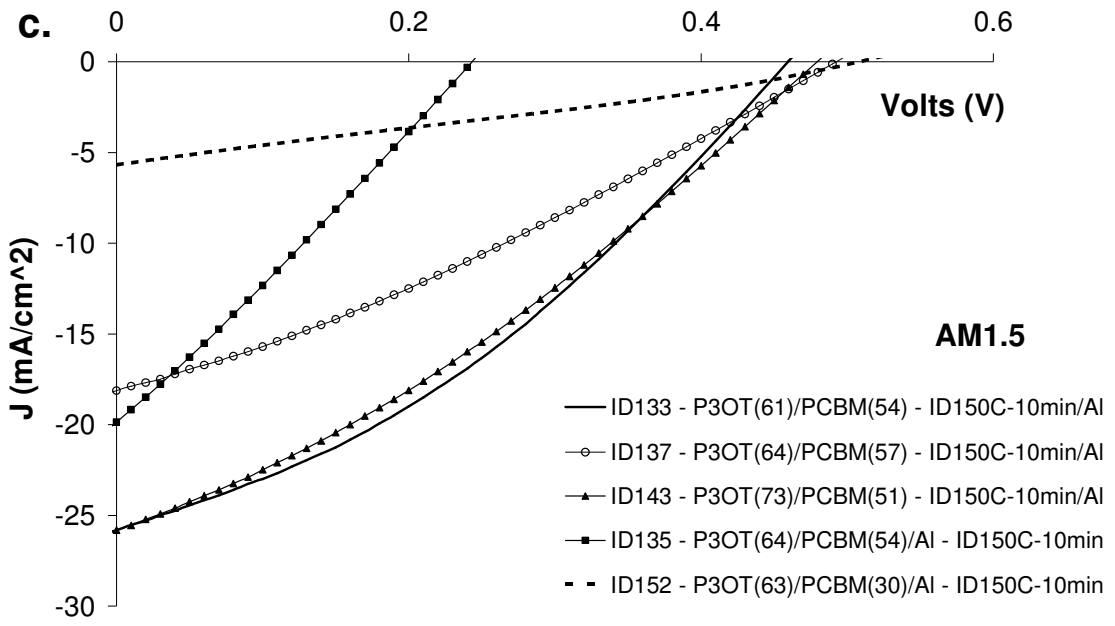

Figure 5.5 (a) EQE and (b) 470 nm illumination and (c) AM1.5 illumination 4th quadrant J-V characteristics for P3OT – PCBM devices heated at 150 °C for 10 minutes under vacuum.

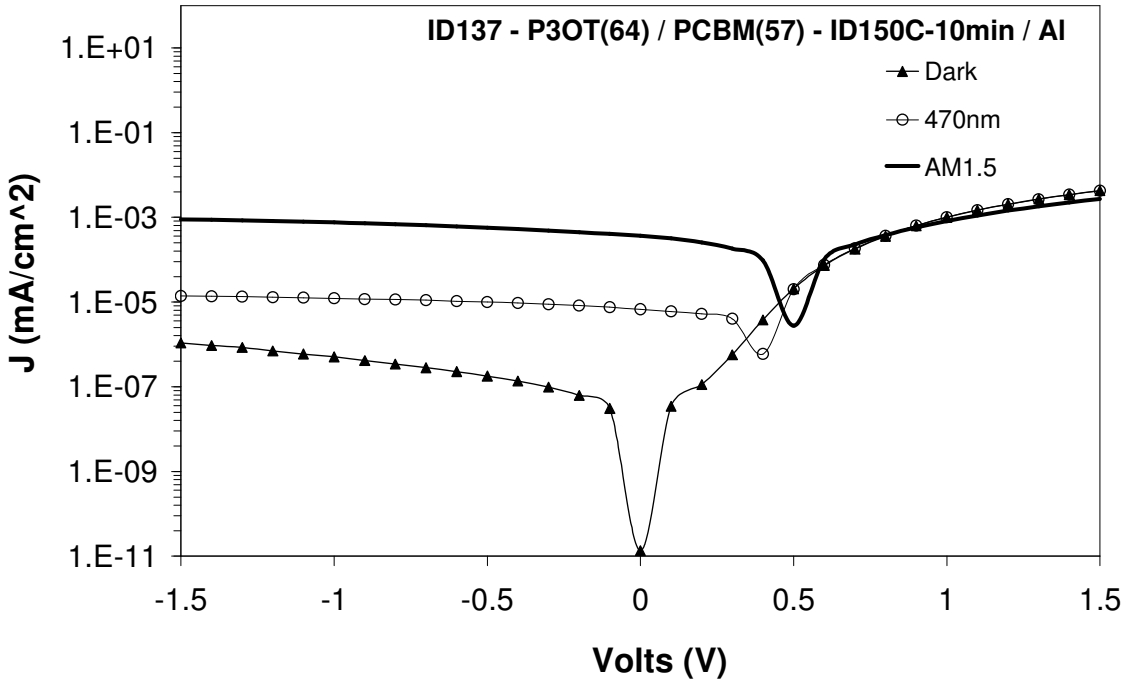

Figure 5.6 Semi-log plot of the J-V characteristics in the dark and under 470 nm and AM1.5 illumination. Rectification (difference between the two asymptotes) in the dark gives the diode quality of the device.

(A) Device	Thickness(nm)		Voc	Jsc	FF	Eff
470 nm	**P3OT**	**PCBM**	**(V)**	**(mA/cm^2)**		**(%)**
ID133B	61	54	0.395	-0.39	0.46	1.75
ID137B	65	57	0.395	-0.33	0.46	1.5
ID143G	73	51	0.375	-0.36	0.46	1.62
ID135A	64	54	0.245	-0.44	0.33	0.88
ID152A	63	30	0.365	-0.16	0.31	0.47

(B) Device	Thickness(nm)		Voc	Jsc	FF	Eff
AM1.5	**P3OT**	**PCBM**	**(V)**	**(mA/cm^2)**		**(%)**
ID133B	61	54	0.455	-25.8	0.35	0.54
ID137B	65	57	0.495	-18.1	0.3	0.35
ID143G	73	51	0.475	-25.8	0.32	0.43
ID135A	64	54	0.245	-19.9	0.26	0.17
ID152A	63	30	0.505	-5.7	0.28	0.14

Table 5.3 Overview of the photovoltaic performance of the devices presented in Figures 5.5 and 5.6. (A) is for 470 nm illumination and (B) is for AM1.5 illumination.

An overall improvement by an order of almost 1.5 to 2 times is seen in the EQEs for these devices as compared to those of similar P3OT thickness heated at 118 °C. Devices that were heated prior to Al deposition (ID133, ID137 and ID143) show higher efficiencies under both 470 nm and AM1.5 illumination. Figure 5.6 gives the J-V curves plotted on a semi-log plot for device ID137, showing the IV curves obtained in the dark and under 470nm and AM1.5 illumination. The rectification gives an idea of the diode like quality of the device. This device shows rectification of around 3.5 orders of magnitude in the dark, indicating a good quality device, although the rectification reduces under illumination. ID135 and ID152 were processed similarly with the heating step being performed after the Al deposition. These devices show inconsistent EQE and J-V characteristic behavior as seen in Figures 5.5a, 5.5b and 5.5c respectively. ID135 shows the best EQE values and ID152, the worst but ID135 has a very low V_{OC} compared to ID152. Auger spectroscopy studies were carried out on a few representative devices and

the curves obtained are shown in Figure 5.7. ID137 and ID135 show more interdiffusion than did the samples heated at 118 °C. In fact, as expected they also show a start of a pile-up of sulfur at the PCBM – air interface that happens when heating is carried out beyond the time required for complete interdiffusion. Blooming of P3OT at the air interface may explain this pile-up. The increased temperature conditions did improve the concentration gradient and hence the device performance. ID152 shows a smaller region of interdiffusion as compared to ID135. It is not clear why this happened since they were both subjected to the same fabrication procedure and ID152 has a significantly thinner PCBM layer. Nevertheless the photovoltaic measurements obtained are consistent with the concentration profile observed for ID152.

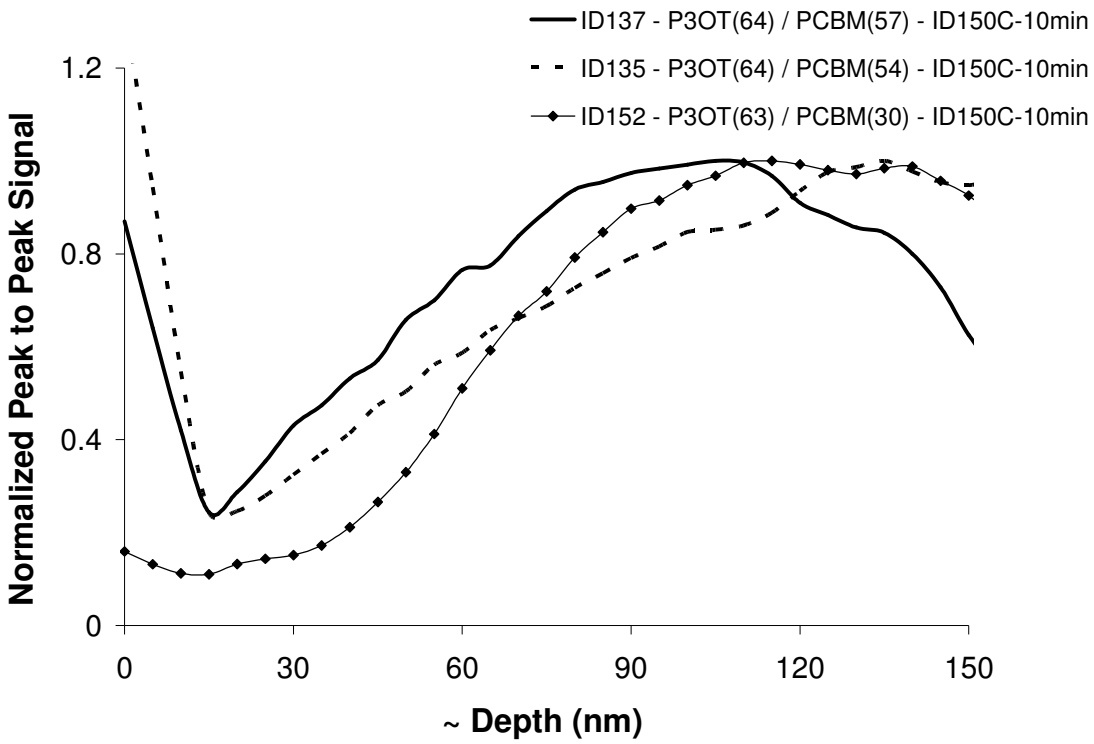

Figure 5.7 Plot of the depth profiles by Auger spectroscopy for various devices interdiffused at 150 °C for 10 minutes.

5.4 Blend Devices

In addition to thermally interdiffused devices, blend devices have also been investigated for the P3OT – PCBM system, for the sake of comparison. Blend solutions

were fabricated by dissolving P3OT and PCBM together in chloroform and spin-coating this at 2000 rpm on the PEDT:PSS layer. 1:1 and 1:2 P3OT : PCBM ratio blend devices were studied. The 1:1 solution was prepared by dissolving 0.010 g P3OT and 0.010 g PCBM, in 1.0 ml chloroform to give a net 2% wt/vol solution. The 1:2 solution was prepared by dissolving 0.0086 g P3OT and 0.0167 g PCBM in 1.0 ml chloroform to give a net 2.5% wt/vol solution. PCBM seemed less viscous than P3OT in solution so as the relative concentration of PCBM was increased the net concentration of the solution was also increased to 2.5%. Early blend devices were measured immediately after casting and Al electrode deposition. Subsequently, post production treatment of heating the blend to 150 °C for 25 minutes after Al deposition was carried out. This heat treatment was done in the vacuum chamber.

Figure 5.8a and 5.8b show the EQE curves and the 4^{th} quadrant J-V curves under 470 nm illumination, respectively, for a set of unheated and heated 1:1 blend devices. AM1.5 measurements are only available for ID153 and are shown on a semi-log plot in Figure 5.8c. The highest EQEs were obtained for an annealed blend (ID153) device but the highest monochromatic efficiency was obtained for a non-annealed blend (ID34). No real pattern of improvement was seen for either fabrication procedure. On the other hand, there is such a variation in device thickness that it would be difficult to discern a trend anyway. While the EQEs are roughly 5 to 10% higher than for the interdiffused (150 °C for 10 minutes) devices, the blends show an overall significant improvement in the monochromatic efficiency at 470 nm, as seen in Table5.4. But the disadvantage of the blend devices was inconsistency in performance. Four out of the five devices presented show good device performance. ID93, which was also subjected to post-production treatment, showed bubbly Al electrodes on all the devices on the substrate. This was regularly observed for devices that were subjected to post-production heat treatment. In fact, out of the four devices measured on ID153, two gave the highest EQEs while the other two were completely shorted.

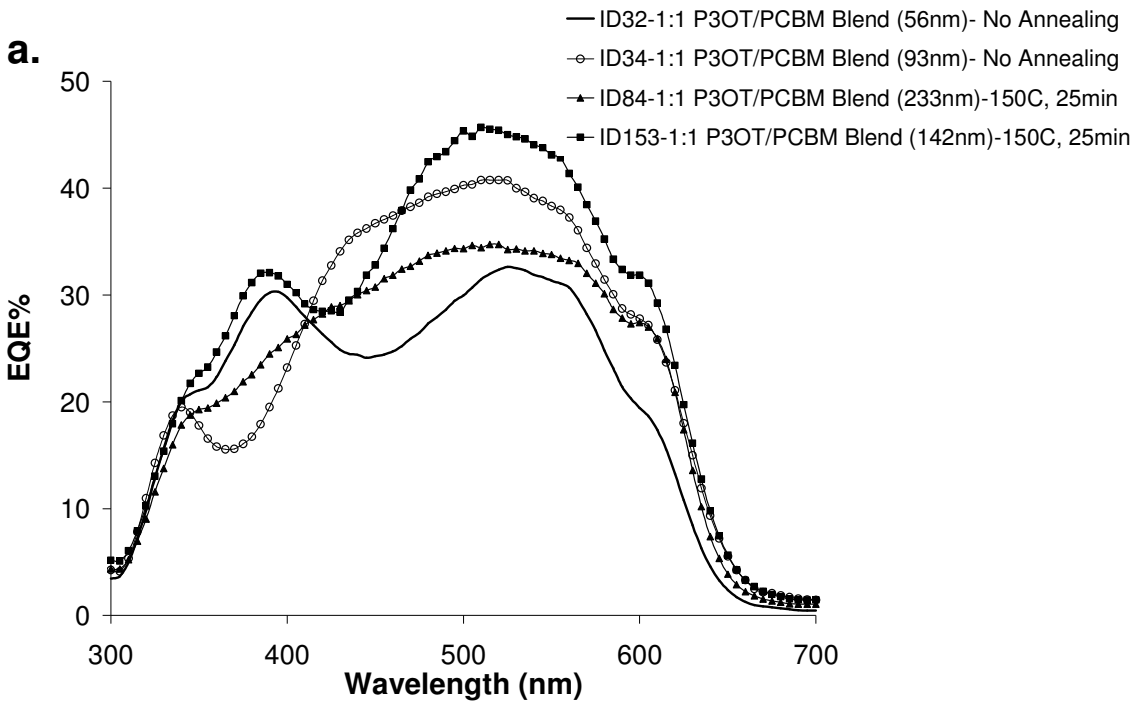
a.
ID32-1:1 P3OT/PCBM Blend (56nm)- No Annealing
ID34-1:1 P3OT/PCBM Blend (93nm)- No Annealing
ID84-1:1 P3OT/PCBM Blend (233nm)-150C, 25min
ID153-1:1 P3OT/PCBM Blend (142nm)-150C, 25min
EQE%
Wavelength (nm)

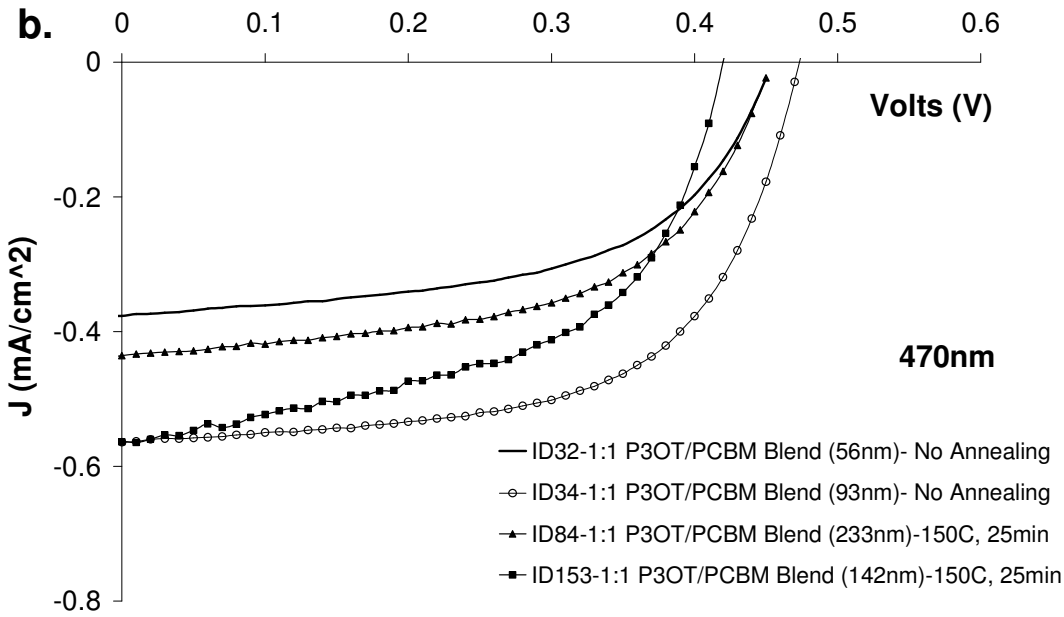
b.
Volts (V)
J (mA/cm^2)
470nm
ID32-1:1 P3OT/PCBM Blend (56nm)- No Annealing
ID34-1:1 P3OT/PCBM Blend (93nm)- No Annealing
ID84-1:1 P3OT/PCBM Blend (233nm)-150C, 25min
ID153-1:1 P3OT/PCBM Blend (142nm)-150C, 25min

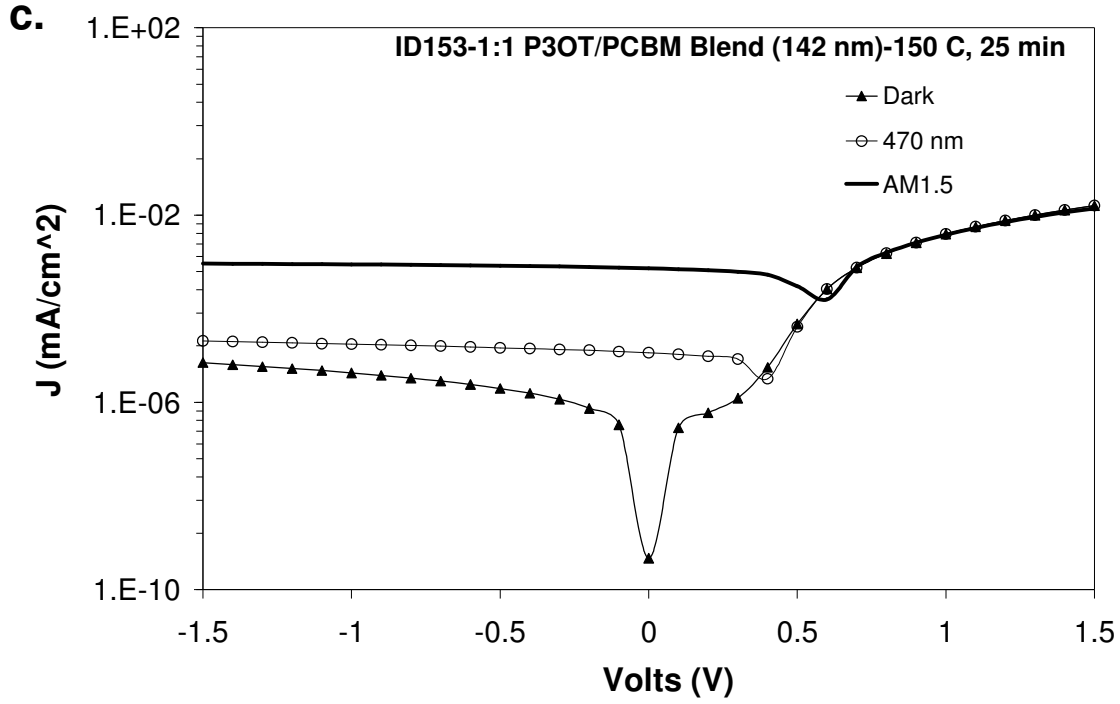

Figure 5.8 (a) EQE and (b) 470 nm illumination, 4th quadrant J-V characteristics for P3OT – PCBM 1:1 blend devices, either not annealed or annealed at 150 °C for 25 minutes after Al deposition, under vacuum. (c) semi-log plot of the J-V characteristics in the dark and under 470 nm and AM1.5 illumination for ID153.

Device	Thickness(nm)	Voc	Jsc	FF	Eff
	P3OT/PCBM (1:1 Blend)	(V)	(mA/cm^2)		(%)
ID32A (470 nm)	56	0.455	-0.38	0.55	2.45
ID34A (470 nm)	93	0.475	-0.56	0.6	4.17
ID84B (470 nm)	233	0.455	-0.44	0.56	3.14
ID153H (470 nm)	142	0.415	-0.56	0.54	3.29
ID153H (AM1.5)	142	0.575	-36	0.51	1.39

Table 5.4 Overview of the photovoltaic performance of the devices presented in Figure 5.8 for 470 nm illumination and AM1.5 illumination when applicable.

Figure 5.9a and 5.9b show the EQE curves and the 4th quadrant J-V curves under 470 nm illumination, respectively, for examples of unheated and heated 1:2 blend devices and Table 5.5 gives an overview of the performance of these devices under 470 nm illumination and AM1.5 illumination when available. These devices show marginally lower EQEs and considerably lower monochromatic efficiencies as compared to the 1:1 blends that were similarly prepared. The post production treatment was also less successful in these devices than in the 1:1 blends, and it showed damaged Al electrodes for most of the devices. ID155 is an example of one such device. It seems to have respectable EQEs but the J-V curves indicate that the device is pretty much shorted. In order to reduce the risk of device damage, the heat treatment was reduced to 150 °C for just 10 minutes (device ID156). AM1.5 measurements for ID156 are shown on a semi-log plot in Figure 5.9c.

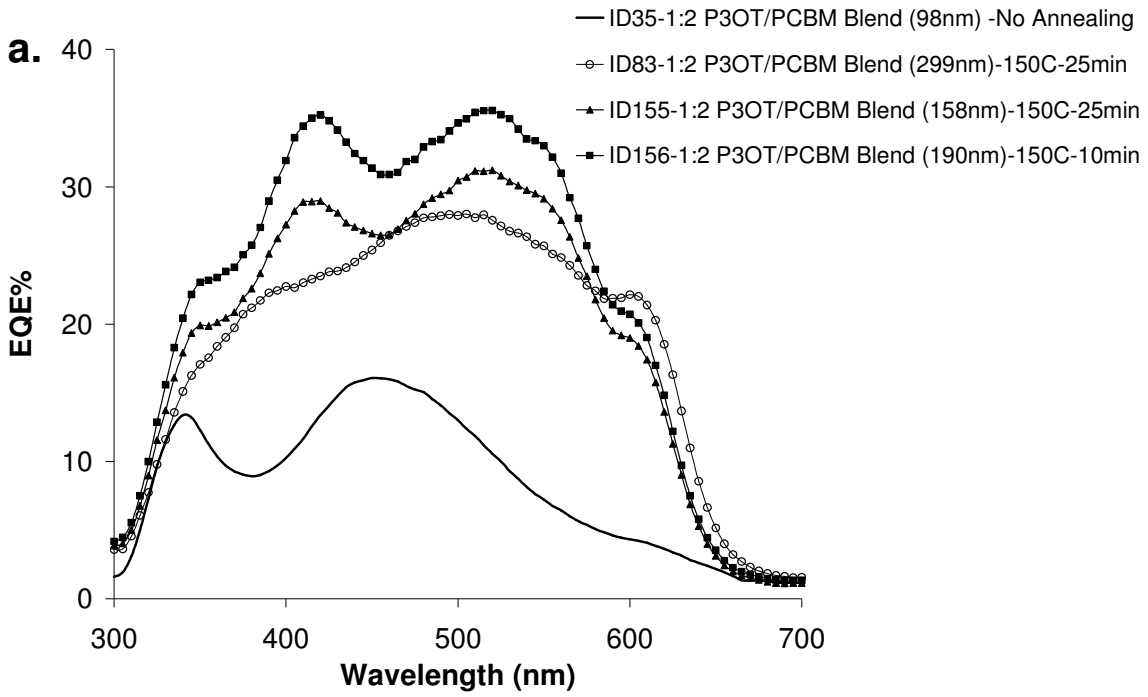

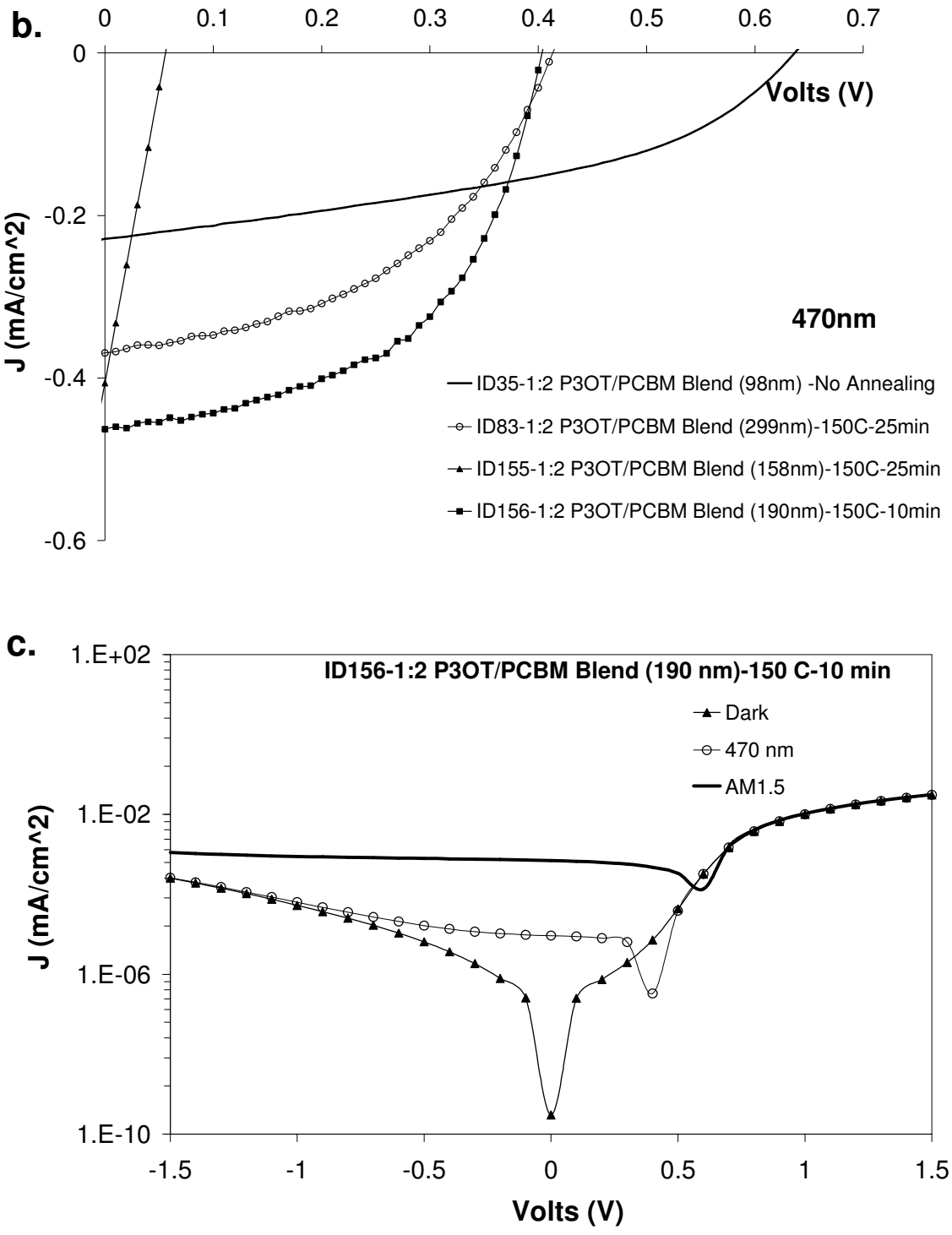

Figure 5.9 (a) EQE and (b) 470 nm illumination, 4th quadrant J-V characteristics for P3OT – PCBM 1:2 blend devices, either not annealed or annealed at 150 °C for 10 minutes after Al deposition, under vacuum. (c) semi-log plot of the J-V characteristics in the dark and under 470 nm and AM1.5 illumination for device ID156.

Device	Thickness(nm)	Voc	Jsc	FF	Eff
	P3OT/PCBM (1:2 Blend)	(V)	(mA/cm^2)		(%)
ID35E (470 nm)	98	0.635	-0.23	0.43	1.61
ID83G (470 nm)	299	0.415	-0.37	0.46	1.98
ID155B (470 nm)	158	0.055	-0.41	0.28	0.15
ID156G (470 nm)	190	0.405	-0.46	0.53	2.57
ID155B (AM1.5)	158	0.565	-19.8	0.27	0.4
ID156G (AM1.5)	190	0.585	-34.9	0.46	1.05

Table 5.5 Overview of the photovoltaic performance of the devices presented in Figure 5.9 for 470 nm illumination and AM1.5 illumination when applicable.

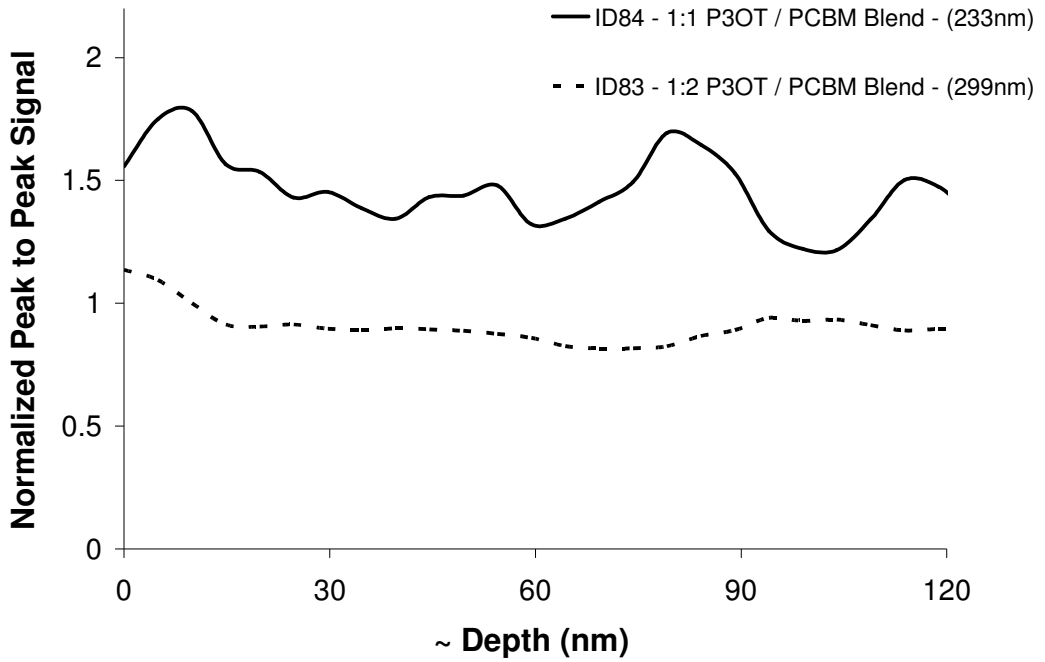

Figure 5.10 Plot of the depth profiles by Auger spectroscopy for 1:1 and 1:2 P3OT – PCBM blend devices, annealed after Al deposition at 150 °C for 25 minutes.

Figure 5.10 shows the Auger spectroscopy depth profiles for these blends after heat treatment. This was done so as to see if the heat treatment produced any macroscopic

trends in the compositional morphology of the devices. Both the 1:1 and the 1:2 blends show a random, constant sulfur content throughout the film as would be expected from a homogeneous mixture of P3OT and PCBM.

5.5 Concluding Remarks: P3OT - PCBM

This was a preliminary study to investigate PCBM as an acceptor in thermally interdiffused concentration gradient devices. PCBM does seem to be a suitable acceptor for such devices. It shows a higher V_{OC} than did C_{60} and it is solution processable, which makes device fabrication easier and quicker. This preliminary study has revealed some interesting factors that require further investigation. For the case of devices heated from a bilayer to produce interdiffusion, the PCBM films cast from pyridine solutions were slightly murky. This might be indicative of aggregation and hence might be a factor that hinders interdiffusion. It is also not yet clear whether or not annealing the P3OT layer prior to PCBM deposition helped improve the device performance. Also, heating the sample after Al deposition leads to inconsistent behavior in both heated bilayers and blend devices. This could be due to the increased risk of pin hole shorts and device damage. Hence, the method post-production heat treatment to improve the photovoltaic performance requires more study. Investigation into these factors and optimization of the interdiffusion parameters would make PCBM a promising solution – processable alternative for C_{60} in thermally induced concentration gradient devices.

---

[1] V.D. Mihailetchi, P.W.M. Blom, J.C. Hummelen, M.T. Rispens, "Cathode Dependence of the Open – Circuit Voltage of Polymer:Fullerene Bulk Heterojunction Solar Cells," *J. Appl. Phys.* **94**(10), 6849-6854 (2003).
[2] C. Lungenschmied, *et al.*, "Internal Electric Field in Organic-Semiconductor-based Photovoltaic Devices," *Appl. Phys. Lett.* **89**, 223519 (2006).
[3] C.J. Brabec, *et al.*, "Origin of Open Circuit Voltage of Plastic Solar Cells," *Adv. Funct. Mater.* **11**(5), 374-380 (2001).
[4] Private communication from Luna nanoWorks, Danville, VA.
[5] C.J. Brabec, *et al.*, "The Influence of Materials Work Function on the Open Circuit Voltage of Plastic Solar Cells," *Thin Solid Films* **403-404**, 368-372 (2002).
[6] W. Ma, *et al.*, "Thermally Stable, Efficient Polymer Solar Cells with Nanoscale Control of the Interpenetrating Network Morphology," *Adv. Funct. Mater.* **15**, 1617-1622 (2005).

CHAPTER SIX

P3OT Donor - $Sc_3N@C_{80}$ Acceptor: First Study of an Endohedral Fullerene as a Photovoltaic Electron Acceptor

The endohederal fullerene trimetasphere, $Sc_3N@C_{80}$, is a new material that has been investigated ere for the first time as a potential donor in organic photovoltaic devices. It consists of a Sc_3N cluster enclosed in a C_{80} cage. A detailed description of its chemical structure and characteristics can be found in section 3.4.4. The main reason for interest in this material is that the LUMO level, and consequently, the band gap can be tuned by varying the metal atoms that are enclosed. As far as we know, there is no published work on the use of $Sc_3N@C_{80}$ as an acceptor. The endohederal fullerene is a black soot-like powder. It was deposited on P3OT by thermal evaporation in the vacuum deposition unit described in chapter 3. It was more difficult to evaporate than C_{60} and required almost five to seven times longer heating to accomplish deposition. Thicknesses obtained were typically of the order of 15 nm to 30 nm. Presented in this chapter is a preliminary study of the use of this material in organic photovoltaic devices, with a focus on concentration gradient devices. Bilayer and interdiffused devices have been fabricated and a study of varying interdiffusion conditions was conducted to optimize device performance by maximizing the concentration gradient. This was monitored using Auger spectroscopy.

The study on endohederal fullerenes was conducted over a period of around 10 to 12 months. Samples were supplied to us by Luna nanoWorks, (Danville, VA, and were stored in clear glass vials in a plexiglass dessicator. Three batches of slides were fabricated and measured, and the experimental processing procedures were changed each time to attempt to obtain better concentration gradients and devices. Towards the end of this study, a gradual time-wise reduction of device performance was observed from batch to batch even though all other factors (such as the supporting Auger data) indicated that the device performance should go up. This seemed to suggest a temporal degradation of the material though we can not be certain of this. Studies at Luna nanoWorks have indicated that the material is quite stable over a period of years. For future work, the

material is being stored away from light and oxygen, in a glove box that provides an inert nitrogen environment. While there are clear trends in device performance within each group of devices fabricated within the same time period, there was a significant decrease in overall efficiency between the three sets fabricated over the course of one year. Hence the work done will be presented chronologically and all the data values should be compared with other devices measured around the same period of time.

6.1 Bilayers and Heated Devices

Bilayer devices were fabricated by evaporating the $Sc_3N@C_{80}$ onto a P3OT layer that had been annealed at 120 °C for over 35 minutes in the vacuum chamber. The initial heated devices were fabricated by heating a bilayer in the argon box at 118 °C for 5 minutes (during which the temperature over-shot to 134 °C) and allowed to cool in an atmosphere of mildly circulating argon gas, following the main interdiffusion conditions used in the P3OT – C_{60} study. As a note of comparison with the results in subsequent sections, these devices were fabricated in April 2006.

Figure 6.1a shows a comparison of a single P3OT layer, a bi-layer and an interdiffused device for the P3OT – $Sc_3N:C_{80}$ system, with P3OT thicknesses of 35 nm and $Sc_3N:C_{80}$ thickness of around 15 to 20 nm each for the bilayer and heated devices. We see an order of magnitude improvement in the EQE upon adding a layer of the endohedral fullerene which indicates that it acts as an acceptor material when used with P3OT. Upon heating the bilayer, only a marginal improvement is seen in the EQE. Figure 6.1b shows the comparison of the 4^{th} quadrant current density (J) – voltage (V) curves of the same devices, measured under 470 nm illumination. We see an overall improvement in the short circuit current density (J_{SC}) and the open circuit voltage (V_{OC}) and a marginal improvement in the fill factors for heated devices as compared to the unheated bilayers.

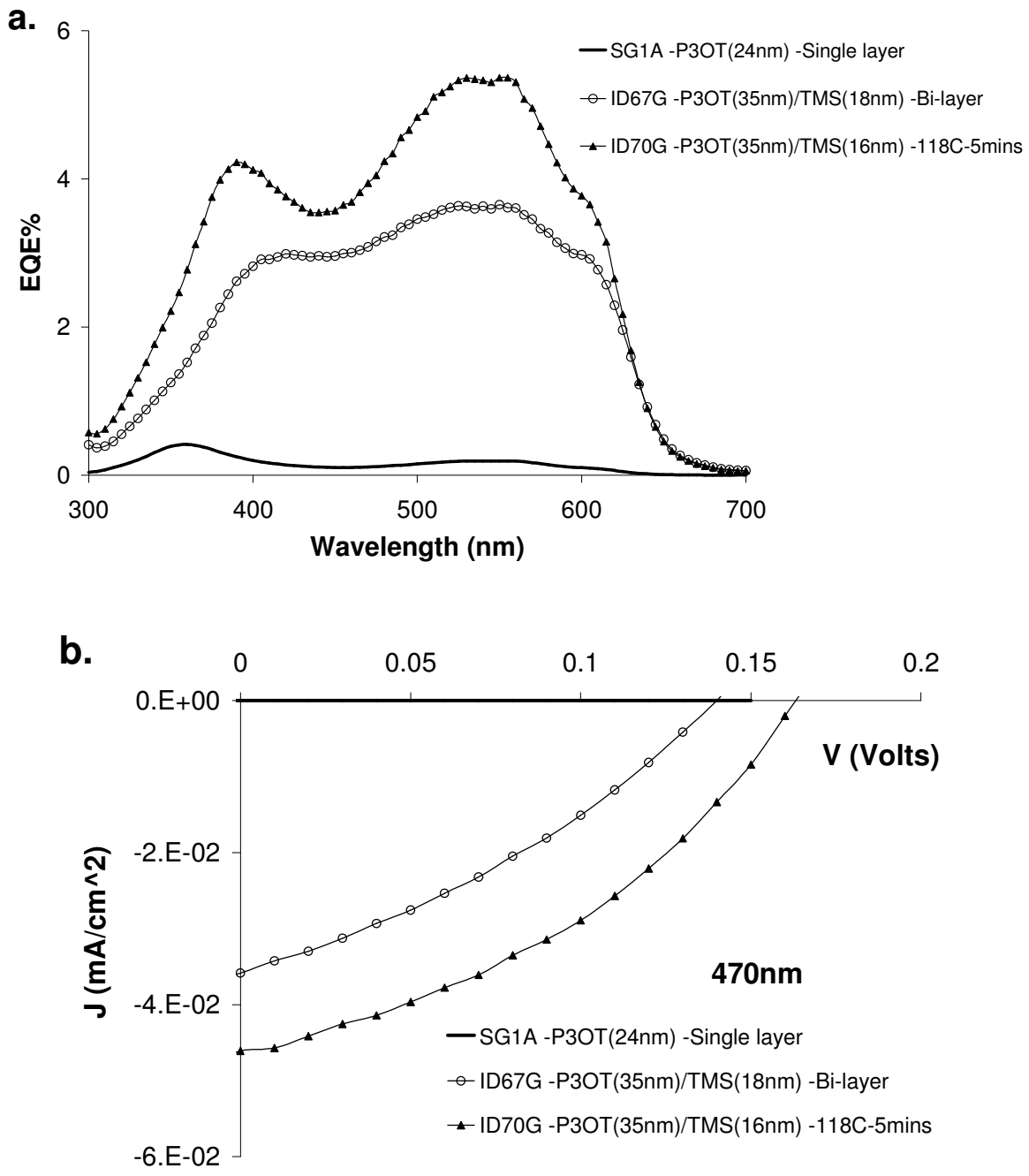

Figure 6.1 (a) EQE and (b) 470 nm illumination, 4th quadrant J-V characteristics for a single layer, bilayer and heated device of comparable P3OT and trimetasphere (TMS) $Sc_3N@C_{80}$ (TMS) layer thicknesses. For all these devices, the P3OT layer was annealed under vacuum, prior to TMS deposition, at 120 °C for over 35 minutes.

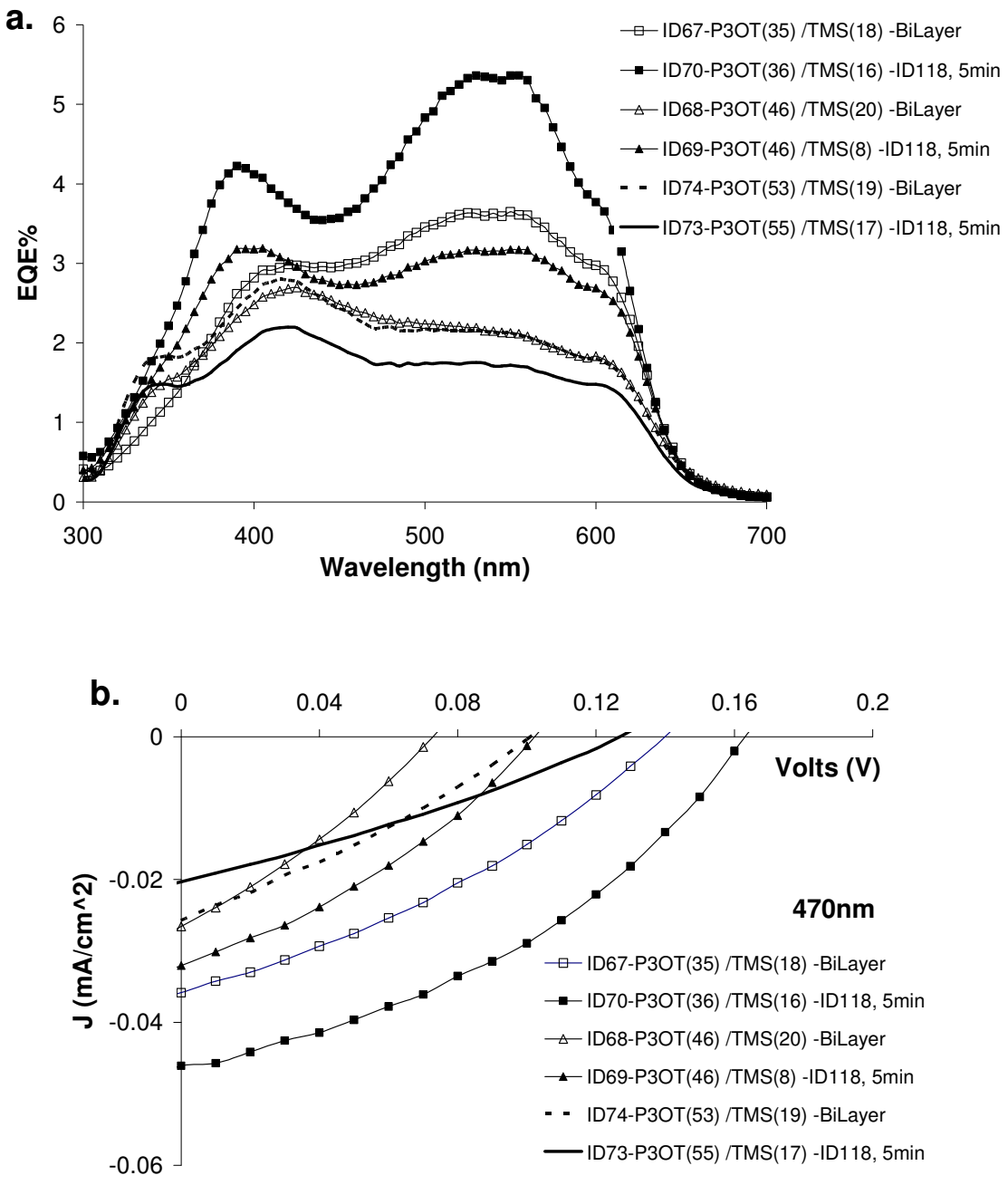

Figure 6.2 (a) EQE and (b) 470 nm illumination, 4th quadrant J-V characteristics. Bilayer and heated devices with comparable P3OT and $Sc_3N@C_{80}$ (TMS) layer thicknesses have been compared. For all these devices, the P3OT layer was annealed under vacuum, prior to TMS deposition, at 120 °C for over 35 minutes.

Device	Thickness(nm)		Voc	Jsc	FF	Eff
(470nm)	P3OT	$Sc_3N@C_{80}$	(V)	(mA/cm^2)		(%)
ID67G(Bilayer)	35	18	0.135	-0.046	0.34	0.05
ID68A(Bilayer)	46	20	0.075	-0.027	0.32	0.02
ID74B(Bilayer)	53	19	0.105	-0.026	0.28	0.03
ID70G(Heated)	36	16	0.165	-0.046	0.38	0.09
ID69A(Heated)	46	8	0.105	-0.032	0.32	0.04
ID73A(Heated)	55	17	0.125	-0.020	0.30	0.02

Table 6.1 Overview of the photovoltaic performance at 470 nm of the devices presented in Figure 6.2.

Figures 6.2a and 6.2b show the EQE curves and the 4th quadrant J-V curves measured under 470 nm illumination, obtained for bilayer and heated bilayer devices, for varying P3OT layer thicknesses. When comparing the EQE curves for bilayer and heated devices of similar thickness, a slight improvement is seen in the performance for the thin P3OT layer devices (ID67 and ID70). The overall EQE as well as the relative improvement from bilayer to heated device seems to reduce as the P3OT layer thickness is increased. The appearance of the filter effect is also seen with increasing thickness, indicating that the concentration gradient, if present, was small. If this were true, it would justify the first observation; as the layers get thicker, the relative thicknesses of the pure polymer layer increases with respect to the interdiffused layer. The net optical power reaching either the sharp bilayer junction or bulk heterojunction would be reduced so much so that the final photocurrent contributions from both junctions are almost the same. Table 6.1 gives an overview of the photovoltaic performance of these devices, also under 470 nm illumination.

The extent of interdiffusion is observed using Auger spectroscopy, seen in Figure 6.3, which analyses a thick P3OT bilayer (ID74), a moderate thickness heated device (ID69) and a thick P3OT layer heated device (ID73). While fabricating the slide, one portion of the slide was reserved for Auger spectroscopy by wiping off the PEDT:PSS layer and protecting it during Al deposition. An added advantage for this system is that in addition to the polymer being tagged by the sulfur (solid symbols), the acceptor layer can

now be tagged by the scandium (open symbols) in the cage. The S and Sc plateaus of ID73 clearly look like a bilayer feature. It is not clear why the S is seen earlier in ID74 than in ID73 since they have comparable acceptor layer thicknesses. The important point to note is that the two heated devices show similar concentration gradients in both the S and the Sc curves as the bilayer device, indicating a lack of interdiffusion. Hence, to increase the extent of interdiffusion, a study was conducted on the effects of varying the thermal treatment step, based on the assumption that the best devices would be obtained if a concentration gradient of sulfur and scandium, which stretched through the entire active layer of the film, could be achieved.

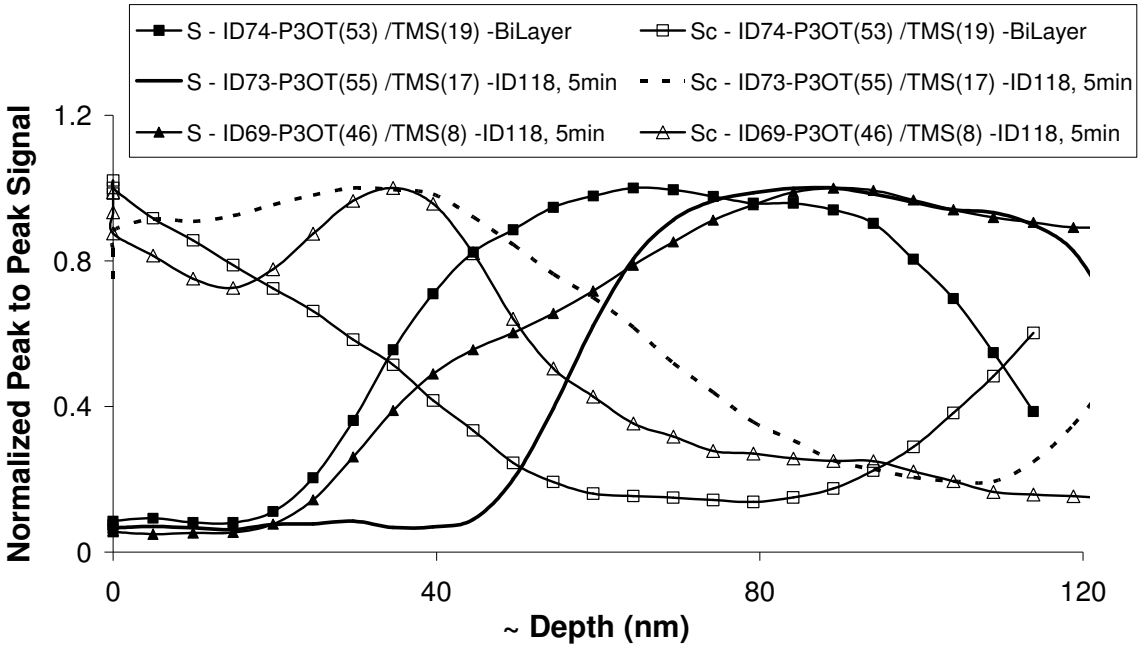

Figure 6.3 Plot of the depth profiles by Auger spectroscopy for the bilayer and heated devices shown in Figure 6.2. The approximate depth into the film is given on the x-axis while the y-axis is the peak to peak signal intensity normalized to one.

6.2 Heated Devices: Varying Thermal Treatments

The P3OT – $Sc_3N@C_{80}$ system displays very different interdiffusion parameters as compared to either the P3OT – C_{60} or the P3OT – PCBM systems. Given the difficulty of sublimation of the material, it is expected that higher interdiffusion temperatures,

interdiffusion times or a combination of both would be required to achieve the required concentration gradient.

6.2.1 Overview of Thermal Treatments

A spectrum of temperatures and times has been tried for the heating step, and the gradients thus obtained have been recorded by Auger spectroscopy and compared. One possible explanation we considered for what might affect the interdiffusion process was that, as the $Sc_3N@C_{80}$ films were deposited, the increased time of deposition increased the substrate temperature slightly. This might be inducing the $Sc_3N@C_{80}$ film to crystallize at the interface, preventing further interdiffusion in subsequent heating cycles. To overcome this, for some devices the substrate was heated during the deposition, at temperatures above the glass transition temperature of P3OT. It was expected that this would make the polymer soft and allow the $Sc_3N@C_{80}$ to diffuse in as it was depositing in a molecular form. We also tried temperatures above the melting point of the polymer. Although it had been shown that this was not conducive to concentration gradient formation for the P3OT – C_{60} system, given the difficulty of interdiffusion here, we thought it might show different results for this system. In later experiments, devices were also made with non-annealed P3OT layers, prior to $Sc_3N@C_{80}$ deposition in the hope that the less crystalline nature of the polymer films would allow for easier interdiffusion. A detailed discussion of the merits and demerits of this procedure can be found in previous chapters (section 4.3.1 and section 5.3).

Table 6.2 shows a summary of these various heat treatments that were carried out on the bilayer, including the ones described in the previous section. The details of the heating environment mentioned here have been explained in sections 3.2.3 and 3.2.5 chapter 3. A number of these heating cycles were carried out in the argon box and demonstrated an over-swing of temperature. The over-swing has been mentioned in the table within parentheses and, in each case, the temperature would settle back to the set temperature within 5 minutes and stay stable for the remainder of the set time (similar to the temperature profiles shown in Figure 4.15. Also mentioned in the table is whether the heat treatment was conducted during or after the $Sc_3N@C_{80}$ deposition.

Device	Batch Date	Heating Setup	Anneal	Heat Treatment: Temp. (Over-swing)-Time-During or After $Sc_3N@C_{80}$ Deposition
ID67, ID68, ID74	Apr '06	-	Yes	- (Bilayer)
ID69, ID70, ID73	Apr '06	Ar Box	Yes	118°C (134°C) – 5min. – After
ID79	July '06	Ar Box	Yes	145°C (159°C) – 10min. – After
ID82, ID92	July '06	Ar Box	Yes	150°C (164°C) – 10min. – After
ID91	July '06	Ar Box	Yes	150°C (164°C) – 20min. – After
ID89, ID90	July '06	Vacuum	Yes	150°C (154°C) – 10min. – During
ID125, ID126	Jan '07	Vacuum	No	150°C (154°C) – 30min. – During
ID138	Jan '07	Ar Box	No	160°C (175°C) – 10min. – After
ID140	Jan '07	Ar Box	No	160°C (175°C) – 25min. – After
ID142	Jan '07	Ar box	Yes	160°C (175°C) – 25min. – After
ID136	Jan '07	Ar box	No	165°C (180°C) – 10min. – After
ID132	Jan '07	Vacuum	Yes	180°C (190°C) – 10min. – During
ID134	Jan '07	Vacuum	No	180°C (190°C) – 10min. – During
ID129, ID130	Jan '07	Ar Box	No	200°C (216°C) – 10min. – After

Table 6.2 Overview of the different heat treatments performed on P3OT – $Sc_3N@C_{80}$ bilayers to try and achieve concentration gradient devices. They have been arranged in order of increasing exposure to heat treatment.

Due to the long-term degradation seen in EQE and conversion efficiency, the following results will be presented in two separate sections, as per the dates of fabrication shown in the table. In many cases, only one or two devices were done for each set of parameters. This was done so as to achieve a more comprehensive coverage so that the most suited interdiffusion temperature and time could be identified for further device optimization.

6.2.2 Devices Fabricated July, 2006: 150°C

The study from the previous set, done in April, 2006, revealed an expected P3OT thickness dependence, similar to the ones seen for the P3OT – C_{60} and the P3OT – PCBM systems. Henceforth, the P3OT thicknesses were maintained constant at 60 nm ± 5 nm and the difficulty of deposition of $Sc_3N@C_{80}$ ensured that the acceptor layer thickness stayed within approximately 15 nm to 25 nm. Thus, the interdiffusion parameters were the only ones varied for this optimization study.

Following the Auger data of the previous section, the heat treatment was ramped up to 150 °C for 10 minutes. This temperature was applied either after or during the $Sc_3N@C_{80}$ deposition. The details of each individual device's heat treatment can be found in Table 6.2, for batch dates corresponding to July '06. Figures 6.4a and 6.4b show the EQE curves and the 470 nm illumination 4th quadrant J-V curves for these devices.

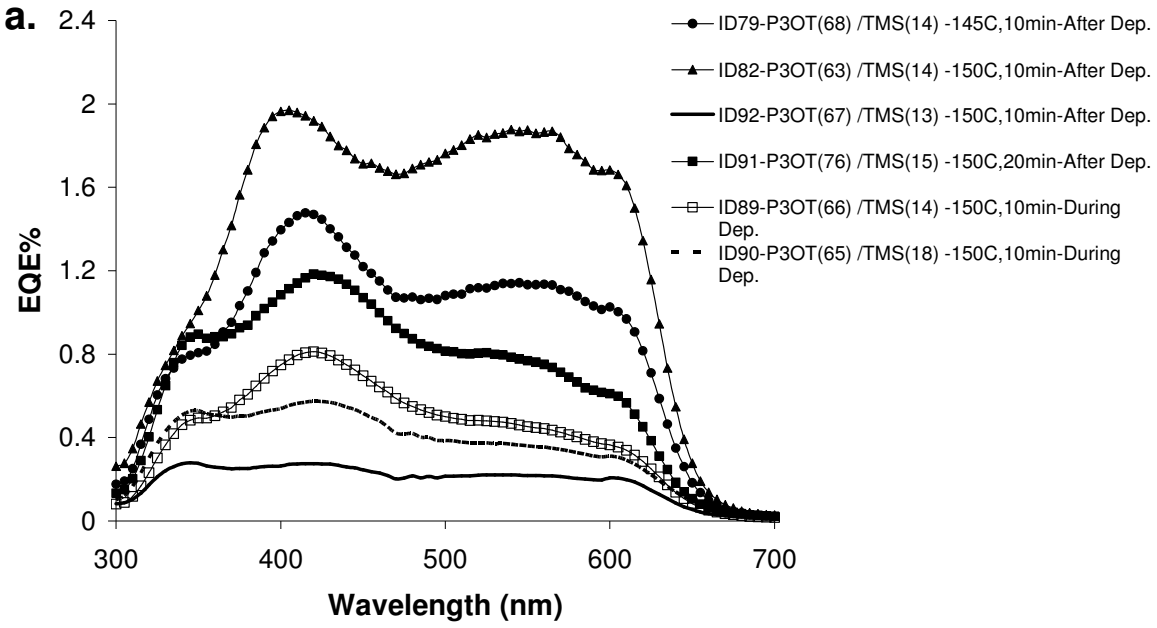

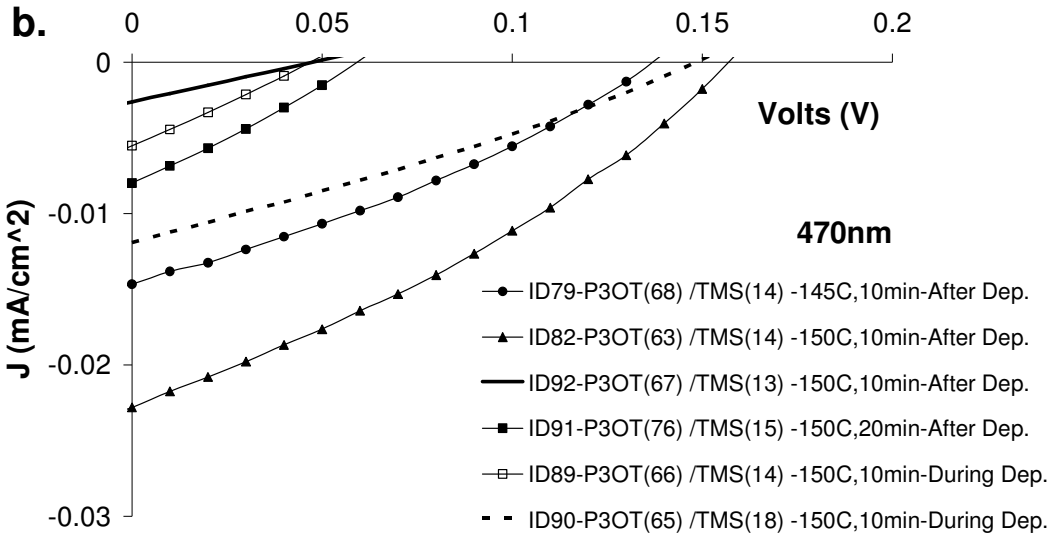

Figure 6.4 (a) EQE and (b) 470 nm illumination, 4th quadrant J-V characteristics for devices heated either during or after $Sc_3N@C_{80}$ (TMS) deposition. The P3OT layers were annealed prior to TMS deposition.

Device	**Thickness(nm)**		**Heat Treatment**	**Voc**	**Jsc**	**FF**	**Eff**
(470nm)	**P3OT**	**$Sc_3N@C_{80}$**		**(V)**	**(mA/cm^2)**		**(%)**
ID79	68	14	145°C, 10m-After Deposition	0.135	-0.015	0.32	0.018
ID82	63	14	150°C, 10m-After Deposition	0.155	-0.023	0.32	0.032
ID92	67	13	150°C, 10m-After Deposition	0.045	-0.003	0.26	0.001
ID91	76	15	150°C, 20m-After Deposition	0.145	-0.012	0.29	0.015
ID89	66	14	150°C, 10m-During Deposition	0.055	-0.008	0.30	0.004
ID90	65	18	150°C, 10m-During Deposition	0.045	-0.006	0.27	0.002

Table 6.3 Overview of the photovoltaic performance at 430 nm of the devices presented in Figure 6.4.

Contrary to what we expected, the devices that were heated after $Sc_3N@C_{80}$ deposition seem to show a marginally better performance than the ones heated during the deposition both in terms of the EQE curves and the V_{OC} data (with the exception of ID92). Table 6.3 gives an overview of the photovoltaic performance of these devices, also under 470 nm illumination.

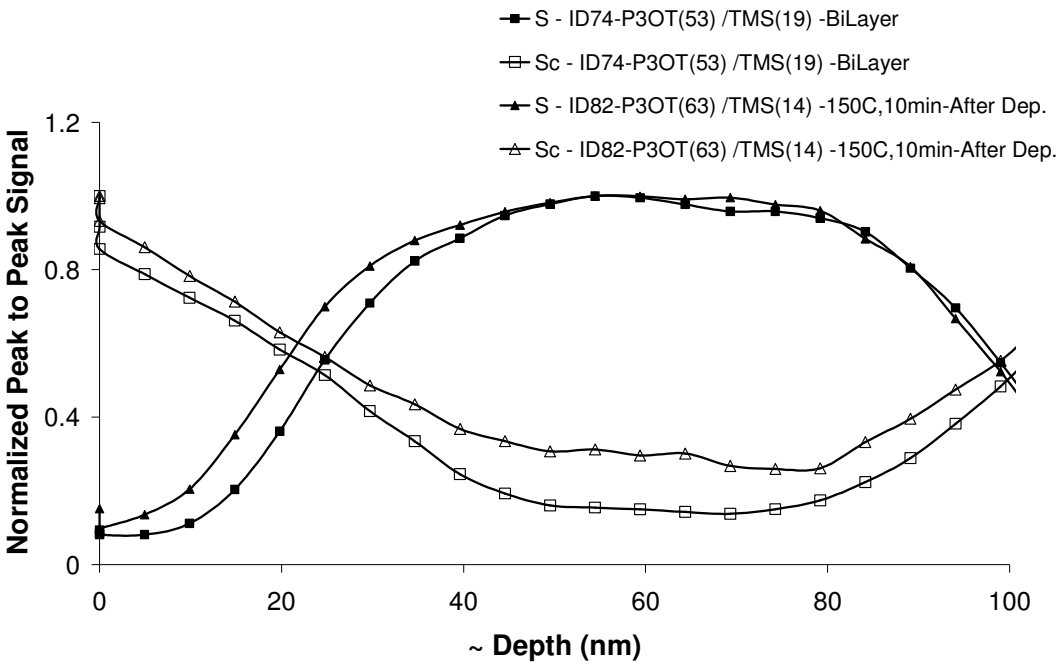

Figure 6.5 Plot of the depth profiles by Auger spectroscopy for a device heated at 150 °C for 10 minutes compared to a bilayer device. The peak to peak signal intensity of the y-axis is normalized to one.

Figure 6.5 shows the Auger spectroscopy depth profiles for sulfur and scandium for ID82, the device which demonstrated the best performance for this data set. This is compared with the Auger curves for a bilayer presented earlier (since the time degradation does not permit a comparison of the EQE or J-V curves). Even though the interdiffusion temperature was increased, the Auger results still show a large plateau for P3OT (pure donor layer) and the slope of the interdiffusion region is also similar to that of the bilayer. Thus, even for this temperature, no significant interdiffusion was achieved. It should also be noted that because the $Sc_3N@C_{80}$ layer is so thin, it would be difficult

for it to extend deep into a thick P3OT layer and sunstantially decrease the P3OT concentration.

6.2.3 Devices Fabricated January, 2007: 150 °C – 200 °C

Following the results from the July, 2006 data set, the interdiffusion conditions were increased further. Temperatures were tried above and below the melting point of P3OT (187 °C). These devices were all fabricated and measured around the same time, but the results have been presented split up for the sake of easier analysis and comparison. Figures 6.6a and 6.6b show the EQE and 4^{th} quadrant J-V curves under 470 nm illumination for devices heated below the melting point of P3OT. Figures 6.7a and 6.7b show similar curves for devices heated at and above the melting point of P3OT. Table 6.4 shows the overview of the photovoltaic performance of these devices (shown in both Figure 6.6 and Figure 6.7) under 470 nm, monochromatic illumination. The AM1.5 solar simulator had been set up at the time these devices were fabricated. Table 6.5 shows the photovoltaic performance data for these devices under AM1.5 illumination.

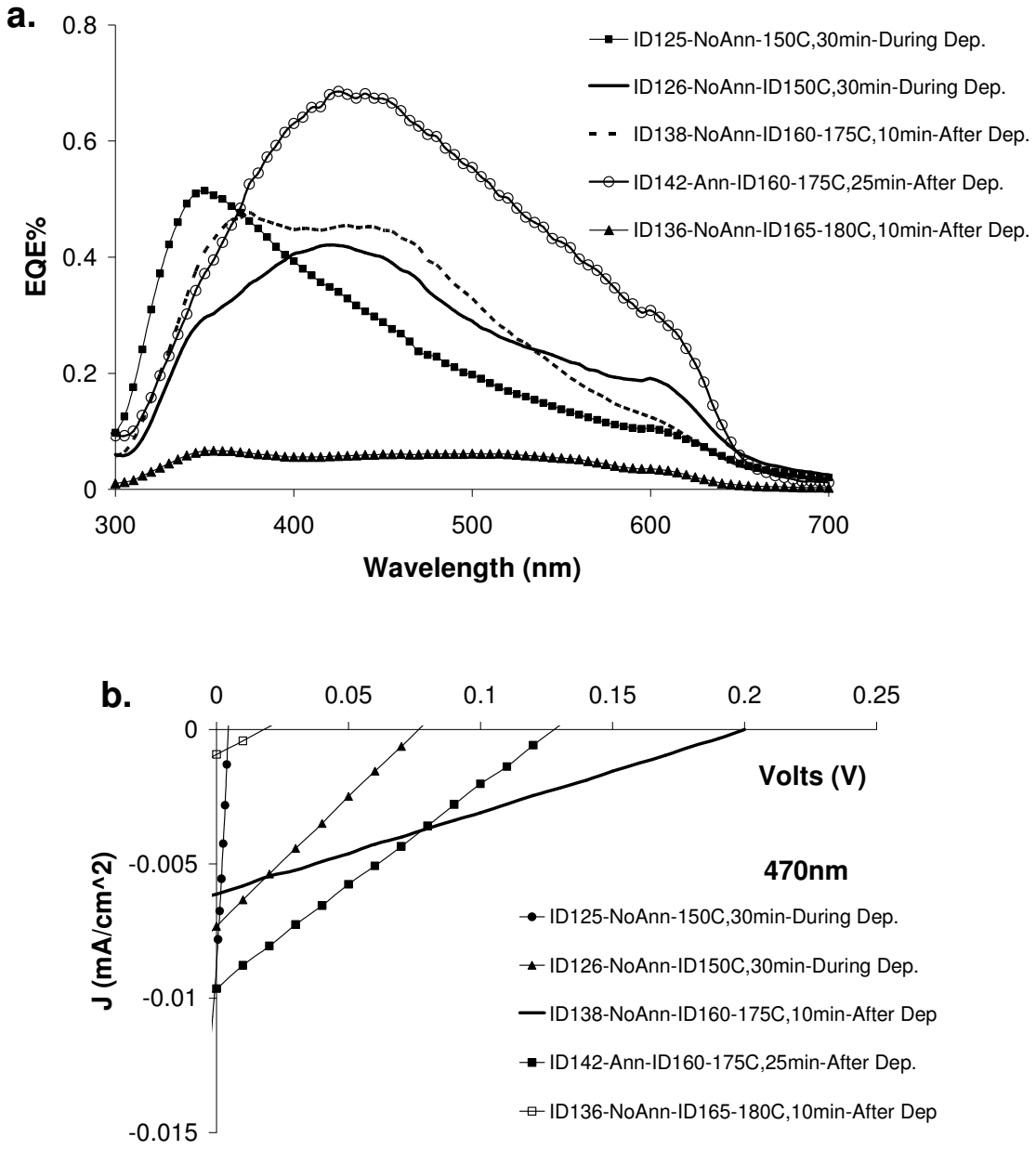

Figure 6.6 (a) EQE and (b) 470 nm illumination, 4th quadrant J-V characteristics for devices heated for interdiffusion at temperatures below the melting point of P3OT. The thicknesses were all within 60 nm ±5 nm for P3OT and under 30 nm for $Sc_3N@C_{80}$. The annealing and interdiffusion conditions for each device are given in the legend. The thickness are listed in Table 6.4.

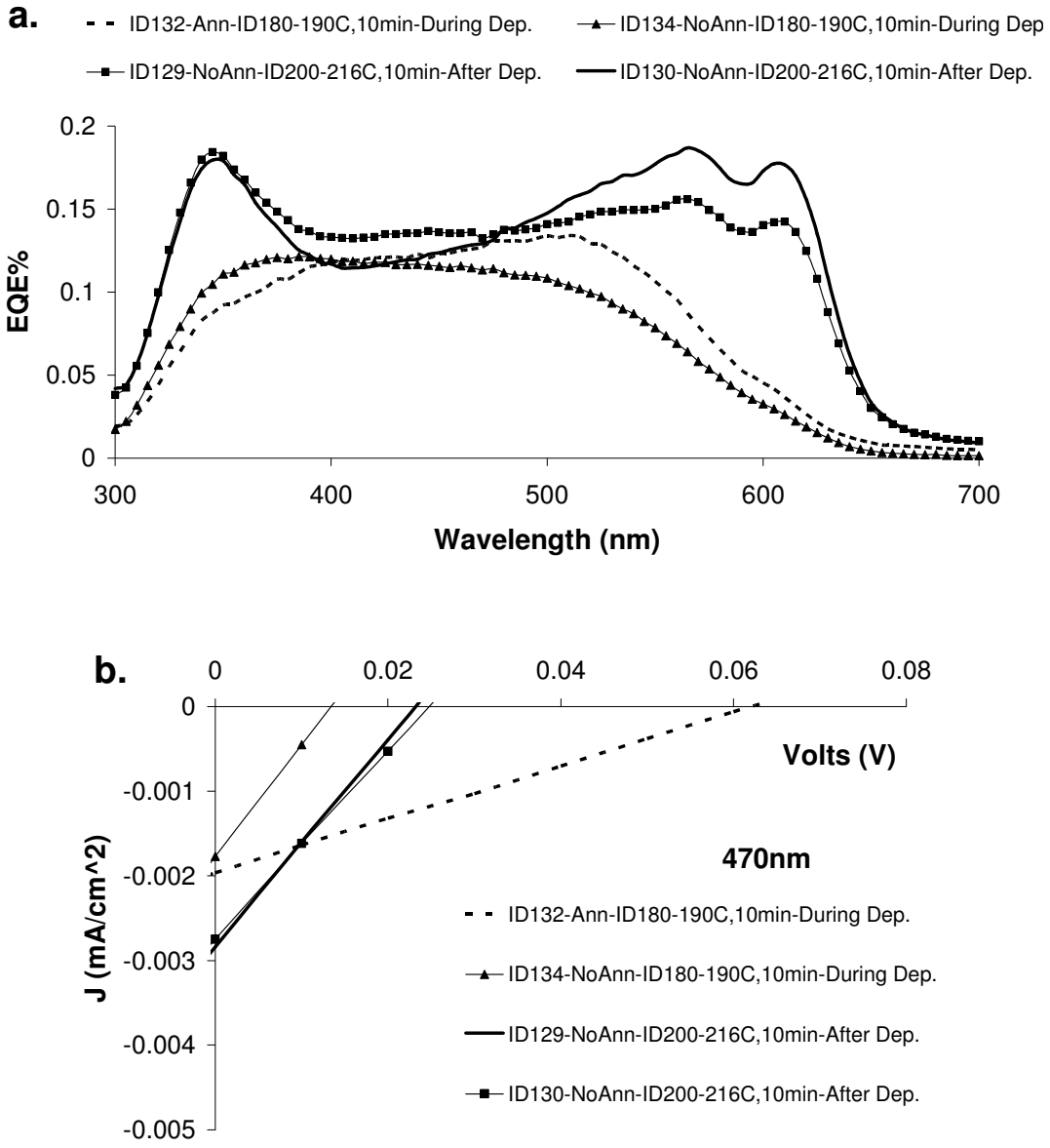

Figure 6.7 (a) EQE and (b) 470 nm illumination, 4th quadrant J-V characteristics for devices heated for interdiffusion at temperatures at and above the melting point of P3OT. The thicknesses were all within 60 nm ±5 nm for P3OT and under 30 nm for $Sc_3N@C_{80}$. The annealing and interdiffusion conditions for each device are given in the legend.

Device	Thickness(nm)		Heat Treatment	Voc	Jsc	FF	Eff
(470nm)	P3OT	$Sc_3N@C_{80}$		(V)	mA/cm^2		(%)
ID125 No Ann	62	10	150°C, 30m-During Deposition	0.075	-0.005	0.24	0.0016
ID126 No Ann	57	28	150°C, 30m-During Deposition	0.075	-0.007	0.26	0.0026
ID138 No Ann	61	27	160°C, 10m-After Deposition	0.205	-0.006	0.25	0.0081
ID142 Ann	66	25	160°C, 25m-After Deposition	0.125	-0.009	0.25	0.0080
ID136 No Ann	65	14	165°C, 10m-After Deposition	0.025	-0.001	0.26	0.0001
ID132 Ann	60	26	180°C, 10m-During Deposition	0.065	-0.002	0.24	0.0008
ID134 No Ann	59	14	180°C, 10m-During Deposition	0.015	-0.002	0.17	0.0001
ID129 No Ann	57	10	200°C, 10m-After Deposition	0.025	-0.003	0.23	0.0003
ID130 No Ann	60	~ 14	200°C, 10m-After Deposition	0.025	-0.003	0.24	0.0003

Table 6.4 Overview of the photovoltaic performance under 470 nm illumination of the devices presented in ***Figures 6.6 and 6.7***.

Device	Thickness(nm)		Heat Treatment	Voc	Jsc	FF	Eff
(AM1.5)	P3OT	$Sc_3N@C_{80}$		(V)	(mA/cm^2)		(%)
ID125 No Ann	62	10	150°C, 30m-During Deposition	0.235	-0.03	0.25	-
ID126 No Ann	57	28	150°C, 30m-During Deposition	0.255	-0.65	0.23	0.0042
ID138 No Ann	61	27	160°C, 10m-After Deposition	0.375	-0.40	0.25	0.0047
ID142 Ann	66	25	160°C, 25m-After Deposition	0.465	-0.69	0.23	0.0086
ID136 No Ann	65	14	165°C, 10m-After Deposition	0.265	-0.08	0.24	0.0005
ID132 Ann	60	26	180°C, 10m-During Deposition	0.205	-0.10	0.24	0.0005
ID134 No Ann	59	14	180°C, 10m-During Deposition	0.275	-0.08	0.25	0.0008
ID129 No Ann	57	10	200°C, 10m-After Deposition	0.225	-0.20	0.27	0.0016
ID130 No Ann	60	~ 14	200°C, 10m-After Deposition	0.235	-0.23	0.24	0.0017

Table 6.5 Overview of the photovoltaic performance under AM1.5 illumination of the devices presented in ***Figures 6.6 and 6.7***.

The best device from this set is the one interdiffused in the argon box at a set point of 160 °C (over-swing to 175 °C), for 25 minutes. The EQE is less than 1% and we believe this is because of the unexpected degradation of the material and not due to the morphology. This was confirmed from the Auger spectroscopy data collected for these devices which are discussed next:

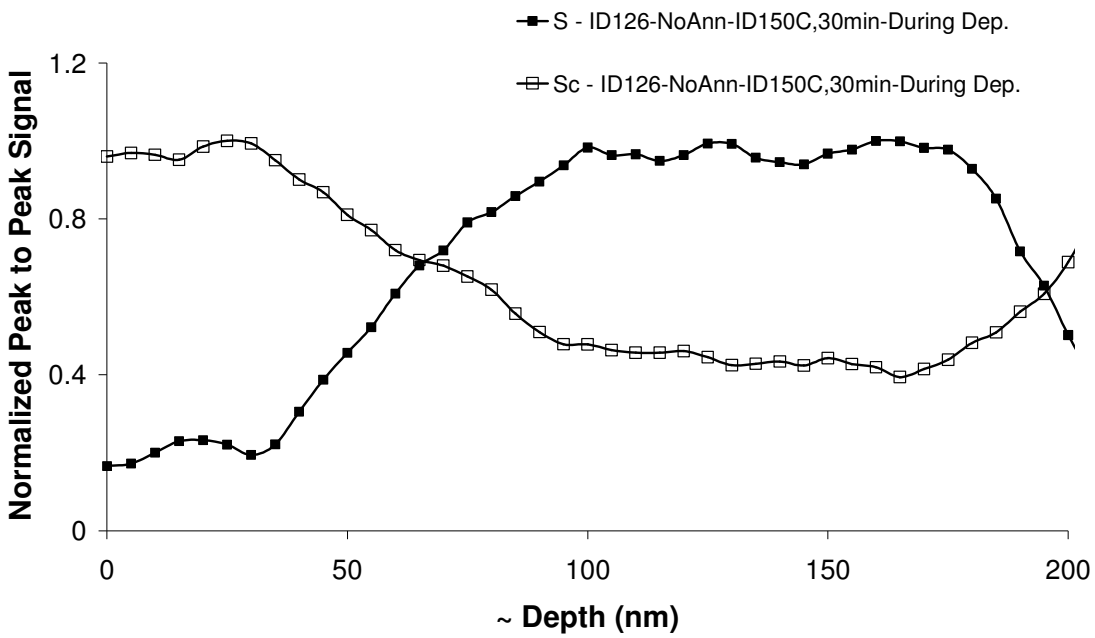

Figure 6.8 Concentration depth profile by Auger spectroscopy for device ID126, heated at 150 °C for 30 minutes during $Sc_3N@C_{80}$ (TMS) deposition. The P3OT layer was not annealed prior to the TMS deposition.

Initially, the time of interdiffusion was increased from 10 minutes to 30 minutes and heat application during $Sc_3N@C_{80}$ deposition was again attempted (ID125, ID126). This time, the P3OT layer was not annealed to see if interdiffusion would be easier. Figure 6.8 shows the Auger data for such a device. The data is a little noisy due to instrumentation issues, but it still shows the sulfur plateau for pure P3OT. It should be noted that there is an apparent rise seen in the Sc signal at the P3OT – ITO interface. This is a false signal and is seen because a secondary Auger peak for indium falls within the same energy range as the primary peak for scandium. Hence, as the ITO layer is entered, the scan for Sc detects the indium and rises. A thicker $Sc_3N@C_{80}$ film than usual (28 nm) was deposited and a plateau is seen even for the acceptor material, indicating poor interdiffusion. Hence, it was concluded that 150 °C was still too low to achieve a sufficient concentration gradient.

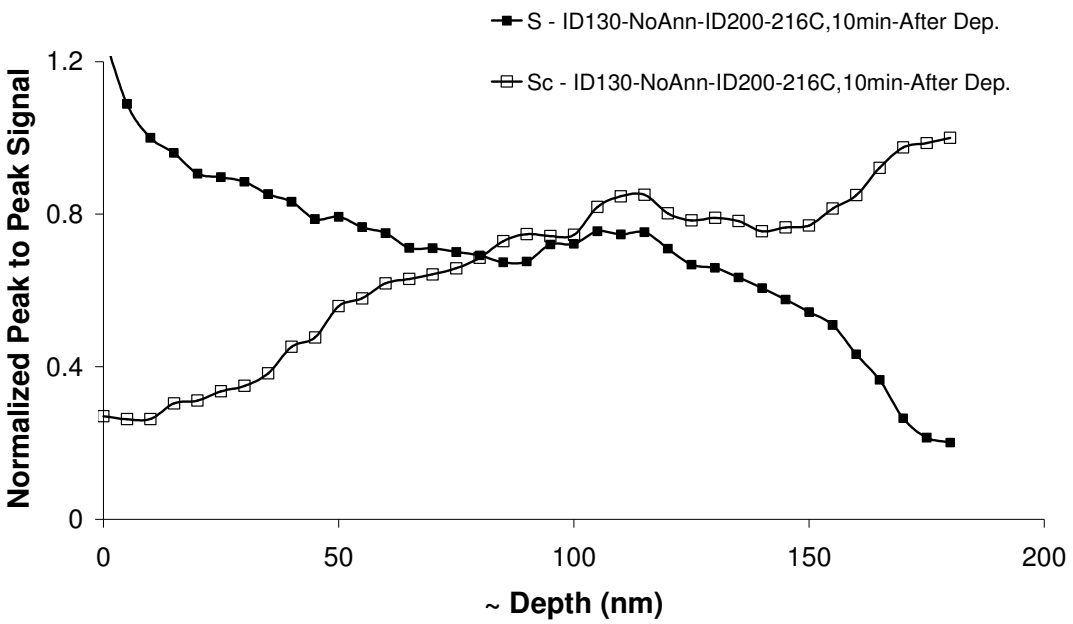

Figure 6.9 Concentration depth profile by Auger spectroscopy for device ID130, heated at 200 °C to 210 °C for 10 minutes after $Sc_3N@C_{80}$ (TMS) deposition. The P3OT layer was not annealed prior to the TMS deposition.

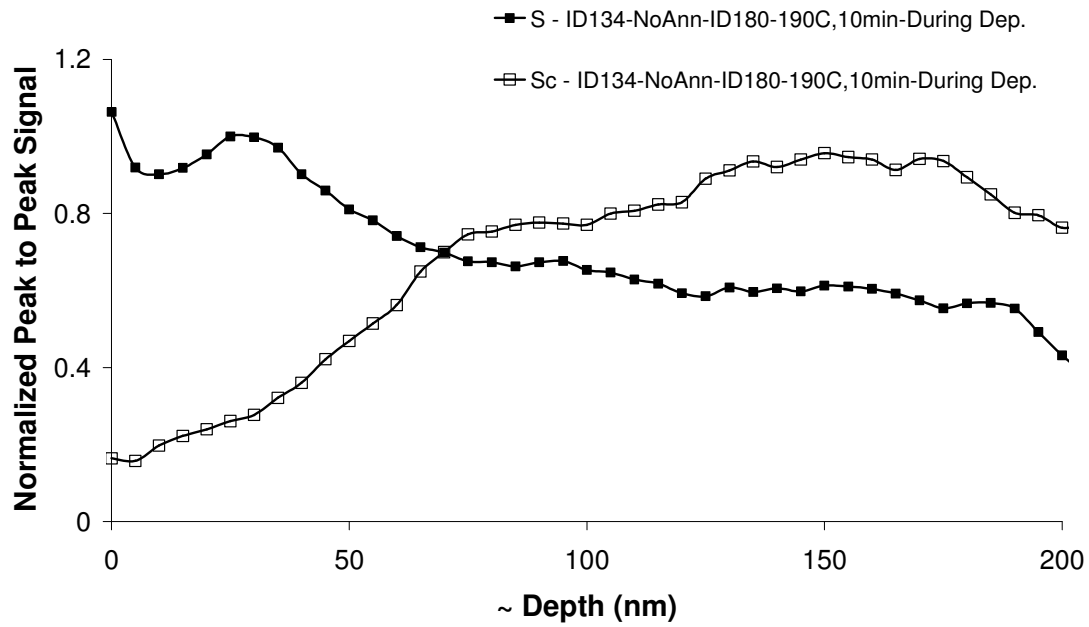

Figure 6.10 Concentration depth profile by Auger spectroscopy for device ID134, heated at 180 °C to 190 °C for 10 minutes after $Sc_3N@C_{80}$ (TMS) deposition. The P3OT layer was not annealed prior to the TMS deposition.

The next temperatures tried were above the melting point of the polymer. First the samples were heated well above the melting point (200 °C), in the argon box, after

$Sc_3N@C_{80}$ deposition (ID129, ID130). The next set of devices were made by heating at temperatures close to the melting point (T_m) in the vacuum chamber during $Sc_3N@C_{80}$ deposition. Figures 6.9 and 6.10 show sample Auger data for the devices heated at 200°C and 180 °C respectively. Both display a curious effect of reversal of the P3OT and $Sc_3N@C_{80}$ layers. We think this might be because the polymer reached temperatures above the T_m in both cases and because $Sc_3N@C_{80}$ layer is so thin. Unlike in the rubbery phase (above the glass transition temperature (T_g) and below the T_m), where there is some resistance offered to the diffusion of the acceptor into the polymer that helps regulate the rate of diffusion and concentration gradient formation, the polymer in the melted state is such that very little resistance is offered to interdiffusion. Due to the driving motivation of a concentration gradient, interdiffusion would occur and eventually end up as a blend. It is not clear why the P3OT - $Sc_3N@C_{80}$ reversal happens. One explanation may be that having P3OT on the surface of the device lowers the net surface energy of the system which would induce the blend to phase separate in this manner and result in layer reversal. In any case, this would explain why the overall performance of these devices was almost five times lower than the best devices obtained, as seen when Figures 6.6 and 6.7 are compared. In the temperature optimization study, this served an important purpose of establishing an upper limit within which the ideal temperature could be found.

From the devices presented so far, it can be concluded that the temperature required for the formation of optimum concentration gradients should lie between 150 °C and 180 °C. The mid-point 165 °C was first selected (ID136) but, since the over-swing touched 180 °C, the temperature was brought down to 160 °C (over-swing of 175 °C) and heated for first 10 minutes (ID138) and then increased to 25 minutes (ID140). These devices had non-annealed P3OT layers. Since these devices showed reasonably high EQEs (comparing with the rest of this data set), next, the same heating conditions were attempted for devices fabricated with an initially annealed P3OT layer to increase the crystallinity and mobility. This device (ID142) showed us the best performance for this data set.

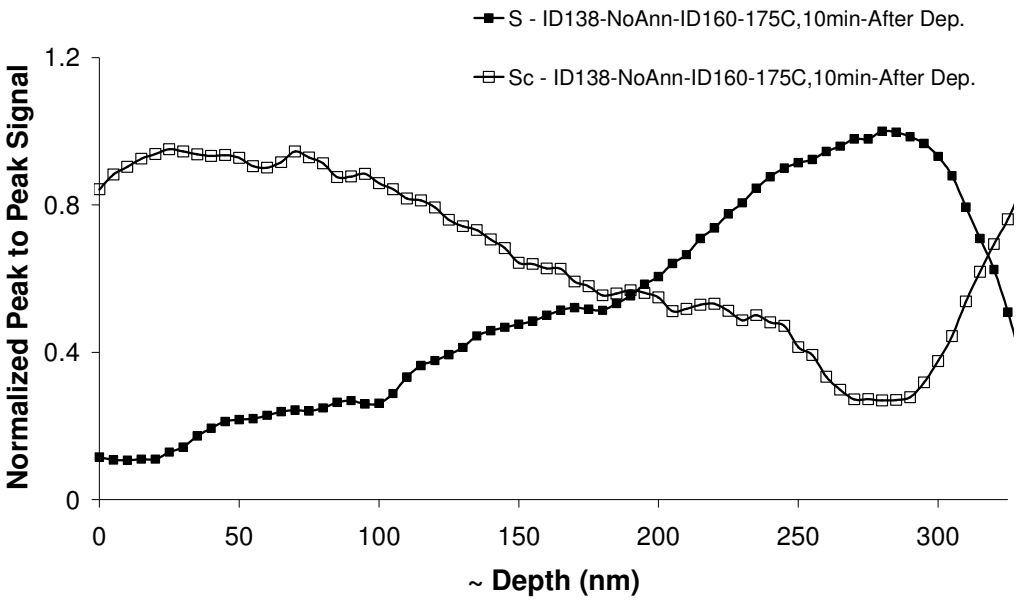

Figure 6.11 Concentration depth profile by Auger spectroscopy for device ID138, heated at 160 °C to 175 °C for 10 minutes after $Sc_3N@C_{80}$ (TMS) deposition. The P3OT layer was not annealed prior to the TMS deposition.

The Auger spectroscopy measurements are done on devices with similar thicknesses and subjected to similar interdiffusion conditions. The curves, thus obtained, also show very small plateaus for Sc and S and a gradual slope for both materials extending throughout the film, indicating thin layers of pure donor and acceptor and a concentration gradient that extends almost all the way through the active layer. This was the ideal morphology for optimum device performance in the previous two systems studied (P3OT – C_{60} and P3OT – PCBM) and hence is expected to be the ideal morphology for the P3OT – $Sc_3N@C_{80}$ system, too. The corresponding device showed the best EQE and J-V measurements within the data set collected at one period of time, but the overall performance is rather low when compared to devices fabricated almost 11 months before this. As already mentioned, we believe that there may have been some degradation of the materials for unknown reasons.

6.3 Concluding Remarks: P3OT – $Sc_3N@C_{80}$

From the bilayer study we have confirmed that $Sc_3N@C_{80}$ is indeed suitable for use as an acceptor material. Since this is the first investigation of this material as an acceptor,

various heat treatment procedures had to be applied before a standard procedure could be identified for creating concentration gradient devices of this material with P3OT. Unfortunately, in the course of this 12 month long study, there seemed to be a time-wise degradation of device performance which may be due to degradation of the $Sc_3N@C_{80}$. Since this material is rather new, such phenomena are yet to be fully investigated. Hence, the heat treatment optimization was done relying heavily on the concentration depth profile obtained from Auger spectroscopy to confirm the optimum extent of the gradient. The device with a pre-annealed P3OT layer, heated at set-point of 160 °C for 25 minutes in the argon box, seemed to show the best concentration gradient and highest EQE and V_{OC} within its comparison set. Temperatures above and below this condition seem to show poorer performance. This result was interpreted from just one or two devices made for each thermal parameter variation. Although the best devices presented here are still not comparable with the best organic photovoltaic devices currently available, it is hoped that the trends demonstrated would serve as a strong starting point for further investigation into P3OT - $Sc_3N@C_{80}$ systems.

An important area of work for the future would be to develop a deposition procedure that would allow for thicker films of the acceptor material. The first obvious advantage would be the increase of material leading to increased absorption power and availability of material to form more donor – acceptor junctions for exciton dissociation. Furthermore, judging by the thickness variation study done for P3OT – C_{60}, the maximum thicknesses obtained for this study still falls well short of the optimum thickness (~ 40 nm) that would maximize the incident light intensity in the main region of exciton generation and dissociation (due to interference effects caused by light reflection at the acceptor – Al electrode interface). This provides much room for improvement of device performance based on just increasing the $Sc_3N@C_{80}$ layer thickness.

It will be very important to understand and prevent the apparent degradation seen in devices fabricated over 12 months using $Sc_3N@C_{80}$ as an acceptor. It is highly desirable to use the optimized interdiffusion conditions determined here on fresh $Sc_3N@C_{80}$ material. Attempts to functionalize these endohederal fullerenes is currently being conducted at Luna nanoWorks. If a solution-processable form of $Sc_3N@C_{80}$ can be

produced, it would also open the doors to investigation of this material in blend bulk heterojunction devices.

CHAPTER SEVEN

Model of EQE for Varying Thicknesses Based on Absorption in the Region of Interdiffusion

In the thesis so far, experimental studies has been described for the variation of the EQE curves with thickness. In this chapter, a simple calculation is described that models the EQE curves based solely on the absorption of light as it passes through the layers after incidence and reflection off the acceptor – Al boundary. This model is applicable for any concentration gradient system, but the results presented in this model are for P3OT and C_{60}.

7.1 Derivation of the Model

The light enters the ITO, PEDT:PSS, P3OT, C_{60}, and finally the aluminum where it reflects and goes back through these layers and out the ITO. This model considers three regions as an approximation to our concentration gradient: a pure P3OT region, a region of homogeneous blend of P3OT and C_{60}, and a region of pure C_{60}. (Figure 7.1). The absorption in each region is determined from Beer's Law:

$$I_{final} = I_0 e^{-\alpha l} \tag{7.1}$$

where α is absorptivity and l is the thickness of the region.

The absorptivities of each region are denoted as α_1 for P3OT, α_2 for C_{60}, and α_b ($= (\alpha_1 + \alpha_2)/2$) for the P3OT-$C_{60}$ blend.

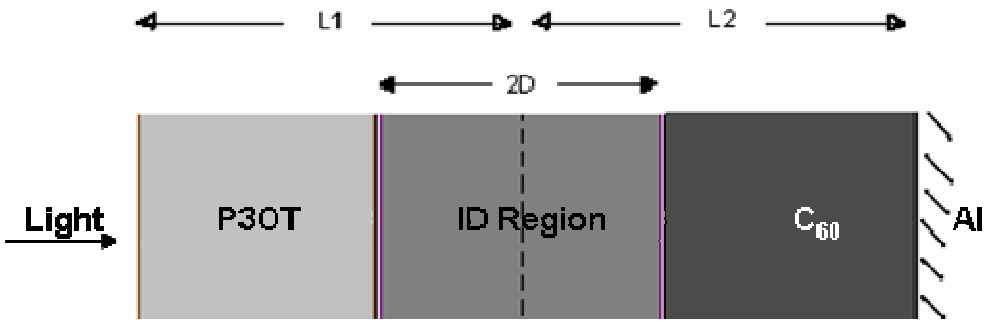

Figure 7.1 Schematic of the three regions of the device considered for the model. L_1 and L_2 are the original deposited thicknesses of P3OT and C_{60}. The central interdiffused (ID) region is taken to have a width of 60 nm (2D) and is approximated as a perfect blend of P3OT and C_{60}.

When multiple layers are present, then I_{final} of the first layer serves as the incident intensity I_0 for the next layer. Applying equation (7.1), the intensity after each layer is thus:

P3OT: $I_0 e^{-\alpha_1(L_1-D)}$ (7.2)

P3OT+ID: $I_0 e^{-\alpha_1(L_1-D)} \cdot e^{-(\alpha_1+\alpha_2)D}$ (7.3)

P3OT+ID+C_{60}: $I_0 e^{-\alpha_1(L_1-D)} \cdot e^{-(\alpha_1+\alpha_2)D} \cdot e^{-\alpha_2(L_2-D)}$ (7.4)

P3OT+ID+C_{60}+C_{60}: $I_0 e^{-\alpha_1(L_1-D)} \cdot e^{-(\alpha_1+\alpha_2)D} \cdot e^{-2\alpha_2(L_2-D)}$ (7.5)

P3OT+ID+C_{60}+C_{60}+ID: $I_0 e^{-\alpha_1(L_1-D)} \cdot e^{-2(\alpha_1+\alpha_2)D} \cdot e^{-2\alpha_2(L_2-D)}$ (7.6)

P3OT+ID+C_{60}+C_{60}+ID+P3OT: $I_0 e^{-2\alpha_1(L_1-D)} \cdot e^{-2(\alpha_1+\alpha_2)D} \cdot e^{-2\alpha_2(L_2-D)}$ (7.7)

The EQE is taken to be proportional to the energy absorbed in the interdiffused (ID) region, both during the first pass and after reflection:

EQE $\propto$ [(7.2) – (7.3)] + [(7.5) – (7.6)] (7.8)

Simplifying the algebra, we obtain

$$EQE \propto e^{-\alpha_1(L_1-D)}(1-e^{-\alpha_b(2D)}) + e^{-[\alpha_1 L_1+\alpha_2 L_2+\alpha_2(L_2-D)]}(1-e^{-\alpha_b(2D)}) \quad (7.9)$$

7.2 Assumptions of the Model

This model is based on the following assumptions:

1. Absorption by the ITO and PEDT:PSS layers is negligible.
2. Perfect reflection at the C_{60}–Al interface.
3. Only the photons absorbed in the interdiffused (ID) region contribute to the EQE.
4. The ID region has a concentration gradient going from pure polymer to pure C_{60} and hence the absorption coefficient at any point in the layer will be a weighted average of the absorption coefficients of the polymer and fullerene depending on their relative concentrations at that point. Since the entire ID region contributes to the photocurrent, the integration over the whole layer gives rise to an absorption coefficient which is a simple average the polymer and fullerene coefficients, $[\alpha_b = (\alpha_1 + \alpha_2)/2]$.
5. All photons absorbed in the ID region result in charge separation and hence contribute to current.
6. 100% collection of charges separated in the ID Region

7.3 Results and Discussion

Figure 7.2 shows experimental data that was collected for varying thicknesses of P3OT (90 nm, 50 nm, and 30 nm), while keeping the thickness of C_{60} constant at around 90 nm. This was done to isolate the effect of just the thickness of P3OT on device performance. We see that a reduction in the polymer thickness yields overall larger EQEs. Also, the filter effect is reduced as the P3OT thickness decreases, as evidenced by the peak from 450 nm to 500 nm becoming more prominent.

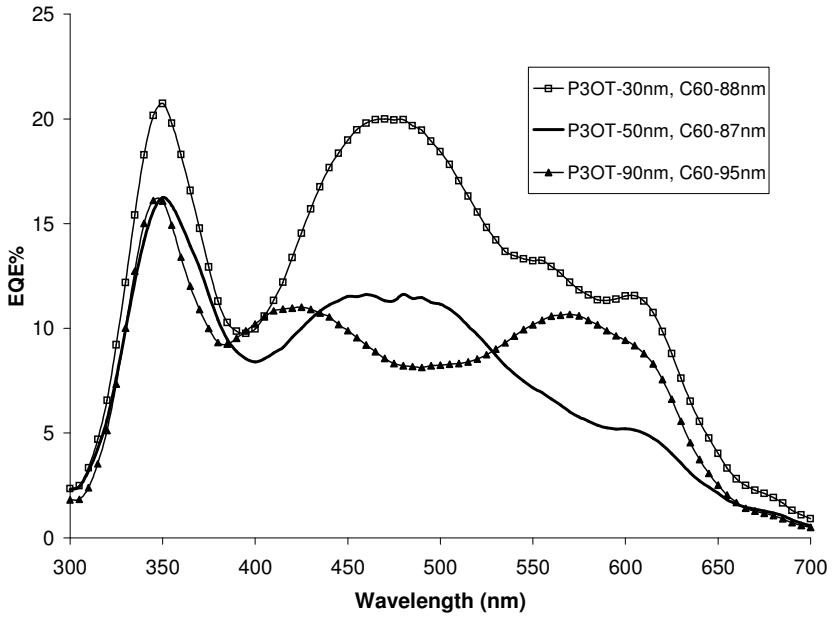

Figure 7.2 Experimentally measured EQE curves for P3OT – C_{60} devices thermally interdiffused at 130 ^{0}C. The initial bilayer thicknesses are 30 nm P3OT and 88 nm C_{60} (open squares), 50 nm P3OT and 87 nm C_{60} (solid line), and 90 nm P3OT and 95 nm C_{60} (solid triangles)

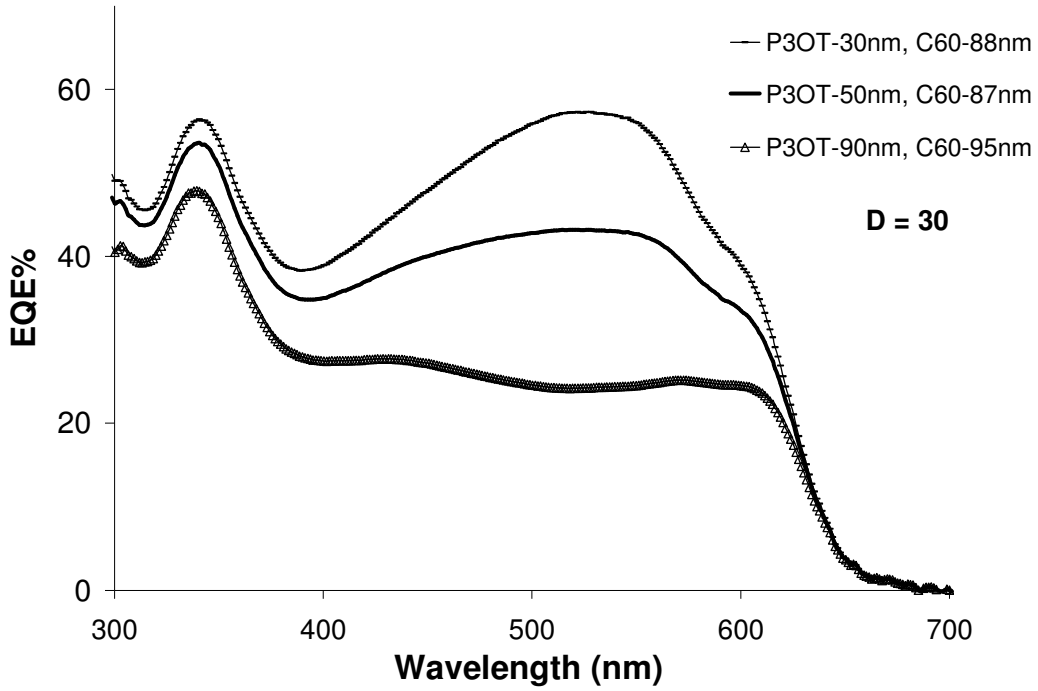

Figure 7.3 EQE curves generated by the model for P3OT – C_{60} devices for thicknesses comparable to the devices experimentally measured. The device layer thicknesses are 30 nm P3OT and 88 nm C_{60} (open squares), 50 nm P3OT and 87 nm C_{60} (solid line), and 90 nm P3OT and 95 nm C_{60} (solid triangles)

Figure 7.3 shows the EQE values calculated using equation 7.9, and the α values given in Sections 3.4.1 and 3.4.2 for the same P3OT and C_{60} thicknesses as in Figure 7.2. The value of 2D used was 60 nm based on the Auger depth profiling data for device ID47 shown in Section 4.2.4. The model reproduces several key features of the experimental data. As the P3OT thickness decreases, the EQE increases and the 450 nm to 500 nm peak becomes more pronounced. The shapes of the calculated EQE curves are quite similar to the experimental results. But the overall magnitudes of the EQE from the model are much larger than that of the experimental data. This is because we assumed perfect charge transfer and transport and because we have not accounted for the standing wave optical field distribution in the film.

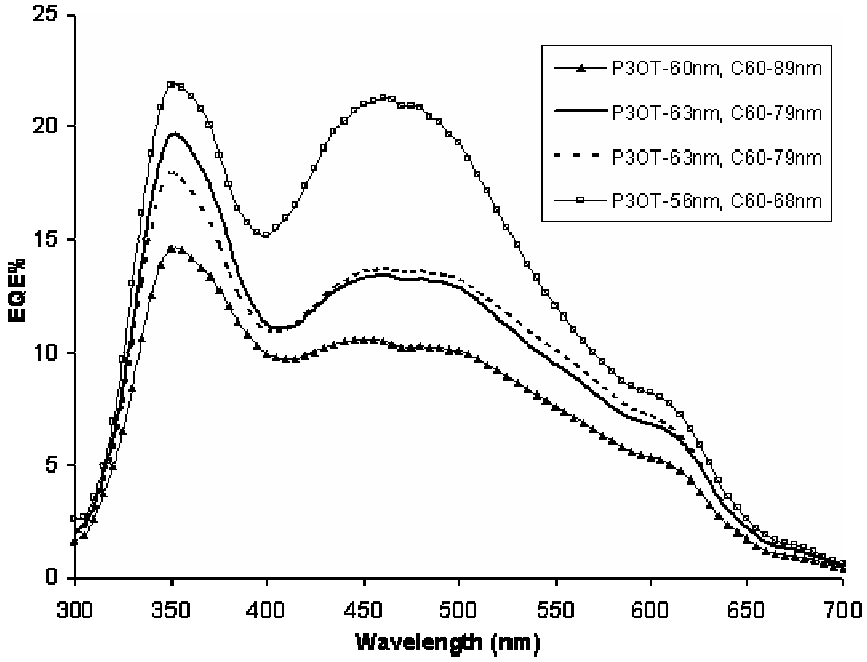

Figure 7.4 Experimentally obtained EQE curves for P3OT – C_{60} devices thermally interdiffused at 130 ^{0}C with constant P3OT thickness and varying C_{60} thickness. The layer thicknesses are 56 nm P3OT and 68 nm C_{60} (open squares), 63 nm P3OT and 79 nm C_{60} (2 devices; dashed line and solid line), 60 nm P3OT and 89 nm C_{60} (solid triangles).

Thus, although the model does not generate absolute magnitudes of measured EQE, it does, to a high degree of accuracy, describe the qualitative features observed in the shape of the experimental EQE curves as a function of P3OT thickness.

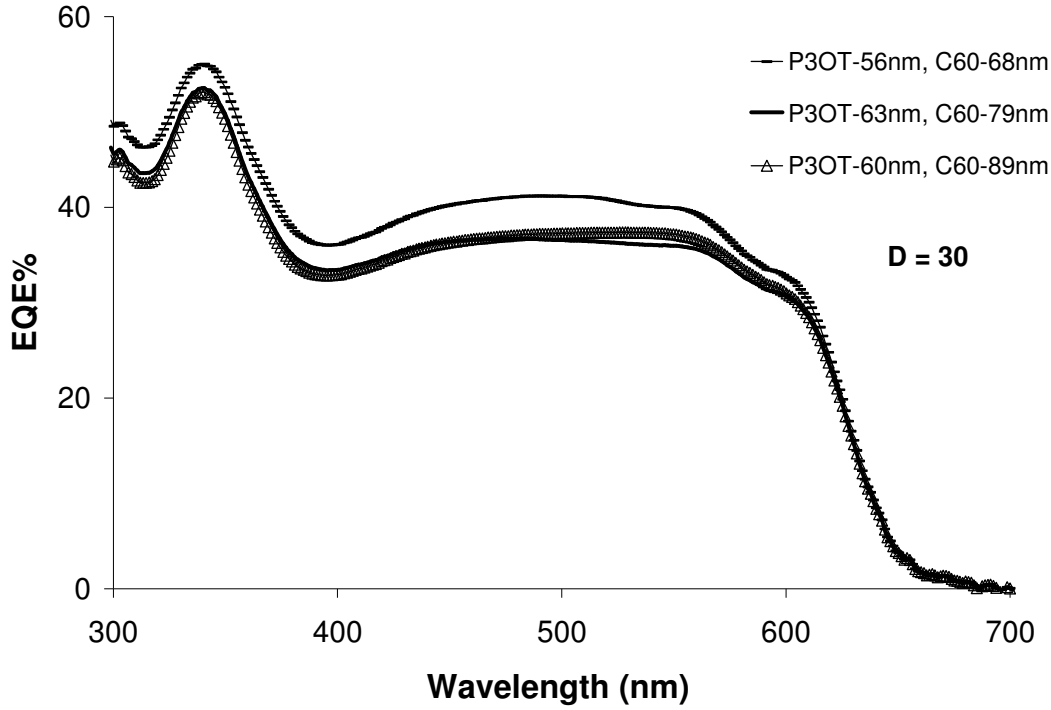

Figure 7.5 EQE curves generated by the model for P3OT – C_{60} devices for thicknesses comparable to the experimentally measured devices with constant P3OT thickness and varying C_{60} thickness. The device layer thicknesses are 56 nm P3OT and 68 nm C_{60} (open squares), 63 nm P3OT and 79 nm C_{60} (solid line), and 60 nm P3OT and 89 nm C_{60} (solid triangles).

Figure 7.4 shows experimental data for varying C_{60} thickness (68 nm, 79 nm, 89 nm), while the P3OT thickness was kept constant at around 60 nm. Once again, the EQEs improve as the C_{6s0} thickness reduces. This change is quite pronounced even for such small variations in thickness.

Figure 7.5, which is the model, does not replicate experimental data nearly as well as in the P3OT thickness variation case. It should be noted that this model only accounts for the contributions to EQE from absorption. One of the most crucial factors that is influenced by the thickness of the C_{60} layer is the electric field distribution within the film that arises from the interference of incident light with reflected light.[1,2] This is described in section 4.2. By employing a model that does not take this contribution into account, we can tell by comparison to experimental data (Figure 7.5 as well as Figure 4.7a) how important the electric field distribution in the film really is. Other factors that might also contribute to the thickness dependence and have been ignored are limitations

in charge transport (e.g. traps), which are more pronounced in C_{60} and the differences in the efficiencies of charge separation following C_{60} vs. P3OT excitation.

7.4 Variations to the Model

The electric field distribution vis-à-vis the initial donor-acceptor interface is a critical factor that determines the effectiveness of photon absorption at the interface. This distribution can be accounted for using the transfer matrix formalism. Incorporation of the standing wave intensity distribution introduced by the node at the Al is expected to increase the effectiveness of the model in predicting the EQE trends for varying C_{60} thickness. But this model cannot be directly applied to our system since it was formulated for a multilayer case where exciton dissociation occurs only at the interface between two layers. In our case, the concentration gradient consists of a gradually decreasing density of donor – acceptor interfaces as the electrodes are approached from where the initial bilayer interface, prior to interdiffusion, was located. Hence, in order to incorporate the varying electric field intensity within the film, the following factors and modifications must be considered:

1. The phase of the field will be modulated by the refractive indices of the layers in which it is present. Hence, for a concentration gradient device, the refractive index at any point in the active layer should be an average of the refractive index values of each individual component weighted by their relative concentrations at the point of consideration.
2. The absorption (α) too would be affected depending on the position in the film and would similarly be an average of the αs of the individual layers, weighted by the relative concentrations of the materials within the film.
3. The transfer matrix model proposes the efficiency parameter θ_1, which is the exciton generation efficiency (# of excitons generated for the # of photons absorbed). This is a material dependent property and hence would be different for the donor and acceptor materials. Thus the net θ_1 would also show a dependence on the position in the active layer under consideration and would be an average of the θ_1s of the

individual layers, weighted by the relative concentrations of the materials within the film.

4. The transfer matrix model also proposes the efficiency parameter θ_2, which is the exciton dissociation efficiency (# of electrons separated for the # of excitons generated). This parameter is dependent on the availability of the interface and hence dependent on the concentrations of *both* the components at any point in the film. Thus it would be a product of the relative concentrations of each component at any point in the film. It will be a maximum at the center and zero at the electrodes for an ideal concentration gradient profile. It is also dependent on the ability of the interface, when present, to dissociate an exciton that is near it (which is the effectiveness of the choice of the donor and acceptor materials).
5. Charge transport factors should have to be considered. This could be assumed to have a probability distribution of transport starting from a low value at the center of the film going to 1 at the electrodes, dependent the lack of interfaces. The density of interfaces at any point in the films is given by the product of the relative concentrations as seen from point 4. Thus, this could be given by 1 minus the product of the donor and acceptor concentrations, as a simple approximation for the concentration gradient.

It should be noted that phase-separated regions, mobilities of the separated charges and charge collection efficiencies have not been considered in these proposed changes. Most of these parameters are constants in the proposed model and hence do not contribute to the integrals in the calculation. Including these parameters would make the calculation rather involved but would probably accurately predict the EQE curves for concentration gradient devices.

[1] L. A. A Pettersson, L. S. Roman, O. Inganäs, "Modeling Photocurrent Action Spectra of Photovoltaic Devices Based on Organic Thin Films," *J. Appl. Phys*. **86**(1), 487-496 (1999).
[2] P. Peumans, A. Yakimov, S.R. Forrest, "Small Molecular Weight Organic Thin – Film Photodetectors and Solar Cells," *J. Appl. Phys*. **93**(7), 3693-3723 (2003).

Chapter 8

Conclusions & Suggestions for Future Work

An in-depth study of the concentration gradient in thermally-interdiffused polymer – fullerene photovoltaic devices, with a focus on the thickness and heat treatment dependence, has been conducted and presented in this thesis. P3OT has been the donor material for this work and the main study was conducted with C_{60} as acceptor. PCBM and $Sc_3N@C_{80}$ have also been investigated as acceptor materials, and a brief study was done to optimize concentration gradients using these materials. All devices have been characterized and compared with respect to external quantum efficiency curves (EQEs) and the current density – voltage (J-V) characteristics. The short circuit current densities (J_{SC}), open circuit voltages (V_{OC}), fill factors (FF) and overall power conversion efficiencies (η) have been extracted from the fourth quadrant of these characteristic curves, as obtained under 470 nm monochromatic illumination. An experimental set up to simulate AM1.5 solar irradiance was constructed towards the end of the work. Therefore, similar values under AM1.5 illumination have also been presented, where applicable.

<u>P3OT – C_{60}</u>

For the P3OT – C_{60} system, initial studies were conducted on the different types of device morphologies such as the single polymer layer, bilayer and blend devices and were compared with thermally-interdiffused (ID) devices to see if this method of fabrication was a useful option for the P3OT – C_{60} system. Blend devices consisted of a 1:1 ratio of the polymer and fullerene. The comparison was made between devices of similar active layer thicknesses. Upon addition of C_{60} to the polymer layer, more than two orders of magnitude increase was seen in the EQEs, as compared to the single layer device, confirming C_{60} as a good choice for use as an acceptor with P3OT. The ID device showed the highest EQEs, almost 3 times that of the bilayer or blend devices. The blend showed values comparable to that of the bilayer, which is unexpectedly low and leads us to believe that we have probably not achieved the optimal blend morphology for this

system. Nevertheless, this study served to show that interdiffusion was a useful viable device processing option.

To confirm that the heat treatment of the bilayer did indeed produce interdiffusion and a concentration gradient, Auger spectroscopy studies were done on the films. Auger spectroscopy, combined with argon ion-beam milling, was used to obtain the concentration depth profile of films by monitoring the presence of P3OT by the detection of sulfur in a film. The ID device showed a gradual increase in the polymer content of the film as compared to a sharp increase in the case of the bilayer. This served as evidence of interdiffusion and concentration gradient formation when a bilayer is heated.

Blend devices were briefly investigated for optimization by studying the solution processing steps prior to film deposition as well as various thermal treatments of the deposited films. Films cast from these blends showed visible phase separation which we attempted to reduce by trying to dissolve the C_{60} more efficiently before mixing the two components. C_{60} was either sonicated in solution for a few minutes or it was stirred over night, prior to mixing with P3OT and spin-casting. The solutions that were stirred overnight showed marginally better performance over most of the wavelength range. Thermal treatments consisted of either annealing the blends for about 10 minutes before Al electrode deposition, in order to compare it with similarly thermally processed ID devices, or annealing it for about 30 minutes after Al deposition to compare it with a similar procedure reported for P3HT – PCBM blends. Blend devices showed almost 4 to 5 times improvement when annealed, with EQEs at 470 nm going from 1.1 for no annealing to 6.3 for annealing post – Al deposition to 8.2 for annealing pre – Al deposition. This study indicated that annealing blends improved the device performance, probably due to the increased crystallinity of the individual components, but it remained inconclusive about which annealing method yields better results. These results may serve as a starting point in a more extensive blend optimization study so that a fair comparison may be made to evaluate the effectiveness of the ID process.

The main part of this thesis consisted of the study of the dependence of device performance on the thickness of the initial donor and acceptor layers for a constant set of ID conditions (heating at 118 °C for 5 minutes, with an over-swing to 134 °C, and then allowing the sample to cool naturally under an atmosphere of argon). The P3OT layer

was annealed at 120 °C for over 35 minutes, prior to C_{60} deposition and interdiffusion. By fixing the annealing and ID conditions, the extent of the concentration gradient region produced by the ID process was fixed. Thicknesses of the layers were varied from 15 nm to 110 nm each.

A comparison of the devices with either very high or very low thicknesses gave us an insight into how individual layers affect the shape of the EQE curve, especially in terms of the absorption efficiency of each layer. The filter effect, seen as a dip in the curve in high absorption regions, occurs as a consequence of imbalanced layer thicknesses, where the excess of P3OT would reduce the peak at 450 nm and the excess of C_{60} would reduce the peak at 350 nm. When either layer is thin, the absorption efficiency of that layer is reduced. Extreme thicknesses did not yield optimum device performance. The best device had a 59 nm thick P3OT layer and 38 nm thick C_{60} layer and reached an EQE maximum of around 36% at 430 nm. In comparison, the EQEs for the extreme thickness devices were all within a few percent of 15%. Similarly for η at 470 nm illumination, the best device showed 2.05 % while the rest were distributed within 0.35% to 0.75%. The V_{OC} and FF values showed very minor variations with thickness.

After considering the extremes, gradual thickness variation for each individual layer while keeping the other layer constant at the predicted optimum thickness value was studied. For C_{60} layer thickness kept constant around 40 to 50 nm, as the P3OT thickness went from low to high values, P3OT absorption efficiency improved, seen as an increase in the 450 nm peak as well as the overall EQE. A maximum was reached for P3OT thickness of 59 nm, beyond which filter effect due to pure P3OT was observed. η (470 nm) showed a similar trend going from 0.61% to 2.05% and back down to 0.37% for P3OT thicknesses increasing from 15 nm to 108 nm. When P3OT was kept constant between 50 to 60 nm and C_{60} thickness varied, the overall EQE reached a maximum for C_{60} thickness of 38 nm. This trend in overall performance is in agreement with the ~ 40 nm optimum thickness value predicted by the model for the distribution of electric field intensity within the film as proposed by Pettersson *et al*. In addition to this, the absorption efficiency and filter effect consideration (similar to the P3OT thickness variation case) are also observed for the 350 nm peak. The η (470 nm) showed an

increase from 0.35% for 22 nm to 2.05% for 38 nm and back down to 0.54% for 84 nm C_{60} thicknesses.

The previous two comparisons yielded specific thickness values since specific devices were considered. Practically, the optimum values fall within a range of thicknesses which was inferred by taking into account all 50 to 60 devices that were measured. These devices were categorized into 20 nm thickness bins and averaged within each bin. Maximum EQE (470 nm) and η (470 nm) were obtained for P3OT and C_{60} thickness within the 40 to 60 nm bins, each. The V_{OC} and FF however, did not show any significant trends which is consistent with the theory that V_{OC} is affected more by choice of materials and intensity of incident light than internal device morphology.

Concentration depth profiles, measured using Auger spectroscopy, showed trends in the concentration gradients that allowed us to correlate morphology with device performance as well as deduce the optimum gradient morphology that would yield the most efficient devices. Auger spectroscopy confirmed our assumption that, given enough material, a constant set of annealing and thermal ID conditions will yield the same concentration gradient (seen as similar slopes in the profile). Thick layers showed regions of pure material flanking the concentration gradient, which is in agreement with the filter effect observed for these devices. The profile for thin layers (when P3OT or C_{60} thickness is less than half the thickness range of the concentration gradient) showed a pile up of P3OT at the cathode (Al boundary) and C_{60} at the anode (ITO boundary) which would affect the charge collection efficiency at the electrodes and hence would also contribute to the reduction in device performance. A reduction in the slope of the concentration gradient also indicated back diffusion of material due to this inversion in concentrations which would give the device a more blend-like character. The profile observed for the best devices had a concentration gradient that extends throughout the active layers of the device, ending just short of the electrodes, thereby maintaining a thin layer of pure material to facilitate charge collection.

The observations made from the thickness variation study and subsequent analysis using Auger spectroscopy agreed with our prediction of the ideal morphology based on an optimum balance of the charge transfer, transport and collection processes. To achieve this, the ID conditions were kept constant and the thicknesses varied. Such morphology

can also be achieved by varying the extent of ID for a given set of thicknesses. The dependence of the extent of ID on the ID time and temperature was briefly investigated. The importance of annealing the P3OT, prior to C_{60} deposition was also studied. We initially expected that the crystalline P3OT that is obtained after annealing would hinder the ID process, and so devices were fabricated both with and without the initial annealing step and Auger measurements were done to see if any variation in the concentration gradients could be detected. The aim of the following mini-investigations was to identify basic trends in device performance based on the thermal considerations in concentration gradient devices so as to establish a direction for future work on further concentration gradient device optimization.

In the time variation study, annealed and non-annealed devices were heated for ID at 135 °C under vacuum for either 5 or 20 minutes Thick (~ 90 nm) and intermediate (between 50 and 60 nm) P3OT and C_{60} thickness devices were studied. Auger spectroscopy was used to measure the concentration depth profiles of these devices. In general, annealed devices were better than the non-annealed ones. For devices interdiffused for 5 minutes, there was a noticeable difference between these two cases, showing an improvement in the EQEs upon annealing, from around 6.5% to almost 10%, for 2 devices with similar layer thicknesses. On the other hand, the devices heated for 20 minutes showed less of a performance dependence on prior annealing. Annealing the POT layer increases the hole transport mobility of the polymer by increasing its crystallinity. In the case of heat treatment for 20 minutes, the non-annealed P3OT would undergo some crystallization during the ID step and hence bridge the gap in the crystallinity between the two devices. On the other hand, the 5 minute heat step is too short to make up for the lack of annealing and hence the larger difference in the device performance. Auger spectroscopy revealed no difference in the concentration gradients of the annealed and non-annealed devices, indicating a lack of dependence of the ID process on the initial crystallinity of the P3OT layer. This would allow for devices to be made with increasingly more crystalline polymer layers without having to worry about the interdiffusion morphology being affected and thereby increasing the efficiency of the devices. The Auger study also revealed that the longer ID time produced a more spread out and gradual rising concentration gradient than when heated for 5 minutes. The best

devices were once again obtained for cases where the concentration gradient extended through most of the film, thereby reaffirming the similar conclusion from the thickness variation study. A value of 1.8% was obtained for the η (470 nm) of this device.

A similar study was conducted for varying the ID temperature for a constant ID time. This time all the devices had prior annealed P3OT layers. The devices were heated for ID for 10 minutes, at 80 °C and 125 °C, in an argon atmosphere. P3OT thicknesses of ~ 50 nm and ~ 95 nm were considered while C_{60} thickness was maintained between 30 and 45 nm. The Auger spectroscopy showed less ID for the lower temperature and consequently worse device performance (0.34% efficiency at best, for 470 nm illumination). The device heated at 125 °C showed a more extended concentration gradient and higher efficiencies of up to 1.2 %, under 470 nm illumination.

This investigation has opened up scope for further improvement of concentration gradient devices through thermal control of interdiffusion parameters. Device optimization may be tried for thicker P3OT and C_{60} layers in order to increase the absorption efficiency and hence device performance.

P3OT – PCBM

PCBM was investigated as a solution-processable alternative to C_{60}. It was discovered that PCBM could not be evaporated without destroying its structure. Hence, PCBM was deposited by spin-coating from a solution in pyridine, the only solvent we found that would not remove the P3OT layer below. An initial study was done to ensure that no P3OT was washed away in this process. Optical density measurements were taken for a layer of P3OT before and after spin-coating a layer of pure pyridine. There was no noticeable change detected in the spectrum, confirming that the P3OT layer was not removed and that PCBM could be deposited from a solution in this solvent.

PCBM in pyridine did not effectively wet the P3OT surface, giving rise to non-uniform films. PCBM film quality was improved by first dropping pyridine on a spinning P3OT coated substrate and subsequently dropping the PCBM solution on it while the earlier pyridine had not yet evaporated. The pyridine provided an intermediate wetting layer that improved the uniformity of the films.

Bilayers and heated bilayers (118 °C, 5 minutes) were studied for varying thicknesses conditions. Both sets of devices mirrored the thickness variation trends discussed for the P3OT – C_{60} system (low absorption efficiencies for thin layers and filter effect for thick layers). A varied trend was observed for the heated devices. There was an improvement by a factor of 2 in the case of the thin layer devices where as the thicker ones did not show much difference before and after heating. Auger spectroscopy revealed evidence of interdiffusion in the bilayer device which might be because bilayers were cast with a pyridine wetting layer before the PCBM layer and may show some solution induced interdiffusion due to the swelling of P3OT in prolonged exposure to pyridine. Heating a bilayer at 118 °C for 5 minutes does not seem to yield as much interdiffusion as it did for the P3OT – C_{60} system and hence higher temperatures were attempted for interdiffusion.

Heat treatment of a bilayer at 150 °C for 10 minutes yielded better results than the lower temperature case. Post production heat treatment, which involved annealing after the electrode deposition, was investigated for these devices. Devices that were heated prior to Al deposition all showed consistently large EQEs, almost reaching 30% at around 500 nm. Monochromatic efficiencies of up to 1.75% were obtained for these devices at 470 nm illumination. The post production heat treatment showed potentially better results in terms of the EQE (~ 33%), but they did not have a very high efficiency (0.88% at best). In the future, more work on optimizing this method might improve the output of interdiffused P3OT – PCBM devices.

1:1 and 1:2 P3OT – PCBM blends were also studied in order to provide a comparison for the interdiffused devices. These devices were either not heated or they were heated after Al deposition at 150 °C for 25 minutes. The post-Al heating showed inconsistent results due to damage of some of the electrodes during heating. On the other hand, the unheated devices seemed to show some of the largest efficiencies at 470 nm, reaching up to 4.17%.

The studies conducted on PCBM with P3OT were preliminary. Hence, more work needs to be done to optimize the post-production heating process as well as to identify appropriate interdiffusion temperatures and times. A better understanding of the effects of annealing and crystallinity might improve the interdiffused device performance.

P3OT – $Sc_3N@C_{80}$

The trimetasphere (TMS) endohederal fullerene $Sc_3N@C_{80}$ has shown promise as an acceptor material suitable for use with P3OT. In this first investigative study, various heat treatment procedures have been applied in order to obtain a suitable set of thermal parameters that would produce a concentration gradient. It was seen that this system required much more heat in order for the layers to interdiffuse.

This study was done over a course of 12 months and a long time-scale deterioration of device performance was seen which is attributed to unknown degradation mechanisms. Hence, in the future, the material should be stored in an inert environment when not being used. Due to this degradation, a comparison cannot be made between data taken over the whole 12 months. Therefore, the deduction of the optimized interdiffusion parameters was done with the aid of Auger spectroscopy and by the comparison of devices fabricated within short spans of time. Hence, the conclusions from this section will also be given in terms of the chronology of the experiments performed.

Early experiments were done on bilayers and devices heated at 118 °C for 5 minutes as in the case of the P3OT – C_{60} system. An order of magnitude improvement was seen for the bilayer device when compared with a P3OT single layer device, showing an EQE of around 3.75% for 540 nm. When this bilayer is heated, only a marginal improvement is seen in the EQE which shows a maximum of 5.3% at 540 nm. These devices were seen to follow thickness variation trends as described for the P3OT – C_{60} system; as the layers increase in thickness, there is an appearance of the filter effect. The Auger spectroscopy show similar concentration gradients as for the heated device and the bilayer, which would explain why there was only a marginal improvement.

In the next set of experiments, heat treatment conditions were varied. The ID temperature was raised to 150 °C and the time increased to either 10 or 20 minutes. Interdiffusion was also attempted during deposition of the TMS by heating the substrate during deposition. Within this set, the highest EQEs obtained were around 2% for the peak at 430 nm which was for the device that was heated for ID at 150 °C for 10 minutes.

Even at this temperature, the Auger curves yielded a large P3OT plateau as well as curves that were still very similar to that of a bilayer.

To establish an upper limit to the ID temperature, the devices were heated at and above the melting point of P3OT at 180 °C and 200 °C. The Auger for these have shown a curious reversal of layers that could occur due to free diffusion (the polymer is very soft above the melting point) and preferential accumulation of P3OT on the surface. Hence, the optimum temperature was deduced to lie between 150 °C and 180 °C. This was found to be at 160 °C at which the interdiffused devices showed the best concentration gradients and also the best device performance within their circle of comparison. The highest EQE obtained for this set was around 0.7 % at 430 nm, for a device heated at 160°C for 25 minutes. The Auger for a device that was similarly processed showed a concentration gradient that stretched all through the film, which is like the optimum gradient seen for the previous two cases.

Judging by the Auger spectroscopy data obtained, we have identified the optimum temperature and time required to interdiffuse the P3OT – $Sc_3N@C_{80}$ at 160 °C for 25 minutes. This is just a starting step for further investigation into this system. To prevent degradation, the TMS should be stored in an inert environment. Also, the current films are too thin and so thickness of the deposited layer needs to be improved. A calculation of the solubility parameters of the TMS might yield solvents that would allow for either dual spin-casting of the donor and acceptor layer as in the case of the P3OT – PCBM system, which might yield thicker films of the acceptor. Functionalization of the TMS would also render it more soluble. Enhanced solubility would also allow for usage of this acceptor in blend devices.

Modeling of EQE Spectra

A model for EQE spectra has been developed based on Beer's law of absorption and approximating the interdiffused device to three regions. The model only correctly follows the measured relative magnitudes of the EQE spectra for the case of varying P3OT thickness. This initial model does not reflect the changes in the EQE experimentally observed for varying C_{60} thickness. Including the dependence of absorption in the

interdifffused region on the electric field distribution after reflection is expected to improve the predictive capability of the model.

General Concluding Remarks

A universal conclusion that has come out of the study of all three systems is that the best devices are obtained for a concentration gradient that extends all the way through the film ending just before the electrodes are reached, thereby creating a bulk heterojunction in the middle of the device (for efficient charge transfer), with materials that get purer as the electrodes are approached (to improve charge transport) and finally end in pure material at the electrode (to not hinder the charge collection process).

Annealing the P3OT layer is generally beneficial and does not hinder the interdiffusion process. Hence, greater annealing conditions may be investigated for future devices.

The interdiffusion study in this thesis was subjected to non-controlled cooling rates. The time taken to cool the device could determine the crystallinity and internal molecular morphology of the device. An active cooling approach, with well defined cut-off temperatures, combined with a morphology study by means of TEM might give us a better idea of the molecular morphology of the interdiffused devices at various stages of the heating and cooling cycle which could help control and optimize concentration gradient devices on a more microscopic level.

In certain temperature controllers, external parameters may be tuned to obtain a more controlled heating profile. In this case the heating rates could be better adjusted to suit specific required interdiffusion conditions. A Linkam hot-stage may be a good starting point to achieve more controlled heating and for use in in-situ heating studies.

When organic photovoltaic devices are exposed to air and light they tend to deteriorate due to photo-oxidation of the polymer. Generally, the exposure of the devices to air during fabrication and characterization is minimized as far as possible. But an encapsulating material that acts as a barrier to oxygen and moisture, while allowing it to perform as a solar cell, would be ideal. One factor for consideration would be to find an

epoxy that would not deteriorate the device either through mechanical contact or due to outgassing during the curing process.

Throughout this study, limitations due to charge transport have not been considered. This may be investigated by studying device performance dependence on the number of oxidative traps present in the film. Baking the device in an atmosphere of ammonia might reduce the number of oxidation sites on the polymer, thereby increasing charge transport and eventually the efficiency. Such a study could prove more valuable if PPVs were investigated as donor materials.